

Advanced Steel Design of Structures

Srinivasan Chandrasekaran



@Seismicisolation



CRC Press
Taylor & Francis Group

Advanced Steel Design of Structures



Taylor & Francis

Taylor & Francis Group

<http://taylorandfrancis.com>

@Seismicisolation

Advanced Steel Design of Structures

Srinivasan Chandrasekaran



CRC Press

Taylor & Francis Group

Boca Raton London New York

CRC Press is an imprint of the
Taylor & Francis Group, an **informa** business

@Seismicisolation

MATLAB® is a trademark of The MathWorks, Inc. and is used with permission. The MathWorks does not warrant the accuracy of the text or exercises in this book. This book's use or discussion of MATLAB® software or related products does not constitute endorsement or sponsorship by The MathWorks of a particular pedagogical approach or particular use of the MATLAB® software.

CRC Press
Taylor & Francis Group
6000 Broken Sound Parkway NW, Suite 300
Boca Raton, FL 33487-2742

© 2020 by Taylor & Francis Group, LLC

CRC Press is an imprint of Taylor & Francis Group, an Informa business

No claim to original U.S. Government works

International Standard Book Number-13: 978-0-367-23290-0 (Hardback)

This book contains information obtained from authentic and highly regarded sources. Reasonable efforts have been made to publish reliable data and information, but the author and publisher cannot assume responsibility for the validity of all materials or the consequences of their use. The authors and publishers have attempted to trace the copyright holders of all material reproduced in this publication and apologize to copyright holders if permission to publish in this form has not been obtained. If any copyright material has not been acknowledged, please write and let us know so we may rectify in any future reprint.

Except as permitted under U.S. Copyright Law, no part of this book may be reprinted, reproduced, transmitted or utilized in any form by any electronic, mechanical or other means, now known or hereafter invented, including photocopying, microfilming and recording, or in any information storage or retrieval system, without written permission from the publishers.

For permission to photocopy or use material electronically from this work, please access www.copyright.com (www.copyright.com/) or contact the Copyright Clearance Center, Inc. (CCC), 222 Rosewood Drive, Danvers, MA 01923, 978-750-8400. CCC is a not-for-profit organization that provides licenses and registration for a variety of users. For organizations that have been granted a photocopy license by the CCC, a separate system of payment has been arranged.

Trademark Notice: Product or corporate names may be trademarks or registered trademarks and are used only for identification and explanation without intent to infringe.

Visit the Taylor & Francis Web site at
www.taylorandfrancis.com

and the CRC Press Web site at
www.crcpress.com

Contents

List of Figures	ix
List of Tables	xiii
Foreword by Jeom Kee Paik	xv
Foreword by Mubarak Wahab.....	xvii
Preface	xix
About the Author	xxi
Chapter 1 Introduction.....	1
1.1 Introduction	1
1.2 Compliant offshore platforms	2
1.3 New-generation offshore platforms	5
1.3.1 Buoyant leg structures.....	5
1.3.2 Triceratops.....	6
1.3.3 Buoyant leg storage regasification platform	7
1.4 Design of stiffened cylindrical shell structures.....	9
1.5 Unsymmetrical bending	15
1.6 Curved beams.....	32
1.6.1 Bending of curved beams with small initial curvature.....	33
1.6.2 Deflection of the curved beam with small initial curvature.....	35
1.6.3 Curved beam with large initial curvature	36
1.6.4 Simplified equations to estimate stresses in the extreme fiber	41
Exercise problems	41
Chapter 2 Plastic Design of Structures	49
2.1 Plastic Behavior of Structures.....	49
2.2 Shape Factor	54
2.2.1 Rectangular Section	54
2.2.2 Triangular Section.....	55
2.2.3 Circular Section	57
2.3 MATLAB® Code for Calculating Shape Factor	58
2.4 Moment Curvature Relationship.....	63
2.5 Mechanism	65
2.6 Static Theorem	66
2.7 Kinematic Theorem.....	66
2.8 Uniqueness Theorem.....	68

2.9	Exercises to Estimates Collapse Load.....	68
2.9.1	Fixed Beam with a Central Point Load.....	68
2.9.2	Fixed Beam with Uniformly Distributed Load	70
2.9.3	Simply Supported Beam with Eccentric Load.....	71
2.9.4	Simply Supported Beam with a Central Point Load	73
2.10	Advantages and Disadvantages of Plastic Analysis	74
2.10.1	Advantages	74
2.10.2	Disadvantages.....	74
2.11	Comparison of Elastic and Plastic Analysis	74
	Exercises	75
Chapter 3	Blast, Fire, and Impact-Resistant Design	89
3.1	Introduction	89
3.2	Blast-Resistant Design.....	89
3.2.1	Personnel Safety.....	90
3.2.2	Controlled Shutdown.....	90
3.2.3	Financial Consideration.....	90
3.2.4	Preliminary Design	91
3.2.5	Detailed Design	91
3.3	Blast Loads	91
3.4	Classification of Explosions.....	92
3.4.1	Vapour Cloud Explosions.....	92
3.4.2	Pressure Vessel Explosions.....	93
3.4.3	Condensed Phase Explosion	94
3.4.4	Dust Explosions.....	94
3.5	Blast Wave Parameters	94
3.5.1	Peak Reflected Pressure.....	96
3.5.2	Peak Dynamic Pressure.....	97
3.5.3	Shock Front Velocity	97
3.5.4	Blast Wavelength.....	97
3.6	Design Blast Load for Buildings.....	99
3.6.1	Front Wall Load	99
3.6.2	Side Wall Load	100
3.6.3	Roof Load	102
3.6.4	Rear Wall Load.....	102
3.6.5	Frame Loading	103
3.6.6	Negative Pressure, Leakage Pressure and Rebound Load	104
3.7	Design Example: Computation of Blast Overpressure for a Rectangular-Shaped Building.....	104
3.8	Fire Load	108

3.9	Categorization of Fire	109
3.10	Characteristics of Fire	110
3.10.1	Auto-Ignition Temperature	110
3.10.2	Flashpoint.....	111
3.10.3	Fire Point	111
3.11	Classification of Fire	111
3.12	Fire Protection Systems in the Design	113
3.13	Steel at High Temperature.....	114
3.14	Example Case Study: Behavior of an Offshore Deck Plate Under Hydrocarbon Fire.....	116
3.15	Design for Fire	119
3.15.1	Zone Method	119
3.15.2	Linear Elastic Method	119
3.15.3	Elastic–Plastic Method	119
3.16	Impact Loads Due to Ship–Platform Collision	120
3.16.1	Kinetic Energy	121
3.17	Energy Absorption	122
3.18	An Example Problem on Ship Collision	124
3.19	Impact Analysis of Buoyant Legs of Offshore Triceratops	124
3.20	Functionally Graded Material.....	129
3.20.1	Material Characteristics of FGM.....	132
Chapter 4	Stability of Structural Systems	133
4.1	Conditions of Stability	133
4.2	Buckling and Instability	134
4.3	Euler Critical Load.....	139
4.4	Standard Beam Element, Neglecting Axial Deformation.....	141
4.4.1	Rotational Coefficients.....	147
4.5	Stability Functions	150
4.5.1	Rotation Functions Under Axial Compressive Load	150
4.5.2	Rotation Functions Under Zero Axial Load (Special Case).....	154
4.5.3	Rotation Functions Under Axial Tensile Load	155
4.5.4	Translation Function Under Axial Compressive Load	156
4.6	Lateral Load Functions Under Uniformly Distributed Load	159
4.7	Fixed Beam Under Tensile Axial Load.....	163
4.8	Lateral Load Functions for Concentrated Load.....	164

4.9	Exercise Problems on Stability Analysis	168
4.10	Critical Buckling Load	201
Chapter 5	Mathieu Stability of Compliant Structures.....	231
5.1	Introduction	231
5.2	Mooring Systems	231
5.3	Mathieu Equation	233
5.4	Mathieu Stability for Compliant Structures	234
5.5	Mathieu Stability of Triceratops.....	235
5.5.1	Formulation of Mathieu Equation.....	236
5.5.2	Mathematical Model.....	238
5.6	Influence of Parameters on Stability.....	239
5.6.1	Influence of Wave Height	239
5.6.2	Influence of Wave Period	242
5.6.3	Influence of Water Depth.....	243
5.6.4	Influence of Tether Stiffness	245
5.6.5	Influence of Increased Payload	246
5.7	Mathieu Stability of BLSRP.....	248
5.7.1	Numerical Modeling.....	248
5.7.2	Mathieu Stability Under Tether Pullout.....	250
5.7.3	Mathieu Stability Analysis Under Eccentric Loading	255
5.8	Numerical Modeling Example of Triceratops.....	258
5.8.1	Typical Plots of Members Showing Instability.....	263
5.9	Numerical Model of BLSRP	263
References.....	265	
Index.....	277	

List of Figures

Figure 1.1	Conceptual figure of TLP (Chandrasekaran, 2015b).....	3
Figure 1.2	Neptune TLP (Chandrasekaran, 2015b)	3
Figure 1.3	Tension Leg Platform mechanics (Chandrasekaran, 2015b).....	4
Figure 1.4	Buoyant leg structures.....	6
Figure 1.5	Triceratops	7
Figure 1.6	Buoyant leg storage regasification platforms	8
Figure 1.7	BLSRP scaled model installed in the wave flume.....	8
Figure 1.8	Buckling modes in orthogonally stiffened cylinders (DNV-RP-C202)	9
Figure 1.9	Uniform bending.....	15
Figure 1.10	Typical cross section.....	17
Figure 2.1	Bending of beams.....	50
Figure 2.2	Plastic deformation	51
Figure 2.3	Force-equilibrium condition.....	51
Figure 2.4	Elastic core.....	53
Figure 2.5	Rectangular section	55
Figure 2.6	Triangular section	56
Figure 2.7	Fully plastic triangular section	56
Figure 2.8	Circular section	57
Figure 2.9	T-section	61
Figure 2.10	T-section with equal area axis	62
Figure 2.11	I-section	62
Figure 2.12	I-section with equal area axis	63
Figure 2.13	Collapse mechanisms	67
Figure 2.14	Plastic analysis theorems	68
Figure 2.15	Fixed beam with a central concentrated load	69
Figure 2.16	Fixed beam mechanism	69
Figure 2.17	Fixed beam with uniformly distributed load	70
Figure 2.18	Fixed beam mechanism under udl.....	71
Figure 2.19	Simply supported beam with eccentric load	71
Figure 2.20	Simply supported beam mechanism	72
Figure 2.21	Simply supported beam with a central concentrated load	73
Figure 2.22	Simply supported beam mechanism	74
Figure 2.23	Pinned cantilever beam with uniformly distributed load	75
Figure 2.24	Bending moment diagram	75
Figure 2.25	Beam mechanism	77
Figure 2.26	Fixed beam eccentric concentrated load.....	77
Figure 2.27	Fixed beam mechanism	78
Figure 2.28	Fixed beam example.....	78
Figure 2.29	Fixed beam mechanism	79
Figure 2.30	Frame example	80
Figure 2.31	Beam mechanism	80

Figure 2.32	Sway mechanism	81
Figure 2.33	Combined mechanism	82
Figure 2.34	Frame example	83
Figure 2.35	Beam mechanism	83
Figure 2.36	Sway mechanism	84
Figure 2.37	Combined mechanism	85
Figure 2.38	Continuous beam example	85
Figure 2.39	Beam mechanism 1	86
Figure 2.40	Beam mechanism 2	86
Figure 2.41	Beam mechanism 3	87
Figure 3.1	Shock wave	95
Figure 3.2	Pressure wave	95
Figure 3.3	Idealized shock wave	98
Figure 3.4	Idealized pressure wave	98
Figure 3.5	Idealized equivalent pressure load	98
Figure 3.6	Front wall load	100
Figure 3.7	Equivalent load factor for side wall and roof load. (Courtesy: UFC: 3-340-02, 2008.)	101
Figure 3.8	Roof and sidewall load	101
Figure 3.9	Rear wall loading	102
Figure 3.10	Net lateral load on the rectangular building	103
Figure 3.11	Building block and shock wave history	105
Figure 3.12	Variation of front wall load	106
Figure 3.13	Variation of side wall load	107
Figure 3.14	Variation of roof load	107
Figure 3.15	Variation of rear wall load	108
Figure 3.16	Material characteristics of carbon steel at high temperature	115
Figure 3.17	Thermal conductivity of carbon steel	115
Figure 3.18	Specific heat of carbon steel	116
Figure 3.19	Thermal strain of carbon steel	116
Figure 3.20	Stiffened steel plate of offshore deck	117
Figure 3.21	Middle bay under fire	117
Figure 3.22	Time–temperature curves for different fire conditions	118
Figure 3.23	Temperature distribution in the stiffened plate	118
Figure 3.24	Maximum deformation in the plate	118
Figure 3.25	Energy dissipation and design principles	121
Figure 3.26	Dissipation of strain energy in ship and platform	123
Figure 3.27	True stress–strain curve of AH36 marine steel	125
Figure 3.28	Cylindrical shell and indenter model	125
Figure 3.29	Indenter velocity	126
Figure 3.30	Indenter displacement	126
Figure 3.31	Deformation of the buoyant leg	127
Figure 3.32	Deformation of ring stiffener at the collision zone	127
Figure 3.33	Load versus nondimensional displacement curve	128
Figure 3.34	Energy absorbed by buoyant leg	128
Figure 3.35	Section of the functionally graded riser	130

Figure 3.36	Stress-strain curve of FGM	131
Figure 3.37	Comparison of stress-strain curves of individual materials used for grading	131
Figure 4.1	Unstable condition	135
Figure 4.2	Stability illustrations: (a) stable; (b) neutrally stable; (c) unstable	136
Figure 4.3	Torsional buckling of slender compression member	137
Figure 4.4	Cantilever under flexural torsional buckling	137
Figure 4.5	Lateral-torsional buckling of I-section	138
Figure 4.6	Euler column.....	139
Figure 4.7	Free-body diagram of the column member.....	140
Figure 4.8	Standard beam element	142
Figure 4.9	Rotational and translational moments in the standard beam ...	142
Figure 4.10	Unit rotation at the j th end of standard beam	143
Figure 4.11	Unit rotation at the j th end of standard beam	143
Figure 4.12	Unit displacement at the j th end of standard beam	143
Figure 4.13	Unit displacement at the k th end of standard beam	144
Figure 4.14	Rotation coefficients of standard beam	145
Figure 4.15	Unit rotation at the j th end of the simply supported beam.....	147
Figure 4.16	Unit rotation at the k th end of the simply supported beam.....	147
Figure 4.17	Unit rotation at the j th end of fixed beam	148
Figure 4.18	Unit rotation at the k th end of fixed beam	148
Figure 4.19	Simply supported beam with the unit moment at the j th end ...	149
Figure 4.20	Conjugate beam	149
Figure 4.21	Fixed beam under axial compressive load	150
Figure 4.22	Unit rotation at the j th end of fixed beam	150
Figure 4.23	Free-body diagram under axial load and unit rotation at the j th end	151
Figure 4.24	Unit rotation at the k th end under axial load	155
Figure 4.25	Unit translation at the j th end of the fixed beam under axial load.....	157
Figure 4.26	Fixed beam under uniformly distributed load and axial compressive load	159
Figure 4.27	Free-body diagram ($x < aL_i$)	159
Figure 4.28	Free-body diagram ($x > aL_i$)	161
Figure 4.29	Fixed beam under concentrated load and axial compressive load	164
Figure 4.30	Free-body diagram ($x < aL_i$)	165
Figure 4.31	Free-body diagram ($x > aL_i$)	167
Figure 5.1	Turret-mooring system	232
Figure 5.2	Mathieu stability chart	234
Figure 5.3	Mathieu extended stability chart (Patel & Park, 1991)	239
Figure 5.4	Numerical model of offshore triceratops	240
Figure 5.5	Tether tension variation in buoyant leg 1.....	241
Figure 5.6	Tether tension variation in buoyant leg 2.....	241
Figure 5.7	Tether tension variation in buoyant leg 3.....	241

Figure 5.8	Mathieu stability for different water depths.....	244
Figure 5.9	Mathieu stability chart for different tether stiffness	246
Figure 5.10	Mathieu stability chart for increased payload cases.....	248
Figure 5.11	Numerical model of BLSRP	249
Figure 5.12	Tether tension variation in buoyant leg 1.....	251
Figure 5.13	Tether tension variation in buoyant leg 2.....	251
Figure 5.14	Tether tension variation in buoyant leg 3.....	251
Figure 5.15	Tether tension variation in buoyant leg 4.....	252
Figure 5.16	Tether tension variation in buoyant leg 5.....	252
Figure 5.17	Tether tension variation in buoyant leg 6.....	253
Figure 5.18	Postulated failure cases: (a) one leg affected and (b) two legs affected	253
Figure 5.19	Mathieu stability chart for BLSRP under tether pullout cases.....	254
Figure 5.20	Eccentric loading on top of the buoyant leg (case 2)	255
Figure 5.21	Eccentric load between two buoyant legs (case 3).....	256
Figure 5.22	Eccentric load on top of two consecutive buoyant legs (case 4)	256
Figure 5.23	Mathieu stability chart for eccentric loading	257

List of Tables

Table 2.1	Shape factors.....	58
Table 3.1	Impulse functions.....	96
Table 3.2	Auto-ignition temperature for different materials.....	111
Table 3.3	Functionally graded marine riser details	130
Table 3.4	Structural properties of individual materials used for grading....	132
Table 4.1	Stability functions (negative sign indicates tensile axial load)....	218
Table 5.1	Properties of triceratops	240
Table 5.2	Tension variation in tethers for different wave height (wave period 15 s)	242
Table 5.3	Influence of wave height on Mathieu parameters (wave period 15 s)	242
Table 5.4	Tension variation in tethers for different wave frequencies	243
Table 5.5	Mathieu parameters for different wave frequencies (wave height 8 m)	243
Table 5.6	Dynamic tension variation in tethers for different water depths.....	244
Table 5.7	Mathieu parameters for different water depth	244
Table 5.8	Tension variation in tethers for different stiffness	245
Table 5.9	Mathieu parameters for different stiffness	245
Table 5.10	Total mass and reduced pretension	246
Table 5.11	Maximum tension variation under the increased payload	247
Table 5.12	Mathieu parameters for increased payload	247
Table 5.13	Structural properties of BLSRP (Chandrasekaran et al., 2015b).....	250
Table 5.14	Maximum tension amplitude in tethers for postulated cases of failure.....	254
Table 5.15	Mathieu parameters under postulated failure	254
Table 5.16	Tether tension variation for different eccentric loading cases	257
Table 5.17	Mathieu parameters under eccentric loading	257
Table 5.18	Structural properties of triceratops and BLSRP of example problems	258



Taylor & Francis

Taylor & Francis Group

<http://taylorandfrancis.com>

@Seismicisolation

Foreword

Jeom Kee Paik

Department of Mechanical Engineering, University College London

Steel-framed structures are found in many engineering systems, including infrastructures such as building, bridge, tower and offshore platforms. While in service, they are rarely subjected to extreme conditions and accidents such as fires, explosions and collisions, which may lead to catastrophes to personnel, asset and the environment.

This book introduces advanced methods for designing steel-framed structures in association with extreme conditions and accidents. Load characteristics of accidents such as fires, explosions and collisions are presented. Analysis of impact load effects is given in closed-form solutions. Structural instability due to extreme conditions is described in detail with analytical solutions. The structural responses under extreme conditions and accidents are obviously highly nonlinear, and thus the book presents elastic-plastic design methods. Reliability of steel-framed structural design largely depends on the degree of rotational restraints at joints of steel-frame elements, among other factors. This book describes the details to accurately take into account the effects of the rotational restraints at joints of steel frames.

Analysis and design of structures under extreme conditions and accidents is a challenging area, not only because of the highly nonlinear aspects but also because of the difficulties in interacting between multiple physical processes and multiple criteria. Nonlinear structural responses are due to not only geometrical nonlinearities (e.g., buckling, large deformation) but also material nonlinearities (e.g., plasticity). Thus, it is important to better understand the nonlinear behavior of structures under extreme conditions and accidents. Approximate but closed-form solution methods are useful at the preliminary design stage, although more refined numerical computations and large-scale physical model testing may need to be applied at later design stages.

This book is a handy source covering most of these aspects in varying degrees in the individual chapters and associated exercises. I believe that this book will be useful for university students and industry practitioners who deal with advanced design of steel-framed structures under extreme conditions and accidents.



Taylor & Francis

Taylor & Francis Group

<http://taylorandfrancis.com>

@Seismicisolation

Foreword

Mubarak Wahab, PE, PhD

Deputy Head, Offshore Engineering Center, Universiti Teknologi
PETRONAS, Malaysia

I am honored to write this foreword as advances in steel structure design is a highly sought-after topic in the domain of design of offshore structures. The offshore industry is a capital-intensive industry and is mostly dominated by steel structures. Any advances in design mean efficiency, effectiveness and cost-saving. Thus, the players in the offshore industry always welcome improvements. At the time of low oil price, as it currently is, any improvement, that is, lowering of the cost in capital expenditure as well as in operating expenses, means big changes in profitability and sustainability. The capital-intensive industry is vulnerable to economic slowdown than labor-intensive industry because of fixed costs such as overhead for structures, appurtenances, plants, equipment and depreciation on the assets. In addition to this, utilizing steel structures in the offshore industry has numerous advantages. Higher strength-to-weight ratio justifies the choice of material, cylindrical and sturdy shape justifies the geometry, lower life-cycle cost considering rapid construction process yields early return on investment, higher ductility and toughness to resist accidental loads enables it to be the better choice for the rough and busy ocean environment and so on. Meanwhile, Professor Srinivasan Chandrasekaran, whom I know for the past couple of years, has been instrumental in providing significant contributions to the engineering fraternity with his numerous activities in the area of teaching, research, publication, undergraduate and postgraduate student supervision, conducting short courses and seminars as well as involving himself in national and international consultancies. His current venture into publication of this book is timely, considering that the demand for oil and gas is ever-increasing due to the economic growth of developing countries and the depletion of near-shore resources, which has left us with no choice than moving toward deeper waters. Advancements in technology in exploration and drilling have also made it possible to move into deeper waters. This book aptly discussed the so-called new-generation offshore platforms (compliant platforms) where steel is used as the main constructional material. When discussing compliant platforms, stability of structural systems is critical. Stability is achieved by ensuring good structural configuration, satisfying static equilibrium conditions and compatibility and force-displacement relationships in all cases, including extreme and accidental cases. Concerning extreme cases, it is inappropriate not to talk about plastic design methodology, considering extreme loadings coming from fire, blast and impact. The book covers vastly on these topics, including shape factor, MATLAB® coding for calculating shape factor, moment-curvature relationship, static and kinematic theorems, uniqueness

theorem, classification of explosions, blast wave parameters, design blast loads, fire load, fire categorization, characteristics and classification, fire protection systems, steel at high temperature, design for fire, impact loads due to ship–platform collision, energy absorption, impact analysis of buoyant legs of offshore triceratops and functionally graded material. Meanwhile, touching on the stability of structural systems, the book extensively covers such topics as conditions of stability, buckling and instability, Euler critical load, standard beam element, neglecting axial deformation, stability functions, lateral load functions under uniformly distributed load, fixed beam under tensile axial load, lateral load functions for concentrated load, critical buckling load and MATLAB® code for stability chart. Finally, a specific chapter on Mathieu stability is presented. This has covered the mooring systems, compliant platforms specifically on Buoyant Leg Storage Regasification Platforms and Triceratops. This chapter also has presented the Mathieu's equation, Mathieu's equation for compliant structures, Mathieu stability of triceratops, influence of parameters on stability, Mathieu stability of BLSRP and numeric modeling example of Triceratops and BLSRP. Throughout the book, descriptions are available for compliant platforms, namely Buoyant Leg Structures, Triceratops and Buoyant Leg Storage Regasification Platforms, deriving the concept and fundamental principles from TLP. In short, this book explains the current advances in steel structure design related to floating compliant offshore platforms. The design principles are viewed from the perspective of plastic design; blast, fire and impact resistance design and stability of structural systems. Numerous exercises and problems are shown to be solved in MATLAB® code, which is an added value to the theoretical background provided by the book. Upon reading this book, one will find it easy to follow through the fundamental theorem, mechanics involved, design principle and procedure as well as the MATLAB® coding to solve the encountered problems. I hope that this book will become a premier reference for teachers, educators, students and professionals across the globe to learn, teach, and practice the essence of design of offshore structures relating to advances in structural steel design.

Preface

Advanced steel design explores the domain of research and understanding both analysis and design of steel structures in general and offshore compliant structures in particular. The convenience that steel possesses to recycling, repair and retrofit in comparison to other construction materials, both commercial and eco-friendly points of view is one of the primary advantages. The material strength of steel beyond yield value intuits the plastic design of structures but also warrants about the permanent plastic deformation under excessive loading. A chapter in plastic design deals with a few examples, highlighting the basics. Loads, acting on the offshore structures, are special that induces unsymmetrical bending. Also, geometric sections like curved beams are quite common in form-dominant elements. Both these topics are covered in detail while the concept is presented with many exercise problems, solved using MATLAB® code. Design of steel structures under conventional loads is well discussed in the literature. However, special attention is required to understand the design procedure under special loads such as blast, fire and impact. This book explains the concepts in a separate chapter dedicated to the structural design under fire, blast and impact loads. Recent advancement on functionally graded material and its use in marine risers are also presented.

Form-dominant design is highly advantageous in structures that require the recentering capability of a high order. Offshore compliant structures are special geometric forms of floating structures that operate under positive buoyancy. Common examples are offshore platforms and naval rescue vessels. While their stability is mainly governed by their hydrodynamic characteristics, structural stability can be examined using Mathieu stability equations and charts. One of the chapters of this book deals with the Mathieu stability of compliant structural systems, with applied examples on new-generation offshore production and exploration platforms. Numerical studies that are carried out on such offshore platforms are presented in detail for the benefit of the users as the details of the discussed subject are very scarce in the literature. Mathieu stability is investigated for two types of compliant structures, wherein various parameters that influence their stability are addressed through detailed numerical investigations.

Stability of structural systems is extremely important. They become more vital in offshore structures, as they alleviate the encountered environmental loads by their geometric form and not by their strength. While the configuration of any structural system is posed to a challenge under the given loads and boundary conditions, under the satisfied conditions of static equilibrium, compatibility and force-displacement relationships, it is said to be stable. Stability, therefore, demands an understanding of failure. This book includes a separate chapter which deals with the derivation of stability functions for fixed beam, using the classical matrix method of structural analysis. Numerical examples of frames under lateral loads are solved using MATLAB® program. Complete

coding, along with detailed input and output for the example problems are given in this chapter.

The author expresses his immense gratitude to all his teachers, research scholars, Graduate students and colleagues for their support and advice at various capacities. The author also expresses thanks to the Centre of Continuing Education, Indian Institute of Technology Madras, for extending administrative support in preparing the manuscript of this book. The author also thanks MATLAB® for permitting usage of MATLAB® codes throughout the text of this book.

About the Author

Srinivasan Chandrasekaran is currently a Professor in the Department of Ocean Engineering, Indian Institute of Technology Madras, India. He has teaching, research and industrial experience of about 27 years during which he has supervised many sponsored research projects and offshore consultancy assignments both in India and abroad. His active areas of research include dynamic analysis and design of offshore platforms, development of geometric forms of compliant offshore structures for ultra-deep water oil exploration and production, sub-sea engineering, rehabilitation and retrofitting of offshore platforms, structural health monitoring of ocean structures, seismic analysis and design of structures and risk analyses and reliability studies of offshore and petroleum engineering plants. He has been also a visiting fellow under the invitation of Ministry of Italian University Research to University of Naples Federico II, Italy for a period of 2 years during which he conducted research on advanced nonlinear modelling and analysis of structures under different environmental loads with experimental verifications. He has about 110 research publications in International journals and refereed conferences organized by professional societies around the world. Fourteen text books authored by him are quite popular among graduate students of civil and ocean engineering and recommended as reference material for class room studies and research as well. He also delivered 15 web-based courses on various subjects namely (i) dynamic analysis of ocean structures, (ii) ocean structures and materials, (iii) advanced marine structures, (iv) health, safety and management in offshore and petroleum engineering, etc. He is a member of many National and International professional bodies and delivered many invited lectures and key note address in the international conferences, workshops and seminars in India and abroad.



Taylor & Francis

Taylor & Francis Group

<http://taylorandfrancis.com>

@Seismicisolation

1 Introduction

1.1 INTRODUCTION

Steel, as a construction material, possesses a lot of salient advantages. High ratio of strength to weight overcomes the increase in cost (Chandrasekaran & Gupta, 2007a; Chandrasekaran & Srivastava, 2007; Chandrasekaran, Dubey and Tripati, 2006). Further, a lower life-cycle cost resulting from rapid construction process yields an early return on investment (RoI). Special structural properties of steel, namely increased ductility and toughness to resist accidental loads, make it the best choice for the infrastructure industry (Chandrasekaran et al., 2005, 2008a, 2010b, 2011b, 2006; Chandrasekaran & Gupta, 2007b). Convenience, steel possess to recycling, repair and retrofit are added advantages, both in commercial and eco-friendly points of view (Chandrasekaran et al., 2005, 2006c, 2007, 2003). With an increased initial cost of steel, as a construction material, it can result in a low life-cycle cost because of its early return (Chandrasekaran & Chandak, 2004b, 2003b; Chandrasekaran et al., 2003; Chandrasekaran, Dubey et al., 2006a). Steel structures enjoy lower periodic maintenance in addition to a lower cost of dismantling the structure. Further, from the architectural perspective, steel also possesses 3Fs namely feasibility, functionality and suitability for form-dominant design (Chandrasekaran and Roy, 2004a, 2004b, 2006; Chandrasekaran & Srivastava, 2006; Chandrasekaran et al., 2005, 2005a, 2007c, 2010a; Chandrasekaran & Roy, 2006; Chandrasekaran et al., 2005b). In particular, steel is the most commonly used construction material for offshore structures (Chandrasekaran, 2015a, 2015b; Chandrasekaran & Chandak, 2004a; Chandrasekaran, Jain et al., 2007a, 2007c). It is necessary to use steel in offshore structures as they are subjected to the environmental loads that arise from waves, wind, current, ice load, seabed movement, shock and impact caused by vessels, and fire loads that arise from hydrocarbon leaks (Chandrasekaran et al., 2007, 2004a, 2007b; Chandrasekaran & Jain, 2016b). For increased serviceability conditions, stiffness of the members are enhanced to avoid large deflections, while safety to both the user and the environment can be achieved by using material of higher strength and robustness (Chandrasekaran & Dubey, 2006; Chandrasekaran, Jain et al., 2006a). Steel, as a construction material, possesses both sets of advantages.

Stability of structural systems in general and steel structures, in particular, is extremely important; it shall continue to remain as a common domain of interest in structural engineering applications (Chandrasekaran, 2015b; Chandrasekaran, Muranjan et al., 2006b; Chandrasekaran, Seriono et al., 2008b, 2007c, 2009b). Stability is extremely important in offshore structures, as most of the compliant structures alleviate the encountered environmental loads by their geometric form and not by strength (Agarwal & Jain, 2003; Chandak & Chandrasekaran, 2009;

Chandrasekaran & Jain, 2002a, 2002b; Chandrasekaran et al., 2004a, 2004b; Chandrasekaran & Sharma, 2010a; Chandrasekaran & Thailammai, 2018). The configuration of any structural system is posed to a challenge under the given loads and boundary conditions (Chandrasekaran, Chandak et al., 2006a; Chandrasekaran, Jain et al., 2006b). However, if the structural configuration satisfies the conditions of static equilibrium, compatibility and force–displacement relationships, then it is said to be stable (Chandrasekaran & Gaurav, 2008; Chandrasekaran & Gupta, 2007a; Chandrasekaran et al., 2003; Chandrasekaran et al., 2008b; Chandrasekaran & Tripati, 2005, 2004). It is furthermore interesting to note that it has to remain stable even under the disturbances caused by accidental loads, geometric imperfections and eccentricities caused by construction irregularities (Chandrasekaran & Thomas, 2016a; Chandrasekaran et al., 2006, 2007d, 2007e, 2008b; Davenport, 1961). An unstable condition is often referred to as a failed state (Chandrasekaran & Khader, 2016). Even though such structure can withstand loads (maybe in a decreased magnitude), but it is considered as failed as it cannot perform its intended function (Chandrasekaran et al., 2009a).

Stability, therefore, demands an understanding of failure. Two types of failures are common in structural systems: material and geometry. In case of material failure, stresses exceed the permissible limits imposed by the codes for a pre-agreed design procedure (Fraldi et al., 2009; Serino et al., 2008a, 2008b, 2008c). Complications that arise due to the changes (or degradation) in the stress–strain relationship follow in such cases. However, more concern is with the latter type of failure, as this will disable the structural system to perform its intended function. It is more important in offshore structures for a simple reason that most of the compliant offshore platforms bank upon the recentering capacity (Chandrasekaran et al., 2006c, 2007, 2007h, 2007g). The following section explains the necessity of geometric stability in compliant new-generation offshore platforms.

1.2 COMPLIANT OFFSHORE PLATFORMS

The demand for oil and gas and the depletion of resources near shore have made the companies move toward deeper waters. Also, the sophisticated drilling and extraction technology also enhanced the possibility of oil and gas extraction in deep waters (Chandrasekaran et al., 2007a, 2007b, 2007c, 2007d, 2007e, 2007f, 2007g, 2007h). With the improved geophysical exploration technology, oil and gas deposits in the seabed can now be detected to a depth of 12 km. Thus, many new oil deposits have been discovered recently, and 481 larger fields have been discovered between 2007 and 2012 in deep and ultra-deep waters. It is highly important to note that the newly discovered offshore fields are comparatively larger than newly discovered onshore fields. It makes the ultra-deepwater production more attractive despite the higher extraction costs (Chandrasekaran et al., 2008a; Ertas & Lee, 1989; Glanville et al., 1991; Halkyard, 1996; Harding et al., 1983; Reddy & Swamidas, 2016). For example, let us consider offshore Tension Leg Platforms (TLPs). TLPs consist of vertical columns and pontoons, which are position-restrained by tethers as shown in Fig. 1.1. The columns and pontoons are designed as tubular members

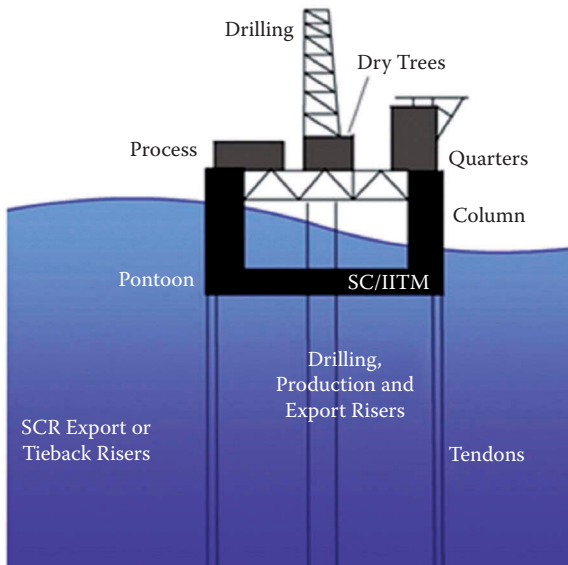


FIGURE 1.1 Conceptual figure of TLP (Chandrasekaran, 2015b).

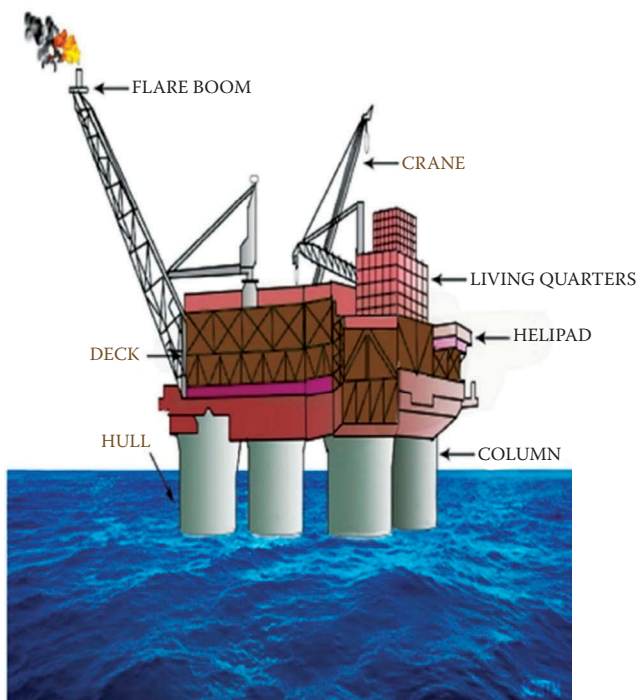


FIGURE 1.2 Neptune TLP (Chandrasekaran, 2015b).

to enhance the buoyancy of the structure (Chandrasekaran et al., 2012; Chandrasekaran & Thomas, 2016a). Figure 1.2 shows the Neptune TLP, indicating the main components. Taut-moored tethers balance the excess buoyancy (Chandrasekaran et al., 2010a, 2014, 2013c, 2011a, 2010b; Haritos, 1985). These tethers are wired ropes which are under very high initial pretension and are capable of sustaining very large tensile loads. TLPs are vertically moored compliant structures with a restrained heave, roll and pitch motions in a vertical plane and are compliant in a horizontal plane by allowing surge, sway and yaw motions (Chandrasekaran & Madavi, 2014a, 2014b, 2014c, 2014d, 2014e; Chandrasekaran et al., 2013c).

Figure 1.3 shows the TLP mechanics. Under the action of wave loads, the platform will move along the direction of waves, causing a set-down in the platform in the vertical plane (Chandrasekaran & Koshti, 2013; Jain & Chandrasekaran, 2004, 1997; Jefferys & Patel, 1982). This structural action also modifies the tether tension significantly. Apart from this fact, the most important is the recentering

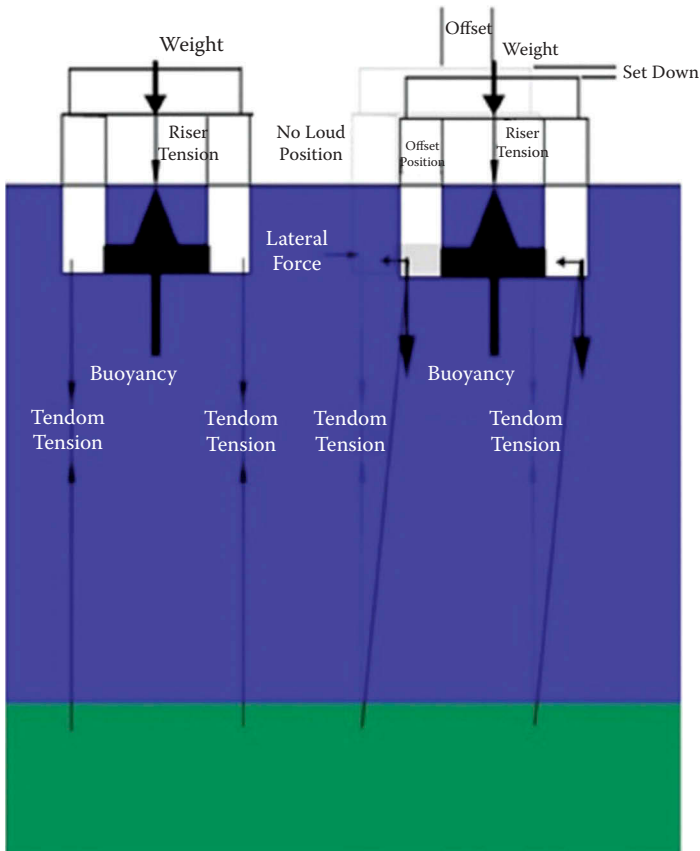


FIGURE 1.3 Tension Leg Platform mechanics (Chandrasekaran, 2015b).

capability, inherited by the geometric design (Chandrasekaran, 2014, 2015a, 2017a, 2017b; Chandrasekaran & Srinath, 2013). While the platform undergoes offset, a set-down effect imposes hydrodynamic stability and controls the effect of offset on the geometric motion of the platform (Chandrasekaran & Madhavi, 2015a, 2015b, 2015c, 2015d, 2015e). Change in tether tension imposes an additional resistance in the opposite direction to that of the wave (or any other lateral) load, enabling the platform to regain its original geometric position (Chandrasekaran et al., 2014a, 2014b; Siddiqui & Ahmad, 2001; Wang et al., 2016). While this is referred to as *recentering*, geometric stability is inherently imposed in the design. Such methods of design are often referred to as form-dominant design, which forms the basis for most of the compliant offshore structures (Chandrasekaran, 2013a, 2013b, 2013c; Chandrasekaran et al., 2017).

1.3 NEW-GENERATION OFFSHORE PLATFORMS

The need for an innovative and adaptable structural form had paved the way for the development of new-generation offshore platform (Chandrasekaran, 2018a, 2018b, 2018c, 2019a, 2019b). New-generation offshore platforms are developed to meet the complexities that arise in deep and ultra-deepwater conditions (Chandrasekaran & Nassery, 2015b; Chandrasekaran & Roy, 2005). The hostile and harsh environmental conditions necessitate an innovative and adaptive structural form with compliant characteristics that are cost effective and advantageous (Chandrasekaran & Jain, 2016; Chandrasekaran & Sharma, 2010a; Roy et al., 2017). Due to the non-availability of preceding similar geometry for comparison, it is highly important to analyze and understand the structural behavior of the newly developed platforms under different environmental conditions (Chandrasekaran & Nagavinothini, 2017a, 2017b, 2018a, 2018b, 2018c). Offshore platforms that are conceptualized very recently are discussed below.

1.3.1 BUOYANT LEG STRUCTURES

Buoyant leg structures (BLS) consist of a cylindrical hull connected to the seabed by cylindrical tubes of smaller diameter or tethers (Shaver et al., 2001). The long water-piercing cylindrical hull makes the platform positive buoyant, which enables stability even under the removal of tethers. The hull also protects the risers from the wave and current action. The tension buoyant tower concept was first proposed by Halkyard (1996). Later, the structural form was suitably modified by other researchers to enhance the suitability of the platform in deep waters. BLS is a deep drafted structure which is relatively insensitive to water depth. The structural form of BLS resembles Spar, and the structural action resembles TLP, where tethers restrain the vertical motion. BLS is a very simple structure which enables easy fabrication, transportation and installation. It is installed by ballasting, pull down, or both pull down and ballasting methods. It is advantageous than the spar platform because of its simple hull form with improved motion characteristics. They are also more economical than TLPs and spars due to less commissioning cost. The structural form is shown in Fig. 1.4.

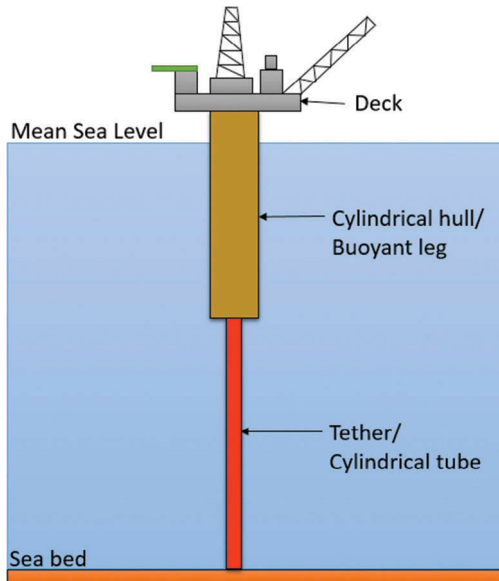


FIGURE 1.4 Buoyant leg structures.

1.3.2 TRICERATOPS

The concept of triceratops was developed by White et al. (2005), considering the various advantages of buoyant leg structures. Triceratops consists of a deck and three buoyant legs, which are position restrained by a set of taut moored tethers as shown in Fig. 1.5. The innovative component of triceratops which makes it different from other new-generation platforms is the ball joint. The ball joints are used for connecting the deck and buoyant legs. Ball joints restrain the transfer of rotational motion and allow only translational motion between the deck and buoyant legs. Thus, under the action of wave loads on buoyant legs, the rotational degrees such as roll, pitch and yaw motions will not be transferred to the deck and thus provide a convenient workspace for the crew on top of the deck (Chandrasekaran & Bhattacharyya, 2012; Chandrasekaran & Madhuri, 2012; Chandrasekaran et al., 2015a). Thus, a combined response of the deck and the buoyant legs should be studied while analyzing this structure, unlike other offshore platforms (Chandrasekaran & Chithambaram, 2016; Chandrasekaran et al., 2016; Chandrasekaran & Thailammai, 2018). These distinct motion characteristics also provide uniqueness to this platform. Triceratops is stiff in the vertical plane and compliant in the horizontal plane, similar to that of TLPs (Chandrasekaran & Nagavinothini, 2019a, 2019b). The buoyant legs of triceratops resemble the hull of the spar platform. This platform derives advantages from both TLP and spar. Also, triceratops attracts fewer forces due to the reduced waterplane area.

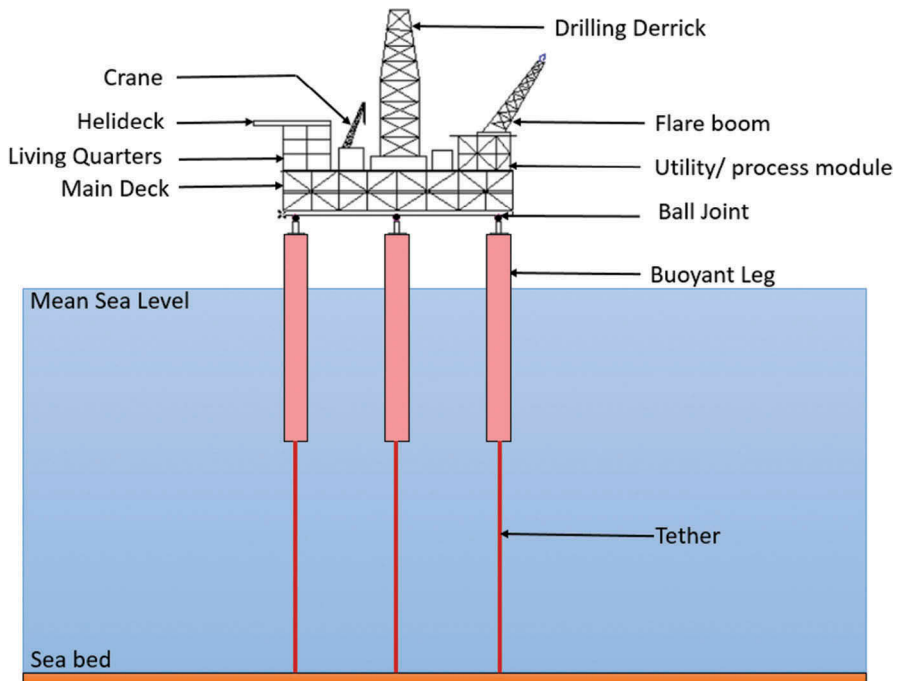


FIGURE 1.5 Triceratops.

1.3.3 BUOYANT LEG STORAGE REGASIFICATION PLATFORM

Buoyant leg storage regasification platform (BLSRP) is developed to overcome the limitations in storage capacity of floating storage regasification units (FSRU). BLSRP consists of a circular deck and six buoyant legs, which are inclined at 20° to the deck as shown in Fig. 1.6. The deck of the platform consists of regasification equipment, storage tanks and seawater pumps. The buoyant legs are position restrained by taut-moored tethers. The structure remains stiff in the vertical plane and compliant in the horizontal plane. The buoyant legs are connected to the deck by hinged joints, which restrain the transfer of rotational motion and allow only translation motion. Thus, this platform has combined advantages of TLP, spar and triceratops. The symmetrical geometric form also makes the platform insensitive to the direction of wave load action.

One of the common facts among all the new-generation offshore platforms is the strong dependency on their geometric form to ensure stability while in action. In such situations, a stability failure will commonly refer to the configuration failure, in general, and inability toward recentering, in particular. It is important to note that the loss of stability is a function of type (or nature) of load, in addition to its magnitude. The loss of stability due to tensile loads falls in material instability, whereas the loss of stability under compression loads is

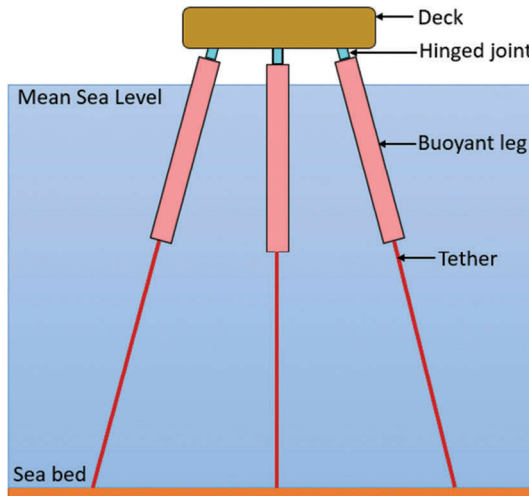


FIGURE 1.6 Buoyant leg storage regasification platforms.

commonly referred to as buckling failure. Hence, instability in any form, be it material specific or geometry specific, is emphasized that the load at which instability occurs depends upon the sectional properties of the members like stiffness by all large, not depends on the material strength. In clear terms, the material of the member may be strong enough to resist the failure, but the member is said to be failed if it is unstable. It is because the member is unfit to disburse the encountered loads, which is the intended function.

BLSRP is one of the recent innovative structural geometry developed to suit the requirements of the offshore industry. It consists of a deck, which is connected to six buoyant legs through hinged joints. The buoyant legs are position restrained by a set of taut-moored tethers. The hinged joints restrain the

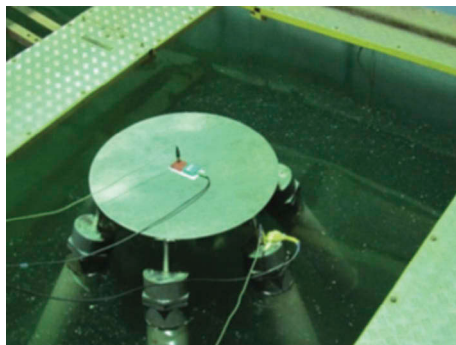


FIGURE 1.7 BLSRP scaled model installed in the wave flume.

transfer of rotational motion and allow only the transfer of translational motion between the leg and buoyant legs. This platform provides increased storage facility and regasification capacity of natural gas. The experimental model of BLSRP is shown in Fig. 1.7.

1.4 DESIGN OF STIFFENED CYLINDRICAL SHELL STRUCTURES

The stiffened cylinders are one of the major structural components of floating and compliant structures. It can be classified into ring-stiffened, stringer-stiffened and ring-stringer-stiffened cylinders. The former is known as orthogonally stiffened cylinders. Stringers are longitudinal stiffeners, which are attached either externally or internally to the cylinder at equidistance apart. The stiffeners may be of a flat bar, angle or T section. Stiffeners, when integrally welded to the shell, help resist the lateral loads. The structure is fabricated from hot- or cold-formed plates with butt welding to establish structural integrity between the cylinders and the stringers. Geometrical distortion and residual stresses are some of the common problems that occur due to the welding process. Upon the types of failure, the orthogonally stiffened cylinder shall buckle and fail in different modes namely shell buckling, panel stiffener buckling, panel ring buckling and column buckling (DNV-RP-C202). Figure 1.8 shows some of these modes of failure.

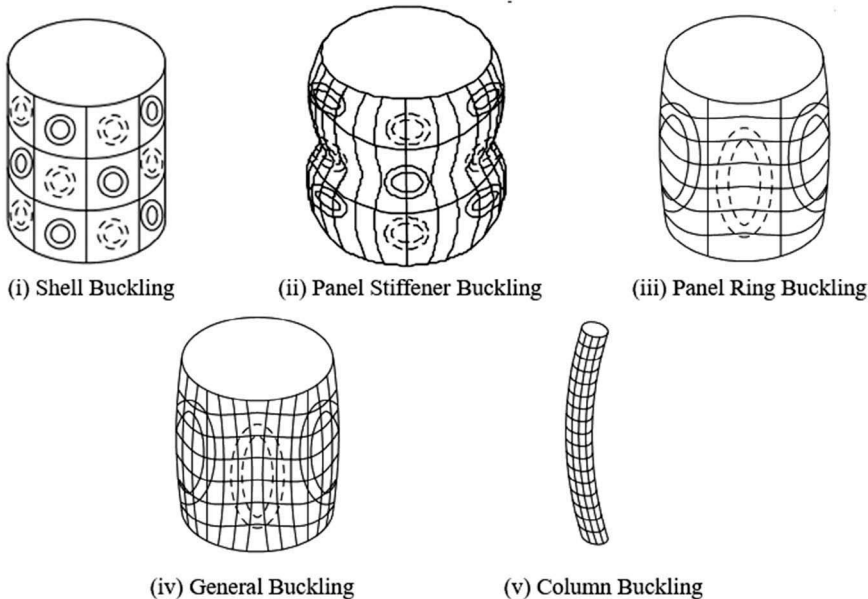


FIGURE 1.8 Buckling modes in orthogonally stiffened cylinders (DNV-RP-C202).

Exercise 1

Check the stability of the ring-stiffened circular cylinder under an axial compressive stress of 30 N/mm² against shell buckling. Take the diameter of cylinder as 5.0 m, the thickness of cylinder as 30 mm, length of the cylinder as 8.0 m, spacing of the ring stiffeners as 800 mm c/c and yield strength of steel as 433 N/mm².

Solution

(i) Stability requirements:

According to Section 1.3.1 of DNV-RP-C202, the stability requirements of a circular cylinder subjected to axial stress is given as

$$\sigma_d \leq f_{ksd} \quad (1.1)$$

where σ_d is the design shell buckling strength, $f_{ksd} = \frac{f_{ks}}{\gamma_M}$ f_{ks} , is the characteristic buckling strength.

(ii) Characteristic buckling strength

$$f_{ks} = \frac{f_y}{\sqrt{1 + \bar{\lambda}^4}} \quad (1.2)$$

$$\bar{\lambda}^2 = \frac{f_y}{\sigma_d} \left[\frac{\sigma_{ao}}{f_{Ea}} + \frac{\sigma_{mo}}{f_{Em}} + \frac{\sigma_{ho}}{f_{Eh}} + \frac{\tau_o}{f_{Et}} \right] \quad (1.3)$$

$$\sigma_d = \sqrt{(\sigma_a + \sigma_m)^2 - (\sigma_a + \sigma_m)\sigma_h + \sigma_h^2 + 3\tau^2} \quad (1.4)$$

Following values hold good:

Design axial stress, $\sigma_a = -30$ N/mm²

Design bending stress, $\sigma_m = 0$

Design circumferential stress, $\sigma_h = 0$

Design shear stress, $\tau = 0$

Substituting in Eq. (1.4), we get:

$$\sigma_d = 30 \text{ N/mm}^2$$

Characteristic buckling strength of circular cylinder for check under shell buckling is given as (Section 3.4.2, p. 15)

$$f_E = C \frac{\pi^2 E}{12(1 - \gamma^2)^2} \left(\frac{t}{l} \right)^2 \quad (1.5)$$

Reduced buckling coefficient is as follows:

$$C = \Psi \sqrt{1 + \left(\frac{\rho \xi}{\Psi}\right)^2} \quad (1.6)$$

From Table 3.2 of the code, we get: $\Psi = 1$ (1.7a)

$$\xi = 0.702 Z_l$$

$$Z_l = \frac{l^2}{rt} \sqrt{1 - \gamma^2} \quad (1.7b)$$

$$\rho = 0.5 \left[1 + \frac{r}{150t}\right]^{-0.5} \quad (1.7c)$$

where

Distance between ring stiffeners, $l = 800$ mm

Cylinder radius, $r = 2500$ mm

Cylinder thickness, $t = 30$ mm

Poisson's ratio, $\gamma = 0.3$

Substituting in Eq. (1.7), we get:

$$Z_l = 7.765$$

$$\xi = 5.451$$

$$\rho = 0.401$$

From Eq. (1.6), we get:

$$C = 2.404$$

Thus, characteristic buckling strength is given by the following relationship:

$$f_E = C \frac{\pi^2 E}{12(1 - \gamma^2)^2} \left(\frac{t}{l}\right)^2 \quad (1.8)$$

$$f_E = 2.404 \times \frac{\pi^2 \times 2.1 \times 10^5}{12(1 - 0.3^2)^2} \left(\frac{30}{800}\right)^2 = 641.643 \text{ N/mm}^2 \quad (1.9)$$

(iii) Check for stability

From Eq. (1.3), we get:

$$\bar{\lambda}^2 = \frac{f_y}{\sigma_d} \left[\frac{\sigma_{ao}}{f_{Ea}} \right] = 0.675$$

Substituting in Eq. (1.2), we get:

$$f_{ks} = \frac{f_y}{\sqrt{1 + \bar{\lambda}^4}} = 297.514 \text{ N/mm}^2$$

From Section 3.1, we get:

$$\gamma_M = 0.85 + 0.60\bar{\lambda} \quad \text{for } 0.5 \leq \bar{\lambda} \leq 1.0$$

Thus, $\gamma_M = 1.343$

$$\text{Now, } f_{ksd} = \frac{f_{ks}}{\gamma_M} = 221.538 \text{ N/mm}^2$$

Since $\sigma_d = 30 \text{ N/mm}^2$, $\sigma_d < f_{ksd}$

Hence, the circular cylinder is safe against shell buckling.

Exercise 2

Calculate the characteristic buckling strength of orthogonally stiffened cylindrical shell with the following details:

Shell dimensions:

Diameter of the shell = 10.0 m

Thickness of the outer shell = 40 mm

Stiffeners details:

Type: flat bar (300×40 mm)

Ring frames spacing = 1000 mm

Longitudinal stiffener spacing = 600 mm

Load and material details:

Axial compressive stress = 40 N/mm²

Circumferential compressive stress = 70 N/mm²

Yield strength of steel = 433 N/mm²

Solution:

(i) Characteristic buckling strength

$$f_{ks} = \frac{f_y}{\sqrt{1 + \bar{\lambda}^4}} \quad (1.10)$$

$$\bar{\lambda}^2 = \frac{f_y}{\sigma_d} \left[\frac{\sigma_{ao}}{f_{Ea}} + \frac{\sigma_{mo}}{f_{Em}} + \frac{\sigma_{ho}}{f_{Eh}} + \frac{\tau_o}{f_{Et}} \right] \quad (1.11)$$

$$\sigma_d = \sqrt{(\sigma_a + \sigma_m)^2 - (\sigma_a + \sigma_m)\sigma_h + \sigma_h^2 + 3\tau^2} \quad (1.12)$$

Design axial stress, $\sigma_a = -40 \text{ N/mm}^2$

Design bending stress, $\sigma_m = 0$

Design circumferential stress, $\sigma_h = -70 \text{ N/mm}^2$

Design shear stress, $\tau = 0$

Substituting in Eq. (1.4), we get:

$$\sigma_d = 60.828 \text{ N/mm}^2$$

(ii) Elastic buckling strength

According to Section 3.3.2, p. 14, aspect ratio = l/s
where

Distance between ring stiffeners, $l = 1000 \text{ mm}$

Distance between longitudinal stiffeners, $s = 600 \text{ mm}$

Thus, aspect ratio = $1.667 > 1.0$

So, the characteristic buckling strength of cylindrical shells under check for shell buckling is given as follows:

$$f_E = C \frac{\pi^2 E}{12(1 - \gamma^2)^2} \left(\frac{t}{l}\right)^2 \quad (1.13)$$

Reduced buckling coefficient is as follows:

$$C = \Psi \sqrt{1 + \left(\frac{\rho \xi}{\Psi}\right)^2} \quad (1.14)$$

(a) Elastic buckling strength under axial stress:

From Table 3.2, $\Psi = 4$

$$\xi = 0.702 Z_s, Z_s = \frac{s^2}{rt} \sqrt{1 - \gamma^2} \quad (1.15)$$

$$\rho = 0.5 \left[1 + \frac{r}{150t}\right]^{-0.5}$$

where

Distance between longitudinal stiffeners, $s = 600 \text{ mm}$

Cylinder radius, $r = 5000 \text{ mm}$

Cylinder thickness, $t = 40 \text{ mm}$

Poisson's ratio, $\gamma = 0.3$

Substituting the values from the above equations, we get:

$$Z_l = 1.638$$

$$\xi = 1.150$$

$$\rho = 0.369$$

From Eq. (1.14), we get $C = 4.022$

Thus, characteristic buckling strength is given as

$$\begin{aligned} f_{Ea} &= C \frac{\pi^2 E}{12(1 - \gamma^2)^2} \left(\frac{t}{l}\right)^2 \\ &= 4.022 \times \frac{\pi^2 \times 2.1 \times 10^5}{12(1 - 0.3^2)^2} \left(\frac{40}{600}\right)^2 \\ &= 3392.782 \text{ N/mm}^2 \end{aligned}$$

(b) Elastic buckling strength under circumferential stress

From Table 3.2,

$$\begin{aligned} \Psi &= \left[1 + \left(\frac{s}{l}\right)^2 \right]^2 \\ \xi &= 1.04 \frac{s}{l} \sqrt{Z_s}, \quad Z_l = \frac{s^2}{rt} \sqrt{1 - \gamma^2} \\ \rho &= 0.6 \end{aligned} \tag{1.16}$$

Distance between longitudinal stiffeners, $s = 600 \text{ mm}$

Cylinder radius, $r = 5000 \text{ mm}$

Cylinder thickness, $t = 40 \text{ mm}$

Poisson's ratio, $\gamma = 0.3$

Substituting in Eq. (1.14), we get:

$$\Psi = 1.85$$

$$\xi = 0.799$$

From Eq. (1.12), we get:

$$C = 1.911$$

Thus, characteristic buckling strength is given as

$$\begin{aligned} f_{Eh} &= C \frac{\pi^2 E}{12(1 - \gamma^2)^2} \left(\frac{t}{l}\right)^2 \\ &= 1.911 \times \frac{\pi^2 \times 2.1 \times 10^5}{12(1 - 0.3^2)^2} \left(\frac{40}{600}\right)^2 \\ &= 1612.035 \text{ N/mm}^2 \end{aligned}$$

Substituting the values from the above equations, we get:

$$\bar{\lambda}^2 = \frac{f_y}{\sigma_d} \left[\frac{\sigma_{ao}}{f_{Ea}} + \frac{\sigma_{ho}}{f_{Eh}} \right] = 0.393$$

$$\bar{\lambda} = 0.627$$

Thus, the characteristic buckling strength is given as

$$f_{ks} = \frac{f_y}{\sqrt{1 + \bar{\lambda}^4}} = 402.996 \text{ N/mm}^2$$

1.5 UNSYMMETRICAL BENDING

In members generally idealized as one dimensional, it is comfortable to compute the stresses in the cross section for the loads applied at the prefixed points, as the bending takes place parallel to the plane of applied moment. While using the simple bending equation, it is assumed that the neutral axis of the cross section is perpendicular to the plane of loading.

In Fig. 1.9, the YY -axis is the trace of the plane of the applied moment. Bending moment in the YY -axis is said to be zero and mathematically as follows:

$$\sum M_y = \int_A \sigma_x dA = 0 \quad (1.17)$$

and $\int zy dA = 0$ only when the ZZ -axis and YY -axis are the principal axes of inertia.

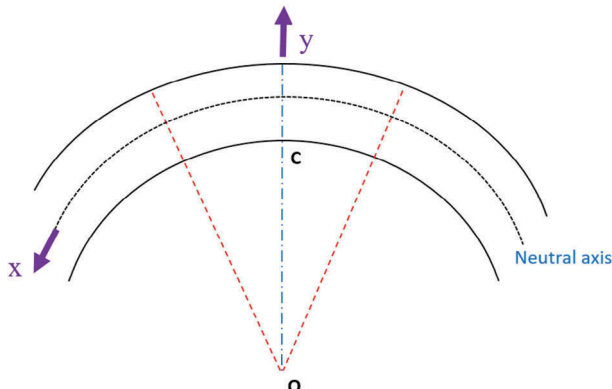


FIGURE 1.9 Uniform bending.

For symmetrical bending,

- i. It is essential that the plane containing none of the principal axes of inertia, the plane of the applied moment and the plane of deflection should coincide.
- ii. It is also obvious that the neutral axis will coincide with other principal axes of inertia.

When the trace of the plane of the applied moment does not coincide with any of the principal axes of inertia, then this type of bending is called *unsymmetrical bending* or *non-uniplanar bending*. Under such conditions in unsymmetrical bending, neutral axis is no longer perpendicular to the trace of the applied moment plane, and the deflection curve is not plane. The major consequence of unsymmetrical bending is that the members that are symmetric about a vertical axis with thin-walled sections will undergo twisting under transverse loads. The reasons for the unsymmetrical bending are as follows:

- i. The section is symmetrical, but the line of action of the load is inclined to both the principal axes.

The section is unsymmetrical, and the line of action of the load is along any centroidal axis.

In the case of unsymmetrical bending, the applied moment will cause bending about both the principal axes of inertia, which should be located to calculate the stresses at any point in the cross section. If the moment acts on the plane of symmetry, then the conventional simple bending equation can be used to calculate the stresses:

$$\sigma_b = \frac{M}{I} y \quad (1.18)$$

However, if the load acts on another plane, then it becomes unsymmetric where one cannot use the conventional equation of flexure to obtain the stresses. In such a case, the following procedure has to be followed to estimate the stresses:

Step 1: To transform the problem of unsymmetric bending to uniplanar bending

Consider a cross section of the beam under the action of a bending moment M (Fig. 1.10)

Let,

ZZ and YY = co-ordinate axes passing through the centroid.

UU and VV = principal axes inclined at an angle α to the ZZ and YY axes, respectively.

The axes are shown in the figure.

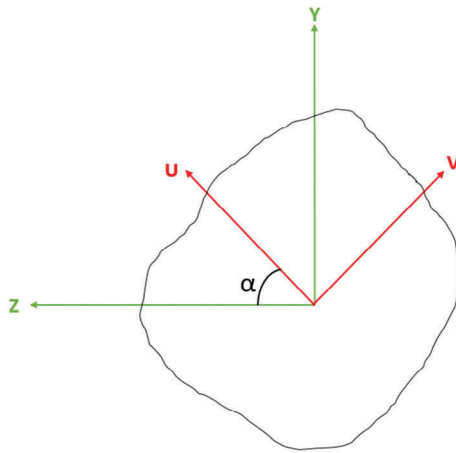


FIGURE 1.10 Typical cross section.

To locate the principal axes of inertia, the following relationship is valid:

$$u = z \cos \alpha + y \sin \alpha \quad (1.19a)$$

$$v = -z \sin \alpha + y \cos \alpha \quad (1.19b)$$

The angle is measured in the positive coordinate. The moment of inertia about UU and VV axes should be calculated to estimate the bending stresses, as discussed below:

$$\begin{aligned} I_u &= \int_A v^2 dA \\ &= \int_A (-z \sin \alpha + y \cos \alpha)^2 dA \\ &= \int_A (z^2 \sin^2 \alpha + y^2 \cos^2 \alpha - 2z \sin \alpha \cos \alpha) dA \\ &= \sin^2 \alpha \int_A z^2 dA + \cos^2 \alpha \int_A y^2 dA - \sin 2\alpha \int_A yz dA \\ &= I_y \sin^2 \alpha + I_z \cos^2 \alpha - I_{yz} \sin^2 \alpha \\ \cos 2\alpha &= 1 - 2 \sin^2 \alpha \\ &= 2 \cos^2 \alpha - 1 \end{aligned}$$

Substituting in the above equation,

$$I_u = \frac{I_y}{2}(1 - \cos 2\alpha) + \frac{I_z}{2}(1 + \cos 2\alpha) - I_{yz}\sin 2\alpha$$

$$= \frac{I_Y + I_Z}{2} + \frac{I_Z + I_Y}{2}\cos 2\alpha - I_{YZ}\sin 2\alpha$$

$$I_u = \frac{I_Y + I_Z}{2} + \frac{I_Z + I_Y}{2}\cos 2\alpha - I_{YZ}\sin 2\alpha$$

$$I_V = \int_A u^2 dA$$

$$= \int_A (z\cos\alpha + y\sin\alpha)^2 dA$$

$$= \int_A (z^2\cos^2\alpha + Y^2\sin^2\alpha + 2zy\sin\alpha\cos\alpha) dA$$

$$I_V = \cos^2\alpha \int_A Z^2 dA + \sin^2\alpha \int_A y^2 dA + \sin 2\alpha \int_A zy dA$$

$$= \cos^2\alpha I_y + \sin^2\alpha I_z + I_{zy}\sin^2\alpha$$

$$= (1 + \cos 2\alpha) \frac{I_y}{2} + \frac{1 - \cos 2\alpha I_z}{2} + I_{zy}\sin 2\alpha$$

$$I_V = \frac{I_z - I_y}{2} - \frac{I_z - I_y}{2}\cos 2\alpha + I_{zy}\sin 2\alpha$$

$$I_u + I_V = I_z + I_y$$

$$I_{uv} = \int_A (uv) dA$$

$$= \int_A (z\cos\alpha + y\sin\alpha)(-z\sin\alpha + \cos\alpha) dA$$

$$= \int_A (-z^2\sin\alpha\cos\alpha - yz\sin^2\alpha - yz\cos^2\alpha - y^2\sin\alpha\cos\alpha) dA$$

$$\int_A z^2 dA = I_y$$

$$\int_A yz^2 dA = I_z$$

$$\int_A yz^2 dA = I_{yz}$$

Using the above relationship,

$$I_{uv} = -I_y \sin \alpha \cos \alpha + I_z \sin \alpha \cos \alpha + I_{yz} (\cos^2 \alpha - \sin^2 \alpha)$$

$$I_{uv} = \frac{I_z + I_y}{2} \sin 2\alpha + I_{yz} \cos 2\alpha$$

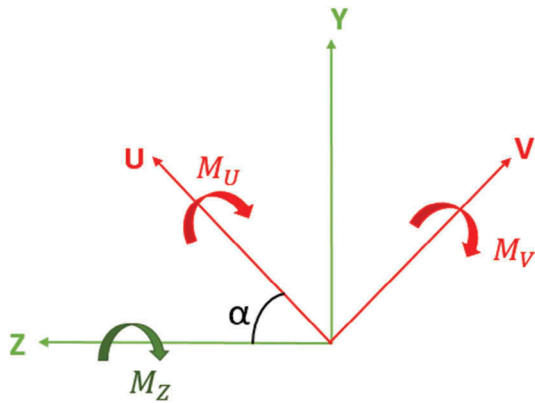
for u, v being the principal axes of inertia,

$$I_{uv} = 0$$

$$I_{uv} = \frac{I_z + I_y \sin 2\alpha}{2} + I_{yz} \cos 2\alpha = 0$$

$$\tan(2\alpha) = -\frac{2I_{yz}}{I_z - I_y}$$

Step 2: To determine the bending stress at any point in the cross section



The moment about the principal axes are given as

$$M_u = M_z \cos \alpha$$

$$M_v = M_z \sin \alpha$$

Stress at any point $p(u,v)$,

$$\frac{M_u}{I_v}(v) - \text{compressive stress}$$

$$\frac{M_u}{I_v}(u) - \text{tensile stress}$$

Consider the following tensile stress:

$$\begin{aligned}\sigma_p &= \frac{M_u}{I_u}v + \frac{M_v}{I_u}u \\ &= -\left[\frac{M_u}{I_u}v + \frac{M_v}{I_u}u\right]\end{aligned}$$

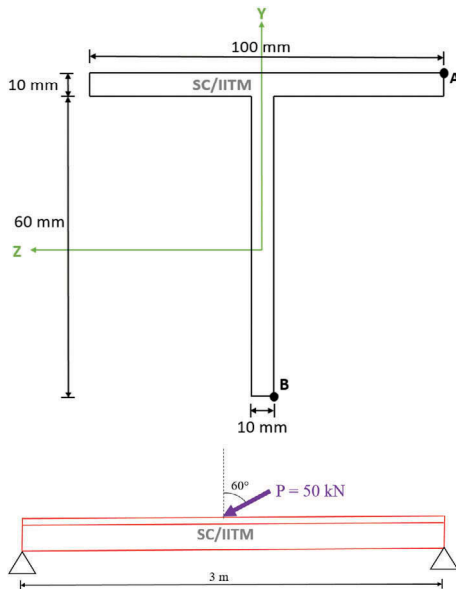
Negative sign indicates compressive stress.

The nature of the resultant bending stress will always depend upon the quadrant in which it lies. So that the signs of u and v have to be taken into account while determining the resultant stress. It is also to be noted that the maximum stress will occur at a point which is at the greatest distance from the neutral axis. On one side of the neutral axis, all the points will carry the stresses of the same nature and opposite nature on the other side.

Exercise problems

Example 1

Find the stresses on the simply supported beam shown in the figure.



$$\bar{y} = \frac{\sum ay}{\sum a}$$

$$\bar{y} = \frac{(60 \times 10 \times 5) + (70 \times 10 \times 45)}{(60 \times 10) + (70 \times 10)} = 26.54 \text{ mm}$$

$$I_Y = \frac{10 \times 60^3}{12} + \frac{70 \times 10^3}{12}$$

$$= 1.858 \times 10^5 \text{ mm}^4$$

$$I_Z = \frac{60 \times 10^3}{12} + 60 \times 10 \times (21.54)^2 + \frac{10 \times 70^3}{12} + 70 \times 10 \times (18.46)^2$$

$$= 8.0078 \times 10^5 \text{ mm}^4$$

Moment about Z -axis = load \times perpendicular distance = $50 \times 3/4 = 37.5 \text{ kNm}$.

MATLAB® Code

```
%% INPUT
% calculate the values of moment of inertia of the section in mm^4
Iy = 1.858e5;
Iz = 8.877e5;
Mz = 37.5; % Moment about Z axis in kNm
ybar = 26.54; % location of centroidal axis in mm
zbar = 0;
te = 60; %angle of inclination of load

%% Principal axis location
Iu = Iz;
Iv = Iy;

%% Stress calculation
Mu = Mz*cosd(te); Mv = -Mz*sind(te);

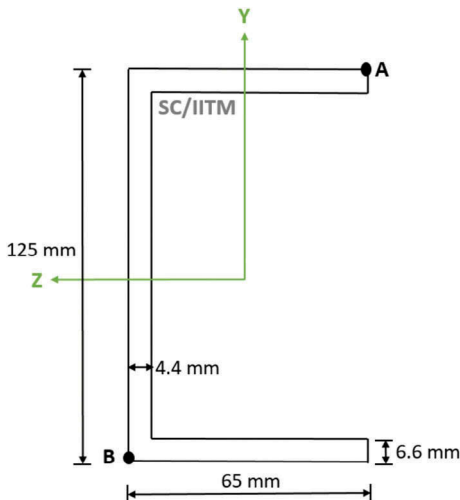
% calculation for point A
ua = 30;
va = 26.54;
sa = -(Mu*(10^6)*va/Iu) + (Mv*(10^6)*ua/Iv);

% calculation for point B
ub = 5;
vb = -53.46;
sb = -(Mu*(10^6)*vb/Iu) + (Mv*(10^6)*ub/Iv);

fprintf('Stress at point A = %6.2f N/mm^2 \n',sa);
fprintf('Stress at point B = %6.2f N/mm^2 \n \n',sb);
```

Output:Stress at point A = -5804.27 N/mm²Stress at point B = 255.23 N/mm²**Example 2**

A purlin of a roof truss ISLC 125 is placed at an angle of 45°. Purlins are placed at 500 mm c/c along the principal rafter within 3.0 m spacing. Assume the purlin will act as a simply supported beam with the uniformly distributed load. Find the maximum stresses at A and B due to the self-weight of the member. Dead load in the member is 2 kN/m².



$$\text{Load from purlin} = \frac{(1.5 \times 2) + \frac{(10.7 \times 10)}{1000}}{3} = 1.107 \text{ kN/m}$$

$$\text{Moment} = \frac{wl^2}{8} = \frac{1.107 + (3)^2}{8} = 1.245 \text{ kNm}$$

$$\alpha = 45^\circ$$

$$M_U = M_Z \cos \alpha = 0.88 \text{ kNm}$$

$$M_V = -M_Z \sin \alpha = -0.88 \text{ kNm}$$

For ISLC 125,

$$I_U = I_Z = 356.8 \times 10^4 \text{ mm}^4$$

$$I_V = I_Y = 57.2 \times 10^4 \text{ mm}^4$$

Point A: (44.6 mm, 62.5 mm)
 Point B: (-20.4 mm, -162.5 mm)

MATLAB® Code

```
%% Unsymmetrical bending - Channel section
clc;
clear;

%% INPUT
% calculate the values of moment of inertia of the section in mm^4
Iy = 57.2e4;
Iz = 356.8e4;
Mz = 1.245; % Moment about Z axis in kNm
ybar = 62.5; % location of centroidal axis in mm
zbar = 20.4;
te = 45; % angle of inclination of load

%% Principal axis location
Iu = Iz;
Iv = Iy;

%% Stress calculation
Mu = Mz*cosd(te);
Mv = -Mz*sind(te);

% calculation for point A
ua = 44.6;
va = 62.5;
sa = -(Mu*(10^6)*va/Iu) + (Mv*(10^6)*ua/Iv);

% calculation for point B
ub = -20.4;
vb = -62.5;
sb = -(Mu*(10^6)*vb/Iu) + (Mv*(10^6)*ub/Iv);

fprintf('Stress at point A = %6.2f N/mm^2 \n',sa);
fprintf('Stress at point B = %6.2f N/mm^2 \n \n',sb);
```

Output:

Stress at point A = -84.06 N/mm²
 Stress at point B = 46.82 N/mm²

Example 3

Consider a simply supported beam of length 3.0 m with a uniformly distributed load of 10 kN/m. The beam has a rectangular cross section of 100 mm × 150 mm. The applied load makes an angle 30° with the vertical plane. Calculate the stresses at points A (top right corner of the section) and B (bottom left corner of the section). Also locate the neutral axis of the section.

$$\text{Moment} = \frac{wl^2}{8} = \frac{10 + (3)^2}{8} = 11.25 \text{ kNm}$$

$$\alpha = 30^\circ$$

$$M_U = M_Z \cos \alpha = 27.735 \text{ kNm}$$

$$M_V = -M_Z \sin \alpha = -41.6 \text{ kNm}$$

Point A: (50 mm, 75 mm)

Point B: (-50 mm, -75 mm)

MATLAB® Code:

```
%% Unsymmetrical bending - Rectangular section
clc;
clear;

%% INPUT
% calculate the values of moment of inertia of the section in mm^4
Iy = 2.813e7;
Iz = 1.25e7;
Mz = 11.25; % Moment about Z axis in kNm
te = 30; %angle of inclination of load

%% Principal axis location
Iu = Iz;
Iv = Iy;

%% Stress calculation
Mu = Mz*cosd(te);
Mv = -Mz*sind(te);

% calculation for point A - on flange top
ua = 50;
va = 75;
sa = -(Mu*(10^6)*va/Iu) + (Mv*(10^6)*ua/Iv);

% calculation for point B - on web bottom
ub = -50;
vb = -75;
sb = -(Mu*(10^6)*vb/Iu) + (Mv*(10^6)*ub/Iv);

fprintf('Stress at point A = %6.2f N/mm^2 \n',sa);
fprintf('Stress at point B = %6.2f N/mm^2 \n \n',sb);

% location of neutral axis
vbyu=Iu*Mv/(Iv*Mu);
be=atand(vbyu);
fprintf('Beta = %6.2f degrees \n',be);
```

Output:Stress at point A = -68.45 N/mm²Stress at point B = 68.45 N/mm²

Beta = -14.39 degrees

Location of neutral axis:

$$\sigma_X = - \left(\frac{M_U}{I_U} v - \frac{M_V}{I_V} u \right)$$

To locate the neutral axis, substituting $\sigma_X = 0$,

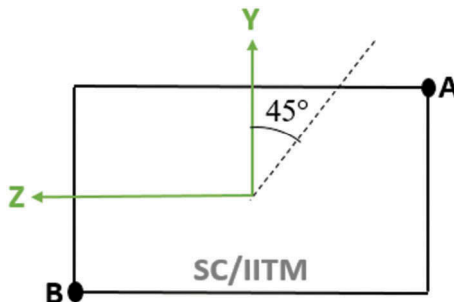
$$\frac{v}{u} = \tan \beta$$

where β is the inclination between the neutral axis and U.

$$\beta = -14.39^\circ$$

Example 4

A simply supported beam of section 190 mm × 50 mm has a span of 3.0 m. It rests on the support such that 190 mm face makes an angle of 45° with the horizontal. It carries a load of 100 kN at the mid-span. Find the stresses at points A and B. Also locate the neutral axis of the section.



$$I_Y = \frac{50 \times 190^3}{12} = 2.858 \times 10^7 \text{ mm}^4$$

$$I_Z = \frac{190 \times 50^3}{12} = 0.198 \times 10^7 \text{ mm}^4$$

$$M_z = \frac{wl}{4} = 75 \text{ kNm}$$

$$\theta = 45^\circ$$

Point A: (95 mm, 25 mm)

Point B: (-95 mm, -25 mm)

MATLAB® Code

```
%% Unsymmetrical bending - Rectangular section
clc;
clear;

%% INPUT
% calculate the values of moment of inertia of the section in mm^4
Iy = 2.858e7;
Iz = 0.198e7;
Mz = 75; % Moment about Z axis in kNm
te = 45; %angle of inclination of load

%% Principal axis location
Iu = Iz;
Iv = Iy;

%% Stress calculation
Mu = Mz*cosd(te);
Mv = -Mz*sind(te);

% calculation for point A - on flange top
ua = 95;
va = 25;
sa = -(Mu*(10^6)*va/Iu)+(Mv*(10^6)*ua/Iv);

% calculation for point B - on web bottom
ub = -95;
vb = -25;
sb = -(Mu*(10^6)*vb/Iu)+(Mv*(10^6)*ub/Iv);

fprintf('Stress at point A = %6.2f N/mm^2 \n',sa);
fprintf('Stress at point B = %6.2f N/mm^2 \n \n',sb);

% location of neutral axis
vbyu=Iu*Mv/(Iv*Mu);
be=atand(vbyu);
fprintf('Beta = %6.2f degrees \n',be);
```

Output:

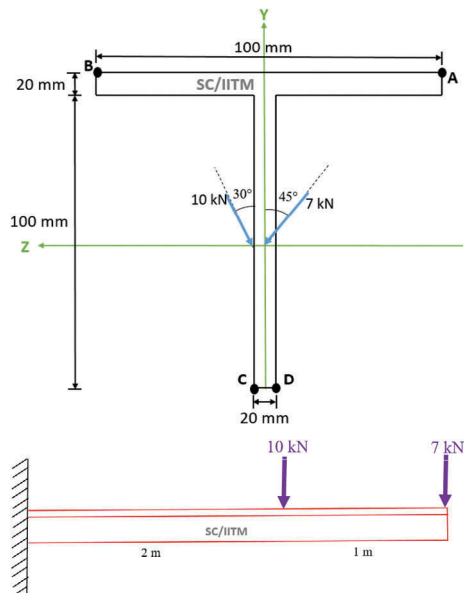
Stress at point A = -845.89 N/mm²

Stress at point B = 845.89 N/mm²

Beta = -3.96 degrees

Example 5

Consider a cantilever beam with two concentrated loads of 10 kN and 7 kN at 2.0 m and 3.0 m from the left end, acting at 30° and 45°, respectively, at the centroid of the T section. Find the stresses at points A, B, C and D.



$$\bar{y} = \frac{\sum ay}{\sum a}$$

$$\bar{y} = \frac{(100 \times 20 \times 10) + (80 \times 20 \times 60)}{(100 \times 20) + (80 \times 20)} = 38.89 \text{ mm}$$

$$I_Y = \frac{20 \times 100^3}{12} + \frac{80 \times 20^3}{12} = 1.72 \times 10^6 \text{ mm}^4$$

$$I_Z = \frac{100 \times 20^3}{12} + 10 \times 20 \times (28.89)^2 + \frac{20 \times 80^3}{12} + 80 \times 20 \times (60 - 38.89)^2 \\ = 1.832 \times 10^7 \text{ mm}^4$$

$$M_U = M_Z \cos \alpha$$

$$M_U = [(10 \times 2 \times \sin 30) + (7 \times 3 \times \cos 45)] = 32.17 \text{ kNm}$$

$$M_V = -M_Z \sin \alpha$$

$$M_V = -[(10 \times 2 \times \sin 30) + (7 \times 3 \times \cos 45)] = -24.85 \text{ kNm}$$

- Point A: (50 mm, 38.80 mm)
 Point B: (-50 mm, 38.80 mm)
 Point C: (-10 mm, -61.11 mm)
 Point D: (10 mm, -61.11 mm)

MATLAB® Code

```
%% Unsymmetrical bending - T section
clc;
clear;

%% INPUT
% calculate the values of moment of inertia of the section in mm^4
Iy = 1.72e6;
Iz = 8.877e5;
Mz = 37.5; % Moment about Z axis in kNm
ybar = 38.89; % location of centroidal axis in mm
zbar = 0;
te = 60; %angle of inclination of load

%% Principal axis location
Iu = Iz;
Iv = Iy;

%% Stress calculation
Mu = 32.17; % in kNm
Mv = 24.85;

% calculation for point A - on flange top right
ua = 50;
va = 38.89;
sa = -(Mu*(10^6)*va/Iu) + (Mv*(10^6)*ua/Iv);

% calculation for point B - on flange top left
ub = -50;
vb = 38.89;
sb = -(Mu*(10^6)*vb/Iu) + (Mv*(10^6)*ub/Iv);

% calculation for point C - on web bottom left
uc = -10;
vc = 61.11;
sc = -(Mu*(10^6)*vc/Iu) + (Mv*(10^6)*uc/Iv);

% calculation for point D - on web bottom right
ud = 10;
vd = -61.11;
sd = -(Mu*(10^6)*vd/Iu) + (Mv*(10^6)*ud/Iv);
```

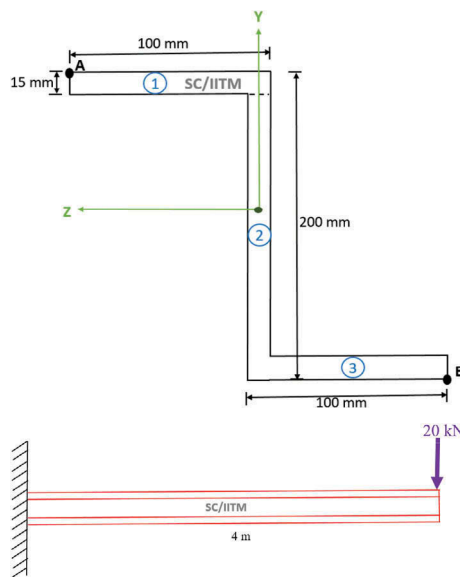
```
fprintf('Stress at point A = %6.2f N/mm^2 \n',sa);
fprintf('Stress at point B = %6.2f N/mm^2 \n',sb);
fprintf('Stress at point C = %6.2f N/mm^2 \n',sc);
fprintf('Stress at point D = %6.2f N/mm^2 \n',sd);
```

Output:

Stress at point A = -686.98 N/mm²
 Stress at point B = -2131.75 N/mm²
 Stress at point C = -2359.09 N/mm²
 Stress at point D = 2359.09 N/mm²

Example 6:

Find the stresses at points A and B for the following.



$$I_Y = \left\{ \left[\frac{50 \times 100^3}{12} + (100 \times 15 \times 42.5^2) \right] \times 2 \right\} + \frac{170 \times 15^3}{12} \\ = 7.97 \times 10^6 \text{ mm}^4$$

$$I_Z = \left\{ \left[\frac{100 \times 15^3}{12} + 100 \times 15 \times (92.5)^2 \right] \times 2 \right\} + \frac{15 \times 170^3}{12} \\ = 3.187 \times 10^7 \text{ mm}^4$$

$$\begin{aligned}
 I_{YZ} &= \int zy \, dA \\
 &= [(100 \times 15 \times 42.5 \times 92.5)] + [100 \times 15 \times (-42.5) \times (-92.5)] \\
 &= 1.179 \times 10^7 \text{ mm}^4
 \end{aligned}$$

Moment about Z-axis = load \times perpendicular distance = $20 \times 4 = 80 \text{ kNm}$.

MATLAB® Code

```

%% Unsymmetrical bending - Z section
clc;
clear;

%% INPUT
% calculate the values of moment of inertia of the section in mm^4
Iy = 7.97e6;
Iz = 3.187e7;
Iyz = 1.179e7;
Iuv = 0;
Mz = -80; % Moment about Z axis in kNm

%% Principal axis location
tt = (-2*Iyz) / (Iz-Iy);
al = (atand(tt)+180)/2;
Iu = ((Iy+Iz)/2)+(((Iz-Iy)*cosd(2*al))/2)-(Iy*sind(2*al));
Iv = (Iz+Iy)-Iu;

%% Stress calculation
Mu = Mz*cos(al);
Mv = -Mz*sin(al);
ra = Mv*Iu/(Mu*Iv);
be = atand(ra);

% calculation for point A - on flange top
ya = 92.5;
za = 100;
ua = (za*cos(al))+(ya*sin(al));
va = -(za*sin(al))+(ya*cos(al));
sa = -(Mu*(10^6)*va/Iu)+(Mv*(10^6)*ua/Iv);

% calculation for point B - on web bottom
yb = -92.5;
zb = -100;
ub = (zb*cos(al))+(yb*sin(al));
vb = -(zb*sin(al))+(yb*cos(al));
sb = -(Mu*(10^6)*vb/Iu)+(Mv*(10^6)*ub/Iv);

fprintf('Stress at point A = %6.2f N/mm^2 \n',sa);
fprintf('Stress at point B = %6.2f N/mm^2 \n \n',sb);

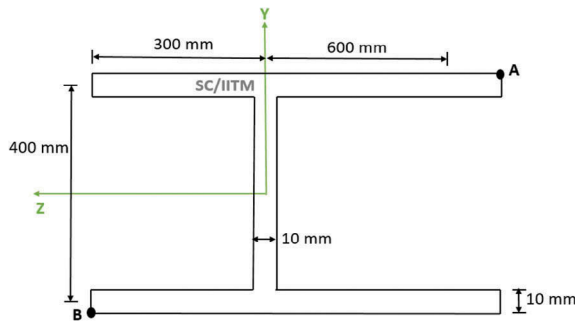
```

Output:

Stress at point A = 407.93 N/mm²
Stress at point B = -407.93 N/mm²

Example 7

For a beam cross section shown in the figure, locate the point of the neutral axis and maximum stresses at points A and B, under the action of the external moment of 1 MNm.



$$\bar{x} = \frac{\sum ax}{\sum a}$$

$$\bar{x} = \frac{(90 \times 100 \times 450) \times 2 + (390 \times 10 \times 300)}{(90 \times 10) \times 2 + (390 \times 10)} = 123.28 \text{ mm}$$

$$I_Y = \left\{ \left[\frac{10 \times 900^3}{12} + (900 \times 10 \times (450 - 423.28)^2) \right] \times 2 \right\}$$

$$+ \frac{390 \times 10^3}{12} + (390 \times 10 \times 123.28^2)$$

$$= 1.287 \times 10^9 \text{ mm}^4$$

$$I_Z = \left\{ \left[\frac{900 \times 10^3}{12} + 900 \times 10 \times (200)^2 \right] \times 2 \right\} + \frac{10 \times 390^3}{12}$$

$$= 7.696 \times 10^8 \text{ mm}^4$$

Point A: (-476.72 mm, 205 mm)

Point B: (423.28 mm, -205 mm)

MATLAB® Code

```

%% Unsymmetrical bending - Rectangular section
clc;
clear;

%% INPUT
% calculate the values of moment of inertia of the section in mm^4
Iy = 1.287e9;
Iz = 7.696e8;
Mz = 1000; % Moment about Z axis in kNm
te = 30; %angle of inclination of load

%% Principal axis location
Iu = Iz;
Iv = Iy;

%% Stress calculation
Mu = Mz*cosd(te);
Mv = -Mz*sind(te);

% calculation for point A - on flange top
ua = -476.72;
va = 205;
sa = -(Mu*(10^6)*va/Iu)+(Mv*(10^6)*ua/Iv);

% calculation for point B - on web bottom
ub = 423.28;
vb = -205;
sb = -(Mu*(10^6)*vb/Iu)+(Mv*(10^6)*ub/Iv);

fprintf('Stress at point A = %6.2f N/mm^2 \n',sa);
fprintf('Stress at point B = %6.2f N/mm^2 \n \n',sb);

% location of neutral axis
vbyu=Iu*Mv/(Iv*Mu);
be=atand(vbyu);
fprintf('Beta = %6.2f degrees \n',be);

```

Output:

Stress at point A = -45.48 N/mm²
 Stress at point B = 66.24 N/mm²
 Beta = -19.05 degrees

1.6 CURVED BEAMS

The curved beams are classified based on the initial curvature into:

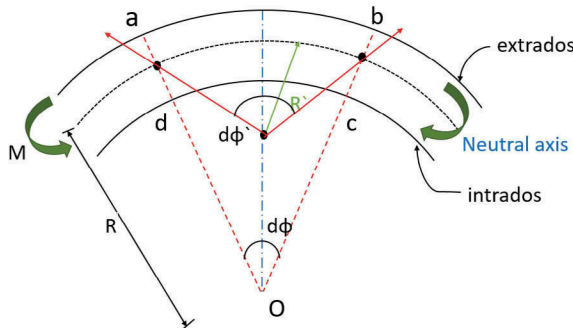
i. Beams with small initial curvature

The ratio of the initial radius of curvature and the depth of the section is greater than 10.

ii. Beams with large initial curvature

The ratio of the initial radius of curvature and the depth of the section is less than or equal to 10.

1.6.1 BENDING OF CURVED BEAMS WITH SMALL INITIAL CURVATURE



Let,

$d\varphi'$ be the angle subtended after deformation.

R be the initial radius of curvature.

$d\varphi$ be the angle subtended at the center of curvature by the portion 'abcd.'

R' be the radius of curvature after moment M is applied.

If $R' < R$, then the applied moment will tend to close the curvature. Let us consider a fiber PQ at a distance y from the neutral axis.

Then,

The original length of the fiber = $(R + y) d\varphi$

Length of the fiber after application of the moment = $(R' + y) d\varphi'$

Change in length of the fiber = $(R' + y) d\varphi' - (R + y) d\varphi$

$$\text{Strain, } \epsilon = \frac{(R'y)d\varphi'(R+y)d\varphi}{(R+y)d\varphi}$$

As the length of the fiber at the neutral axis remains unchanged,

$$ds = Rd\varphi = R'd\varphi'$$

Substituting the above equation in the strain equation,

$$\epsilon = \frac{y(d\varphi' - d\varphi)}{(R+y)d\varphi}$$

In the above equation, y may be neglected, since $y \ll R$.

Hence,

$$\varepsilon = \frac{y(d\varphi' - d\varphi)}{Rd\varphi}$$

On simplification,

$$\varepsilon = \frac{yd\varphi'}{Rd\varphi} - \frac{yd\varphi}{Rd\varphi} = y\left(\frac{d\varphi'}{ds} - \frac{d\varphi}{ds}\right)$$

$$\varepsilon = y\left(\frac{1}{R'} - \frac{1}{R}\right)$$

Substituting $\varepsilon = \sigma/E$,

$$y\left(\frac{1}{R'} - \frac{1}{R}\right) = \frac{\sigma}{E}$$

$$\frac{\sigma}{y} = E\left(\frac{1}{R'} - \frac{1}{R}\right)$$

The assumptions made in deriving the equation are as follows:

- i. Every cross section of the curved beam remains plane and perpendicular to the centroidal axis, before and after the application of the external moment.
- ii. To satisfy the above condition, it is to be agreed that the net force acting on any cross section of the curved beam should be zero. If the net force is not equal to zero, then it may result in warping.

Mathematically,

$$\int_A \sigma dA = 0$$

$$\int E y \left(\frac{1}{R'} - \frac{1}{R} \right) dA = 0$$

$$E \left(\frac{1}{R'} - \frac{1}{R} \right) \int y dA = 0$$

Since $E((1/R') - (1/R)) \neq 0$

$\int y dA = 0$ which implies that the geometric axis of the curved beam should coincide with the neutral axis of the curved beam. As the curved beam is in equilibrium condition under the applied moment, it can be stated that

$$\int \sigma y dA = M$$

Substituting for σ in the above equation,

$$E\left(\frac{1}{R'} - \frac{1}{R}\right) \int y^2 dA = M$$

Since $\int y^2 dA = I$,

$$E\left(\frac{1}{R'} - \frac{1}{R}\right)I = M$$

Thus,

$$\frac{M}{I} = \frac{\sigma}{y} = E\left(\frac{1}{R'} - \frac{1}{R}\right)$$

1.6.2 DEFLECTION OF THE CURVED BEAM WITH SMALL INITIAL CURVATURE

For deriving the deflection of the curved beam, the Castigliano's theorem is used. The strain energy of the curved beam is given as

$$U = \int \frac{1}{2} M \Delta d\varphi'$$

where $d\varphi'$ is the change in the angle produced by the moment M at the center of curvature.

From the following equation,

$$\frac{M}{I} = E\left(\frac{1}{R'} - \frac{1}{R}\right)$$

Multiplying ds on both the sides of the equation,

$$\frac{M}{I} ds = E\left(\frac{1}{R'} - \frac{1}{R}\right) ds$$

Since the length of the fiber remains unchanged,

$$ds = R d\varphi = R' d\varphi'$$

$$\frac{M}{I} ds = E(d\varphi - d\varphi') ds$$

$$\frac{M}{EI} ds = \Delta d\varphi$$

Thus, the strain of the curved beam is given as

$$U = \int \frac{1}{2} \frac{M^2 ds}{EI}$$

By partially differentiating U with respect to p ,

$$\Delta = \frac{\partial U}{\partial p} = \int \frac{M}{EI} \frac{\partial M}{\partial p} ds$$

Similarly, the angular rotation may be obtained by partially differentiating U with respect to the angular momentum M_o ,

$$\theta = \frac{\partial U}{\partial M_o} = \int \frac{M}{EI} \frac{\partial M}{\partial M_o} ds$$

1.6.3 CURVED BEAM WITH LARGE INITIAL CURVATURE

Consider a strip in the cross section of the curved beam, the concave side is called *intrados*, and the convex side is called *extrados*. The important points to be noted are:

- i. Stress variation is nonlinear across the cross section; it is hyperbolic. Experimental studies showed that stress on the concave side is large than that of the convex side.
- ii. Neutral axis will shift toward the center of curvature.
- iii. Neutral axis will not pass through the centroid of the cross section since, $\sigma_{concaveside} \neq \sigma_{convexside}$

Let us consider a curved beam with radius, R . It is subjected to a moment, M , which tends to decrease the radius of curvature. The cross-section details are shown in the above figure. It causes tension in the extrados compression in the intrados.

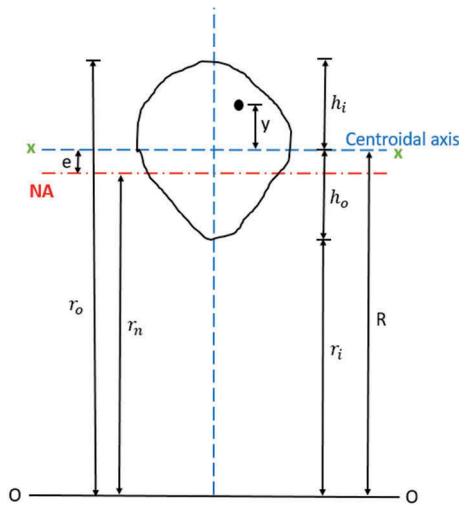
Consider an element ABDC, subtending an angle ($d\varphi$) at the center. Under the applied moment, M , this element deforms to AB D'C' for curvature. It is assumed that AB is fixed and only plane CD rotates and thus face \overline{CD} rotates to C'D' subtending an angle $\Delta d\varphi$.

Initial lengths of the fiber \overline{PQ} at distance y from the centroidal axis is given as

$$(R + y)d\varphi$$

Change in length of the fiber on the application of the moment, M , is given as

$$(y + e)\Delta d\varphi$$



where

e is the distance of the neutral axis measured from the centroidal axis

M is applied in such a manner that the neutral axis is shifted towards the center of curvature

$$\text{Strain, } \epsilon = \frac{(y + e)\Delta d\varphi}{(R + y)d\varphi}$$

Assuming that the longitudinal fibers do not undergo any deformation, stress is given as

$$\sigma = E \left(\frac{y + e}{R + y} \right)$$

It shows that the stress distribution is nonlinear and hyperbolic.

The basic assumption made is that every section normal to the centroid axis remains plane and perpendicular, before and after application of moment M .

total compressive force = total tensile force

Since the average stress on the concave side is more than the convex side, the neutral axis will shift toward the center of curvature.

Equate the sum of internal forces to zero at the cross section.

Mathematically,

$$\int_A \sigma dA = 0$$

Substituting the expression for stress, we get

$$\int_A E \frac{Ad\varphi}{d\varphi} \left(\frac{y+e}{y+R} \right) dA = 0$$

$$E \frac{\Delta d\varphi}{d\varphi} \int_A \left(\frac{y+e}{y+R} \right) dA = 0$$

Since $E \frac{\Delta d\varphi}{d\varphi} \neq 0$ and it is a constant,

$$\int_A \left(\frac{y+e}{y+R} \right) dA = 0$$

$$\int_A \left(\frac{y}{R+y} \right) dA + e \int_A \left(\frac{1}{y+R} \right) dA = 0$$

We know that the first integral term, $\int_A \frac{y}{R+y} dA = mA$, where m is a constant depending on the geometry of the X section. The quantity mA is termed as the modified area of the cross section which is modified due to the application of moment, M .

The second integral term is $e \int_A \frac{1}{(R+y)} dA$

$$e \int_A \frac{1}{(R+y)} dA = e \int \frac{R+y-y}{R} \cdot \frac{1}{(R+y)} dA$$

$$= \frac{e}{R} \int_A \frac{R+y}{R+y} dA - \int_A \frac{ydA}{R+y} = \frac{eA}{R} - \frac{e}{R}(mA)$$

Thus,

$$mA + \frac{eA}{R} - \frac{emA}{R} = 0$$

$$m + \frac{e}{R} - \frac{em}{R} = 0$$

$$m = e \left(\frac{m}{R} - \frac{1}{R} \right)$$

$$m = \frac{e}{R}(m-1)$$

$$e = \left(\frac{m}{m-1} \right) R$$

where m is the geometry property of the section.

It is to be noted that the applied moment in the cross section should be equal to the resisting moment for any equation.

Hence, by applying the following condition:

$$\int_A (\sigma dA)y = M$$

Substitution for stress, $\int_A \frac{y^2 + ye}{R+y} dA$ is to be evaluated.

$$\int_A \frac{y^2 dA}{R+y} + e \int_A \frac{y}{R+y} dA = \int_A \left(y - \frac{Ry}{R+y} \right) dA + e \int_A \frac{y}{R+y} dA$$

We know that

$$\int_A y dA = 0$$

Hence,

$$\begin{aligned} \int_A \left(\frac{y^2 + ye}{R+y} \right) dA &= -R \int_A \left(\frac{y}{R+y} \right) dA + e \int_A \frac{y dA}{R+y} \\ &= -R(mA) + emA = -mA(R - e) \\ -E \left(\frac{\Delta d\varphi}{d\varphi} \right) &= \frac{M}{mA(R - e)} \end{aligned}$$

Since, $m = \frac{e}{R-e}$

$$E \frac{\Delta d\varphi}{d\varphi} = \frac{M}{Ae}$$

On simplification,

$$e = \frac{M}{Ae} \left(\frac{y+e}{R+y} \right)$$

It is also known that,

$$\sigma = \frac{M}{(m-1)} R$$

$$\sigma = \frac{M}{AR} \frac{(m-1)}{m} \left[\frac{y + \left(\frac{m}{m-1} \right) R}{R+y} \right]$$

$$\begin{aligned}
 &= \frac{m}{AR} \frac{(m-1)}{m} \left[\frac{(m-1)y + mR}{(m-1)(R+y)} \right] \\
 \sigma &= \frac{M}{ARm} \left[\frac{m(y+R) - y}{y+R} \right] \\
 \sigma &= \frac{M}{AR} \left[1 - \frac{1}{m} \left(\frac{y}{R+y} \right) \right]
 \end{aligned}$$

The above equation named as *Winkler Bach equation*, in which

σ is the tensile/compressive stress at distance y from the centroidal axis (not from the NA),

M is the applied moment (causing a decrease in curvature),

A area of cross section,

m is the section properties (geometry/shape of the cross section),

R is the radius of curvature of the unstressed curved beam.

Sign convention

y is negative when measured toward the concave side and positive when measured toward the convex side. With the sign convention, negative stress indicates compressive stress, and positive stress indicates tensile stress.

In the plastic design to enable maximum load capacity, designers use sections with large shape factors

$$\sigma = \frac{M}{Ae} \left[\left(\frac{y+e}{y+R} \right) \right]$$

where e is the offset of the neutral axis from the center of gravity measured toward the center of curvature. Specific stress equations for intrados and extrados to be used to find the maximum stress are the extreme fibers as follows:

$$\begin{aligned}
 \sigma_{intrados} &= \frac{M}{Ae} \left[\frac{-h_i + e}{R - h_i} \right] = -\frac{M}{Ae} \left[\frac{h_i - e}{r_i} \right] \\
 \sigma_{extrados} &= \frac{M}{Ae} \left[\frac{h_o + e}{R + h_o} \right] = \frac{M}{Ae} \left[\frac{(e + h_o)}{r_o} \right]
 \end{aligned}$$

From the above equations, it is clear that stress is a function of the parameter ' m '. We already know that

$$mA = \int_A \frac{y}{R+y} dA$$

1.6.4 SIMPLIFIED EQUATIONS TO ESTIMATE STRESSES IN THE EXTREME FIBER

$$\sigma = K \frac{Mh}{I}$$

where K is a factor to be used for intrados and extrados as below:

$$K_{intrados} = \frac{\frac{M}{Mh} \frac{(h_i - e)}{r_i}}{\frac{Mh_i}{2I}}$$

$$K_{extrados} = \frac{\frac{h_o + e}{r_0}}{\frac{Mh_0}{2I}}$$

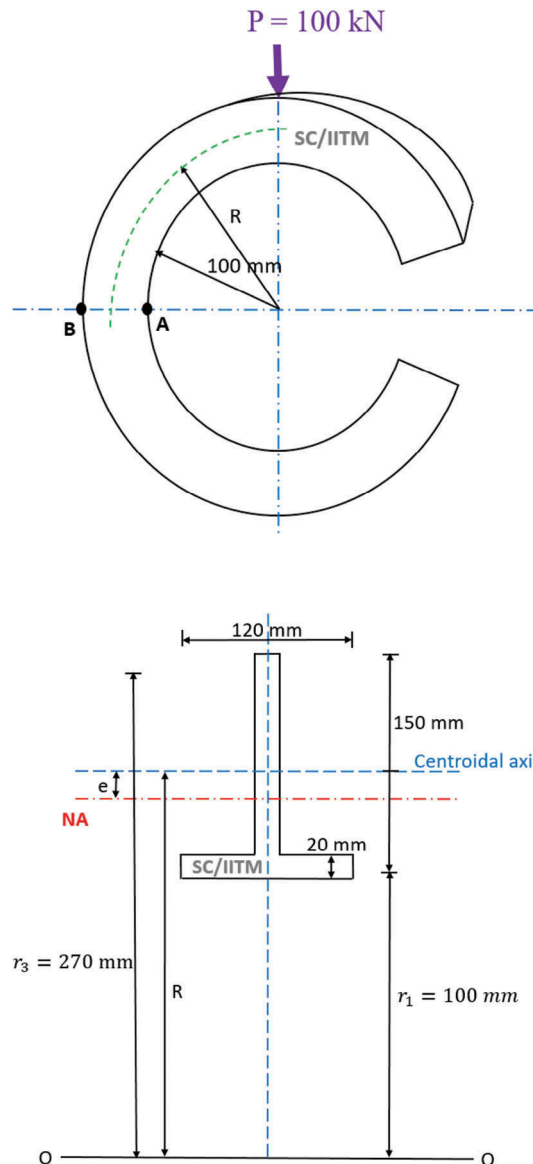
k_i and k_0 are called stress correction factors as given in the following table:

Cross section	R/h	Factors		ϵ
		K_i	K_o	
Circular	1.2	3.41	0.54	0.224R
	1.4	2.40	0.60	0.151R
	1.6	1.96	0.65	0.108R
	1.8	1.75	0.68	0.084R
	2.0	1.62	0.71	0.009R
	3.0	1.33	0.79	0.030R
	4.0	1.23	0.84	0.016R
	6.0	1.14	0.89	0.007R
Rectangular	1.2	2.89	0.57	0.305R
	1.4	2.13	0.63	0.204R
	1.6	1.79	0.67	0.149R
	1.8	1.63	0.70	0.112R
	2.0	1.52	0.73	0.090R
	3.0	1.30	0.81	0.041R
	4.0	1.20	0.85	0.021R
	6.0	1.12	0.90	0.0093R

EXERCISE PROBLEMS

Example 1

Consider an open section, comprising of 100 MN load as shown in the figure. Compute the stresses at points A and B in the curved beam.



MATLAB® Code

```
% Curved beam - T section
clc;
clear;

%% INPUT
p=100; % load acting on the beam in kN
%Geometric properties
```

```

r1=100;
r2=120;
r3=270;
r=157.22;
h1=112.78;
h2=57.22;
h3=37.22;
b1=120;
b2=20;
a= 5400;% cross sectional area in mm^2
m=1-(r/a)*((b1*log(r2/r1))+(b2*log(r3/r2))); % sectional property (no unit)
e=m*r/(m-1); % eccentricity in mm

%% Section AB on the centroidal axis
sd=-p*1000/a; % direct stress in N/mm^2
M=p*r/1000; % moment at CG in kNm
si=-(M*1000000*(h2-e)/(a*e*r1)); % stress at intrados in N/mm^2
so=(M*1000000*(h1+e)/(a*e*r3)); % stress at extrados in N/mm^2
sa=sd+si; % total stress at intrados
sb=sd+so; % total stress at extrados
fprintf('SOLUTION: \n');
fprintf('Stress at point A = %6.2f N/mm^2 \n',sa);
fprintf('Stress at point B = %6.2f N/mm^2 \n',sb);

```

Output:

Stress at point A = -97.04 N/mm²
 Stress at point B = 70.84 N/mm²

Example 2

A circular ring of the rectangular cross section has a horizontal slit as shown in the figure. Find the stresses at A and B.

MATLAB® Code

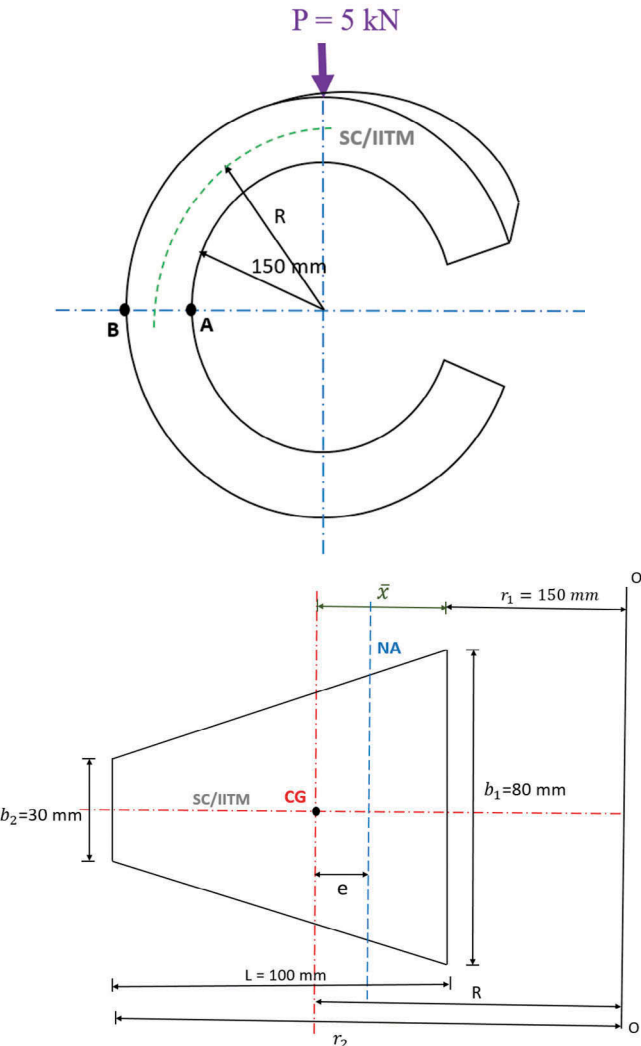
```

% Curved beam with a trapezoidal cross section
clc;
clear;

%% INPUT
h=100; % height of the section in mm
b1=80; % breadth of the section in mm
b2=30;
r1=150; % inner radius of the beam in mm
p=5; % load action on the beam in kN

%% Geometric properties
b3=(b1-b2)/2;
x=((2*h*b3/3)+(b2*h)) / (b1+b2); % Location of neutral axis
hi=x;
ho=h-x;
R=r1+x; % radius of the curved beam in mm
r2=r1+h; % outer radius of the curved beam in mm
a=(b1+b2)*h/2; % cross sectional area in mm^2

```



```

m=1-((R/a)*((b2+((r2*(b1-b2))/(r2-r1)))*log(r2/r1)-(b1-b2)); %  
sectional property  
e=m*R/(m-1); % eccentricity in mm  
I=(2*((b3*(h)^3)/36)+(0.5*b3*h*((h/3)-x)*((h/3)-x)))+(((b2*(h)^3)/12)+(b2*h*((h/2)-x)*((h/2)-x))); % moment of inertia in mm^2  
  
%% Section AB on the centroidal axis  
sd=-p*1000/a; % direct stress in N/mm^2  
M=p*R/1000; % moment at CG in kNm  
si=-(M*1000000*(hi-e)/(a*e*r1)); % stress at intrados in N/mm^2  
so=(M*1000000*(ho+e)/(a*e*r2)); % stress at extrados in N/mm^2  
sa=sd+si; % total stress at intrados  
sb=sd+so; % total stress at extrados

```

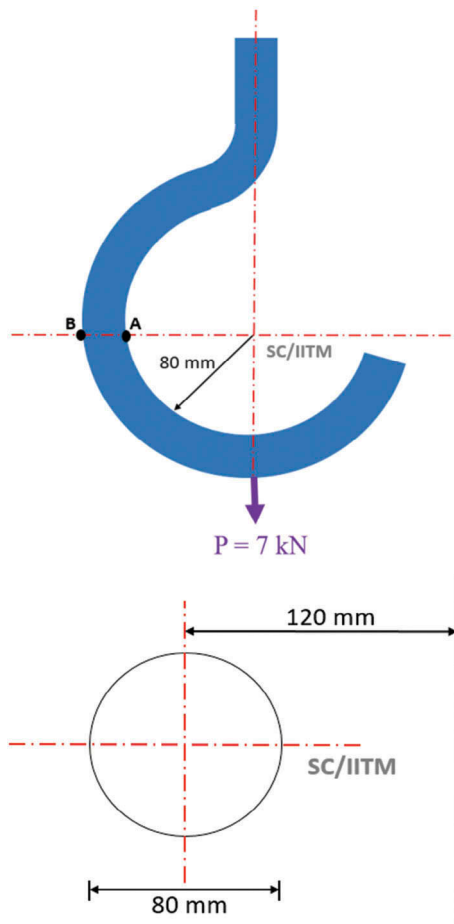
```
fprintf('SOLUTION: \n');
fprintf('Stress at point A = %6.2f N/mm^2 \n', sa);
fprintf('Stress at point B = %6.2f N/mm^2 \n', sb);
```

Output:

SOLUTION:

Stress at point A = -12.35 N/mm²Stress at point B = 10.05 N/mm²**Example 3**

Find the stresses developed at points A and B of the curved beam with a circular cross-section shown in the figure.



MATLAB® Code

```
% Crane hook problem with Circular cross-section
clc;
clear;

%% INPUT

r1=80; % inner radius of the beam in mm
d=80; % diameter of the section in mm
p=7; % load action on the beam in kN

%% Geometric properties
x=d/2; % Location of neutral axis
hi=x;
ho=d-x;
R=r1+x; % radius of the curved beam in mm
r2=r1+d; % outer radius of the curved beam in mm
a=3.14*d*d/4; % cross sectional area in mm^2
m=1-(2*((R/d)^2))+(2*(R/d)*sqrt(((R/d)^2)-1)); % sectional
property
e=m*R/(m-1); % eccentricity in mm

%% Section AB - stress calculation - Winkler Bach equation
sd=p*1000/a; % direct stress in N/mm^2
M=-p*R/1000; % moment at CG in kNm
ri=r1;
ro=r2;
si=-M*1000000*(hi-e)/(a*e*ri); % Stress at intrados
so=M*1000000*(ho+e)/(a*e*ro); % stress at extrados
sa=sd+si; % total stress in intrados
sb=sd+so; % total stress at extrados
fprintf('SOLUTION FROM WINKLER BACH EQUATION: \n');
fprintf('Stress at point A = %6.2f N/mm^2 \n',sa);
fprintf('Stress at point B = %6.2f N/mm^2 \n \n',sb);
```

Output:

SOLUTION FROM WINKLER BACH EQUATION:
 Stress at point A = 4.77 N/mm²
 Stress at point B = -2.39 N/mm²

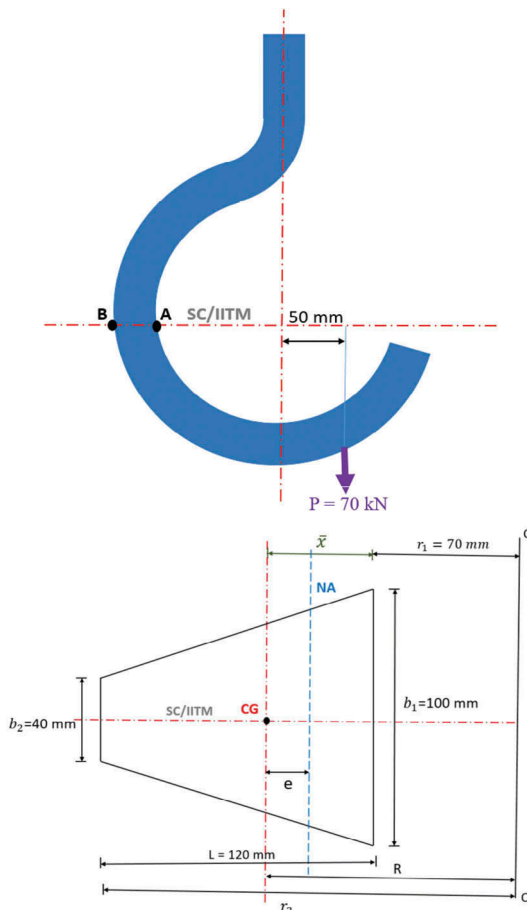
Example 4:

Find the stresses at point A and B of the crane hook of the trapezoidal cross-section under the action of 70 kN load as shown in the figure.

MATLAB® Code

```
% Crane hook problem with a trapezoidal cross section
clc;
clear;

%% INPUT
h=120; % height of the section in mm
b1=100; % breadth of the section in mm
```



```

b2=40;
r1=70; % inner radius of the beam in mm
p=70; % load action on the beam in kN

%% Geometric properties
b3=(b1-b2)/2;
x=((2*h*b3/3)+(b2*h)) / (b1+b2); % Location of neutral axis
hi=x;
ho=h-x;
R=r1+x; % radius of the curved beam in mm
r2=r1+h; % outer radius of the curved beam in mm
a=(b1+b2)*h/2; % cross sectional area in mm^2
m=1-((R/a)*((b2+(r2*(b1-b2))/(r2-r1))*log(r2/r1)-(b1-b2))); %
sectional property
e=m*R/(m-1); % eccentricity in mm

```

```

I=(2*((b3*(h)^3)/36)+(0.5*b3*h*((h/3)-x)*((h/3)-x)))+((b2*(h)^3)/12)+(b2*h*((h/2)-x)*((h/2)-x)); % moment of inertia in mm^2

%% Section AB - stress calculation - Winkler Bach equation
sd=p*1000/a; % direct stress in N/mm^2
M=-p*(R+50)/1000; % moment at CG in kNm
ri=r1;
ro=r2;
si=-M*1000000*(hi-e)/(a*e*ri); % Stress at intrados
so=M*1000000*(ho+e)/(a*e*ro); % stress at extrados
sa=sd+si; % total stress in intrados
sb=sd+so; % total stress at extrados
fprintf('SOLUTION FROM WINKLER BACH EQUATION: \n');
fprintf('Stress at point A = %6.2f N/mm^2 \n',sa);
fprintf('Stress at point B = %6.2f N/mm^2 \n \n',sb);

```

Output:

SOLUTION FROM WINKLER BACH EQUATION:
 Stress at point A = 102.87 N/mm²
 Stress at point B = -55.65 N/mm²

2 Plastic Design of Structures

2.1 PLASTIC BEHAVIOR OF STRUCTURES

Ultimate Limit State design deals with the collapse modes, which converts the structure into a mechanism. The formation of mechanism enables excessive yielding which finally leads to collapse. Steel is common construction material for the land-based and offshore structure. From the stress-strain curve of steel, it is evident that the material has got very good capacity beyond the first yield which is not used in the elastic design of structures. This material strength beyond yield value, which is not utilized in the elastic design principle, is effectively utilized in the plastic design of structures. This excessive material strength beyond the yield value is called *reserve strength*. The load carrying capacity of the structure can be increased by using the reserve strength of the material. However, this also promotes large permanent plastic deformation in the structure under excessive loading. Hence, it is mandatory to check the structure for both loads carrying capacity and ductility (API, 2000). As the reserve strength is also used in the plastic design of structures, the failure occurs by two modes by the load acting on the structure exceeding the maximum load carrying capacity and the strain developed in the structure reaching the ultimate strain. The failure under this case is catastrophic and instantaneous.

The yield stress of the material is not the deciding factor concerning the failure of the structure. An important factor that governs the behavior of the material is residual stress. It is to be noted that the first yield generally occurs due to the presence of the residual stresses and imperfections in the material developed during fabrication. The residual stress essentially develops from the welding process; flame cuttings used to create openings and hot rolling. These stresses are essentially tensile. It can be eliminated by preheating before welding, postheating after welding and peening and hammering of welds to elongate, which reduce the tensile stresses in the weld. The residual stresses are responsible for the following change in material behavior:

- brittle fracture failure,
- stress corrosion,
- buckling strength reduction,
- inelastic behavior in metals.

As the development of residual stresses in the material is unavoidable, the yield stress governs the elastic design of structures is not correct. As the residual stresses also induce inelastic behavior in the material, the designers shifted from

elastic design to ultimate load design. The most advantageous factor of steel is its ductility, which is the sign to use the reserve strength more confidently. The ductility of the material enables the redistribution of the moment from the high stresses region of the member to the adjacent location. Thus, the load carrying capacity can be extended beyond the yield stress. It also shows that plastic design can be effectively used in the design of steel structures to avoid a conservative design. The ultimate load design uses the material capability to the maximum which is a positive point in the design perspective. Failure is the major criteria based on which the design principles are formulated. The failure can occur in a structure through different modes such as

- instability of the structure,
- fatigue failure,
- excessive deformation,
- combination of above.

In practice, the structure may continue to carry the load beyond the first yield, if the failure is initiated by any one of the above modes. Thus, the design should account for the actual failure criteria which are plastic deformation, through which a structure becomes a mechanism.

Consider a beam subjected to pure bending as shown in Fig. 2.1. The top fibers will undergo contraction, and the lower fibers will undergo extension due to the applied moment.

The stress variation along the cross section of the member is shown in Fig. 2.2. Under a purely elastic state, the stresses developed in the top and bottom fibers will be lesser than that of the yield stress. The stresses at the extreme top and bottom fibers will reach the yield stress at the strain hardening stage. When the material enters into the elastoplastic region, the height of the elastic core gets reduced with the top and bottom fibers reaching the yield stress. When the material is fully plastic, the neutral axis will shift down to the equal area axis. The area

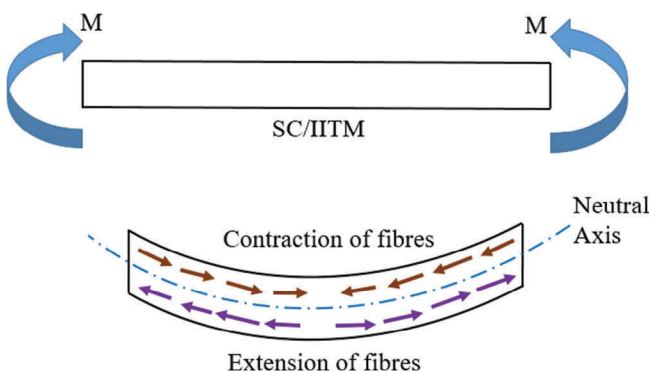
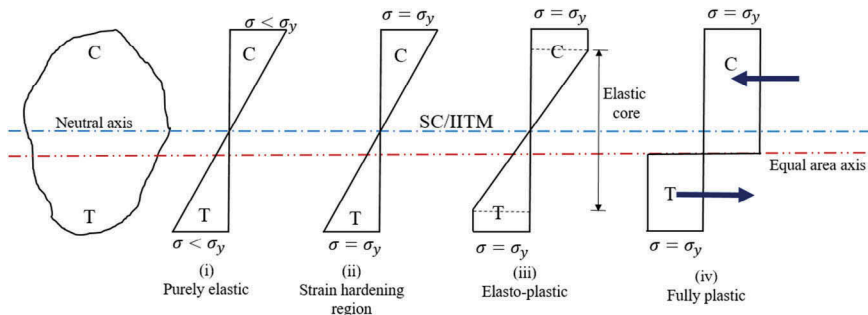


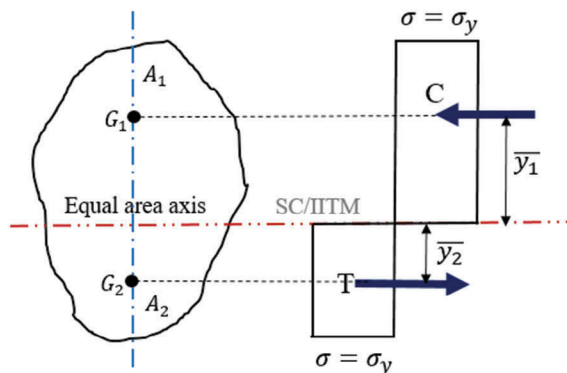
FIGURE 2.1 Bending of beams.

**FIGURE 2.2** Plastic deformation.

above and below this axis is equal as shown in Fig. 2.3. Let the cross-sectional area of the beam above and below the equal area axis be A_1 and A_2 , respectively. The total compressive force acts at a distance of \bar{y}_1 above the equal area axis, and the total tensile force acts at a distance of \bar{y}_2 below the equal area axis.

The assumptions made in the plastic analysis of structures are as follows:

- Material obeys Hooke's law until the stress reaches first yield values. On further straining stress remains constant at yield stress.
- Upper and lower yield points in tension and compression fibers are the same.
- Material is homogeneous, isotropic in both elastic and plastic states.
- The transverse plane section will remain plane and normal to the longitudinal axis of the member after bending.
- There is no resultant force acting on the member.
- The cross section is symmetric about an axis through which its centroid passes, and it is parallel to the plane of bending.

**FIGURE 2.3** Force-equilibrium condition.

- The beam is subjected to moment only, no shear force is considered.
- Every layer is free to expand and contract. It remains independent to the adjacent layer.

In plastic design, the moment acting on the member is increased until stress in the full cross section reaches the yield stress, and thus the entire cross section is effectively utilized. Under the force equilibrium condition, the total compressive force and total tensile equal will be equal. At this condition, the moment acting on the section is equal to the moment of resistance of the plastic section. Thus,

$$C = T \quad (2.1)$$

From the assumptions listed above, we get:

$$\sigma_y A_1 = \sigma_y A_2 \quad (2.2)$$

As the area of the cross section above and below the equal area axis is the same, the area can be expressed as follows:

$$A_1 = A_2 = \frac{A}{2} \quad (2.3)$$

Taking moment about the equal area axis,

$$M = C\bar{y}_1 + T\bar{y}_2 \quad (2.4)$$

$$= \sigma_y A_1 \bar{y}_1 + \sigma_y A_2 \bar{y}_2 \quad (2.5)$$

$$= \sigma_y \frac{A}{2} (\bar{y}_1 + \bar{y}_2) \quad (2.6)$$

$$= \sigma_y Z_p \quad (2.7)$$

Thus,

$$M_p = \sigma_y Z_p \quad (2.8)$$

where the plastic section modulus is given as below:

$$Z_p = \frac{A}{2} (\bar{y}_1 + \bar{y}_2) \quad (2.9)$$

The plastic section modulus, Z_p , is defined as the static moment of the cross section above and below the equal area axis. It is also called as resisting modulus of fully plasticized section. Therefore, the following relationship holds good:

$$M_p = M_{ult} = \sigma_y Z_p \quad (2.10)$$

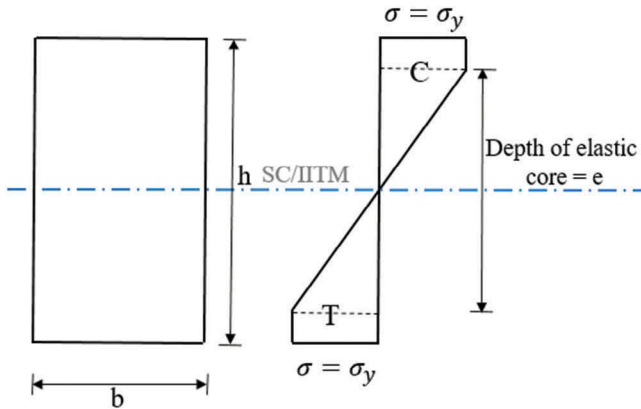


FIGURE 2.4 Elastic core.

We also know the following relationship:

$$M_e = \sigma_y Z_e \quad (2.11)$$

Consider a rectangular section in the elastoplastic region as shown in Fig. 2.4.

The section has moment carrying capacities in both elastic and plastic regions. Let M_1 be the moment capacity of the elastic section, and M_2 is the moment capacity of the plastic section.

Thus, $M_{\text{total}} = M_1 + M_2$. The moment carrying capacity of the elastic section is given as

$$M_1 = \sigma_y \left\{ \left(\frac{1}{2} b \cdot \frac{e}{2} \right) \times \frac{2}{3} \times \frac{e}{2} \right\} \times 2 \quad (2.12)$$

$$M_1 = \sigma_y \frac{be^2}{6} \quad (2.13)$$

If the section is fully plastic, then the section modulus is given as

$$Z_1 = \left(\frac{bh}{2} \right) \times \left(\frac{h}{4} \right) \times 2 = \frac{bh^2}{4} \quad (2.14)$$

In the elastic section of the elastoplastic region, the depth of the elastic core is ' e '. Thus, the section modulus is given as

$$Z_2 = \left(\frac{be}{2} \right) \times \left(\frac{e}{4} \right) \times 2 = \frac{be^2}{4} \quad (2.15)$$

The moment capacity of the plastic section is given by the following relationship:

$$M_2 = \sigma_y \left\{ \frac{bh^2}{4} - \frac{be}{4} \right\} \quad (2.16)$$

Thus, the total moment is the sum of the moments of both the elastic and plastic sections and is given as

$$M = M_1 + M_2 = \sigma_y \left(\frac{bh^2}{4} \right) \left[1 - \frac{e^2}{3h^2} \right] \quad (2.17)$$

For a rectangular section, we know that the plastic section modulus is given as

$$Z_p = \frac{bh^2}{4} \quad (2.18)$$

Thus, the total moment is written as follows:

$$M = \sigma_y z_p \left[1 - \frac{e^2}{3h^2} \right] \quad (2.19)$$

Thus,

$$M = M_p \left[1 - \frac{e^2}{3h^2} \right] \quad (2.20)$$

The depth of the elastic core can be calculated from the above equation if the moment applied to the section is known.

2.2 SHAPE FACTOR

Shape factor is the ratio of the plastic moment and the yield moment. It is given by the following relationship:

$$S = \frac{M_p}{M_e} = \frac{Z_p}{Z_e} \quad (2.21)$$

It is a geometric property of the member and is varied with the change in the cross section of the member. Shape factors for a few standard sections are estimated in the following section.

2.2.1 RECTANGULAR SECTION

Consider a rectangular section of breadth ' b ' and height ' h ' as shown in Fig. 2.5.

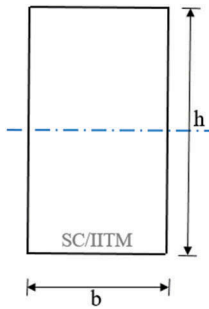


FIGURE 2.5 Rectangular section.

The plastic section modulus is given as

$$Z_p = \frac{A}{2} (\bar{y}_1 + \bar{y}_2) \quad (2.22)$$

Also, for the rectangular section, the plastic section modulus is given as

$$Z_p = \frac{bh}{2} \left(\frac{h}{4} + \frac{h}{4} \right) = \frac{bh^2}{4} \quad (2.23)$$

The elastic section modulus is given by the following relationship:

$$Z_e = \frac{I}{y_{\max}} \quad (2.24)$$

For the rectangular section, the following relationship holds good:

$$Z_e = \frac{bh^3}{12} \times \frac{2}{h} = \frac{bh^2}{6} \quad (2.25)$$

The ratio of the plastic section modulus to the elastic section modulus, which is the shape factor is computed as 1.5 for rectangular section.

2.2.2 TRIANGULAR SECTION

Consider a triangle of breadth 'b' and height 'h' as shown in Fig. 2.6.

Moment of inertia of the section is, $I = \frac{bh^3}{36}$ and $y_{\max} = y_1$

Thus, the elastic section modulus is given as

$$Z_e = \frac{I}{y_{\max}} = \frac{bh^2}{24} \quad (2.26)$$

Consider the triangular section in the fully plastic state as shown in Fig. 2.7.

$$\frac{b_1}{b} = \frac{h_1}{h} \Rightarrow b_1 = b \times \frac{h_1}{h} \quad (2.27)$$

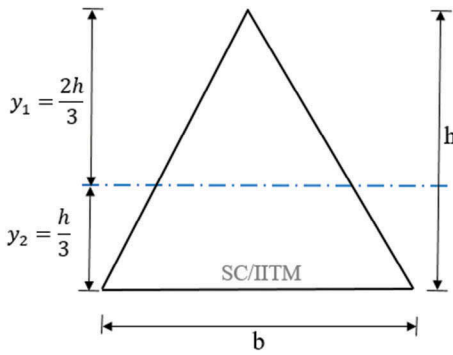


FIGURE 2.6 Triangular section.

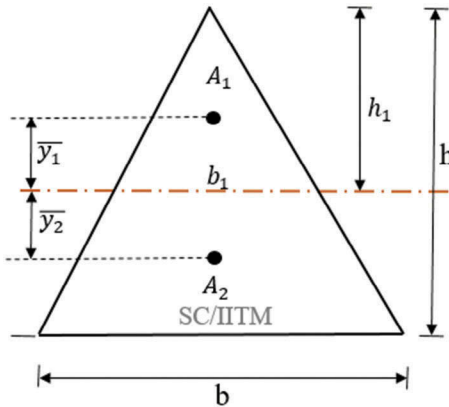


FIGURE 2.7 Fully plastic triangular section.

As the areas above and below the axis are equal, we get the following relationship:

$$A_1 = \frac{A}{2} \quad (2.28)$$

Thus,

$$\frac{1}{2} \times b_1 h_1 = \frac{1}{4} \times b h \quad (2.29)$$

$$h_1 = \frac{h}{\sqrt{2}} \quad (2.30)$$

Similarly, from the geometry, the following equation holds good:

$$b_1 = \frac{b}{\sqrt{2}} \quad (2.31)$$

The distance between the equal area axis and the centroid of the section A_1 is given by the following equation:

$$\bar{y}_1 = \frac{1}{3}h_1 = \frac{h}{3\sqrt{2}} = 0.236h \quad (2.32)$$

$$\bar{y}_2 = \frac{\left(h - \frac{h}{\sqrt{2}}\right)}{3} \left(\frac{\frac{b}{\sqrt{2}} + 2b}{\frac{b}{\sqrt{2}} + b}\right) = 0.155h \quad (2.33)$$

The plastic section modulus of the triangular section is given as follows:

$$Z_p = \frac{A}{2}(\bar{y}_1 + \bar{y}_2) = 0.098bh^2 \quad (2.34)$$

Thus, the shape factor (S) is computed as 2.346.

2.2.3 CIRCULAR SECTION

Consider a circular section of radius ' r ' as shown in Fig. 2.8.

$$\text{For a circular section, } A = \pi r^2, \bar{y} = \frac{4r}{3\pi}, I = \frac{\pi d^4}{64}, y_{\max} = r$$

The plastic and elastic section modulus of the circular section is given as

$$Z_p = \frac{A}{2}(\bar{y}_1 + \bar{y}_2) = \frac{4r^2}{3} \quad (2.34)$$

$$Z_e = \frac{I}{y_{\max}} = \frac{\pi r^2}{4} \quad (2.35)$$

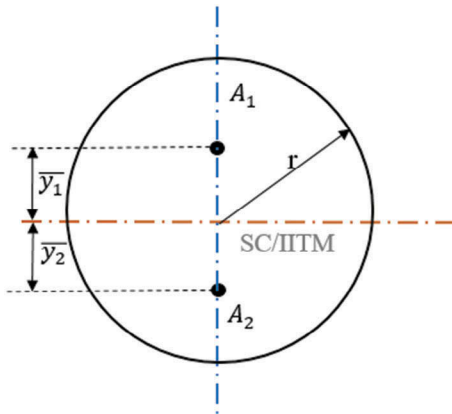


FIGURE 2.8 Circular section.

TABLE 2.1 Shape factors

Sl. no.	Cross section	Shape factor
1	Tubular section (r_1 : outer radius, r_2 : inner radius)	$S = \frac{16r_1}{3\pi} \left(\frac{r_1^3 - r_2^3}{r_1^4 - r_2^4} \right)$
2	I-section	1.1–1.8
3	Box section (square)	1.2
4	Box section (rectangle)	1.25
5	Diamond section of four equal sides	2

Thus, shape factor (S) is computed as 1.7.

The shape factors of other commonly used sections are listed in Table 2.1.

2.3 MATLAB® CODE FOR CALCULATING SHAPE FACTOR

```
%% This MATLAB® code is for the calculation of sectional properties
    and shape factor
% Re-type the following code MATLAB® new script and run the file with
    suitable inputs
clc;
clear;
sy=415; % Yield stress in N/mm2
E=2.1e5; % Young's modulus in N/mm2
%% Shape factor
% Mention the type of section here
% Change the input values under each type
type=3;
% rectangular section - 0
% Circular solid - 1
% Tubular - 2
% Square/ rectangular hollow section - 3
if type == 0
    % rectangular section
    b=100; % smaller dimension of the section in mm
    h=200; % larger dimension of the section in mm
    a=b*h; % area of the section in mm2
    ybar1=h/4;
    ybar2=h/4;
    I=(b*(h^3))/12;
    zp=0.5*a*(ybar1+ybar2);
    zy=I/(h/2);
    sf=zp/zy;
    fprintf ('SECTION DETAILS:\n');
    fprintf ('Section type: Rectangular section\n');
    fprintf ('Smaller dimension,b = %d mm\n',b);
    fprintf ('Larger dimension,h = %d mm\n',h);
    fprintf ('SECTION PROPERTIES:\n');
    fprintf ('Area,A = %d mm^2\n',a);
```

```

fprintf ('Moment of Inertia, I= %d mm^4\n',I);
fprintf ('Shape Factor = %6.3f \n', sf);
elseif type == 1
    % circular solid
    D=100; % Diamter of the section
    A=pi*(D^2)/4;
    r=D/2;
    ybar1=4*r/(3*pi);
    ybar2=ybar1;
    zp=0.5*A*(ybar1+ybar2);
    I=pi*(D^4)/64;
    zy=I/r;
    sf1=zp/zx;
    fprintf ('SECTION DETAILS:\n');
    fprintf ('Section type: Circular section\n');
    fprintf ('Diameter,D = %d mm\n\n',D);
    fprintf ('SECTION PROPERTIES:\n');
    fprintf ('Area,A = %d mm^2\n',A);
    fprintf ('Moment of Inertia, I= %d mm^4\n',I);
    fprintf ('Shape Factor = %6.3f \n', sf1);
elseif type == 2
    % Tubular member
    D=100; % Outer diamter of the section
    d=80; % Inner diameter of the section
    t=(D-d)/2; % Thickness of the section
    A=pi*((D^2)-(d^2))/4;
    Iy=pi*((D^4)-(d^4))/64;
    r1=D/2;
    r2=d/2;
    ybar1=((pi*(r1^2)/2)*(4*r1/(3*pi)))-((pi*(r2^2)/2)*(4*r2/
        (3*pi)))/(0.5*pi*((r1^2)-(r2^2)));
    ybar2=ybar1;
    zy=Iy/r1;
    zp=0.5*A*(ybar1+ybar2);
    sf2=zp/zx;
    fprintf ('SECTION DETAILS:\n');
    fprintf ('Section type: Tubular section\n');
    fprintf ('Outer Diameter,D = %d mm\n',D);
    fprintf ('Inner Diameter,D = %d mm\n\n',d);
    fprintf ('SECTION PROPERTIES:\n');
    fprintf ('Area,A = %d mm^2\n',A);
    fprintf ('Moment of Inertia, Iy= %d mm^4\n',Iy);
    fprintf ('Shape Factor = %6.3f \n', sf2);
elseif type == 3
    % Hollow section
    b=100; %flange width
    d=80; % web depth
    t=10; % thickness
    b1=b-(2*t);
    d1=d-(2*t);
    A=2*(b+d)*t; % Area in mm2
    Iy=d*d*t*((3*b)+d)/6;
    Iz=b*b*t*(b+(3*d))/6;

```

```

zy=Iy/(d/2);
ybar1= ((b*d*d/8)-(b1*d1*d1/8))/(0.5*A);
ybar2=ybar1;
zp=0.5*A*(ybar1+ybar2);
sf3=zp/z;
fprintf ('SECTION DETAILS:\n');
fprintf ('Section type: Hollow section\n');
fprintf ('Flange width,b = %d mm\n',b);
fprintf ('Web depth,d = %d mm\n',d);
fprintf ('Thickness,t = %d mm\n\n',t);
fprintf ('SECTION PROPERTIES:\n');
fprintf ('Area,A = %d mm^2\n',A);
fprintf ('Moment of Inertia, Iy= %d mm^4\n',Iy);
fprintf ('Moment of Inertia, Iz= %d mm^4\n',Iz);
fprintf ('Shape Factor = %6.3f \n\n', sf3);
end

```

a) Output for rectangular section:

SECTION DETAILS:
 Section type: Rectangular section
 Smaller dimension, b = 100 mm
 Larger dimension, h = 200 mm
 SECTION PROPERTIES:
 Area, A = 20000 mm²
 Moment of Inertia, I = 6.666667e+07 mm⁴
 Shape Factor = 1.500

b) Output for solid circular section:

SECTION DETAILS:
 Section type: Circular section
 Diameter, D = 100 mm
 SECTION PROPERTIES:
 Area, A = 7.853982e+03 mm²
 Moment of Inertia, I = 4.908739e+06 mm⁴
 Shape Factor = 1.698

c) Output for tubular section:

SECTION DETAILS:
 Section type: Tubular section
 Outer Diameter, D = 100 mm
 Inner Diameter, d = 80 mm
 SECTION PROPERTIES:
 Area, A = 2.827433e+03 mm²
 Moment of Inertia, Iy= 2.898119e+06 mm⁴
 Shape Factor = 1.403

d) Output for hollow section:

SECTION DETAILS:
 Section type: Hollow section
 Flange width, b = 100 mm
 Web depth, d = 80 mm

Thickness, $t = 10 \text{ mm}$

SECTION PROPERTIES:

Area, $A = 3600 \text{ mm}^2$

Moment of Inertia, $I_y = 4.053333e+06 \text{ mm}^4$

Moment of Inertia, $I_z = 5.666667e+06 \text{ mm}^4$

Shape Factor = 0.868

Example 2.1:

Determine the plastic moment and plastic section modulus for the T-section shown in Fig. 2.9. Take $f_y = 410 \text{ N/mm}^2$.

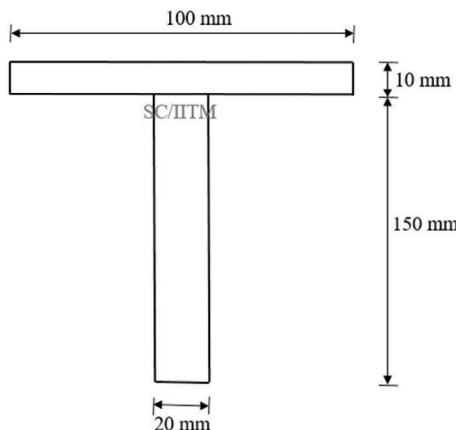


FIGURE 2.9 T-section.

Solution:

$$\text{Area of the section} = (100 \times 10) + (150 \times 20) = 4000 \text{ mm}^2$$

Location of the equal area axis:

Consider the equal area axis is located at a distance 'y' from the bottom of the section.

$$(20 \times y) = 4000/2$$

$$y = 100 \text{ mm}$$

The total cross section is then divided into three sections as shown in Fig. 2.10.

$$\begin{aligned} \text{Plastic section modulus, } Z_p &= (100 \times 10 \times 55) + (20 \times 50 \times 25) + (20 \times 100 \times 50) \\ &= 1.8 \times 10^5 \text{ mm}^3 \end{aligned}$$

$$\begin{aligned} \text{Plastic moment, } M_p &= Z_p \times f_y \\ &= 1.8 \times 10^5 \times 410 \\ &= 73.80 \text{ kNm} \end{aligned}$$

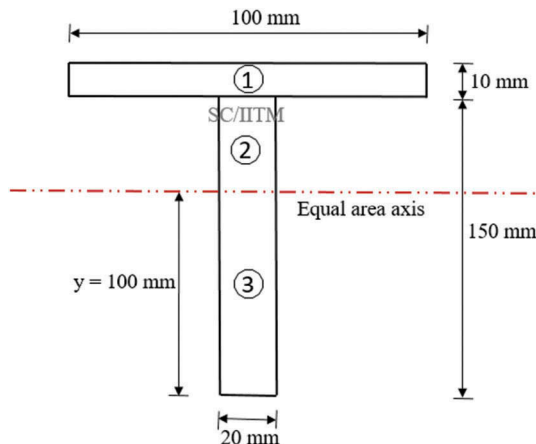


FIGURE 2.10 T-section with equal area axis.

Example 2.2

Determine the plastic moment and plastic section modulus for the I-section shown in Fig. 2.11. Take $f_y = 410 \text{ N/mm}^2$.

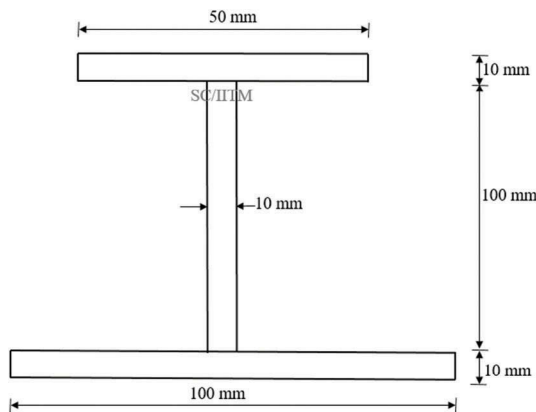


FIGURE 2.11 I-section.

Solution:

$$\text{Area of the section} = (50 \times 10) + (10 \times 100) + (100 \times 10) = 2500 \text{ mm}^2$$

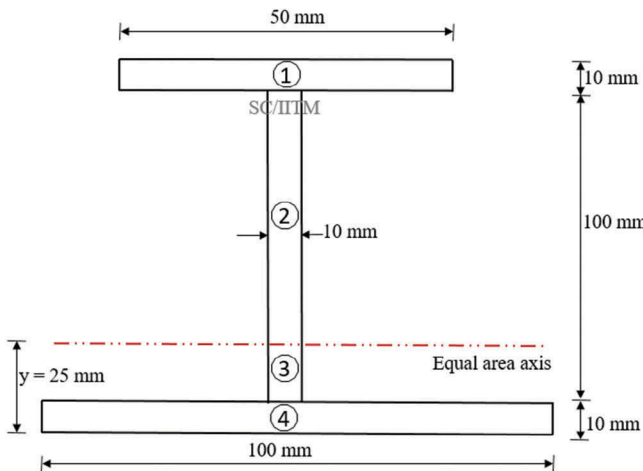


FIGURE 2.12 I-section with equal area axis.

Location of the equal area axis:

Consider the equal area axis is located at a distance 'y' from the bottom of the section.

$$(100 \times 10) + (00 \times y) = 2500/2$$

$$y = 25 \text{ mm}$$

The total cross section is then divided into three sections as shown in Fig. 2.12.

$$\begin{aligned} \text{Plastic section modulus } Z_p &= (50 \times 10 \times 80) + (75 \times 10 \times 37.5) + (25 \times 10 \times 12.5) \\ &\quad + (100 \times 10 \times 17.5) \\ &= 8.875 \times 10^4 \text{ mm}^3 \end{aligned}$$

$$\begin{aligned} \text{Plastic moment } M_p &= Z_p \times f_y \\ &= 8.875 \times 10^4 \times 410 \\ &= 36.39 \text{ kNm} \end{aligned}$$

2.4 MOMENT CURVATURE RELATIONSHIP

For a simple bending problem, the following equation holds good as per classical mechanics:

$$\frac{M}{I} = \frac{\sigma}{y} = \frac{E}{R} \quad (2.36)$$

The curvature is given by the following relationship:

$$\phi = \frac{1}{R} = \frac{M}{EI} \quad (2.37)$$

It is seen that the curvature is directly proportional to the moment. This proportionality is true only until the elastic limit. Consider a rectangular section as shown in Fig. 2.4. In the elastic state, $y = h/2$.

Thus,

$$\frac{E}{R} = \frac{\sigma}{y} = \frac{\sigma}{(h/2)} \quad (2.38)$$

$$\frac{1}{R} = \frac{2\sigma_y}{Eh} \quad (2.39)$$

Under the fully plastic state, the depth of the elastic core is given by ‘ e ,’ which is equal to the depth of the rectangular section ‘ h .’ The curvature under this condition is given by the following relationship:

$$\frac{1}{R} = \frac{2\sigma_y}{Ee} \Rightarrow e = \frac{2R\sigma_y}{E} \quad (2.40)$$

For partially plasticized section,

$$\phi_y = \frac{M_y}{EI} \quad (2.41)$$

$$\phi_p = \frac{M_p}{EI} \quad (2.42)$$

Thus,

$$\frac{\phi_p}{\phi_y} = \frac{M_p}{M_y} = S \quad (2.43)$$

We know that

$$M = M_p \left[1 - \frac{e^2}{3h^2} \right] \quad (2.44)$$

Substituting the equation for the depth of elastic core, the above equation is simplified to the following form:

$$M = M_p \left[1 - \frac{4R^2\sigma_y^2}{3E^2h^2} \right] \quad (2.45)$$

At yield, we know the following:

$$\frac{1}{R} = \frac{2\sigma_y}{Eh} \Rightarrow \frac{2\sigma_y}{E} = \left(\frac{h}{R} \right)_y \quad (2.46)$$

By substituting the above equation in the moment equation, we get:

$$\frac{M}{M_p} = 1 - \frac{1}{3} \left[\frac{(h/R)_y}{(h/R)} \right]^2 \quad (2.47)$$

In the plastic design of structures, the following assumptions are valid:

- The yield strength is assumed to remain constant.
- The allowable stresses are taken only as a fraction of yield strength.

The load factor, which is the ratio of collapse load and working load, is given by the following relationship:

$$Q = \frac{W_p}{W_w} = \frac{M_p}{M_w} \quad (2.48)$$

We know that

$$\frac{M_p}{M_w} = \frac{Z_p}{Z_e} \times \frac{\sigma_y}{\sigma_{all}} = S \frac{\sigma_y}{\sigma_{all}} \quad (2.49)$$

Thus, the load factor is given as

$$Q = S \frac{\sigma_y}{\sigma_{all}} \quad (2.50)$$

where S is the shape factor, σ_y is the yield stress, σ_{all} is the allowable stress and the ratio of yield stress to allowable stress is termed as the factor of safety. The load factor is the product of shape factor and the factor of safety. It shows that the safety factor in plastic design is enhanced by the shape factor.

2.5 MECHANISM

If a body is subjected to any loading, it will offer resistance which is called an internal reaction to the applied loads. This process of offering resistance to the applied load is called load carrying capacity. If the body is unable to offer resistance to the applied load, then it is referred to as a mechanism. The load at which the body stops offering resistance to the external load is called collapse load. A structural system will become a mechanism, only when a sufficient number of plastic hinges are formed. If the degree of indeterminacy of the structural system is ' n ', then ' $n + 1$ ' plastic hinges are required to form a mechanism. The plastic hinges will form at the following locations of the structure:

- fixed supports,
- point of action of concentrated loads,

- the section at which the bending moment is maximum,
- the section where the moment of inertia changes.

These plastic hinges have limited rotation capacity with resistance to rotation. The collapse load for the plastic analysis of structures can be determined from the following theorems:

- static theorem,
- kinematic theorem,
- uniqueness theorem.

2.6 STATIC THEOREM

The static theorem is also called ‘lower bound theorem.’ The statement of this theorem is given below.

For a given frame and loading, if there exists any bending moment distribution throughout the frame, which is both safe and statistically admissible under a set of loads Q , then the value of load W is less than the collapse load.

$$W \leq W_c$$

Thus, the collapse load determined from this theorem will be lower than or equal to the collapse load. The steps involved in the calculation of collapse load by using this theorem are listed as follows:

1. Draw the bending moment diagram for the given structural system.
2. Identify the sections at which the bending moment is maximum. Such sections are called critical sections.
3. Assume the formation of the plastic hinges in the critical sections. It is to be noted that the $(n + 1)$ plastic hinges are required for the formation of mechanism, where ‘ n ’ is the degree of indeterminacy.
4. Calculate the collapse load.

This method is tedious in case of the analysis of statically indeterminate structures, as it requires a bending moment diagram for identifying the critical sections. It is also prone to errors and does not guarantee a true collapse load.

2.7 KINEMATIC THEOREM

The kinematic theorem is also called ‘upper bound theorem.’ The statement of this theorem is given below:

For a given frame and loading, a mechanism is assumed, and value of collapse load is computed based on the assumed mechanism. This computed loads will be either equal to or greater than the collapse load.’

$$W \geq W_c$$

Thus, the collapse load determined from this theorem will be greater than or equal to the collapse load. The steps involved in the calculation of collapse load by using this theorem are listed below.

Assume a certain collapse mechanism for the given structural system. For a complete mechanism, the number of plastic hinges should be equal than $(n + 1)$.

Partial mechanism: $N < n + 1$

Complete mechanism: $N = n + 1$

Overcomplete mechanism: $N > n + 1$

For the assumed mechanism, find the collapse load using the principle of virtual work. The principle of virtual work states that ‘the work done by the external forces during the collapse mechanism is equal to the work absorbed by the plastic hinges.’ Mathematically, it can be written as

$$\text{External work done} = \text{internal work absorbed}$$

$$P\delta = M_p\theta$$

The different types of mechanisms that can be assumed for the plastic analysis of structures using the kinematic theorem are shown in Fig. 2.13. Sometimes, it becomes difficult to assume the mechanism, and the inappropriate selection of a mechanism may lead to the wrong estimate of collapse loads. Thus, this method is iterative.

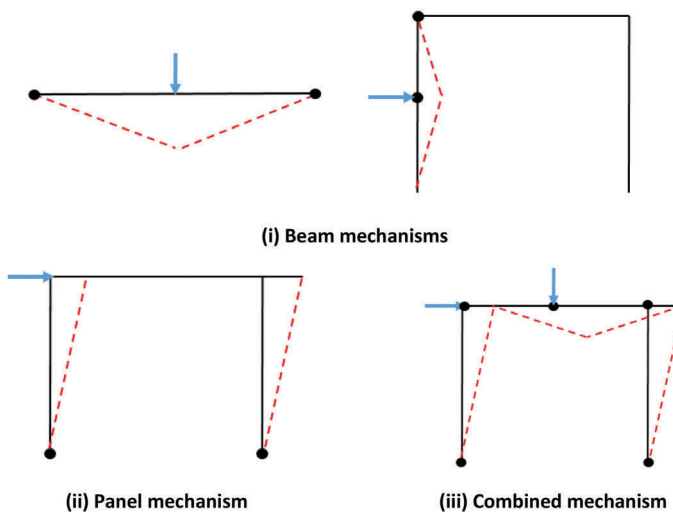


FIGURE 2.13 Collapse mechanisms.

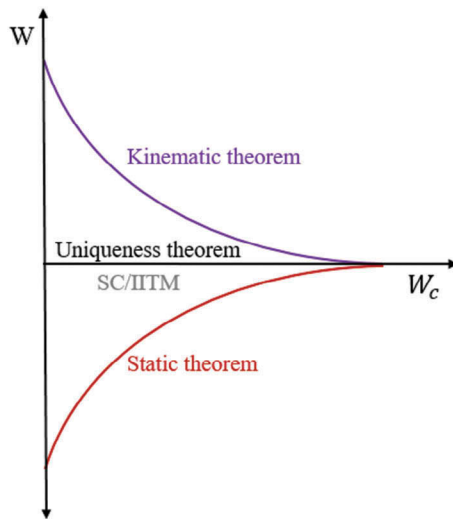


FIGURE 2.14 Plastic analysis theorems.

2.8 UNIQUENESS THEOREM

The statement of uniqueness theorem is as follows:

For a given frame and loading, at least one statically admissible bending moment distribution can be determined, if this bending moment distribution results in a sufficient number of plastic hinges to be formed to convert the frame into a mechanism, then the corresponding load is the collapse load. Thus,

$$W = W_c$$

As this theorem uses both the bending moment diagram and the assumption of mechanism for the estimation of collapse load, it is also called combined theorem. The theorem can be graphically expressed as shown in Fig. 2.14.

2.9 EXERCISES TO ESTIMATES COLLAPSE LOAD

2.9.1 FIXED BEAM WITH A CENTRAL POINT LOAD

Consider a fixed beam of length 'l' with a concentrated load 'W' acting at its center. The bending moment diagram for the fixed beam is shown in Fig. 2.15.

Using static theorem,

$$2M_p = \frac{Wl}{4}$$

$$W_c = \frac{8M_p}{l}$$

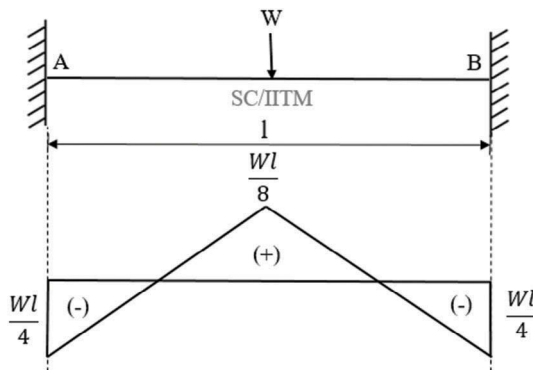


FIGURE 2.15 Fixed beam with a central concentrated load.

The degree of indeterminacy of the fixed beam is 2. Thus, $(n + 1) = 3$ plastic hinges should be formed for a complete mechanism to be developed. Thus, plastic hinges are assumed to be developed at ends A and B, and the point of action of the load as shown in Fig. 2.16 for the estimation of collapse load by the kinematic theorem.

$$\text{External work done} = W\delta$$

$$\text{Internal work} = M_p(\theta + 2\theta + \theta) = 4M_p\theta$$

By the principle of virtual work,

$$W\delta = 4M_p\theta$$

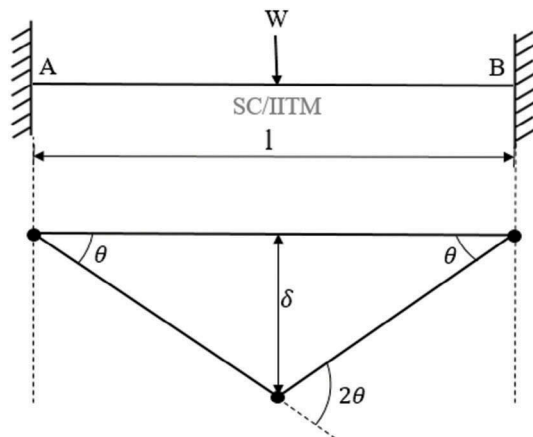


FIGURE 2.16 Fixed beam mechanism.

Substituting, $\theta = \frac{2\delta}{l}$

$$W_c = \frac{8M_p}{l}$$

2.9.2 FIXED BEAM WITH UNIFORMLY DISTRIBUTED LOAD

Consider a fixed beam of length ' l ' with a uniform distributed load ' w ' acting along the length of the member. The bending moment diagram for the fixed beam is shown in Fig. 2.17.

From the bending moment diagram,

$$2M_p = \frac{wl^2}{8}$$

$$w_c = \frac{16M_p}{l^2}$$

The degree of indeterminacy of the fixed beam is 2. Thus, $(n + 1) = 3$ plastic hinges should be formed for a complete mechanism to be developed. Thus, plastic hinges are assumed to be developed at ends A and B, and the midpoint of the length of the member is shown in Fig. 2.18 for the estimation of collapse load by the kinematic theorem.

$$\text{External work done} = \left(\frac{1}{2} \times l \times \delta\right)w = \frac{wl\delta}{2}$$

$$\text{Internal work} = M_p(\theta + 2\theta + \theta) = 4M_p\theta$$

By the principle of virtual work,

$$\frac{wl\delta}{2} = 4M_p\theta$$

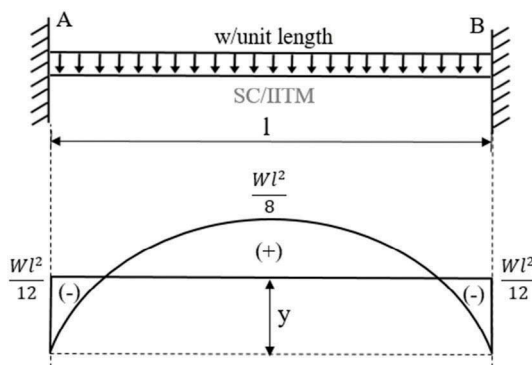
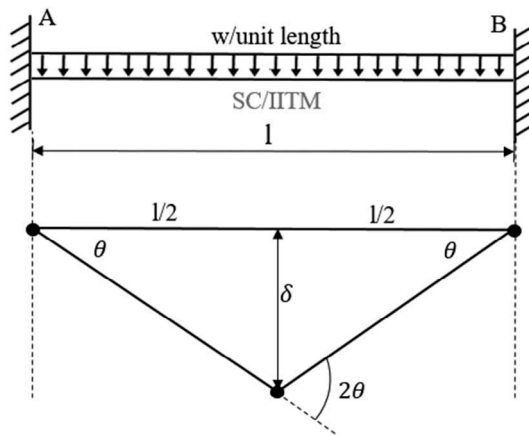


FIGURE 2.17 Fixed beam with uniformly distributed load.

**FIGURE 2.18** Fixed beam mechanism under udl.

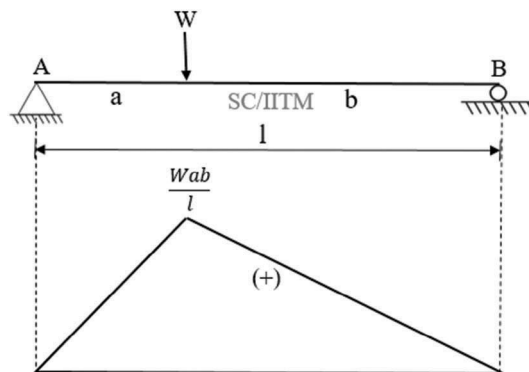
$$\text{Substituting } \theta = \frac{2\delta}{l}$$

$$w_c = \frac{16M_p}{l^2}$$

2.9.3 SIMPLY SUPPORTED BEAM WITH ECCENTRIC LOAD

Consider a simply supported beam of length ' l ' with an eccentric load ' W ' at a distance ' a ' from the left end. The bending moment diagram for the fixed beam is shown in Fig. 2.19.

The reactions at A and B are given as $R_A = \frac{Wa}{l}$, $R_B = \frac{Wb}{l}$

**FIGURE 2.19** Simply supported beam with eccentric load.

$$M_p = \frac{Wab}{l}$$

$$W_c = \frac{M_p l}{ab} = \frac{M_p(a+b)}{ab}$$

The degree of indeterminacy of the simply supported beam is 0. Thus, $(n + 1) = 1$ plastic hinge should be formed for a complete mechanism to be developed. Thus, the plastic hinge is assumed to be developed at the point of action of the load as shown in Fig. 2.20 for the estimation of collapse load by the kinematic theorem.

From the assumed mechanism, $\theta_1 = \frac{\delta}{a} \Rightarrow \delta = a\theta_1$

$$\theta_2 = \frac{\delta}{b} \Rightarrow \delta = b\theta_2$$

External work done = $W\delta$

$$\text{Internal work} = M_p(\theta_1 + \theta_2) = M_p\left(\frac{\delta}{a} + \frac{\delta}{b}\right) = M_p\delta\left(\frac{a+b}{ab}\right)$$

By the principle of virtual work,

$$W\delta = M_p\delta\left(\frac{a+b}{ab}\right)$$

$$W_c = \frac{M_p(a+b)}{ab}$$

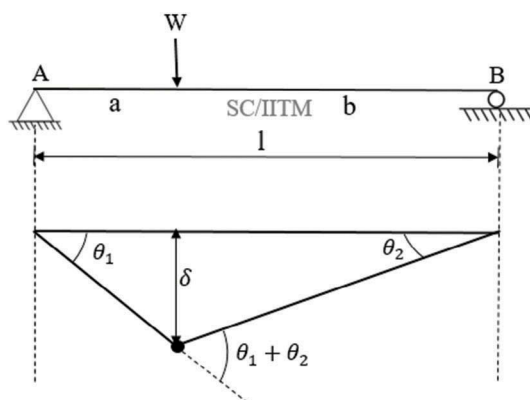


FIGURE 2.20 Simply supported beam mechanism.

2.9.4 SIMPLY SUPPORTED BEAM WITH A CENTRAL POINT LOAD

Consider a simply supported beam of length ' l ' with an eccentric load ' W ' acting at the center of the beam. The bending moment diagram for the fixed beam is shown in Fig. 2.21.

The reactions at A and B are given as $R_A = \frac{W}{2}$, $R_B = \frac{W}{2}$

$$M_p = \frac{Wl}{4}$$

$$W_c = \frac{4M_p}{l}$$

The degree of indeterminacy of the simply supported beam is 0. Thus, $(n + 1) = 1$ plastic hinge should be formed for a complete mechanism to be developed. Thus, the plastic hinge is assumed to be developed at the point of action of the load as shown in Fig. 2.22 for the estimation of collapse load by the kinematic theorem.

From the assumed mechanism, $\theta_1 = \frac{\delta}{l/2} = \frac{2\delta}{l}$

External work done = $W\delta$

Internal work = $M_p(2\theta)$

By the principle of virtual work,

$$W\delta = M_p \frac{4\delta}{l}$$

$$W_c = \frac{4M_p}{l}$$

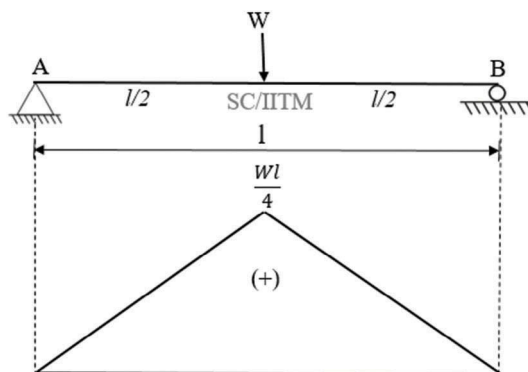


FIGURE 2.21 Simply supported beam with a central concentrated load.

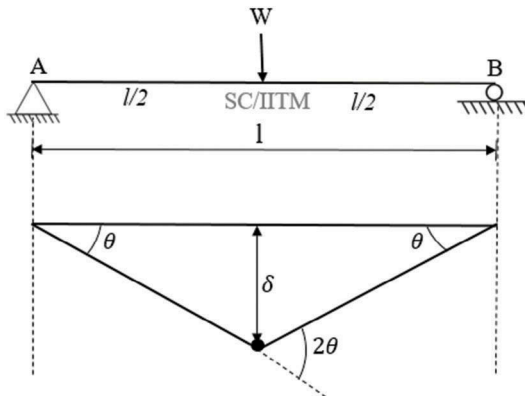


FIGURE 2.22 Simply supported beam mechanism.

2.10 ADVANTAGES AND DISADVANTAGES OF PLASTIC ANALYSIS

2.10.1 ADVANTAGES

1. The plastic analysis enables the effective utilization of the entire cross section by completely plasticizing it.
2. The plastic analysis increases the load carrying capacity of the structural system.
3. Material strength is well utilized even beyond strain at yield.
4. The factor of safety is enhanced by the shape factor.

2.10.2 DISADVANTAGES

1. The member will be subjected to excessive deformation.
2. As this method demands the redistribution of moments, it can be effectively applied to highly indeterminate structural systems.

2.11 COMPARISON OF ELASTIC AND PLASTIC ANALYSIS

Elastic analysis	Plastic analysis
1. Equilibrium condition The structure under any load combination should remain in static equilibrium $\sum F_x = 0, \sum F_y = 0, \sum M_z = 0$	1. Mechanism condition Ultimate load or collapse load is reached when a mechanism is formed, after which it initiates redistribution of moments.
2. Compatibility condition Deformation of different fibers in a given cross section should be compatible with each other.	2. Equilibrium condition The structure should remain in equilibrium under the applied loads, even after the formation of mechanism.
3. Limit stress condition The maximum stress in any section and fiber should not exceed the yield stress	3. Plastic moment condition In any fiber in the cross section, the developed stress is equal to the yield stress.

EXERCISES

Example 2.3

Find the true collapse load of the propped cantilever beam with the uniformly distributed load as shown in Fig. 2.23 using both static and kinematic theorem.

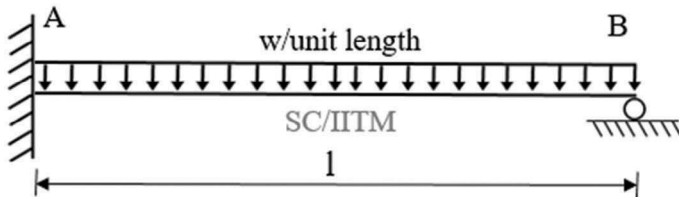


FIGURE 2.23 Propped cantilever beam with uniformly distributed load.

Solution:

Degree of indeterminacy = 1

Thus, the number of plastic hinges required to form a mechanism is 2. The hinges are assumed to form at the fixed support and the point where the bending moment is maximum.

(i) Static theorem

The bending moment diagram of the beam is shown in Fig. 2.24. Assume a section CC at a distance 'x' from the right end, where the bending moment is maximum.

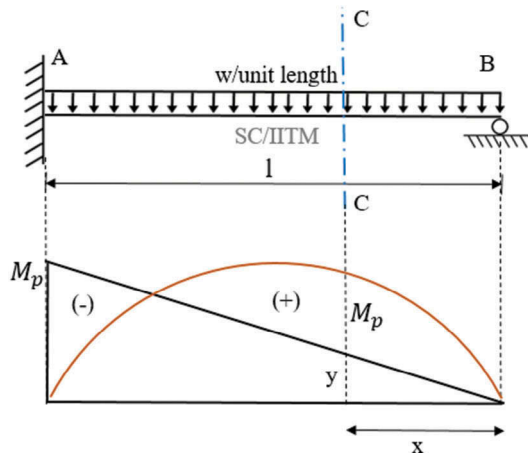


FIGURE 2.24 Bending moment diagram.

Bending moment ordinate at section CC = $M_p + \left(\frac{x}{l}\right)M_p = M_p\left(\frac{l+x}{l}\right)$
 Bending moment at section XX is given as

$$M_{cc} = \frac{wl}{2}(x) - \frac{wx^2}{2} = \frac{wx}{2}(l-x)$$

Equating the above two equations,

$$M_p = \frac{w}{2} \left[xl \left(\frac{l-x}{l+x} \right) \right]$$

For the bending moment to be maximum,

$$\frac{dM_p}{dx} = 0$$

By solving the above equation, $x = 0.414l$.

Thus, the plastic moment is given as

$$M_p = \frac{w}{2} \left[xl \left(\frac{l-x}{l+x} \right) \right] = 0.086wl^2$$

Thus,

$$w_c = \frac{11.66M_p}{l^2} \text{ or } W_c = \frac{11.66M_p}{l}$$

(ii) Kinematic theorem

The plastic hinges are assumed to be developed at the fixed support and at the point where the bending moment is maximum as shown in Fig. 2.25 for the estimation of collapse load by the kinematic theorem.

From the assumed mechanism, $\theta_1 = \frac{\delta}{0.586l}$
 $\theta_2 = \frac{\delta}{0.414l}$

$$\text{External work done} = w_c \left(\frac{1}{2} l \delta \right)$$

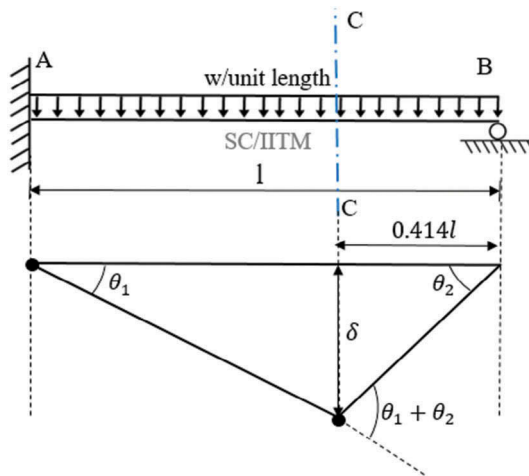
$$\text{Internal work} = M_p(\theta_1) + M_p(\theta_1 + \theta_2) = 2M_p(\theta_1) + M_p(\theta_2)$$

By substituting the values of θ_1 and θ_2 ,

$$\text{Internal work done} = 5.828M_p \left(\frac{\delta}{l} \right)$$

By the principle of virtual work,

$$w_c = \frac{11.66M_p}{l^2} \text{ or } W_c = \frac{11.66M_p}{l}$$

**FIGURE 2.25** Beam mechanism.**Example 2.4**

Find the true collapse load of the fixed beam with the eccentric load as shown in Fig. 2.26 using the kinematic theorem. Also, find the magnitude of collapse load for a concentrated load of 30 kN acting at 2.0 m from the left end of the fixed beam of 5.0 m length.

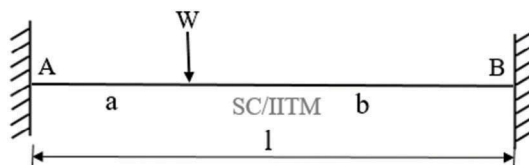
The degree of indeterminacy of the fixed beam is 2. Thus, $(n + 1) = 3$ plastic hinges should be formed for a complete mechanism to be developed. Thus, plastic hinges are assumed to be developed at ends A and B, and the point of action of the load is shown in Fig. 2.27 for the estimation of collapse load by the kinematic theorem.

$$\text{External work done} = W\delta$$

$$\text{Internal work} = 2M_p(\theta_1 + \theta_2)$$

By the principle of virtual work,

$$W\delta = 2M_p(\theta_1 + \theta_2)$$

**FIGURE 2.26** Fixed beam eccentric concentrated load.

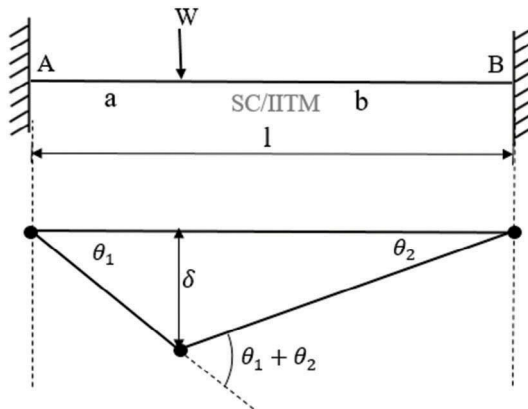


FIGURE 2.27 Fixed beam mechanism.

$$\text{Substituting } \theta_1 = \frac{\delta}{a}, \theta_2 = \frac{\delta}{b}$$

$$W\delta = 2M_p \left(\frac{\delta(a+b)}{ab} \right)$$

$$W_c = \frac{2M_p l}{ab}$$

For a concentrated load of 30 kN acting at 2.0 m from the left end,
 $W = 20 \text{ kN}$, $a = 2 \text{ m}$, $b = 3 \text{ m}$, $l = 5 \text{ m}$.

$$W_c = \frac{2M_p l}{ab}$$

$$M_p = \frac{W_c ab}{2l} = 18 \text{ kNm}$$

Example 2.5

Determine the plastic moment for the fixed beam shown in Fig. 2.28.

The degree of indeterminacy of the fixed beam is 2. Thus, $(n + 1) = 3$ plastic hinges should be formed for a complete mechanism to be developed. Thus,

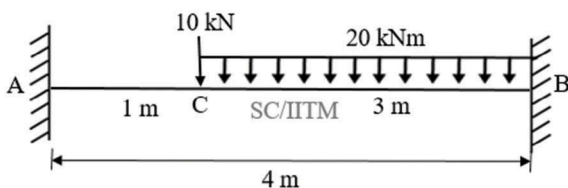
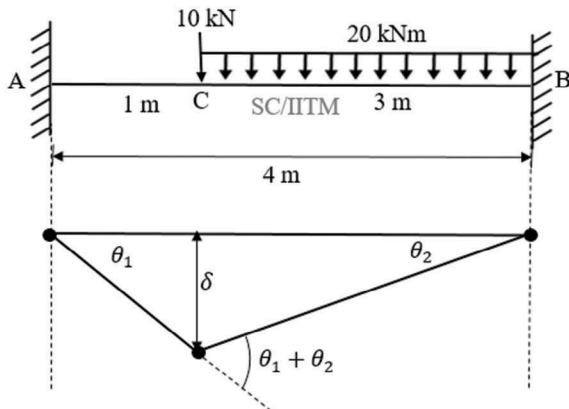


FIGURE 2.28 Fixed beam example.

**FIGURE 2.29** Fixed beam mechanism.

plastic hinges are assumed to be developed at ends A, B and C as shown in Fig. 2.29 for the estimation of collapse load by the kinematic theorem.

$$\text{External work done} = (10 \times \delta) + \left(\frac{1}{2} \times \delta \times 3 \times 20\right) = 40\delta$$

$$\text{Internal work} = 2M_p(\theta_1 + \theta_2)$$

By the principle of virtual work,

$$40\delta = 2M_p(\theta_1 + \theta_2)$$

$$\text{Substituting } \theta_1 = \delta, \theta_2 = \frac{\delta}{3}$$

$$40\delta = \left(\frac{2M_p\delta}{3}\right)$$

$$M_p = 15 \text{ kNm}$$

Example 2.6

Find the true collapse load of the portal frame as shown in Fig. 2.30 using the kinematic theorem.

The degree of indeterminacy of the frame is 3. Thus, $(n + 1) = 4$ plastic hinges should be formed for a complete mechanism to be developed. Thus, plastic hinges are assumed to be developed at ends A, B, C, D and E.

(i) Beam mechanism

$$\text{External work done} = 2W\delta$$

$$\text{Internal work} = 2M_p(\theta_1 + \theta_2)$$

By the principle of virtual work,

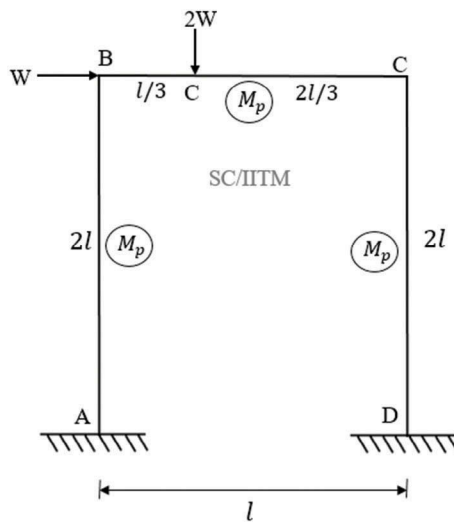


FIGURE 2.30 Frame example.

$$2W\delta = 2M_p(\theta_1 + \theta_2)$$

Substituting $\theta_1 = \frac{\delta}{a}$, $\theta_2 = \frac{\delta}{b}$

$$2W\delta = \left(\frac{2M_p\delta l}{ab} \right)$$

$$W_c = \frac{M_p l}{ab}$$

Substituting $a = \frac{l}{3}$, $b = \frac{2l}{3}$

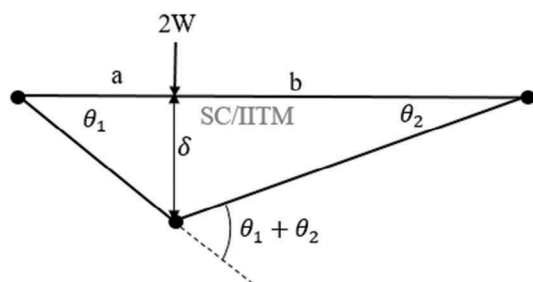


FIGURE 2.31 Beam mechanism.

$$W_c = \frac{9M_p}{2l}$$

Refer to Fig. 2.31 for Beam mechanism.

(ii) Sway mechanism

External work done = $W\Delta$

Internal work = $2M_p\alpha$

By the principle of virtual work,

$$W\Delta = 2M_p\alpha$$

Substituting $\alpha = \frac{\Delta}{2l}$

$$W\Delta = \left(\frac{4M_p\Delta}{2l} \right)$$

$$W_c = \frac{2M_p}{l}$$

Refer to Fig. 2.32 for sway mechanism.

(iii) Combined mechanism

External work done = $2W\delta + W\Delta$

Internal work = $2M_p(\alpha + \theta_1 + 2\theta_2 + 2\alpha) = 2M_p(3\alpha + \theta_1 + 2\theta_2)$

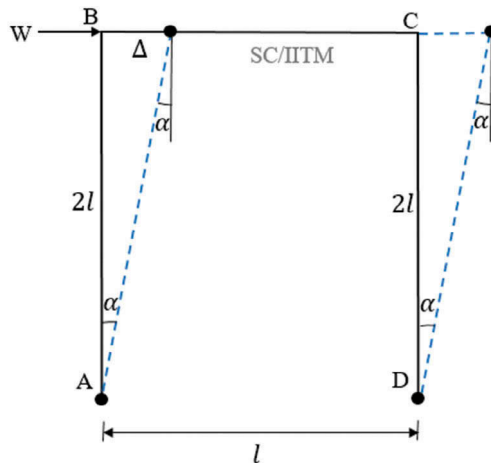


FIGURE 2.32 Sway mechanism.

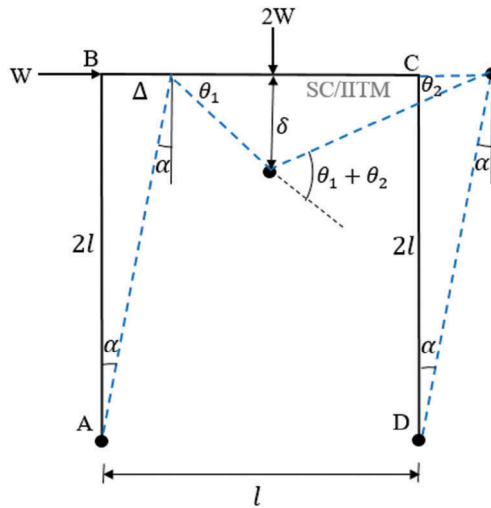


FIGURE 2.33 Combined mechanism.

By the principle of virtual work,

$$W\Delta + 2W\delta = 2M_p(3\alpha + \theta_1 + 2\theta_2)$$

$$Wl\theta_1 = 3M_p\theta_1$$

$$W_c = \frac{3M_p}{l}$$

The true collapse load is the lowest of all the mechanisms. Thus,

$$W_c = \frac{2M_p}{l}$$

Refer to Fig. 2.33 for combined mechanism.

Example 2.7

Find the true collapse load of the portal frame as shown in Fig. 2.34 using the kinematic theorem.

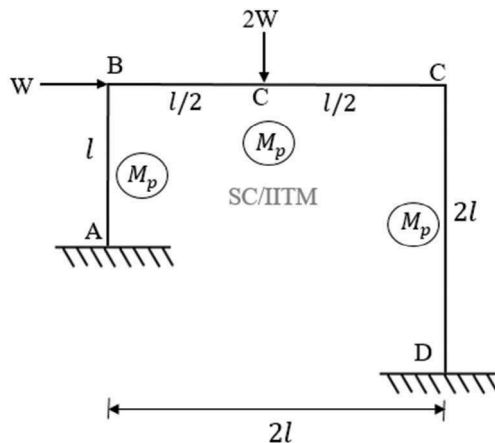
(i) Beam mechanism

External work done = $2W\delta$

Internal work = $4M_p\theta$

By the principle of virtual work,

$$2W\delta = 4M_p\theta$$

**FIGURE 2.34** Frame example.

Substituting $\theta = \frac{\delta}{l}$,

$$2W\delta = \left(\frac{4M_p\delta}{l} \right)$$

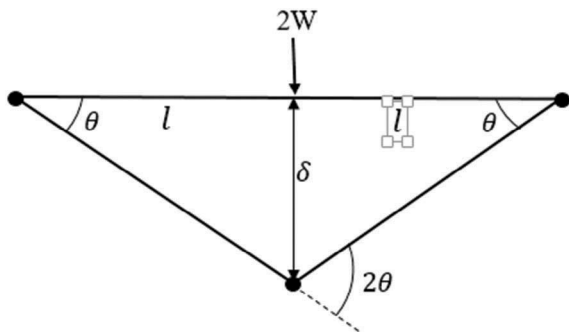
$$W_c = \frac{2M_p}{l}$$

Refer to Fig. 2.35 for beam mechanism.

(ii) Sway mechanism

External work done = $W\Delta$

Internal work = $M_p(2\alpha + 2\beta)$

**FIGURE 2.35** Beam mechanism.

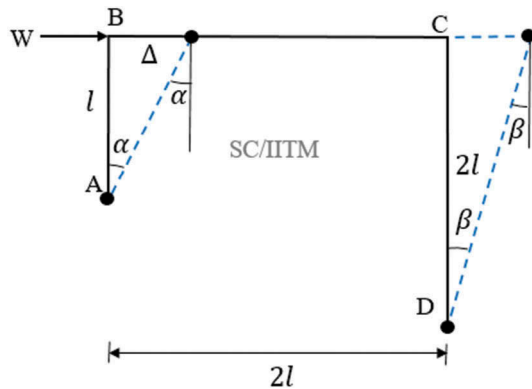


FIGURE 2.36 Sway mechanism.

By the principle of virtual work,

$$W\Delta = 2M_p(\alpha + \beta)$$

$$\text{Substituting } \alpha = \frac{\Delta}{l}, \beta = \frac{\Delta}{2l}$$

$$W\Delta = \left(\frac{3M_p\Delta}{l} \right)$$

$$W_c = \frac{3M_p}{l}$$

Refer to Fig. 2.36 for sway mechanism.

(iii) Combined mechanism

$$\text{External work done} = 2W\delta + W\Delta$$

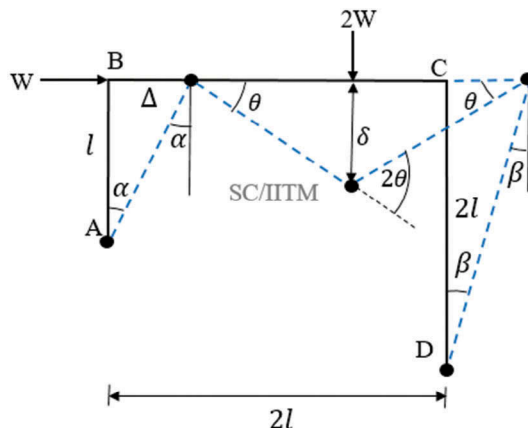
$$\text{Internal work} = 2M_p(4\alpha + 2\beta)$$

By the principle of virtual work,

$$W\Delta + 2W\delta = 2M_p(4\alpha + 2\beta)$$

$$3W\Delta = \frac{5M_p\Delta}{l}$$

$$W_c = \frac{5M_p}{3l}$$

**FIGURE 2.37** Combined mechanism.

The true collapse load is the lowest of all the mechanisms. Thus,

$$W_c = \frac{5M_p}{3l}$$

Refer to Fig. 2.37 for combined mechanism.

Example 2.8

Find the true collapse load of the continuous beam shown in Fig. 2.38 using the kinematic theorem. Also, find the minimum plastic section modulus of the section. Take $f_y = 410$ MPa.

(i) Beam mechanism 1

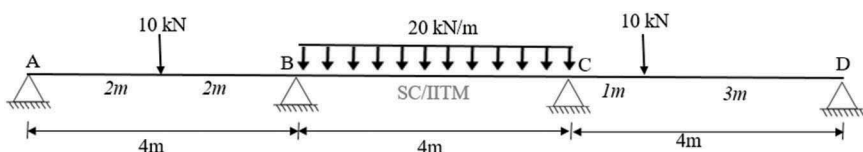
External work done = $W\delta = 10\delta$

Internal work = $3M_p\theta$

By the principle of virtual work,

$$10\delta = 3M_p\theta$$

Substituting $\theta = \frac{\delta}{2}$,

**FIGURE 2.38** Continuous beam example.

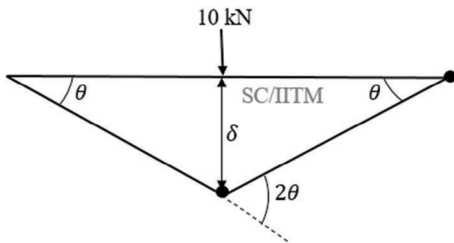


FIGURE 2.39 Beam mechanism 1.

$$10\delta = \left(\frac{3M_p\delta}{2} \right)$$

$$M_p = 6.667 \text{ kNm}$$

Refer to Fig. 2.39 for beam mechanism 1.

(ii) Beam mechanism 2

$$\text{External work done} = W \left(\frac{1}{2} \times \delta \times 4 \right) = 40\delta$$

$$\text{Internal work} = 4M_p\theta$$

By the principle of virtual work,

$$W\Delta = 2M_p(\alpha + \beta)$$

$$\text{Substituting } \theta = \frac{\delta}{2},$$

$$40\Delta = 2M_p\Delta$$

$$M_p = 20 \text{ kNm}$$

Refer to Fig. 2.40 for beam mechanism 2.

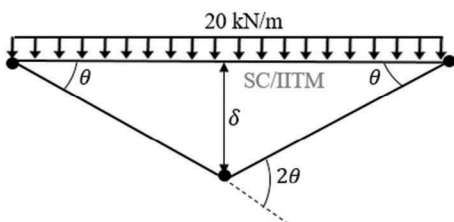


FIGURE 2.40 Beam mechanism 2.

(iii) Beam mechanism 3

External work done = $W\delta = 10\delta$

Internal work = $M_p(2\theta_1 + \theta_2)$

By the principle of virtual work,

$$10\delta = M_p(2\theta_1 + \theta_2)$$

$$10\delta = \frac{7M_p\delta}{3}$$

$$M_p = 4.289 \text{ kNm}$$

The highest value of the plastic moment should be considered for design. Thus,

$$M_p = 20 \text{ kNm}$$

$$\text{Thus, plastic section modulus } Z_p = \frac{M_p}{f_y} = 4.878 \times 10^4 \text{ mm}^3$$

Refer to Fig. 2.41 for beam mechanism 3.

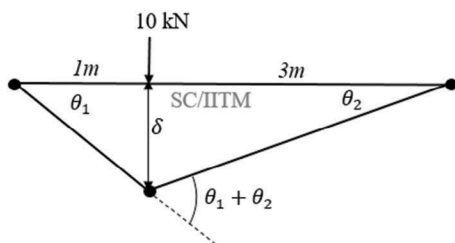


FIGURE 2.41 Beam mechanism 3.



Taylor & Francis

Taylor & Francis Group

<http://taylorandfrancis.com>

@Seismicisolation

3 Blast, Fire, and Impact-Resistant Design

3.1 INTRODUCTION

Blast, impact and fire resistant design of structures aim at reducing the risk to people and facilities from the accidental events that occur in both land-based and offshore structures (Amdahl & Eberg, 1993; Chandrasekaran et al., 2006b; Chandrasekaran et al., 2015; Chandrasekaran et al., 2013a; 2007f). Investigations on the structural systems under a combination of blast, impact and fire loads exhibit their sensitivity to the dynamic effects caused by these loads (Burgan et al., 2003; Cho et al., 2015; Chandrasekaran, Chandak and Anupam, 2006; Chandrasekaran et al., 2013a; 2013b). In particular, offshore platforms are continuously subjected to lateral loads in a hostile environment. Accidental loads arising during the erection of bulk building modules, a ship-platform collision in case of offshore structures are special types of loads, which gain much importance to the structural designer (Cerik et al., 2015; Chandrasekaran & Nassery, 2017a, 2017b; Karroum et al., 2007; Khedmati & Nazari, 2012; Kim et al., 2016). The study on the behavior of deck plates of offshore structures and cargo ships under hydrocarbon fire is also essential to avoid catastrophic failures (Chandrasekaran & Srivastava, 2018; Jin et al., 2005).

3.2 BLAST-RESISTANT DESIGN

Blast-resistant design involves the following steps:

- Quantification of blast overpressures that result from accidental explosions.
- Establishment of design blast loads from the blast overpressure.
- Establishment of structural performance requirements.
- Structural design to withstand blast loads within the required performance limits.

Industrial structures and offshore structures are more susceptible to accidental explosions (Chen et al., 1985; Liu & Soares, 2016; Paik & Czujko, 2013; Ufuah, 2012). Although such incidents are rare in the frequency of occurrence, it may lead to severe consequences and thereby causing very high risk. It results in both the financial and personal loss in addition to a detrimental impact on the public and environment. Apart from several accidents occurred in infrastructure industries, the two well-known accidents such as Piper Alpha

(6 June 1988) and Deep-Water Horizon (20 April 2010) emphasizes the severe impacts of accidents of offshore structures, caused by fire and explosion (Morin et al., 2017; Oltedal, 2012). Thus, the threefold objective of a blast-resistant design of structures is set as follows.

3.2.1 PERSONNEL SAFETY

The level of safety for the person inside the building should be enhanced by the blast-resistant design. The past incidents show that the collapse of the building, resulted from blasts is one of the major reasons for severe injuries. Therefore, one of the main objectives is to reduce the probability that the building itself becoming a hazard in an explosion.

3.2.2 CONTROLLED SHUTDOWN

In case of the process and manufacturing industries, an accidental event occurring at one unit should not affect the continued operation and safety of the other. It is to avoid therefore the loss of control of the process units that are not involved directly in the event.

3.2.3 FINANCIAL CONSIDERATION

The facilities housing critical and expensive equipment should be protected to avoid huge financial loss. Thus, the next objective of a blast-resistant design is to prevent or minimize financial losses. The major considerations in the blast-resistant design are carried out even in the planning stage itself. Crucial decisions to their maintenance are made by following standard guidelines. For example, in the case of offshore structures, the guidelines and recommended the practice for the satisfactory design of offshore structures against blast loading are described in API RP 2FB. The critical requirements of the blast-resistant structure are highly influenced by the following factors:

- distance from the blast source,
- the criticality of the function carried out in the structure.

Expected occupancy

Industrial structures and other structures of strategic importance such as nuclear power plants, coastal structures, offshore platforms and naval dockyards are generally designed to resist a certain level of blast loads. However, it is not realistic to construct a blast-proof building as it is highly impossible to provide an absolute level of blast protection. There is always a probability of exceedance of design basis event or failure of a nonstructural element in the structure. Thus, the blast-resistant design is recommended only for those structures that are expected to perform even under critical situations. Offshore facilities are one of such critical structures where an accidental explosion may

lead to the partial (or) total collapse of the structure, resulting in loss of life and severe environmental impact. It is important to note that a common practice to achieve blast-resistance or minimize the effect of blast on the circumferential equipment is to increase the distance between the equipment installations. On an offshore platform, as the available space is very limited and expensive, significant mitigation of blast effects by increasing the distance between the critical equipment is impractical. Alternatively, the following facilities need to be designed explicitly to resist the blast effects:

1. control rooms,
2. living quarters,
3. escape routes,
4. evacuation facilities,
5. critical structural components,
6. safety-critical items such as fire water lines and their supporting structures.

Offshore facilities commonly employ blast walls that are built integrally with the rest of the structure. Alternatively, prefabricated, precast wall panels using lightweight materials are also used to expedite the construction process. Compared to that of the onshore petrochemical facility, offshore facilities are very congested. Unfortunately, explosion source used to be within a confined source and quite closer to the items that must survive the explosion. The blast-resistant design goes through the following stages.

3.2.4 PRELIMINARY DESIGN

The preliminary design is based on the nominal overpressure and impulse.

3.2.5 DETAILED DESIGN

The detailed design is usually based on the numerical models such as computational fluid dynamics (CFD), which solve the equations describing gas flow, turbulence and combustion processes.

A starting point for the blast-resistant design is therefore during the layout of the critical equipment and arrangements of other plants and equipment. It is highly important to decide that equipment needs to be protected against blast loads. It is because their continuous operation will help mitigate the consequences caused by blast on other service areas. The arrangement should be made in such a way to provide the best inherent protection from blast loads.

3.3 BLAST LOADS

An explosion is a rapid chemical process producing transient air pressure waves called blast waves. The peak overpressure and duration of the overpressure may vary with distance from the source of explosion or the explosive

device in case of a terrorist attack using TNT. In load calculations, it is very important to recognize various scenarios that would have a severe outcome and account for the same in the design. The blast pressure waves will be reflected and refracted by the buildings. As blast waves are intrusive, all sides of a building or structure can be subjected to overpressure. The peak overpressure decreases as the pressure wave propagates ahead from the source of the explosion. Reflection from the building generates multiple wavefronts, which are capable of causing severe damage to the structure.

When a blast impinges directly on to the face of the structure, it is reflected. As a result, the effective pressure applied to that face of the building gets magnified. Blast loads are extremely intense in magnitude and sustain only for a very short duration. However, the energy absorption capacity and dynamic characteristics of the structure govern its response to an explosion. In general, a tall building, having a lower fundamental frequency takes a longer response time about that of the duration of the load. Under such cases, it is important to understand that steel and reinforced concrete structures are capable of absorbing a lot of strain energy due to their ductility. Flexible components can absorb a great deal of the energy delivered by a blast load through an elastic and plastic strain. A high mass causes less energy to be imparted to the system. However, in case of a larger explosion, the structure as a whole is affected by the blast wave.

Protected spaces are areas within the building that are hardened to protect the occupants and equipment against the effects of external explosion; they are named as protected space as they support a critical function even under crisis, such as control rooms. In the design of protected spaces, their limiting blast capacity must be quantified. Protected spaces must be enclosed on all sides by walls and doors so that they should not become extensively hot during its expected occupation. It should possess sufficient cooling capacity to remove the heat loads of the space, to maintain the temperature and humidity for occupancy. Construction of protected spaces with enhanced robustness is necessary.

3.4 CLASSIFICATION OF EXPLOSIONS

Explosions can be classified into four basic types:

1. vapor cloud explosions (VCE),
2. pressure vessel explosions (PVE),
3. condensed phase explosions (CPE),
4. dust explosions (DE).

3.4.1 VAPOUR CLOUD EXPLOSIONS

Four conditions are necessary for a vapor cloud explosion (VCE) to occur. They are listed as follows:

Condition 1: There must be a release of flammable material at suitable conditions of the pressure or temperature. The flammable material list includes

liquefied gases under pressure, ordinary flammable liquids and gases. When a flammable liquid spill, it vaporizes, and this dispersion is termed as a vapor cloud.

Condition 2: Ignition must be sufficiently delayed for a vapor cloud to form a maximum flammable cloud size; this usually takes about 60 s, so that the ignition delay is not too long. If the ignition occurs instantly, a fire or fireball will occur.

Condition 3: The fuel-air ratio of a sufficient amount of the vapor cloud must be present within the flammable range—the more uniform the fuel-air mixture and closer to the stoichiometric fuel-air ratio, the stronger the explosion.

Condition 4: There must be a flame-acceleration mechanism to be present for causing VCE. For example, congested areas within the flammable portion of the vapor cloud are good examples.

The speed of the flame propagation governs overpressures produced by a VCE through the cloud. Objects that are present in the pathway of the flame enhance the turbulence of both the vapor and the flame. Formation of turbulence further enhances the speed of the flame, which further enhances the overpressures. Confinement of the space that limits flame explosion, such as solid decks, also increases the speed of the flame propagation. It is interesting to note that if the flame acceleration is controlled, one can avoid explosion; it shall result only in the formation of a large fireball or flash fire. Thus, the center of VCE is not necessarily where the flammable material is released. It is the conjected area present within the vapor cloud. A better design for explosion-resistance would be to plan more open areas without congestion. Kindly note that workfloors with multiple areas of congestion can cause multiple explosions as the flame shall propagate through each of these congested areas.

3.4.2 PRESSURE VESSEL EXPLOSIONS

The pressure vessel explosions (PVEs) may occur at anyone (or their combination) of the following types:

- Deflagrations and detonations of pure gases, which are not mixed with the oxidants. Example: acetylene.
- Combustion deflagrations and detonations in the enclosures, which can occur in the presence of gaseous, liquid or dust particle fuels. If an enclosure is too weak to sustain the pressure resulting from such combustion, it will result in PVE.
- Runaway exothermic chemical reactions can cause an accelerated condition if there is any delay in the process of removing the released energy. If the pressure in the containment vessel exceeds the pressure capabilities of the vessel, it will result in PVE.

- An overpressure of the equipment with nonreactive gaseous contents can also result in PVE, but they are termed as mechanical explosions.
- Physical vapor explosions occur when two streams of a mixture with a widely different temperature occur suddenly. It will result in the flashing of the relatively cooler liquid to generate vapor and thus develops pressure. If this developed pressure exceeds the vessel capacity, it may result in PVE.
- Boiling liquid expanding vapor explosions (BLEVEs) occurs when a large amount of pressurized liquid is suddenly vented into the atmosphere. Such cases usually occur due to the high pressure of the vessel. BLEVE may cause a huge billowing, emitting radiant fireball. It may be added with the build-up of pressure waves, in rare cases.

3.4.3 CONDENSED PHASE EXPLOSION

It will occur when the materials are in either a liquid or a solid phase. Example: high explosives.

3.4.4 DUST EXPLOSIONS

It occurs mainly due to the presence of suspended combustible solid particles, which are very fine in their molecular structure. Suspended fine solid particles can explode in a fashion similar to that of the flammable gases. In case of dust suspended in air, even a small concentration of flammable gas can contribute to a severe explosion than that of the presence of the dust particles alone. Such suspended dust particles are referred to as hybrid mixtures.

3.5 BLAST WAVE PARAMETERS

Quantum of energy, released into the atmosphere results in a pressure-transient wave or a blast wave. Further, it is important to note that the blast wave propagates outward in all directions from the source at a sonic or supersonic speed. Supersonic speed is defined as the rate of travel of an object exceeding the speed of sound. For objects traveling in dry air at a temperature of about 20°C, the supersonic speed is about 344 m/s, which is equivalent to 667 knots or about 1240 km/h. The magnitude and shape of the blast wave depend upon the nature of the energy released and the distance of the object from the epicenter of the explosion. Blast waves are categorized into two: shock wave (S-waves) and pressure waves (P-waves).

Shock waves are an outcome of a sudden, instantaneous rise in the pressure to a peak, free-field overpressure above under an ambient atmospheric condition. This peak overpressure gradually reduces to the ambient pressure after highly damped pressure oscillations. In the due process, a negative overpressure is generated, which follows the positive phase of the blast wave (see Fig. 3.1).

Pressure waves are the consequence of gradual pressure rise to peak overpressure. Gradual decay of pressure intensity will follow it, also resulting in

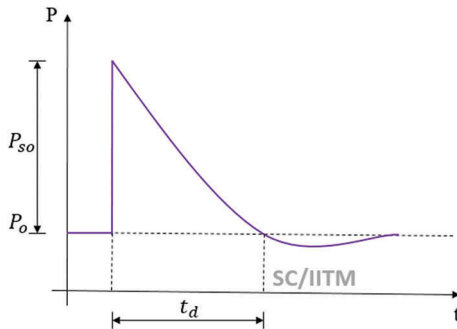


FIGURE 3.1 Shock wave.

the formation of a negative wave phase, which is similar to that of a shock wave (Fig. 3.2).

Shock waves that occur in the near and far fields result from the condensed phase detonations or an extremely energetic VCE. Most of the vapor cloud deflagrations result in high-pressure waves at the near field. These waves generally propagate further as a shock wave to the far-field. In comparison to that of the positive phase, the negative phase of a shock wave is weaker and of a lesser impact. Generally, it is ignored in the blast-resistant design. The duration over which the blast wave overpressure lasts is termed as the positive phase duration (t_d). The area under the pressure–time curve is equivalent to the impulse of the blast wave. Considering only the positive phase, the impulse is defined as follows:

$$I_o = \int_0^{t_d} P(t) dt \quad (3.1)$$

where $P(t)$ is the overpressure function, and t_d is the duration of the positive phase. The impulse function for different types of waves is given in Table 3.1.

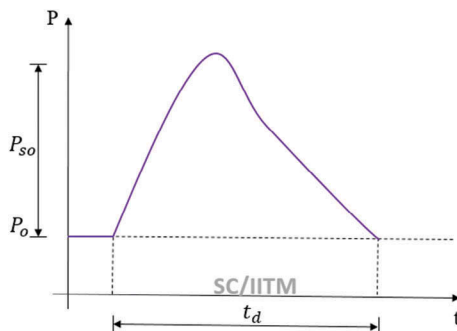


FIGURE 3.2 Pressure wave.

TABLE 3.1 Impulse functions

Sl. no.	Wave	Impulse, I_o
1	Triangular wave	$0.5P_{so}t_d$
2	Half-sine wave	$0.64P_{so}t_d$
3	Exponentially decaying shock wave	$cP_{so}t_d$

where P_{so} is the peak overpressure, and C is a coefficient accounting for the other factors that influence the peak overpressure; this value is assumed to be in the range of 0.2–0.5. Various parameters that define the blast loading are namely peak side-on positive overpressure (P_{so}); positive phase duration (t_d); positive impulse (I_o); peak side-on negative overpressure (P_{so}); negative phase duration (t_d); and the corresponding negative impulse (I_o). Also, other secondary parameters that govern the input for the blast-resistant design are peak reflected pressure (P_r), peak dynamic pressure (q_o), shock front velocity (U) and blast wavelength (L_w). These secondary parameters can be derived from the primary blast wave parameters, as discussed in the following section.

3.5.1 PEAK REFLECTED PRESSURE

When a blast wave hits a plane surface, it is reflected. This reflection will influence the surface, inducing pressure of magnitude higher than that of the incident side-on value. The magnitude of the reflected overpressure is expressed as an amplifying factor of that of the incident pressure and is given by the following relationship:

$$P_r = C_r P_{so} \quad (3.2)$$

where C_r is the reflection coefficient. It depends upon the magnitude of peak overpressure, angle of incidence to the reflecting surface and type of the blast wave. For overpressures up to 138 kPa and 0° incident angle, Newmark's equation, given below is useful:

$$C_r = \frac{P_r}{P_{so}} \cong 2 + 0.0073P_{so} \quad (3.3)$$

Alternatively, the reflection coefficient can also be obtained from the TNO green book. While the duration of reflected pressure depends on the dimensions of the reflecting surface, the maximum duration cannot exceed the positive phase duration of the incident blast wave. This assumption excludes any diffraction around the edges of the reflecting surface.

3.5.2 PEAK DYNAMIC PRESSURE

Blast effect caused in buildings is primarily due to the air movement resulting from the propagation of the blast wave in the atmosphere. Peak dynamic pressure depends on the peak overpressure of the blast wave. For example, in a low over-pressure range under the normal atmospheric conditions, peak dynamic pressure is given by the following relationship:

$$q_o = \frac{2.5(P_{so})^2}{7P_o + P_{so}} \cong 0.0032(P_{so})^2 \quad (3.4)$$

where P_o is the ambient atmospheric pressure. The following relationship gives the dynamic pressure on a structure:

$$q_n = C_d q_o \quad (3.5)$$

where C_d is the drag coefficient, which depends on the shape and orientation of the obstructing surface. For example, in case of a rectangular building, the drag coefficient is taken as 1.0 for the front walls and -0.4 for the side and roof.

3.5.3 SHOCK FRONT VELOCITY

In the free field, blast wave resulting from an explosion travels at (or above) the acoustic speed of the propagating medium. In a low-pressure range, under normal atmospheric conditions, the shock wave front velocity can be approximated using the following relationship:

$$U = 345(1 + 0.0083P_{so})^{0.5} \quad (3.6)$$

3.5.4 BLAST WAVELENGTH

Propagating blast wave at any instant of time generally extends over a radial distance. It is because the shock wave front travels outwards from the explosion. Therefore, the pressure is the largest on the front wall, which encounters the shock wave. It subsequently trails off to ambient conditions over a distance, termed as blast wavelength. In the low-pressure range, the blast wavelength is approximated as follows:

$$L_w = Ut_d \quad (3.7)$$

Blastwave profiles are generally linearized to simplify the blast-resistant design procedure. Further, a pressure wave is also simplified by using an equivalent shock loading with the same peak overpressure and impulse. Figs. 3.3 and 3.4 show the idealized shock wave and pressure wave, respectively, for design purposes. Equivalent shock load can be obtained in Fig. 3.5.

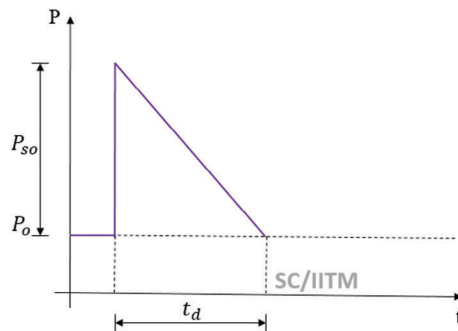


FIGURE 3.3 Idealized shock wave.

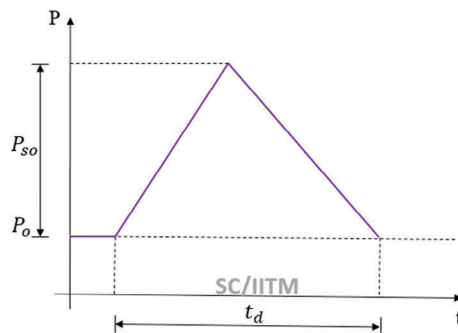


FIGURE 3.4 Idealized pressure wave.

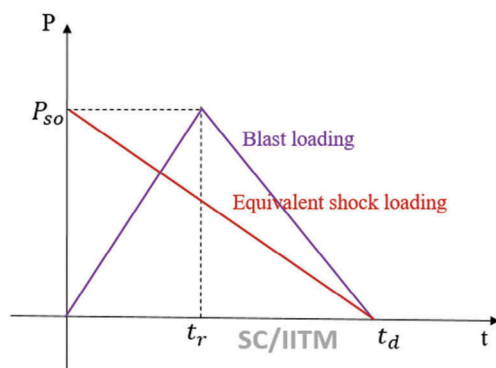


FIGURE 3.5 Idealized equivalent pressure load.

3.6 DESIGN BLAST LOAD FOR BUILDINGS

To estimate the design blast load for buildings, a thorough understanding of the blast wave–structure interaction is necessary. When a blast wave strikes the building, it induces either an overpressure or drag force on the building front. However, the interaction is quite complex. When a blast wave encounters a solid surface, it will reflect from the surface and subsequently diffract around the building. The extent of reflection depends upon the geometry, shape and size of the building (Ronalds & Dowling, 1988). During reflection, energy is exchanged between the blast wave and the object. The incident blast wave is reflected from the building, producing a region of further compression of air, which is dominant around the structure. As a result, air also applies equal and opposite force to the surface. Due to the change of momentum at the local level (member level), pressure increases more than that of the incident pressure, causing reflected pressure (Chandrasekaran et al., 2010b; Singh et al., 2011; Villavicencio & Soares, 2012).

For the sake of design, the resulting blast loading can be idealized as a shock wave (Veritas, 2010b). For example, it is idealized as a blast wave traveling horizontally from left to right. However, depending on the location of the potential explosion hazards present in the vicinity of the building site, the blast could strike the building from any direction. It can result in design loads on the front wall, side wall, rooftop and the rear wall, as discussed in the following section.

3.6.1 FRONT WALL LOAD

Front walls, which encounter the blast wave, shall experience the reflected overpressure, whose amplification is dependent on the following: angle of incidence (α), rise time (t_r) and side-on overpressure pulse (P_{so}). For design purposes, a normal shock reflection is assumed for which the angle of incidence and rise time are assumed to be zero. However, in some cases, oblique reflection may be more critical as it may result from the reflection of two adjacent walls. The reflected overpressure decays to a stagnation pressure (P_s) in the clearing time (t_c) and is given by the following relationship:

$$P_s = P_{so} + C_d q_0 \quad (3.8)$$

$$t_c = \frac{3S}{U} < t_d \quad (3.9)$$

where S is the clearing distance, which is generally lesser than the height of the building. It is usually assumed as half of the width of the building. It is also standard practice to assume that the duration of the reflected overpressure does not exceed the free-field positive overpressure. In mathematical terms,

$$t_c < t_d \quad (3.10)$$

The simplified equivalent triangle of the bilinear pressure–time curve is shown in Fig. 3.6. The equivalent loading is computed by equating the impulse load

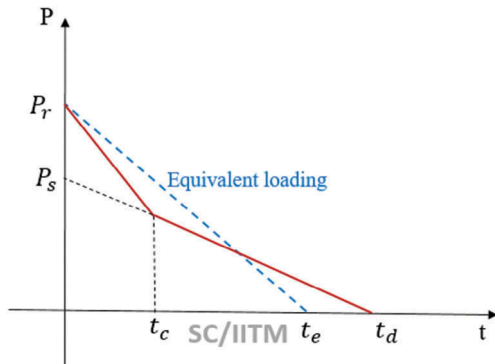


FIGURE 3.6 Front wall load.

shape under the same peak pressure, P_r . The impulse, I_w , under the bilinear pressure-time curve is given as

$$I_w = 0.5(P_r - P_s)t_c + 0.5P_s(t_d - t_c) \quad (3.11)$$

Duration of the equivalent triangle is given as

$$t_e = \frac{2I_w}{P_r} = \frac{(t_d - t_c)P_s}{P_r} + t_c \quad (3.12)$$

3.6.2 SIDE WALL LOAD

Sidewalls of a building under blast also experience blast loading but of a lesser magnitude. It is due to the lack of overpressure reflection and attenuation effect of the blast wave. As a blast wave travels along the length of the structural member, the peak side-on overpressure will not be applied uniformly. It varies with both time and space. Fig. 3.7 shows the equivalent load factor for roof and side wall load while Fig. 3.8 shows the roof and side wall load variations of a building experiencing blast load. If the length of the side wall is equal to that of the length of the blast wave as computed above, then the peak side-on overpressure shall reach the far end of the wall at which it will return to the ambient condition. An equivalent load coefficient, C_e , is used to account for this effect, which depends on the characteristic length of the structural member, measured in the direction of propagation of the blast wave (UFC: 3-340-02, 2008).

The following relationship gives effective side-on pressure on sidewalls:

$$P_a = C_e P_{so} + C_d q_o \quad (3.13)$$

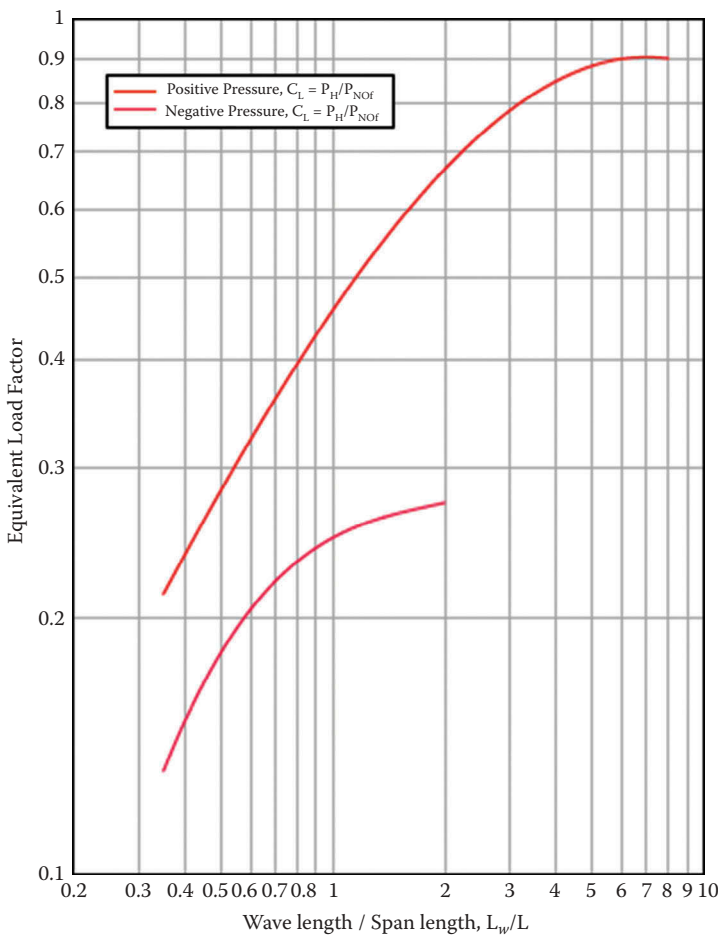


FIGURE 3.7 Equivalent load factor for side wall and roof load. (Courtesy: UFC: 3-340-02, 2008.)

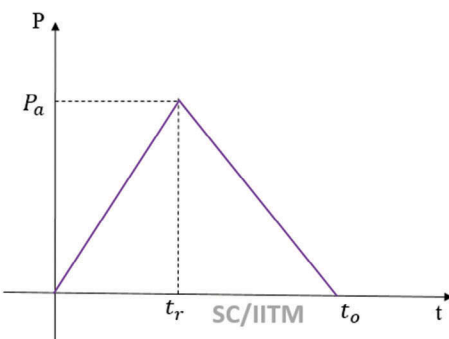


FIGURE 3.8 Roof and sidewall load

where P_a is the effective side-on pressure. The rise time for the sidewall is the time taken by the blast wave to travel across the entire length of the element under consideration and is given by the following relationship:

$$t_r = \frac{B_L}{U} \quad (3.14)$$

The overall duration is the sum of the rise time and the duration of the free-field side-on overpressure, which is given as

$$t_o = t_r + t_d \quad (3.15)$$

3.6.3 ROOF LOAD

Under blast conditions, a building with a flat roof will also experience the effect of the blast. The roof will also experience a side-on overpressure combined with that of the dynamic wind pressure, which is similar to that of the side walls. Wind force on the roof generally acts in the direction opposite to that of the overpressure. The roof load depends upon the following namely: (i) ratio of the blast wavelength to that of the span of the roof element and (ii) its orientation with respect to the incident blast wave.

3.6.4 REAR WALL LOAD

Building experiencing a blast load also influences the rear wall, in addition to that of the front, top and side walls. However, there is a significant reduction in the overall blast force on the rear wall due to the lag in space length and time in comparison to that of the blast wave. In simple terms, blast load in the rear walls lags by that of the front wall by a ratio, which is equal to the ratio of the length of the building (B_L) and blast wave period (U). The effective peak overpressure on the rear wall is similar to that of the side walls. Fig. 3.9 shows the rear wall load, useful for design purposes. According to TNO Green book, time rise for the blast wave in the rear wall is given as follows:

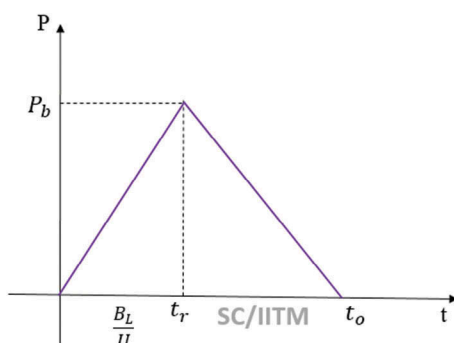


FIGURE 3.9 Rear wall loading.

$$\text{The rise time of the positive phase} = 4S/U \quad (3.16)$$

$$\text{Total duration} = t_d \quad (3.17)$$

$$t_r = \frac{B_L}{U} + \frac{4S}{U} \quad (3.18)$$

$$t_o = t_r + t_d \quad (3.19)$$

According to UFC 3-340-02, the following relationship holds good:

$$\text{Positive phase rise time} = S/U \quad (3.20)$$

$$\text{Total duration} = t_d \quad (3.21)$$

$$t_r = \frac{B_L}{U} + \frac{4S}{U} \quad (3.22)$$

$$t_o = t_r + t_d \quad (3.23)$$

3.6.5 FRAME LOADING

The complete building frame shall experience the blast load, which be the net load that acts on the front and rear walls after accounting for the time and phase lags. While the blast wave travels from the front side of the building to the rear, the building frame will be subjected to a large, horizontal, unbalanced pressure on the front wall. It will be followed by a partial release of blast load on the front wall, which is subsequently transferred to the rear wall. Fig. 3.10 shows the net lateral load that acts on a building of rectangular geometry.

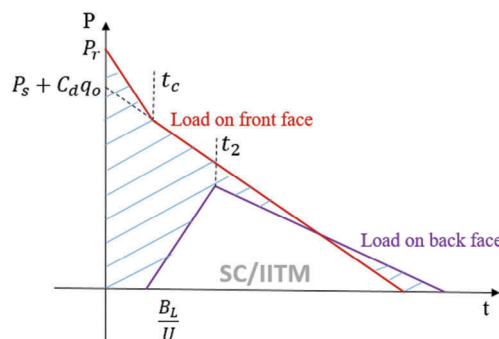


FIGURE 3.10 Net lateral load on the rectangular building.

3.6.6 NEGATIVE PRESSURE, LEAKAGE PRESSURE AND REBOUND LOAD

As seen in the earlier discussions, blast waves also induce negative pressure during its propagation. Due to this negative phase, structural components shall experience blast load effects in the opposite direction to that of the primary load. Further, overpressure may also cause rebound effects on the structural components, which will be relatively high due to large inertia. However, it is conventional to ignore the effects caused by the negative pressure, but rebound effects should be considered in the analysis to ensure satisfactory performance of the structure. Blast loads are also capable of expanding within the confined space of the structure by passing through the shaft holes and openings. These are termed as leakage pressure loads. As a blast wave expands through an opening, the pressure level drops due to the confined passage effect, which results in a sudden adiabatic expansion within the confined volume of the building. Let us illustrate the effects of blast load on a structural system of rectangular geometry in the following section.

3.7 DESIGN EXAMPLE: COMPUTATION OF BLAST OVERPRESSURE FOR A RECTANGULAR-SHAPED BUILDING

Question 1. Calculate the blast load on a living quarter of an offshore platform, subject to the blast wave as shown in the figure. Assume that the residential unit is confined to the shape and size as shown, without any cantilever projections along its sides. Figures show the characteristic dimensions of the unit as 15 m × 20 m × 6 m high. Blastwave is targeting the unit on a plane normal to the length of the unit, as shown in the figure. Peak overpressure is taken as 40 kPa and considered to act for a duration of 0.05 s. Fig. 3.11 shows the building block considered for the analysis and the shock wave time history.

Step 1: Shock wave parameters

Vide Eq. (3.6), shock front velocity is computed as follows:

$$U = 345(1 + 0.0083P_{so})^{0.5}$$

$$U = 345(1 + 0.0083 \times 40)^{0.5} = 398.172 \text{ m/s}$$

Vide Eq. (3.7), length of the pressure wave is given by:

$$L_w = Ut_d = 398.172 \times 0.05 = 19.909 \text{ m}$$

Vide Eq. (3.4), the peak dynamic wind pressure is given as

$$q_o = 0.0032(40)^2 = 5.12 \text{ kPa}$$

Step 2: Front wall loads

Vide Eq. (3.3), the reflection coefficient is computed as

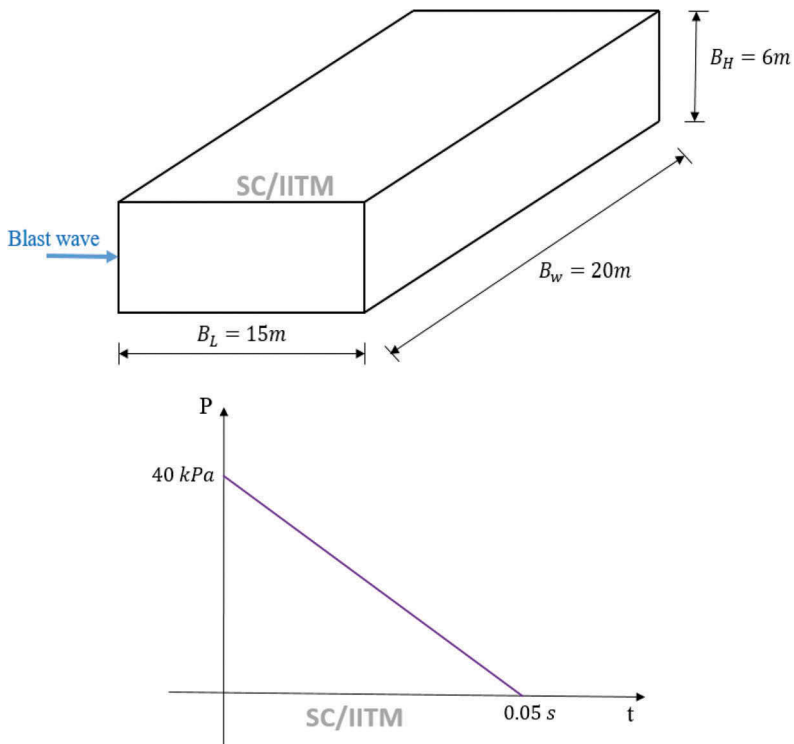


FIGURE 3.11 Building block and shock wave history.

$$C_r = 2 + 0.0073(P_{so}) = 2 + 0.0073(40) = 2.292$$

Vide Eq. (3.2), reflected overpressure is given as

$$P_r = C_r \times P_{so} = 2.292 \times 40 = 91.68 \text{ kPa}$$

Vide Section 3.6 (a), clearing distance (\$S\$), is the minimum of the height of the building and half the width of the building. In the present case, \$S\$ will be the minimum of 6 m and \$(20/2)\$; \$S\$ is taken as 6 m in the current example problem.

Vide Eq. (3.9), the reflected overpressure clearing time is given as

$$t_c = \frac{3S}{U} = \frac{3 \times 6}{398.172} = 0.045s < t_d$$

Vide Section 3.5 (b), the drag coefficient (\$C_d\$) is assumed as unity; the stagnation pressure is given in Eq. (3.8):

Stagnation pressure, \$P_s = P_{so} + C_d q_o\$

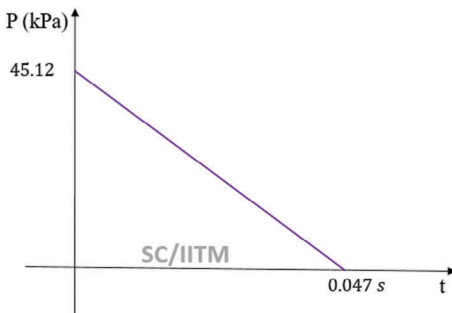


FIGURE 3.12 Variation of front wall load.

$$P_s = P_{so} + C_d q_o = 40 + (1 \times 5.12) = 45.12 \text{ kPa}$$

Vide Eq. (3.11), the front wall impulse is given as

$$I_w = 0.5(P_r - P_s)t_c + 0.5P_s t_d$$

$$I_w = 0.5(91.68 - 45.12) \times 0.045 + 0.5 \times 45.12 \times 0.05 = 2.176 \text{ kPa.s}$$

Vide Eq. (3.12), the effective duration of the blast load on the front wall is given as

Effective duration, $t_e = \frac{2I_w}{P_r} = \frac{2 \times 2.176}{91.68} = 0.047s$. Fig. 3.12 shows the variation of the front wall load, which corresponds to the equivalent load in Fig. 3.6.

Step 3: Sidewall load

Vide Section 3.5 (b), drag coefficient, C_d is assumed as -0.4.

Assuming the thickness of the wall as 300 mm,

Equivalent load coefficient C_e can be obtained as shown in Fig. 3.7, for the known ratio of wavelength by characteristic length, which is given as

$$\frac{L_w}{L_1} = \frac{15}{0.3} = 50.$$

From Fig. 3.7, for the ratio of 50, C_e is obtained as 1.0.

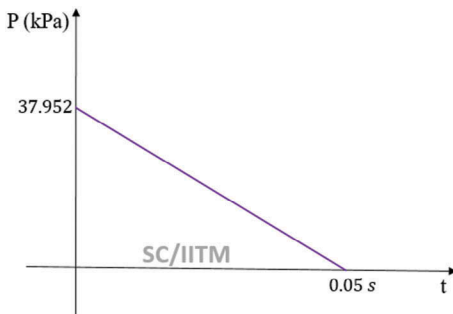
Vide Eq. (3.13), equivalent peak overpressure is given as

$$P_a = C_e P_{so} + C_d q_o = (1.0 \times 40) + ((-0.4) \times 5.12) = 37.952 \text{ kPa}$$

Vide Eq. (3.14), rise time is given as

$$t_r = \frac{B_L}{U} = \frac{0.3}{38.172} = 0.0007 \text{ s}$$

Duration $t_d = 0.05 \text{ s}$. Fig. 3.13 shows the variation of side wall load.

**FIGURE 3.13** Variation of side wall load.***Step 4: Roof load***

For the design of the roof, a section of 0.30 m wide and 2.4 m long is considered.

$$B_L = 2.40 \text{ m}$$

$$\text{Drag coefficient, } C_d = -0.4.$$

$$\text{Equivalent load coefficient, } \frac{L_w}{L_1} = \frac{15}{2.4} = 6.25$$

From Fig. 3.7, and for the ratio of 6.25, we get C_e as 0.98.

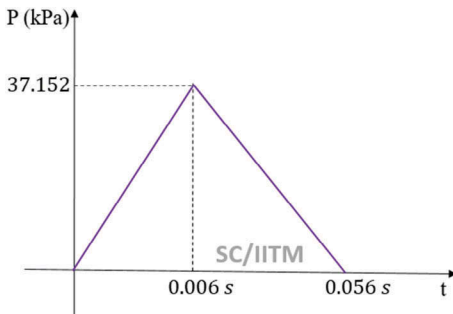
Vide Eq. (3.13), equivalent peak overpressure is computed as

$$P_a = C_e P_{so} + C_d q_o = (0.98 \times 40) + ((-0.4) \times 5.12) = 37.152 \text{ kPa}$$

Vide Eq. (3.14), rise time is given as

$$t_r = \frac{B_L}{U} = \frac{2.4}{398.172} = 0.006 \text{ s}$$

Total positive phase duration = $0.006 + 0.05 = 0.056$ s. Fig. 3.14 shows the variation of roof load.

**FIGURE 3.14** Variation of roof load.

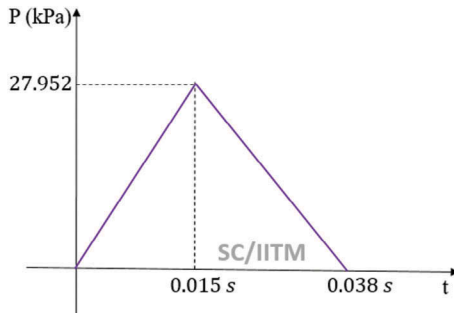


FIGURE 3.15 Variation of rear wall load.

Step 5: Rear wall load

Drag coefficient, $C_d = -0.4$.
Equivalent load coefficient, $\frac{L_w}{S} = \frac{15}{6} = 2.5$

From Fig. 3.7, and for the ratio of 2.5, we get C_e as 0.75.

Equivalent peak overpressure, $P_a = C_e P_{so} + C_d q_o = (0.75 \times 40) + ((-0.4) \times 5.12) = 27.952$ kPa

$$\text{Time of arrival, } t_a = \frac{B_L}{U} = \frac{15}{398.172} = 0.038s$$

$$\text{Rise time, } t_r = \frac{S}{U} = \frac{6}{398.172} = 0.015s$$

$$\text{Duration } t_d = 0.05 \text{ s}$$

Total positive phase duration = $0.015 + 0.038 = 0.053$ s. Fig. 3.15 shows the variation of rear wall load.

3.8 FIRE LOAD

Fire is rapid, exothermal oxidation of an ignition fuel. Fuel can be either in the solid, liquid or gaseous states. The occurrence of fire release energy in the form of exothermal reaction, while with time, released energy reaches its peak intensity. Alternatively, fire can also result from an explosion, which is a rapid expansion of gases caused by the pressure or shock waves. These waves propagate very fast, and their rapidity results in adiabatic expansion. Explosion, resulting from the fire can be either a mechanical or chemical process. It is evident that about 70% of the accidents occurred in offshore facilities are due to hydrocarbon explosion and fire, whose consequences are very serious (Donegan, 1991; Jin & Jang, 2015). The major concern of the designers is to make offshore facilities as fire-resistant (Paik and Czujko, 2103; Paik et al., 2013). If the platform is dealing with LNG, then the potential risk due to fire and explosion is further severe as the physical and chemical conditions of liquid natural gas are different from that of the liquid hydrocarbon (Quiel & Garlock, 2010). The most common oversight that leads to fire accidents are as follows (Manco et al., 2013):

- All heat transfer system should be thoroughly inspected for no leak or smoke.

- In case of smoke, one should not disconnect the smoldering insulation as this will allow an excess of air inside and will result in auto-ignition.
- Do not let the fluid drop on any heat sources as this will ignite the fluid.
- If fluid leaks and gets trapped within a system, it can get oxidized, which results in heat (exothermal).

By avoiding the above, one can avert fire accidents. However, still, the fire-resistant design is imperative for structures that are susceptible to fire accidents (Chandrasekaran & Srivastava, 2017; Soares et al., 1998; Soares & Teixeira, 2000).

3.9 CATEGORIZATION OF FIRE

Based on standard DNV regulations, fire can be categorized as follows:

No fire risk is the condition where the building or the engineering module has no energy sources.

Low fire risk condition is the case that covers those building modules that store nonflammable equipment.

Medium fire risk is the category which includes those building modules that house electric power and major testing equipment. It also includes nonaccommodation modules.

High-risk fire includes building modules where the flammable liquids are stored. It also includes the plant segments that have high-power electrical machinery and accommodation modules.

The potential risk that arises in case of the offshore platforms are blowouts, riser and process leak, fire and explosion, vessel collision, helicopter accidents, dropped objects, structural failure due to the environmental loads and complete capsizing of the platform. The best practices that can be employed to avoid such failures are as follows:

- Fluid should be used above the flash point and fire point temperature but not above the auto-ignition temperature (AIT).
- Fluid can be used up to their maximum bulk temperature. Bulk temperature is much higher than that of the flash point temperature for any liquid.
- Avoid designing confined spaces in the presence of ignition source as it can result in a flash very easily.
- Through proper system design, one can ensure that there is no oxygen or air content present at the heat source. The most common heat sources in an industrial unit are electric heater, heat exchanger and drilling controller.
- Fluid should be well contained within the system.
- Fluid containment should not have direct contact with any external ignition source, directly or indirectly.

Several complexities arise during the fire-resistant design of structures. The fire-resistant design process is not complicated but cumbersome due to the complexity involved in the layout of the process plant. As a common practice, it is seen that most of the topside modules are laid in a congested manner. It is done to ensure compactness in the process flowline, but it inherently introduces a high risk of cross-fire due to lack of space between the facilities. Such complex and congested layout of process plants and equipment increases the proximity of spread of fire or blast waves from one unit to the adjacent. The complication in the layout also arises from the congested network of pipelines, electric mains and water mains. All of the above factors put together to make the fire-resistant design more complex. The level of risk in such conditions is high due to the following reasons:

- Facilities, equipment and even the process design are unique and have to be protected.
- Recreating the facility or retrofitting the damaged platform is very expensive and not worthy. Most of the fire accidents will result in a high degree of catastrophe, both to human and equipment.

In modern practice, offshore platforms are designed to operate in an unmanned manner. It is therefore obvious that they will not have any support of fire-fighting on demand. An offshore platform has various complexities, which makes them vulnerable to fire accidents:

- A congested layout.
- A close network of pipelines, electric cables and water mains.
- Working in a remote and harsh environment.
- Exploration and production of very high flammable mixture.
- Support systems in case of emergency.
- Very high capital investment.
- Very large process of commissioning one on another new facility.

Under the above complexities, it is important to note that an offshore platform can never be designed to remain completely safe. However, by intelligent design, one can improve the degree of safety.

3.10 CHARACTERISTICS OF FIRE

A few important characteristics of fire and explosion materials are the auto-ignition temperature (AIT), flash point and fire point.

3.10.1 AUTO-IGNITION TEMPERATURE

Auto-ignition temperature (AIT), also known as the kindling point of the material, is the lowest temperature above which the material may not require any external source for combustion. The ignition can even take place at

TABLE 3.2 Auto-ignition temperature for different materials

Sl. no.	Material	AIT °C
1	Gasolene	247–280
2	Diesel	210
3	Butane	405
4	Methane	580

normal atmospheric conditions when AIT is reached. It is also the minimum temperature required to supply the activation energy that is needed for combustion and therefore termed as self-ignition temperature. Table 3.2 lists AIT of different material in the atmosphere at 20.9% of oxygen concentration.

3.10.2 FLASHPOINT

Flashpoint is the lowest temperature at which the liquid gives up enough vapor to maintain a continuous flame. It is the temperature at which the vapors are produced from the fluid, resulting in the ignition in the presence of an ignition source. It is important to note that the fluid will not burn at this temperature.

3.10.3 FIRE POINT

The fire point is the temperature at which the fluid will sustain fire if ignited by an external ignition source. For most of the fuels, the fire point is lower than that of its auto-ignition temperature.

3.11 CLASSIFICATION OF FIRE

Fire is triggered when leakage (or spill) of any flammable mixture occurs in the presence of a potential ignition source. Fire can be classified as Pool fire, Jet Fire, Fireball and Flashfire. The subclassification of fire includes Flares, Fire on the sea surface and Running liquid fire. This subclassification can be grouped to the main classification as (i) flares can be treated as a jet fire in modeling and (ii) fire on the water surface and running liquid fire that can be treated as a pool fire.

Pool Fire

It is a turbulent diffusion fire, which burns above the pool that vaporizes hydrocarbon, which has very less momentum. Release of liquid fuel forms a pool on the surface. It vaporizes and causes pool fire by ignition. Probability of occurrence of pool fire in an offshore platform is very high due to the

continuous handling of hydrocarbons. Liquid fuel, released accidentally during the overfilling of storage tanks may also cause pool fire. It may also occur due to the rupture of pipelines, and cracks in the storage tanks caused by the corrosion of metal. The pool diameter is equal to that of the diameter of the bund, which is constructed to contain the spread of pool fire and is given by the following relationship:

$$D_p = \sqrt{\frac{4A}{\pi}} \quad (3.24)$$

where A is the area of the bund in m^2 and D_p is the diameter of the pool. The following relationship gives pool fire length:

$$L = 42 D_p \left[\frac{\text{Burning Rate}}{\rho_{\text{air}} \sqrt{9.81 D_p}} \right]^{0.61} \quad (3.25)$$

Jet Fire

Jet fire is classified by the turbulent diffusion of flame resulting from the combustion of fuel, which is continuously released. It has a significant momentum to propagate in a downwind direction. It can affect offshore installations very seriously, even if they are located far away from the potential source of the fire. Jet fire releases gases while propagates forward, which may be either in the horizontal or vertical direction. Among the two, horizontal jet fire is more catastrophic as it is capable of causing extensive damage on the down-wind side. It may result in the following consequences: structural failure, storage vessel failure and (or) pipe works failure. The heat flux released during a jet fire is about 200–400 kW/m^2 , which is dependent on the type of fuel released. One of the potential sources of a jet fire is pressurized gas pipelines. In case of a leak, the initial gas release rate is given as

$$Q_o = C_D A p_o \sqrt{\frac{MV}{RT_o}} \left(\frac{2}{r+1} \right)^{(r+1)(r-1)} \quad \text{if } p_o > p_a \left(\frac{2}{r+1} \right)^{\left(\frac{r-1}{r} \right)} \quad (3.26)$$

where C_D is the discharge coefficient, A is the area in m^2 , p_o is the operational pressure of the gas, M is the molecular weight of gas in g/mol , V is the rate of specific heat, R is the universal gas constant ($=8314 \text{ J/kg mol k}$), T_o is the operational temperature in Kelvin, and p_a is the absolute pressure. The flame length of a jet fire is given by the Chamberlain equation:

$$m = 11.14(Q_o)^{0.447} \quad (3.27)$$

where Q_o is the initial release rate in kg/s . Jet fire length and the corresponding time frame are estimated based on the following relationship:

$$Q_t = Q_o e^{\left(\frac{Q_o}{M_G}\right)t} \quad (3.28)$$

where

$$M_G = \frac{PM}{0.08314} \pi r^2 L \quad (3.29)$$

where M_G is the mass of the gas in kg, P is the operating pressure of the gas in pa, M is the molecular weight of gas in gm/mol, r is the diameter of the pipe in m, L is the length of the pipe in m and t is the time of release in seconds.

Fireball

It is rapid turbulent combustion of any fuel. Usually, the outcome is in the form of a rising and expanding, radiant ball of fire. When a fireball attacks a vessel or a tank containing pressure liquefied gas, the pressure inside the vessel increases and leads to the catastrophic failure of the vessel or the tank. It may lead to the loss of the complete inventory present in the tank. Under BLEVE release, the released material is flammable which may also ignite, which may cause an explosion and thermal radiation hazards. Duration of the heat pulse in BLEVE is about 10–20 s, causing high-potential damage. The maximum emissive power that results from BLEVE are 270–333 kW/m² in the Up/downwind and 278–413 kW/m² in the crosswind.

Flash Fire

It is the transient fire resulting from the ignition of a gas or vapor cloud. Flashfire is attributed as a special process as this results after a substantial delay between the release of flammable materials and the subsequent ignition. It initially forms a vapor cloud over a larger area, and then expand radially. Subsequently, the cloud explodes because of ignition. It is more catastrophic and causes damage to a large area. Flashfire is characterized by a wall of flame. Similar to fireballs, flash fire can also ignite and remain as a continuous flame. It can also be caused by a delayed ignition and remain for a longer time. The instantaneous effect causes thermal radiation, and the flash fire generates ‘knock-on’ events such as Pool fire, Jet fire and BLEVE. It is important to note that the severity of the flash fire is extremely high.

3.12 FIRE PROTECTION SYSTEMS IN THE DESIGN

Offshore platforms are generally designed to be self-reliant even in the case of fire due to the following reasons: (i) there will be no fire rescue facility available in the near vicinity of offshore platforms and (ii) fire accidents cause significant consequences. Therefore, one of the main fire-protection measures that are generally followed is flame arrestors. It is a passive device that prevents the propagation of gas flames through pipelines. Other common measures are the construction of fire-resistance barriers, fire-insulation, water shower, foams and water spray lines. Source of fire in an offshore platform is the inflammable gases that are produced

by the production units. Preventing sparks will, therefore, be the highest priority. By design, fire protection can be achieved by an appropriate fire-detection system and layout of the fire extinguishing system. They should be automatic and designed with the highest degree of reliability.

Fire-fighting equipment needs to be simple in design and easy to operate so that the personnel on board can readily use them. They should be free from any high-end technique that makes their operation difficult. They should be maintained periodically to check their availability on demand. Fire drills should be conducted at periodic intervals to train the personnel on board about the effective use of fire-fighting equipment. Fire-protection system design should be integrated into the geometric design of the platform, making the fire protection a part of the platform layout itself. All potential hotspots in the platform layout should be enveloped into the fire protection layout to make the platform fire-protected. A few common types of fire protection systems are discussed in the following section.

Foam Systems

These systems are highly suitable for hydrocarbon fire. Foam systems contain air-filled bubbles that are formed from the aqueous solutions. Their density is lower than that of the flammable liquid, making it easy operational. Common types are low expansion systems, which are highly suitable for storage tanks, helideck and loading terminals and (ii) high-expansion systems that are suitable for LPG spills.

High-Pressure Water Mist

Potable water is used for fire-protection systems as other quality may result in corrosion of the fire mains. In this system, potable water is sprayed at high pressure and is well suited for Platform Support Vessels.

3.13 STEEL AT HIGH TEMPERATURE

Steel is one of the most common and popular construction materials used in the industrial structures and offshore platforms. The behavior of steel at high temperature is different from that of the room temperature, making steel design at an elevated temperature different. A few of the material characteristics are modulus of elasticity, stiffness and yield strength of structural steel decreases with the increase in temperature, whereas the material ductility increases showing an indication of strength development. Effective yield strength reduces after 400°C in case of mild carbon steel at 2% strain. The decrease in the proportional limit and modulus of elasticity is seen after 100°C as shown in Fig. 3.16. The other major material properties to be considered in the structural response under fire load are thermal conductivity, specific heat, elastic constants, specific weight, thermal expansion and plasticity. Also, variations of thermal conductivity, thermal strain and thermal expansion are shown in Figs. 3.17–3.19. It is important to define the thermal and mechanical properties under high temperature to evaluate the structural response under fire.

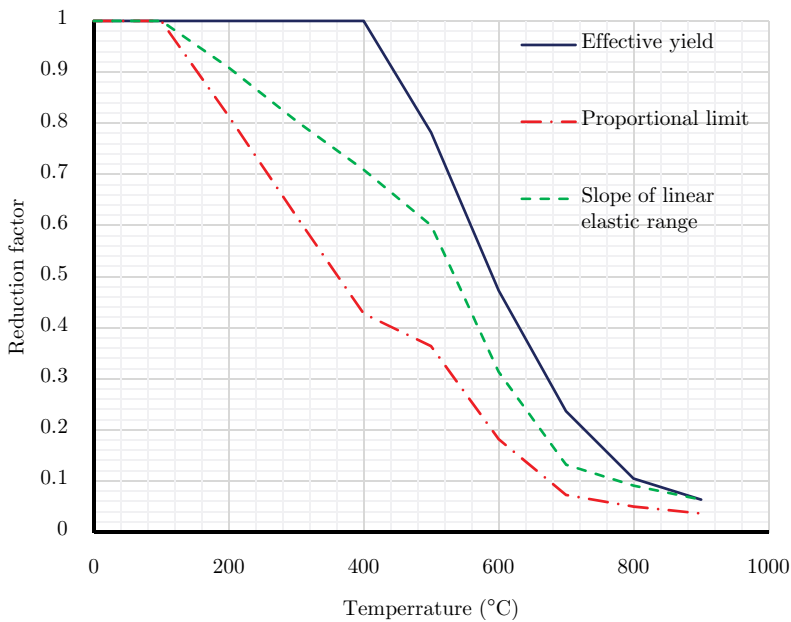


FIGURE 3.16 Material characteristics of carbon steel at high temperature.

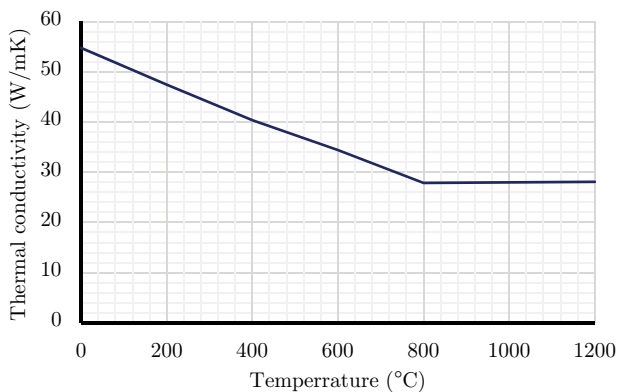


FIGURE 3.17 Thermal conductivity of carbon steel.

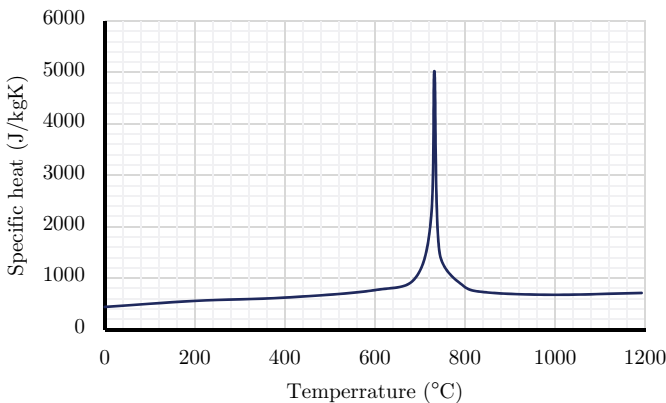


FIGURE 3.18 Specific heat of carbon steel.

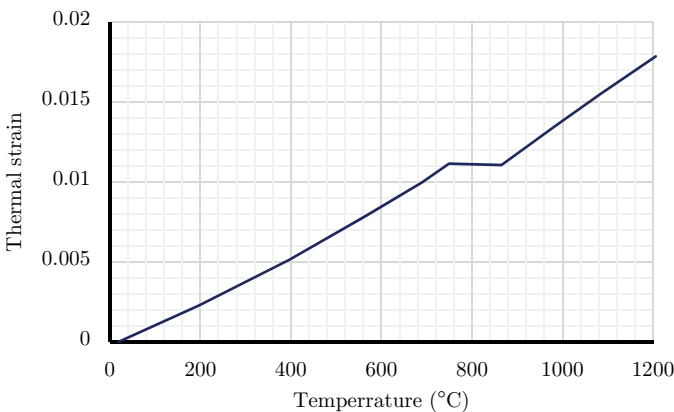


FIGURE 3.19 Thermal strain of carbon steel.

3.14 EXAMPLE CASE STUDY: BEHAVIOR OF AN OFFSHORE DECK PLATE UNDER HYDROCARBON FIRE

A steel deck of an offshore platform is considered for the analysis. Details and location identifications of the platform are masked for strategic reasons. One of the segments of the deck plate of size 1.375×1.25 m and 3 mm thick is modeled in Ansys to estimate the structural behavior of the stiffened steel deck plate. An uncoupled thermal and structural analysis is carried out. Size and shape of the plate are shown in Fig. 3.20.

The top face of the middle bay is exposed to fire as shown in Fig. 3.21, considering its proximity to the drilling operations. Though the plate stiffeners are not directly exposed to fire, they will also receive the heat that is

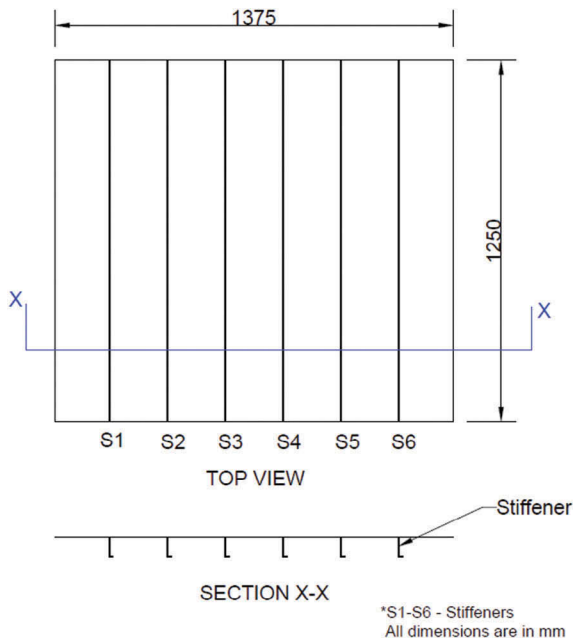


FIGURE 3.20 Stiffened steel plate of offshore deck.

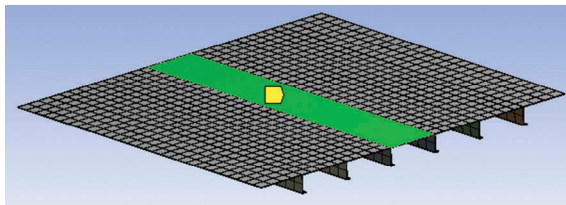


FIGURE 3.21 Middle bay under fire.

transferred from the deck plate. The mid-bay is subjected to the hydrocarbon fire as shown in Fig. 3.22. Numerical analysis is carried out using Ansys transient thermal analysis solver for 3600 s. A larger duration of the simulation is carried out to ensure that the heat from the top face of the plate is transferred to the stiffeners due to convection. The temperature distribution is shown in Fig. 3.23. Increase in temperature induces thermal stresses in the material which may lead to a structural failure. In this example study, plasticity is calculated using Von-Mises yield criteria. Generally, in the fire-resistant design of structures, the design is always associated with the duration to which the structure can resist fire without exceeding the undergoing maximum permissible deformation. Hence, the temperature is found to be more about 400°C at

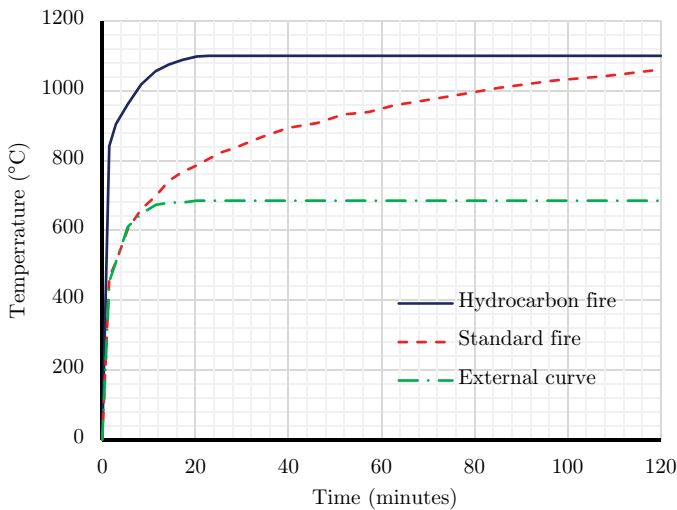


FIGURE 3.22 Time–temperature curves for different fire conditions.

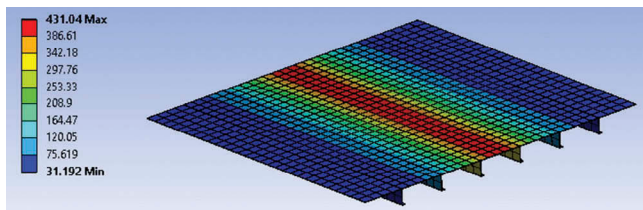


FIGURE 3.23 Temperature distribution in the stiffened plate.

which nearly 13% of the total area of the plate is deformed more than the permissible limit. Thermal stresses induced in the plate due to hydrocarbon fire is evaluated using structural analysis in Ansys. The thermal stresses are found to be increased beyond the yield stress at 1300 s while the maximum displacement of 0.80 mm is observed at 1800 s as shown in Fig. 3.24.

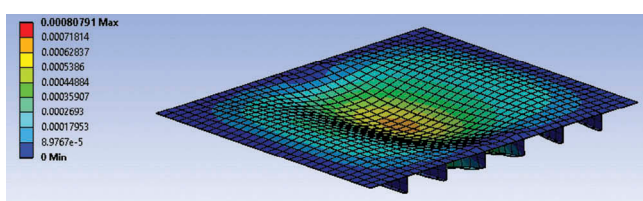


FIGURE 3.24 Maximum deformation in the plate.

3.15 DESIGN FOR FIRE

The fire resistant design of structures can be carried out using the following methods as per API-RP-2A: zone method, linear elastic method and elastic-plastic method. The following section explains them briefly.

3.15.1 ZONE METHOD

In this method, the maximum allowable temperature is assigned to a steel member without any reference to the stress level in the member, before the fire. The basic assumption behind this method is that the member utilization ratio, which is calculated from the basic allowable stressed will remain unaltered even under the fire load condition if the allowable stress is increased to yield. However, yield stress itself is reduced by a factor of 0.6. This assumption is valid when the nonlinear stress-strain characteristics of the steel may be linearized such that the yield strength reduction factor is matching with that of the reduction in the modulus of elasticity. Under this mapping condition, the governing design condition will remain unaffected. However, linearization of the stress-strain characteristics at higher strain level is necessary for the use of the maximum allowable stress of steel at elevated temperature, which corresponds to a higher strain level. Zone method may not be applicable with the unmatched reduction in both yield strength and Young's modulus as the governing design condition may be affected.

3.15.2 LINEAR ELASTIC METHOD

In this method, the maximum allowable temperature is assigned to the steel member under design, based on the stress level in the member before the fire. For example, member utilization ratio remains below 1.0 with the increase in the temperature. For members that do not undergo buckling failure, allowable stress should be such that the extreme fibers on the cross section are at yield. The yield stressed should also correspond to the average core temperature of the member. The linear elastic method may not be applicable with an unmatched reduction in both yield strength and Young's modulus as the governing design condition may be affected.

3.15.3 ELASTIC-PLASTIC METHOD

In the elastic-plastic method, the maximum allowable temperature is assigned to a steel member based on the stress level in the member before the fire. The member utilization ratio is increased beyond 1.0 with the increase in the temperature. A nonlinear structural analysis is performed to investigate the behavior of the structure and verify whether the structure will undergo collapse, but still meet the serviceability criteria. By appropriate selection of the representative value of strain, linearization of the stress-strain relationship at elevated temperature is achieved regardless of the

design method. The commonly used value of strain is 0.2, which is beneficial with the matched reduction in yield strength and Young's modulus. However, it limits the allowable temperature of the steel to 400°C, which is a disadvantage. Selection of higher value of strain will result in a higher maximum allowable temperature, but will also result in an unmatched reduction in yield strength and Young's modulus.

3.16 IMPACT LOADS DUE TO SHIP–PLATFORM COLLISION

The risk of ship–platform collision had increased with the increase in the number of oil production and exploration platforms (Storheim & Amdahl, 2014; Ufuah & Tashok, 2013). A typical tanker collision shall induce a force of about 200 MN on to the obstructing member and can result in a severe local consequence. The ship–platform collision is a dynamic process, which depends upon the type of collision, energy absorption, dissipation and contact time of the collision. Also, the collision zone also affects the structural response significantly. For a typical analysis of a structural member under impact loads, the collision zone is considered on any one side of the platform where a ship could impact during an accident situation, under normal conditions. The vertical height of the collision zone is normally assessed for analysis by considering the type of ship, vessel draft, wave height and tidal elevation.

Existing standard regulations are useful to estimate the impact of vessels on offshore platforms. According to NORSO guidelines for production platforms, a supply vessel of capacity 5000 ton, traveling at a speed of about 2.0 m/s (or lesser) should be considered for the design check during impact analysis. It is important to note that such collision loads are capable of causing significant damage to the encountered members, but will not lead to a progressive collapse of the whole structure. As a comparison, it can be seen that even a Norwegian Maritime Directorate regulation, in combination with DNV standards also suggests the same. Design guidelines of both the international regulations suggest minimum collision energy of magnitude 4 MJ to be considered for the design under vessel impact. Both the kinetic energy of the vessel and energy absorbed by the platform during collision influences the structural response. The ship collision load is calculated based on the kinetic energy, which is governed by the mass and the speed of travel of the vessel just before impact. Depending upon the collision conditions, a part of the kinetic energy will be dissipated as strain energy while the balance will act on the member. Of course, such collision mechanisms are expected to cause damage to both the member receiving the impact and vessel causing the impact. The strain energy dissipation during collision is estimated from the force–deformation relationships of the ship and the platforms, where the deformations shall comply with the ductility and the stability requirements. Nonlinear dynamic finite element analysis is essential to study the structural behavior during impact.

Based on the strain energy distribution, the following principles of design are applicable: strength design, ductility design and shared-energy design.

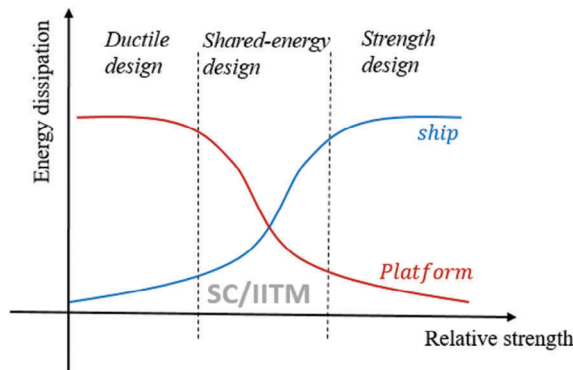


FIGURE 3.25 Energy dissipation and design principles.

Strength Design

According to these design criteria, the platform is considered to be very strong to resist the impact force that arises during the collision with a minor deformation. The deformation is confined to the ship and the ship allowed to dissipate the major part of the strain energy.

Ductility Design

In this design procedure, strain energy is confined to the platform, which undergoes the maximum deformation by absorbing the major part of the strain energy.

Shared-Energy Design

Under this procedure, it is assumed that both the platform and the ship absorb the collision energy. While in most of the cases, ductility design and shared-energy design are used, strength or ductility design is more favorable in computational perspective. Fig. 3.25 shows the energy dissipation and design principles.

3.16.1 KINETIC ENERGY

According to API-RP-2A, the kinetic energy of the vessel can be calculated from the following:

$$E = \frac{1}{2} amv^2 \quad (3.30)$$

where E is the kinetic energy of the vessel, a is the added mass factor (1.4 for broadside collision, 1.1 for bow/stern collision), m is the mass of the vessel and v is the velocity of the vessel at impact. For the design of platforms in mild environments, impact against the ships with the following minimum considerations should be used:

Mass of the vessel = 1000 metric tons

Impact velocity = 0.5 m/s

It is also recommended that for deep water and remote locations, the mass and velocity of the vessel during impact should be increased appropriately. However, it can be reduced in case of shallow waters that have access to small vessels only. According to DNV-RP-C204, the collision energy which is to be dissipated as the strain energy depends upon the type of installation.

(i) Complaint Platforms

Strain energy

$$E_s = \frac{1}{2} (m_s + a_s) v_s^2 \frac{\left(1 - \frac{v_i}{v_s}\right)^2}{\left(1 + \frac{m_s + a_s}{m_i + a_i}\right)} \quad (3.31)$$

(ii) Fixed Platforms

Strain energy

$$E_s = \frac{1}{2} (m_s + a_s) v_s^2 \quad (3.32)$$

where m_s is the mass, a_s is the added mass, v_s is the impact velocity of the ship, while m_i is the mass, a_i is the added mass, v_i is the velocity of the platform, respectively. It is important to note that in the current example study, the platform is assumed to remain compliant and the duration of the impact is small compared to the fundamental period of vibration of the platform.

3.17 ENERGY ABSORPTION

During impact, the offshore platform will absorb energy from the following:

- i. Localized plastic deformation of the tubular wall (in case of fixed jacket platforms).
- ii. Elastic or plastic bending of the member.
- iii. Elastic or plastic elongation of the member.
- iv. Fendering devise.
- v. Global deformation of the platform.
- vi. Ship deformation.

Resistance to ship collision is influenced by the interaction between dent in the member and bending deformation of the member. In the case of jacket structures, which are rigidly fixed to the sea bed on pile foundations, energy absorption mainly occurs mainly through the localized dent of the tubular member also, elastic or the plastic bending of the member also absorbs energy. For assessing the damage of the platform during impact, it is assumed

that the platform retains sufficient residual strength after impact to withstand the environment under normal operating conditions for at least 1 year. Based on research studies, the following relationship between force and dent depth is developed:

$$P_d = 15M_p \left(\frac{D}{t}\right)^{0.5} \left(\frac{X}{R}\right)^{0.5} \quad (3.33)$$

$$M_p = \frac{F_y t^2}{4} \quad (3.34)$$

where P_d is the denting force, M_p is the plastic moment of the tubular member. F_y is the yield strength of the material, D , R are the diameter and radius of the tube, respectively, t is the tube thickness, X is the dent depth.

Alternatively, the following relationship is also useful (Ellinois):

$$P_d = 40F_y t^2 \left(\frac{X}{D}\right)^{0.5} \quad (3.35)$$

The energy used in creating the dent is given as

$$E_d = \int_0^x P_d dx = 14.14M_p \left(\frac{X^{1.5}}{t^{0.5}}\right) \quad (3.36)$$

$$E_d = 3.54F_y(tX)^{1.5} \quad (3.37)$$

Substituting $X = D/B$ for solving for various D/t ratios, we get:

$$E_d = 3.54F_y \left(\frac{tD}{B}\right)^{1.5} \quad (3.38)$$

where B = brace diameter/dent depth.

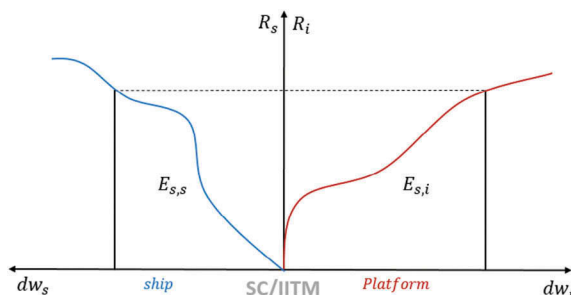


FIGURE 3.26 Dissipation of strain energy in ship and platform.

The dent formation in the members should be reduced to increase the postimpact strength of the member. It can be achieved by carefully selecting the D/t ratios of the members of the jacket legs. The load-deformation relationship can represent the structural response of the ship and platform. The area under the load-deformation curve gives the strain energy dissipated by the platform or ship. Fig. 3.26 shows the dissipation of strain energy in the ship and offshore platform.

3.18 AN EXAMPLE PROBLEM ON SHIP COLLISION

A tubular member of diameter 600 mm and 20 mm thickness of the jacket leg platform is subjected to a broadside collision by 1100 tons supply vessel with 0.5 m/s velocity. Calculate the denting force and the energy used in creating a dent of 20 mm. Take the yield strength of the material as 410 MPa.

$$M_p = \frac{F_y t^2}{4} = \frac{410 \times 20^2}{4} = 4.10 \times 10^4 \text{ Nmm/mm}$$

$$\text{Denting force } P_d = 15 M_p \left(\frac{D}{t} \right)^{0.5} \left(\frac{X}{R} \right)^{0.5}$$

where $D = 600$ mm, $t = 20$ mm, $X = 20$ mm, $R = 300$ mm

$$P_d = 15 M_p \left(\frac{D}{t} \right)^{0.5} \left(\frac{X}{R} \right)^{0.5} = 869.74 \text{ kN}$$

Energy used in creating the dent, $E_d = 3.54 F_y (tX)^{1.5}$

$$E_d = 3.54 F_y (tX)^{1.5} = 11.61 \text{ kNm}$$

3.19 IMPACT ANALYSIS OF BUOYANT LEGS OF OFFSHORE TRICERATOPS

Triceratops is the new-generation offshore compliant platforms with three buoyant legs connected to the deck by ball joints. These buoyant legs are usually designed as orthogonally stiffened cylindrical shell members (Do et al., 2018). The impact analysis of a stiffened cylindrical shell of diameter 15.0 m and length 174.24 m is carried using Ansys, the explicit analysis solver. Freeboard of the buoyant leg is taken as 20.24 m. The cylindrical shell is designed with 70 numbers of flat bar stringers and ring stiffeners at 3.0 m c/c apart. The thickness of the shell is 40 mm made up of AH36 marine steel of yield strength 433 MPa. The Young's modulus of the steel is 206,000 MPa. The true stress-strain curve for AH36 steel considering the yield plateau is shown in Fig. 3.27, which is used in the numerical analysis as they represent the state of the material more accurately. The same data are given as the input for defining the material plasticity in ANSYS.

The cylindrical shell and the stiffeners are modeled as shell elements as shown in Fig. 3.28. The rectangular box-shaped indenter, resembling a stem of

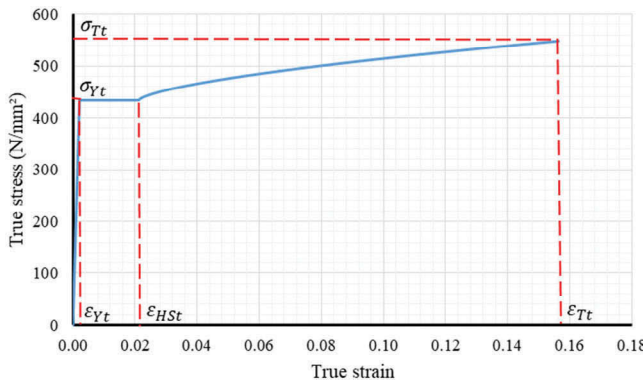


FIGURE 3.27 True stress–strain curve of AH36 marine steel.

the ship of 10.0 m length, 5.0 m breadth and 2.0 m depth, is modeled using solid elements. Further, it is assumed as perfectly rigid without undergoing any deformation. Thus, the energy dissipation is confined to the buoyant leg only as per the ductility design principles (Feng et al., 2017)—the shell meshes with four-node quadrilateral shell elements. The indenter is restrained from moving only in the direction of impact; all other degrees are restrained. The initial collision velocity is 1.0 m/s, and the distance between the centers of the indenter to the Mean Sea Level is 6.0 m, as shown in Fig. 3.28.

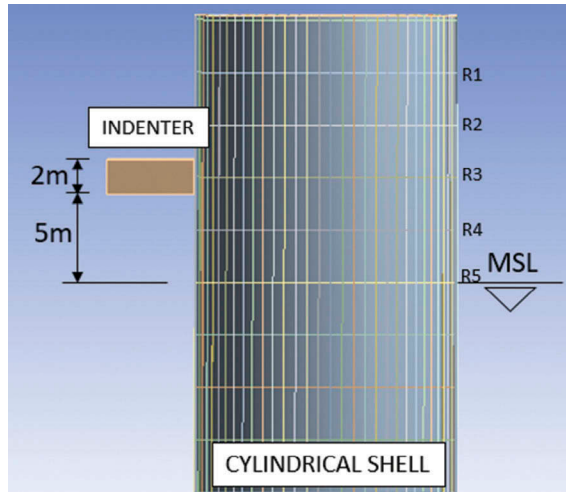


FIGURE 3.28 Cylindrical shell and indenter model.

(i) Damage profile

The collision zone is at 9.0 m below the top end of the buoyant leg. The indenter velocity decreases with the increase in the impact duration as shown in Fig. 3.29. Correspondingly, the indenter displacement increases as seen in Fig. 3.30. The impact causes a local dent in the buoyant leg at collision zone, causing flattening of both the cylindrical shell and the ring stiffener (Gruben et al., 2016).

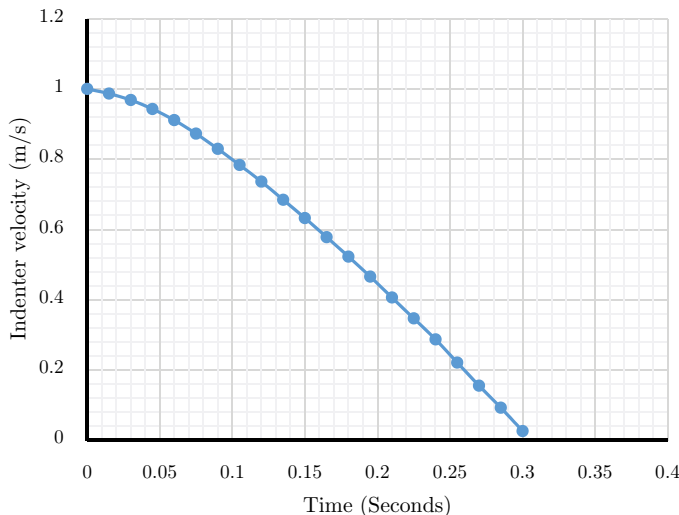


FIGURE 3.29 Indenter velocity.

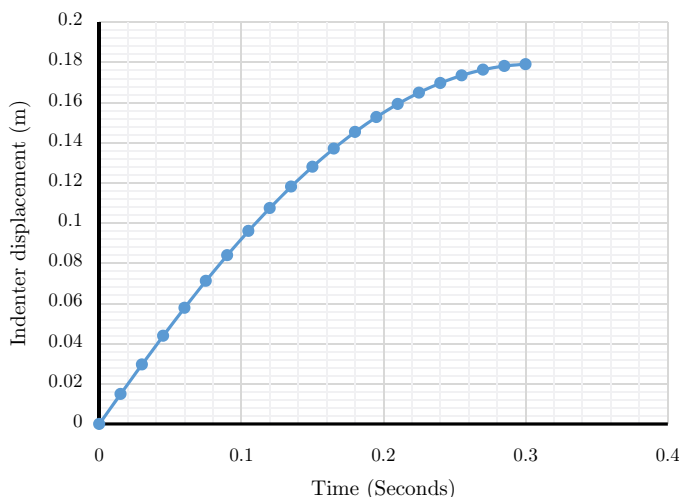


FIGURE 3.30 Indenter displacement.

The ring stiffeners prevent further propagation of damage to the adjacent bays and thus confining the deformation to be within the bays of collision zone as seen from Fig. 3.31. The ring stiffener at the impact location undergoes maximum deformation, whereas the deformation in the adjacent ring

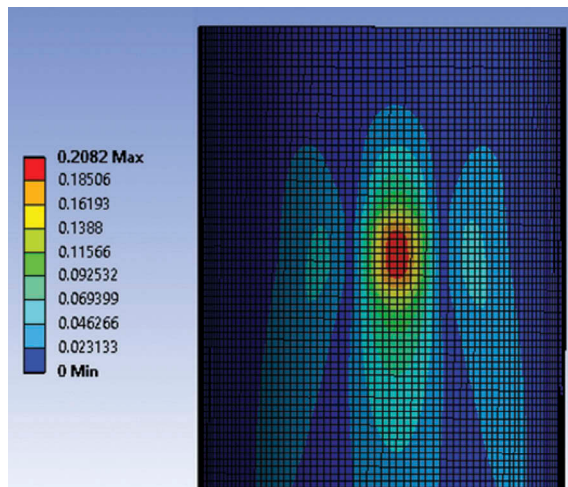


FIGURE 3.31 Deformation of the buoyant leg.

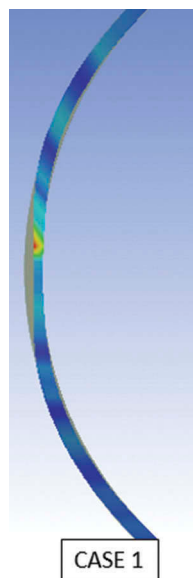


FIGURE 3.32 Deformation of ring stiffener at the collision zone.

stiffeners is only about 35% of that of the maximum deformation. Thus, ring stiffeners play a major role in confining the plastic strain within the bays of the collision zone. The deformation of the ring stiffener at the collision zone is shown in Fig. 3.32. The stringers between the ring stiffeners collapsed as a beam at the impact location, and local tripping is also observed in the stringers close to the ring stiffener.

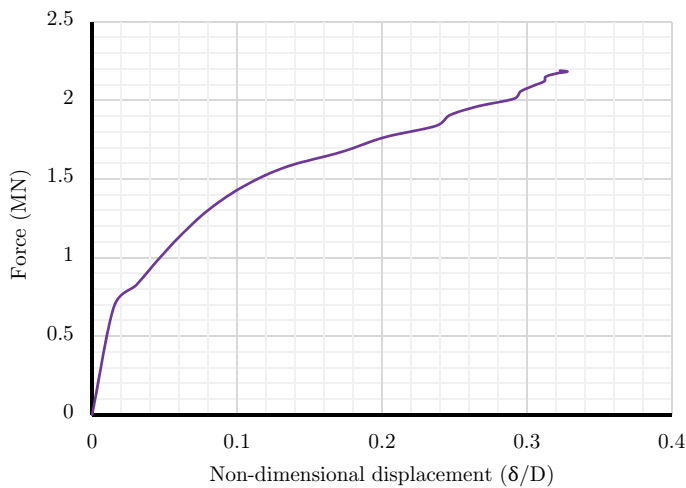


FIGURE 3.33 Load versus nondimensional displacement curve.

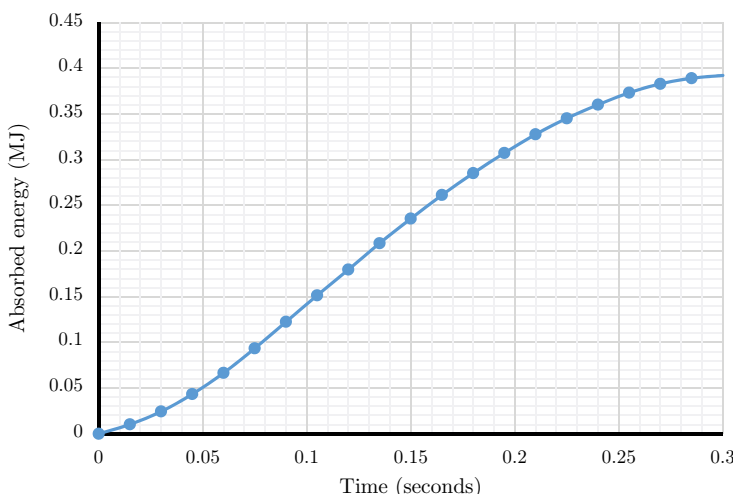


FIGURE 3.34 Energy absorbed by buoyant leg.

(ii) Load-deformation characteristics

The impact force developed during the collision is about 2.19 MN, and it causes a shell deformation of 0.21 m at the collision zone. During the collision, the buoyant leg absorbs maximum energy of 0.39 MJ. The load-deformation curve is shown in Fig. 3.33. Flattening of the curve is attributed to the torsional buckling of the stiffeners. Energy absorbed by the buoyant leg with the increase in impact duration is shown in Fig. 3.34.

3.20 FUNCTIONALLY GRADED MATERIAL

Although steel is favorite construction material for industrial structures and offshore platforms, strength degradation and decrystallization of steel at high temperatures poses a challenge of exploring alternate material. Composites are chosen as alternatives, but mostly for nonstructural components. A recent set of studies have explored the suitability of using functionally graded material (FGM) for high-temperature and high-pressure conditions. A typical application will be marine risers. Materials with a change in their porosity, composition and microstructure along its volume are termed as an FGM. They are intended to perform specific functions, which enable superiority within a set of chosen properties (Hari, 2018).

Marine risers are under a continuous threat of corrosive environment in the presence of hydrogen sulfide gas, chlorides and carbon-di-oxide. This section presents the results of a recent innovative study carried out to assess the suitability of FGM in the marine environment. Marine risers are conduits used to transport oil and gas from the reservoir to the topside of the platform. The catenary shape is a commonly used riser configuration for the field developments in ultra-deep water (Chandrasekaran, 2017, 2015; Chandrasekaran & Madhuri, 2015). During the production process, risers are subjected to the corrosive environment due to the presence of hydrogen sulfide gases, chlorides and CO₂. Riser material is preferred to be a corrosion-resistant alloy of duplex stainless steel, which is functionally graded with carbon manganese steel and nickel as buffer layers along the inner portion of the riser; titanium Grade 2 is graded functionally along the external surface of the riser.

While the design of marine risers could be challenging due to increase in the H₂S content and a significant reduction in fatigue strength at sensitive zones such as weld on thick forged ends, counter-bored riser pipe and cladding are used at the critical locations (Chandrasekaran & Madhuri, 2015; Chandrasekaran & Thomas, 2016a). Alternatively, composite materials are found to be an alternate, but delamination poses a threat to their use under the combination of thermal and mechanical loads of extreme nature. FGM is designed to overcome the damages posed by delamination as they possess no distinct material interfaces. Under high temperature and pressure, thermal stresses occur at the bonding interface of the metals and ceramics due to the difference in their coefficients of thermal expansion. It leads to a crack formation and results in delamination at the interface.

FGMs are used to create thermal barriers, anti-oxidation coatings and cemented-carbide cutting tools. Thermoelectric materials are fabricated using functionally graded materials by grading their carrier concentration (Kawasaki & Watanabe, 1987). Functionally graded materials have a continuous variation or a step-wise grading of materials, which is application specific. In FGM, the composition and microstructure are changed along the structure to generate a property gradient with the combined materials. Pores play a significant role in the mechanical ingredients of the functionally graded materials. Properties such as shock resistance, insulation can be improved with an increase in pore distribution, varying from the interior to the outer surface.

Functional grading combines the advantages of the grouped materials. For example, Duplex stainless steel has high corrosion-resistance to hydrogen sulfide gases, chlorides, CO₂ and acidic environment. Also, it exhibits higher resistance to stress corrosion cracking, which is induced by chlorides (Chandrasekaran & Jain, 2016b). Further, titanium shows a high corrosion resistance under marine conditions (Chandrasekaran & Srivastava, 2017). The yield strength and the tangent modulus of these individual materials are used to arrive at a functionally graded combination; a bilinear strain-hardening approach is commonly used. Manufacturing of FGMs has been a challenge, but alternate manufacturing techniques such as sintering, centrifugal forming and substitutional reactions made this process plausible.

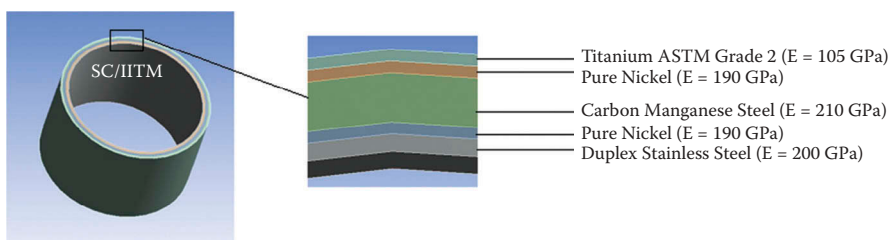


FIGURE 3.35 Section of the functionally graded riser.

TABLE 3.3 Functionally graded marine riser details

Layer	Material	Thickness (mm)
1	Duplex stainless steel (22 Cr) 2209	3
2	Pure nickel buffer layer	2
3	Carbon manganese steel ER70S6	8.47
4	Pure nickel buffer layer	2
5	ASTM Grade 2 titanium	2
Total thickness		17.48

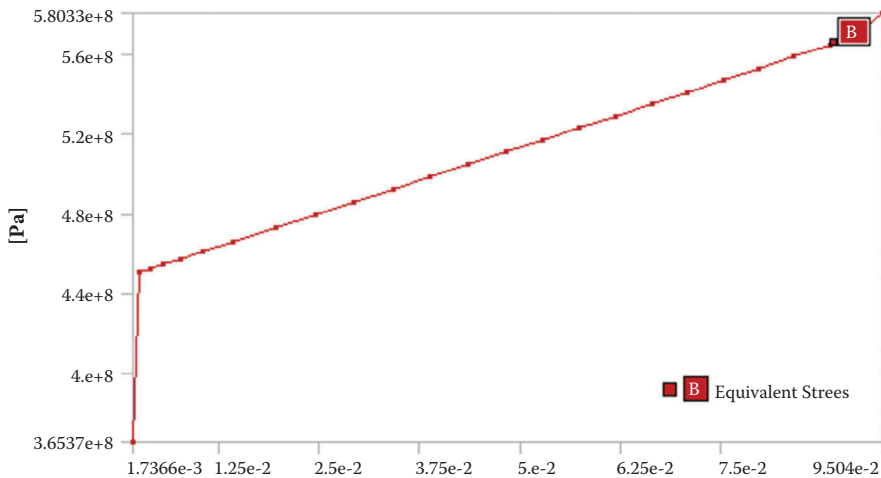


FIGURE 3.36 Stress–strain curve of FGM.

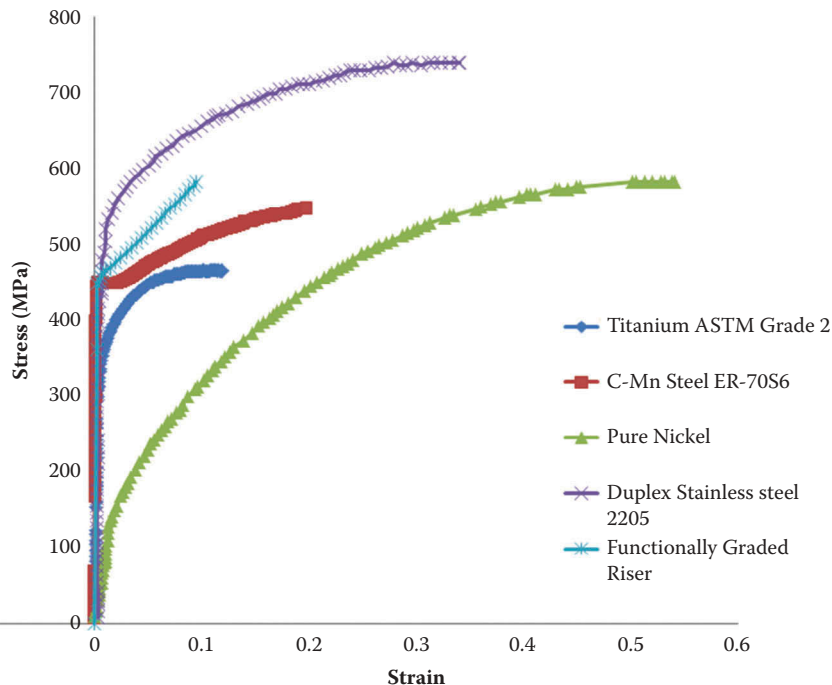


FIGURE 3.37 Comparison of stress–strain curves of individual materials used for grading.

TABLE 3.4 Structural properties of individual materials used for grading

Material	Modulus of elasticity	Poisson's ratio
Carbon manganese steel	210 GPa	0.30
Pure nickel	190 GPa	0.315
Duplex stainless steel	200 GPa	0.30
Titanium ASTM Grade 2	105 GPa	0.37
Functionally graded combination	174.506 GPa	0.2987

Functionally graded with 22Cr Duplex Stainless Steel and ASTM Grade 2 Titanium at the internal and external surface, respectively, are examined for riser application. A buffer layer of Nickel is used to facilitate the manufacturing process to maintain the desired thickness of the member. A typical section of the FGM, being examined for marine riser application is shown in Fig. 3.35, while Table 3.3 shows the details of materials.

3.20.1 MATERIAL CHARACTERISTICS OF FGM

A bilinear, strain-hardening approach is used along with the yield strength and tangent modulus of the individual materials to obtain the stress-strain curve of FGM. Fig. 3.36 shows the stress-strain curve obtained for the FGM, used in the present study. Yield strength of 450.4 MPa and Young's modulus of 174.506 GPa is obtained from the stress-strain curve. Stress-strain curves of the individual materials used for grading are shown in Fig. 3.37. Stress-strain curves of the individual materials are taken from the literature: Pure Nickel (Borkar et al., 2017); ASTM Titanium Grade 2 (Marchenko, 2016) and carbon manganese steel (Zhang, 2015), Duplex Stainless Steel (Tavares, 2015). Table 3.4 shows the structural properties of the individual materials used for grading. The table clearly shows a comparable value of the yield strength of FGM, in addition to making it corrosion-resistant.

4 Stability of Structural Systems

4.1 CONDITIONS OF STABILITY

As seen above, stability is affected significantly under compressive forces. Further, geometric stability is more important than material stability as the former may challenge the functional requirements of the structural member. Therefore, stability refers to a stable state of equilibrium and is defined as the ability of any structural system to remain (or continue to remain) in its geometric form, which is capable of performing the intended function even if the geometric position is disturbed by external forces. By this definition, compliant offshore structures are said to be stable as they can perform their intended function at the disturbed geometric position. For example, a TLP is said to be in a disturbing position under the combined effect of offset and setdown. As long as this change in geometric position does not affect its load-disbursing capacity, TLP is said to be in a stable condition. It is therefore not necessary that structures should remain (or continue to remain) in their original geometric form to classify them as stable. They may continue to remain stable even under the deformed geometric position, if they continue to perform their intended function, successfully.

The three criteria of checking stability are (i) Euler's static criterion, (ii) Lyapunov's dynamic criterion and (iii) potential energy stability criterion. Euler's static criterion is applicable under the nontrivial equilibrium state. It evaluates the stability of a structural system by examining the optimum geometric configuration of the system other than the original (initially straight) configuration at which the structural system can still disburse the applied load (P_{cr}). Under the given boundary conditions and initially perfect straight geometry, structures are examined. Euler's criterion evaluates whether the structure is capable of carrying the load (maybe in lesser magnitude, which is P_{cr} where $P > P_{cr}$) instead of remaining in a state where it is unable to carry any load at all. It is interesting to note that the load carrying capacity of the structural member is reduced from P to P_{cr} , but the important fact is that the structural member is capable of carrying at least P_{cr} even at a changed geometric form, which is quite weak from that of the initial form. This value of load with lesser in magnitude in comparison to that of the originally intended load (P) is termed as critical load or buckling load. It can be easily seen from the standard literature that P_{cr} is easily computed from the boundary conditions, cross-sectional properties of the member and slenderness ratio. However, instability occurs when two or more adjacent equilibrium positions correspond to different mode shapes.

For assessing the stability of offshore compliant structures, it is reasonably simple to disagree application of the Euler's criterion as the boundary conditions

of the member do not permit examining Euler's criterion of stability. They are either completely floating under hydrodynamic stability or compliant, and hence stability is dependent on the high-magnitude pretension of tethers. For example, in the case of TLPs, high pretension imposed on tethers ensures stability and recentering of the platform under the action of lateral loads. Functional working of the platform is not lost even under the deformed position of the platform under wave loads. Note that this condition is true even though the offset values are quite large (about 10% of that of the initial pretension of tethers) causing large deformation. Lyapunov's condition examines the stability of the structural system under dynamic excitations. If a member is subjected to a continuously varying disturbing force, then it is necessary to examine whether the condition of equilibrium under the dynamic forces is satisfied. As explained in the literature (Srinivasan Chandrasekaran, 2015a, 2015b, 2015c, Chandrasekaran & Lognath, 2016, 2017a), stability can be influenced by both varying amplitudes of the exciting force and its period of excitation. While the former can influence the load carrying capacity of the member, which is the strength-dependent criterion, the latter can result in unconditional response at the near-resonance state of vibration. Hence, Lyapunov's assessment of stability is focused on the dynamic response behavior of the structural system instead of purely assessing its load carrying capacity, as in the case of Euler's criterion.

Lyapunov's condition is more significant for structures that are designed to perform their intended function under varying external forces. The most challenging part in the context of stability is that the structure shall also be assuming a different geometric position with time. Structural systems such as ships, offshore compliant platforms and floating production platforms fall under this category of stability check. Stability calculations of ships focus on estimating the center of gravity, the center of buoyancy, metacenter of vessels and their interaction. The saving part of such systems is that they are designed to remain hydrostatically stable at any instant of time. In case of structures that are permitted to undergo large displacements, as in the case of TLPs, then the geometric design ensures proper recentering, which means that the structural system continuously tries to regain its original geometric position with the help of dedicated members present within the system; in case of TLP, it is tethers. A potential energy stability criterion applies to structural systems for which the potential energy of the system ceases to be the minimum, which is more relevant to conservative systems.

4.2 BUCKLING AND INSTABILITY

The loss of structural stability is termed as instability, which can be assessed based on (i) material properties, (ii) geometric configuration, and (iii) nature and magnitude of loads acting on the structure. Assessment based on material strength highlights where the applied load exceeds the accepted strength level of the material, classifying the structure as unstable. Assessment based on the geometric configuration explores the functional success of the member even under the deformed (displaced) position while that based on the nature and magnitude of the loads assesses dynamic instability. In general terms, loss of stability is

expressed by a load-deformation relationship. Fig. 4.1 shows an unstable situation; even a small disturbance, the ball can rollover causing instability.

A significant change in the geometric configuration of a structure or any structural component under compression, resulting in loss of ability to resist the encountered loads is termed as instability. It is important as this can lead to a catastrophic failure, as the load carrying capacity of an unstable structural system is close to zero; hence, it should be properly accounted for in the design. Instability is a strength-related limit state. Structural systems can become unstable upon application of excessive loads. Beyond the threshold limits, stresses developed in the member can magnify the deflections, causing failure. Any structural system, whose deformation exceeds the permissible limits, is termed as unstable. Therefore, the stability of any structural system depends upon its ability to withstand the encountered load without undergoing excessive deformation. It is important to note that a structure, which is found to be stable for a load applied at one section may become unstable under the same magnitude and nature of the load, but applied at a different section. Stability can be simply illustrated in Fig. 4.2. The ball remains in equilibrium in all the three cases, as the specific locations, as shown. However, slight disturbance imposed on the ball can change its behavior differently in the three cases. As seen in case (a), the ball can return to its original position upon removal of any disturbing external force and therefore assumes a stable position. It corresponds to a position in the material stress-strain curve, within elastic limit. In case (b), the ball is considered as neutrally stable, as the ball can continue to move under the influence of disturbing external forces. This state corresponds to a point on the ultimate strength region of the stress-strain curve of the material. However, in case (c), the ball will not be able to return to its original position even under a small disturbance caused by an external force. It is a classical state of instability. It is important to note that loss of stability, arising either from a change in geometry or change in the structural configuration adds a new set of additional loads to the structural system. It may lead to the further classification of instability as flexural buckling, torsional buckling, flexural-torsional buckling and lateral-torsional buckling (Gambhir, 2004).

Flexural buckling (FB) can occur in any compression member, which is undergoing deflection that arises from bending. Two factors that influence flexural buckling are large slenderness ratio and lesser radius of gyration. Torsional buckling

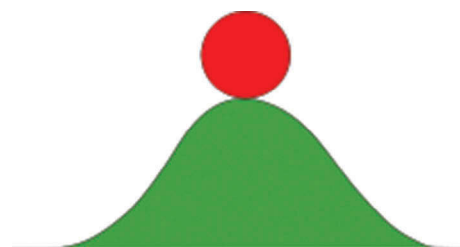


FIGURE 4.1 Unstable condition.

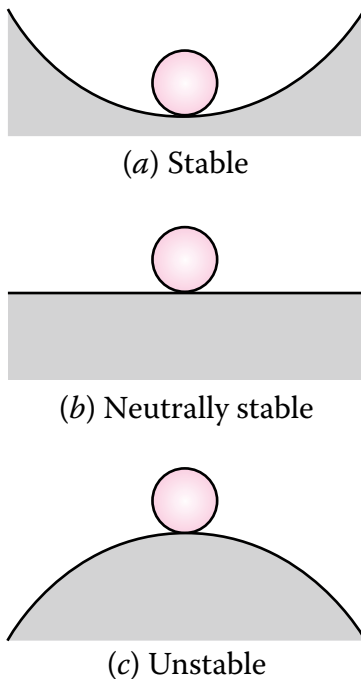


FIGURE 4.2 Stability illustrations: (a) stable; (b) neutrally stable; (c) unstable.

(TB) can occur in slender compression members that are double symmetric in shape and arrangement (Fig. 4.3). As seen in the figure, the longitudinal axis of the members is turned (bent laterally) causing the torsional buckling. It is commonly seen in built-up sections due to design inadequacy in terms of sectional properties along the length of the member. If the loads in any structural system are set to act through the shear center of the section, then no twisting or torsion of the member occurs. As the shear center is located on the axis of symmetry, cross sections that have two axes of symmetry will have a shear center located at the intersection of both the axes of symmetry. For sections with one axis of symmetry, say, for example, a channel section, the shear center can be located from the standard procedure (Srinivasan Chandrasekaran, 2015). While the center of gravity (or the mass center) is the point about which moments generated from the mass of the elements will be zero, the eccentricity of the center of gravity concerning the shear center will result in a couple and causes twisting of the section, referred as torsional buckling. Distortional buckling is a unique mode of buckling where the flange of the section rotates at the intersection of the flange and web of the section. It is also referred to as local-torsional buckling. It occurs mainly due to adequate stiffening of the web in comparison to that of the flange.

On the other hand, compression members with one axis of symmetry undergo flexural-torsional buckling (FTB). FTB is a combination of bending and twisting

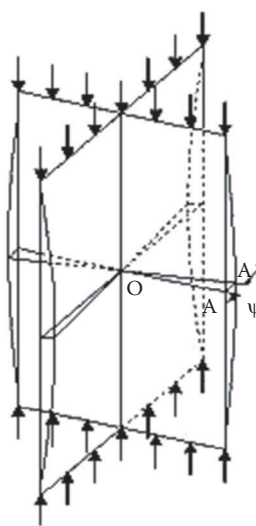


FIGURE 4.3 Torsional buckling of slender compression member.

of a member under compressive loads. This type of buckling is commonly seen in members of open cross sections subjected to compressive loads. A few examples of open sections are channel sections, tee sections and angle sections. The main reason, which is common with these open sections, is the lower torsional stiffness. It is important to note that circular cross sections do not experience such mode of buckling. Fig. 4.4 shows a schematic view of a cantilever beam undergoing flexural-torsional buckling.

Lateral-torsional buckling (LTB) occurs in open sections as well. Consider a simply supported beam under central concentrated load, causing bending. While the top fiber experiences compression, bottom fiber experiences tension.

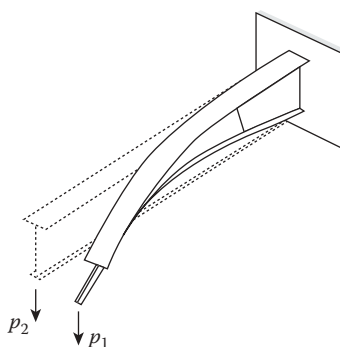


FIGURE 4.4 Cantilever under flexural torsional buckling.

Considering a long-span condition of the beam, if the compression flange is not laterally supported, it experiences both large and lateral deflection. Hence, the beam will twist in addition to a large lateral deflection, whose combination is termed as lateral-torsional buckling. Even the width of the compression flange (b_f) significantly influences the nature of the buckling mode. Sections with wide compression flange will undergo twisting in torsion, but narrow-flange sections experience lateral buckling due to their reduced bending stiffness. Box sections (with a square side), even being hollow, shall not experience lateral-torsional buckling due to their high torsional rigidity. Fig. 4.5 shows a schematic view of an I-section undergoing lateral-torsional buckling. The flexural strength of the member, undergoing lateral torsional buckling, will be modified using a modification factor, as given below:

$$\text{Modification factor} = \frac{12.5 M_{\max}}{[2.5 M_{\max} + 3 M_A + 4 M_B + 3 M_C]} \quad (4.1)$$

where M_{\max} is the maximum moment in the unbraced segment of the member, M_A , M_B and M_C are maximum values of the moments at the quarter, mid and 3/4th points of the unbraced segment of the member. The modification factor allows the use of non-uniform moment diagrams at the end of the beam segments that are braced.

If a compression member is loaded suddenly and then released, it can sustain a higher load than its static buckling load. Let us consider a long, unsupported column used as a drop hammer. The duration of impact load (compression) at one end is the time required for a stress wave to travel along the length of the column and to return. It is seen that the maximum buckling occurs near the impact end as the wavelength is shorter than the length of the member; however, the stress will be much higher than that of the buckling stress of any statically loaded column. It is referred to as dynamic buckling.

Stability analysis evaluates the modes of failure in terms of the structural stability; each mode will yield a corresponding load under which instability

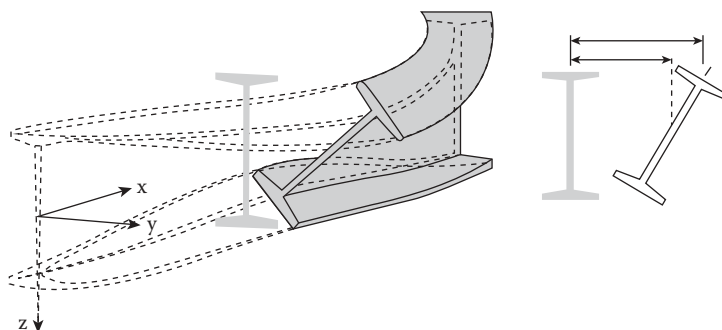


FIGURE 4.5 Lateral-torsional buckling of I-section.

occurs (or initiated). These loads are termed as critical loads. It is important to note that the structural system remains at rest before instability occurs and also remains at rest immediately after when the failure is initiated by buckling. Four classical methods namely (i) equilibrium state approach, (ii) work approach, (iii) energy principle and (iv) dynamic approach are useful in solving the buckling problems. However, in case of the dynamic instability, loss of stability is just a transition from the state of rest to the state of motion.

4.3 EULER CRITICAL LOAD

Consider an ideal column, as shown in Fig. 4.6. The column is assumed to be initially straight and compressed by a concentric load, P as shown in the figure.

The column is pinned at both the supports and uniformly slender. Further, it is assumed to be laterally restrained in position at both the supports. The column section is assumed to be of negligible weight and perfectly elastic. Stresses developed by the axial forces are assumed to be within the proportional limit of the column material. If the applied force, P , is lesser than the critical value, then the column will continue to remain straight and undergoes only axial compression. Under this state, the column is said to be in *stable equilibrium*. Under such condition, if a lateral load is applied at any point, say, for example, at the mid-height of the column, it will result in lateral deflection. However, importantly, the column will return to its original position in terms of geometry and shape and size in terms of its cross section.

However, upon a continuous (in a steady rate) increase of the axial load, P , the straight form of equilibrium tends to become gradually unstable. Under this condition, even the lateral of a very small magnitude can cause lateral deflection,

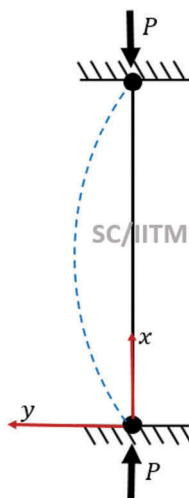


FIGURE 4.6 Euler column.

which will not disappear upon the removal of the lateral load; note that this was not the case when P is lesser than the axial capacity of the member, as discussed earlier. Based on the two sets of explanations, one can define a *critical load*. The critical load is the axial load, which is necessary to maintain (or continue to maintain) the member in its initial-straight position (Timoshenko and Gere, 1961). This critical load can be computed based on the elastic curve equation of a beam (Livesley and Chandler, 1956).

$$\frac{d^2y}{dx^2} = \frac{M}{EI} \quad (4.2)$$

where M is bending moment, I is the moment of inertia and E is the modulus of elasticity. Fig. 4.7 shows the free-body diagram of the column member under the applied load.

With reference to the figure, the equilibrium of the free-body diagram is written as follows:

$$EI \frac{d^2y}{dx^2} = M = -Py \quad (4.3)$$

$$EI \frac{d^2y}{dx^2} + Py = 0 \quad (4.4)$$

$$y = A \sin\left[\frac{\alpha x}{L}\right] + B \cos\left[\frac{\alpha x}{L}\right] \quad (4.5)$$

$$\text{where } \alpha = L \sqrt{\frac{P}{EI}}$$

For the boundary condition at $x = 0$; $y = 0$, $B = 0$

Hence, Eq. (4.5) becomes

$$y = A \sin\left[\frac{\alpha x}{L}\right] \quad (4.6)$$

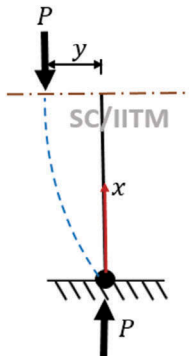


FIGURE 4.7 Free-body diagram of the column member.

Further, at $x = L, y = 0$; applying this boundary condition, Eq. (4.6) becomes as follows:

$$A \sin(\alpha) = 0 \quad (4.7)$$

which means that either $A = 0$ or $\sin(\alpha) = 0$. If $A = 0$, there will no lateral deflection. Therefore, setting $\sin(\alpha) = 0$

$$\alpha = n\pi \text{ for } n = 0, 1, 2, 3, \dots \quad (4.8)$$

Substituting Eq. (4.8), we get:

$$n\pi = L \sqrt{\frac{P}{EI}} \quad (4.9)$$

Squaring,

$$n^2\pi^2 = L^2 \frac{P}{EI} \quad (4.10)$$

$$P = \frac{n^2\pi^2 EI}{L^2} \text{ for } n = 1, 2, 3, 4, \dots \quad (4.11)$$

$n = 0$ is meaningless as this will cause no axial load ($P = 0$)

In Eq. (4.11), P is called a Euler critical load.

$$P_E = \frac{n^2\pi^2 EI}{L^2} \text{ for } n = 1, 2, 3, 4, \dots \quad (4.12)$$

4.4 STANDARD BEAM ELEMENT, NEGLECTING AXIAL DEFORMATION

A beam element, shown in Fig. 4.14, is one of the basic elements to be used in the stability analysis. A few sign conventions are required to be followed before deriving the stiffness matrix of the standard beam element.

1. The end moment, joint rotation and joint moments, which are anti-clockwise in nature, are considered to be positive.
2. Upward force (or displacement) of the joint is considered a positive value.
3. Force or axial displacement toward the right of the joint is also considered as positive.
4. Upward end shear at ends of the beam is positive.
5. Right direction force at ends of the beam is positive.

Consider a fixed beam undergoing deformation due to bending, neglecting the axial deformation. The standard fixed beam is shown in Fig 4.8. End nodes of the beam are designated as j and k ends while the length of the member is

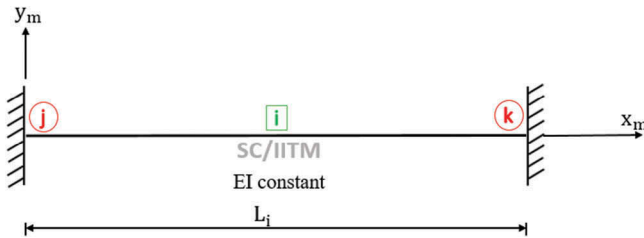


FIGURE 4.8 Standard beam element.

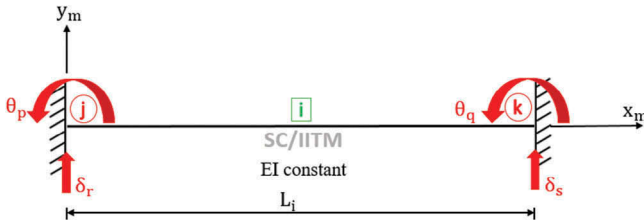


FIGURE 4.9 Rotational and translational moments in the standard beam.

designated as L_i ; subscript 'i' refers to the member index. The beam has a constant EI over its entire length. The axes (x_m , y_m) are the local axes of the member. It is very important to note the axis system. Axis system is such that it has an origin at the j^{th} end; x_m is directed toward a k^{th} end. y_m is counterclockwise 90° to the x_m axis. Therefore, (x_m , y_m) plane defines the plane of bending the beam element.

Neglecting the axial deformation, one should identify both the translational and rotational displacements at each end of the beam, as shown in Fig. 4.9. Suitable subscripts are used for denoting the rotational and translational displacements, as marked in the figure. The displacements at the j^{th} end and k^{th} end are (θ_p, δ_r) and (θ_q, δ_s) , respectively. All these displacements happen in x_m , y_m plane and there is no out of plane bending.

By classical definition, the stiffness coefficient, k_{ij} is the force in the i^{th} degree of freedom by imposing unit displacement (either translational or rotational) in the j^{th} degree of freedom by keeping all other degrees-of-freedom restrained. As seen in the above figure, there are four degrees of freedom (two rotations and two translations). One should give unit displacement (or rotation) in each degree of freedom to find the forces (or moments) in the respective degrees of freedom by keeping the remaining degrees-of-freedom restrained. Imposing unit displacement represents $\delta_r = 1$ or $\delta_s = 1$ and that of unit rotation implies $\theta_p = 1$ or $\theta_q = 1$.

Let us apply unit rotation at the j^{th} end, keeping all other degrees-of-freedom restrained as shown in Fig. 4.10. It will invoke the members with the end forces, k_{pp}^i , k_{qp}^i , k_{rp}^i , k_{sp}^i as seen in the figure. k_{pp}^i is the force in p^{th} degree of freedom by

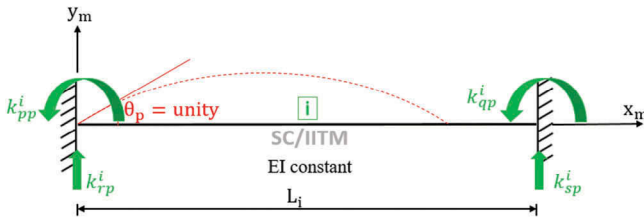


FIGURE 4.10 Unit rotation at the j th end of standard beam.

giving unit displacement in p th degree of freedom; superscript ' i ' refers to the i th member. Similarly, k_{qp}^i is the force in q th degree of freedom by giving unit displacement in p th degree of freedom in the i th member. The second subscript in all the notations is common, which is ' p ', indicating that the unit displacement (in this case, it is unit rotation since p is a rotational degree of freedom) is applied at p th degree. The stiffness coefficients derived column-wise correspond to the first column of the stiffness matrix. Similarly, applying unit rotation at the k th end of the i th member, as shown in Fig. 4.11, develops the stiffness coefficients (k_{pq}^i , k_{qq}^i , k_{rq}^i , k_{sq}^i).

The stiffness coefficients are obtained by applying unit displacements at the j th end and k th end, as shown in Figs. 4.12 and 4.13, respectively, which yields the stiffness coefficients at the j th end as (k_{pr}^i , k_{qr}^i , k_{rr}^i , k_{sr}^i) and at k th end as (k_{ps}^i , k_{qs}^i , k_{rs}^i , k_{ss}^i), respectively. As shown in the figures, a tangent can be drawn

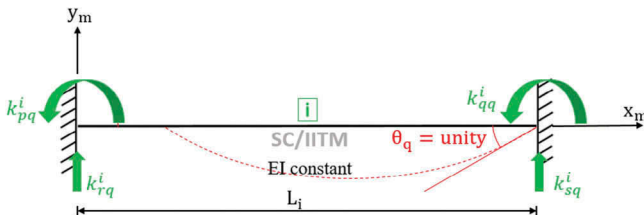


FIGURE 4.11 Unit rotation at the j th end of standard beam.

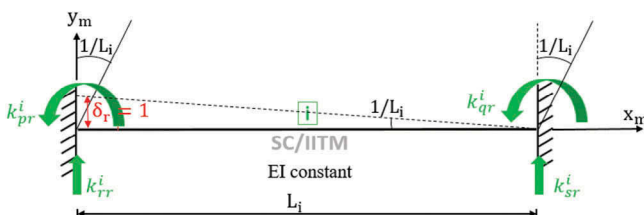


FIGURE 4.12 Unit displacement at the j th end of standard beam.

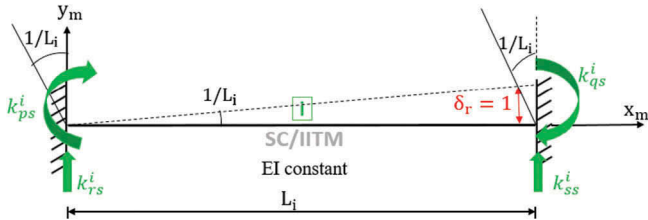


FIGURE 4.13 Unit displacement at the k th end of standard beam.

by connecting the deflected position of the beam at which the unit rotation is applied and the initial position of the beam at the other end. It can be easily inferred that the beam has undergone a rotation of $(1/L_i)$, where L_i is the length of the i th beam element. The rotation at the ends of the beam is equal to $(1/L_i)$.

The corresponding end reactions (moment, shear) for the i th beam element are required to be estimated under the arbitrary end displacements (θ_p, δ_r) and (θ_q, δ_s) at the j th and k th ends of the beam. They are estimated by maintaining the equilibrium of the restrained member. The governing equations are as follows:

$$m_p^i = k_{pp}^i \theta_p + k_{pq}^i \theta_q + k_{pr}^i \delta_r + k_{ps}^i \delta_s \quad (4.13)$$

$$m_q^i = k_{qp}^i \theta_p + k_{qq}^i \theta_q + k_{qr}^i \delta_r + k_{qs}^i \delta_s \quad (4.14)$$

$$p_r^i = k_{rp}^i \theta_p + k_{rq}^i \theta_q + k_{rr}^i \delta_r + k_{rs}^i \delta_s \quad (4.15)$$

$$p_s^i = k_{sp}^i \theta_p + k_{sq}^i \theta_q + k_{sr}^i \delta_r + k_{ss}^i \delta_s \quad (4.16)$$

It can be seen from the above equation that the first subscript corresponds to the end at which the unit rotation (or displacement) is applied. The above set of equations gives the end moments and end shear forces for arbitrary displacements $(\theta_p, \theta_q, \delta_r, \delta_s)$, which are unity at respective degrees of freedom. These equations can be generalized as follows:

$$\{m_i\} = [k]_i \{\delta_i\} \quad (4.17)$$

$$\{m_i\} = \begin{Bmatrix} m_p \\ m_q \\ p_r \\ p_s \end{Bmatrix} \quad (4.18)$$

$$\{\delta_i\} = \begin{Bmatrix} \theta_p \\ \theta_q \\ \delta_r \\ \delta_s \end{Bmatrix} \quad (4.19)$$

$$[k]_i = \begin{bmatrix} k_{pp} & k_{pq} & k_{pr} & k_{ps} \\ k_{qp} & k_{qq} & k_{qr} & k_{qs} \\ k_{rp} & k_{rq} & k_{rr} & k_{rs} \\ k_{sp} & k_{sq} & k_{sr} & k_{ss} \end{bmatrix} \quad (4.20)$$

Fig. 4.14 shows the forces at both the ends of the standard beam member under unit rotation applied at the j th end of the member.

In the standard fixed beam element with unit rotation at the j th end, moments developed at the ends to control the applied unit rotation are (k_{pp}^i, k_{qp}^i) , respectively. It results in the development of an anticlockwise moment $(k_{pp}^i + k_{qp}^i)$, which should be counteracted by a coupled shear. The shear forces at the ends of the beam are determined as $\left[\frac{k_{pp}^i + k_{qp}^i}{L_i}\right]$. At the j th and k th end of the beam, magnitude of the shear will be the same, but it will be in the opposite direction at the j th end of the member. It can be seen that the second subscript in the stiffness coefficients indicates the end at which the unit rotation is applied and the first subscript indicates the forces in the respective degrees of freedom. With reference to the above figure, it is clear that one need to evaluate only a set of rotational coefficients in Eq. (4.20). These rotational coefficients are $(k_{pp}^i, k_{pq}^i, k_{qp}^i, k_{qq}^i)$. Knowing the rotational coefficients, end shear can be expressed as follows:

$$k_{rp}^i = \frac{k_{pp}^i + k_{qp}^i}{L_i} \quad (4.21)$$

$$k_{sp}^i = -\frac{k_{pp}^i + k_{qp}^i}{L_i} \quad (4.22)$$

The negative sign in Eq. (4.22) is because of the direction of k_{sp}^i is opposite to that of the end shear developed by the restraining moments as shown in the Fig. 4.14. For the unit rotation applied at the k th end, end shear, in terms of the rotational coefficients is given as

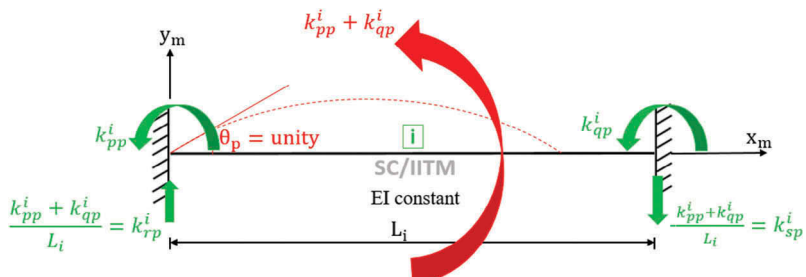


FIGURE 4.14 Rotation coefficients of standard beam.

$$k_{rq}^i = \frac{k_{pq}^i + k_{qq}^i}{L_i} \quad (4.23)$$

$$k_{sq}^i = -\frac{k_{pq}^i + k_{qq}^i}{L_i} \quad (4.24)$$

By applying unit displacement at the j th end of the beam element, the stiffness coefficients can be expressed as

$$k_{pr}^i = \frac{k_{pp}^i + k_{pq}^i}{L_i} \quad (4.25)$$

$$k_{qr}^i = -\frac{k_{qp}^i + k_{qq}^i}{L_i} \quad (4.26)$$

$$k_{rr}^i = \frac{k_{pr}^i + k_{qr}^i}{L_i} = \left[\frac{k_{pp}^i + k_{pq}^i}{(L_i)^2} \right] + \left[\frac{k_{qp}^i + k_{qq}^i}{(L_i)^2} \right] \quad (4.27a)$$

$$k_{rr}^i = \frac{k_{pp}^i + k_{pq}^i + k_{qp}^i + k_{qq}^i}{(L_i)^2} \quad (4.27b)$$

$$k_{sr}^i = -\frac{k_{pp}^i + k_{pq}^i + k_{qp}^i + k_{qq}^i}{(L_i)^2} \quad (4.28)$$

BY giving unit displacement at the k th end of the beam element, the stiffness coefficients are expressed as

$$k_{ps}^i = -\frac{k_{pp}^i + k_{pq}^i}{L_i} \quad (4.29)$$

$$k_{qs}^i = -\frac{k_{qp}^i + k_{qq}^i}{L_i} \quad (4.30)$$

$$k_{rs}^i = -\frac{k_{ps}^i + k_{qs}^i}{L_i} = -\frac{k_{pp}^i + k_{pq}^i + k_{qp}^i + k_{qq}^i}{(L_i)^2} \quad (4.31)$$

$$k_{ss}^i = \frac{k_{pp}^i + k_{pq}^i + k_{qp}^i + k_{qq}^i}{(L_i)^2} \quad (4.32)$$

It can be seen from the above expression that out of 16 coefficients of the stiffness matrix given in Eq. (4.20), one needs to evaluate only the four rotational

coefficients ($k_{pp}^i, k_{pq}^i, k_{qp}^i, k_{qq}^i$). Remaining coefficients can be expressed as a function of these rotational coefficients. The complete stiffness matrix is given as

$$[k] = \begin{bmatrix} k_{pp} & k_{pq} & \frac{k_{pp}+k_{pq}}{L} & -\left(\frac{k_{pp}+k_{pq}}{L}\right) \\ k_{qp} & k_{qq} & \frac{k_{qp}+k_{qq}}{L} & -\left(\frac{k_{qp}+k_{qq}}{L}\right) \\ \frac{k_{pp}+k_{pq}}{L} & \frac{k_{qp}+k_{qq}}{L} & \frac{k_{pp}+k_{pq}+k_{qp}+k_{qq}}{L^2} & \frac{k_{pp}+k_{pq}+k_{qp}+k_{qq}}{L^2} \\ -\left(\frac{k_{pp}+k_{pq}}{L}\right) & -\left(\frac{k_{pq}+k_{qq}}{L}\right) & -\left(\frac{k_{pp}+k_{pq}+k_{qp}+k_{qq}}{L^2}\right) & -\left(\frac{k_{pp}+k_{pq}+k_{qp}+k_{qq}}{L^2}\right) \end{bmatrix} \quad (4.33)$$

4.4.1 ROTATIONAL COEFFICIENTS

Consider a simply supported beam as shown in Figs. 4.15 and 4.16. Unit rotation is applied at the (j, k) ends of the beam to obtain the flexibility coefficients, respectively. The flexibility coefficients ($\delta_{jj}^i, \delta_{kj}^i$) define rotations at end j and k , respectively, of the i th member, caused due to unit moment applied at the j th end (refer Fig. 4.21). Similarly, the flexibility coefficients ($\delta_{jk}^i, \delta_{kk}^i$) define rotations at j th and k th ends of the i th member due to unit moment applied at k th end.

Let us now consider a beam fixed at the k th end, imposed by unit rotation at the j th end (Fig. 4.17) and unit rotation at the k th end as shown in Fig. 4.18. The stiffness coefficients (k_{pp}^i, k_{qp}^i) define end moments required at j th and k th ends to maintain equilibrium when the j th end is subjected to unit rotation while the k th end is restrained. Similarly, the stiffness coefficients (k_{pq}^i, k_{qq}^i) define

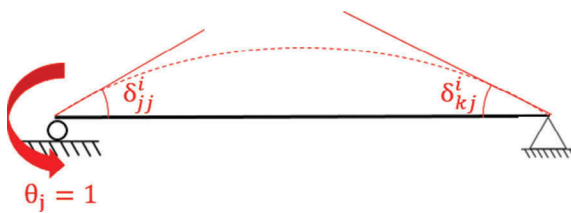


FIGURE 4.15 Unit rotation at the j th end of the simply supported beam.

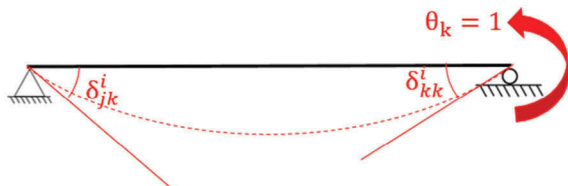


FIGURE 4.16 Unit rotation at the k th end of the simply supported beam.

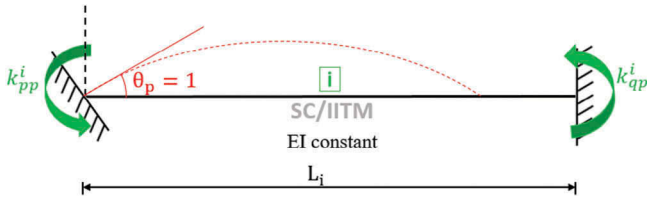


FIGURE 4.17 Unit rotation at the j th end of fixed beam.

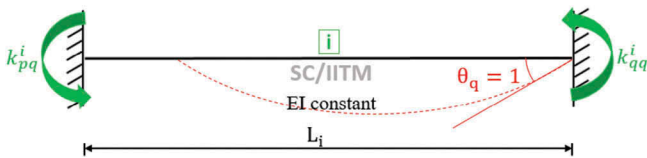


FIGURE 4.18 Unit rotation at the k th end of fixed beam.

end moments required at the j th and the k th ends to maintain equilibrium, when the k th end is subjected to unit rotation and the j th end, is restrained.

Thus,

$$\begin{bmatrix} \delta_{jj} & \delta_{jk} \\ \delta_{kj} & \delta_{kk} \end{bmatrix} \begin{bmatrix} k_{pp} & k_{pq} \\ k_{qp} & k_{qq} \end{bmatrix} = \begin{bmatrix} 1 & 0 \\ 0 & 1 \end{bmatrix} \quad (4.34)$$

Expanding the above equation, we get:

$$k_{pp}^i \delta_{jj}^i + k_{qp}^i \delta_{jk}^i = 1 \quad (4.35a)$$

$$k_{pp}^i \delta_{kj}^i + k_{qq}^i \delta_{kk}^i = 1 \quad (4.35b)$$

$$k_{pq}^i \delta_{jj}^i + k_{qq}^i \delta_{jk}^i = 1 \quad (4.35c)$$

$$k_{pq}^i \delta_{kj}^i + k_{qq}^i \delta_{kk}^i = 1 \quad (4.35d)$$

Let us denote the flexibility matrix as $[D_r]$ and stiffness matrix as $[k_r]$. The subscript r refers to the rotational degrees of freedom. To estimate the flexibility matrix for the beam element, assume the simply supported beam with the unit moment at the j th end as shown in Fig. 4.19. The anticlockwise moment is balanced by the clockwise couple created by the forces. The bending moment diagram is also shown in the figure with tension at top and compression at the bottom.

Let us replace the loading diagram with a conjugate beam as shown in Fig. 4.20. Taking moment about A ,

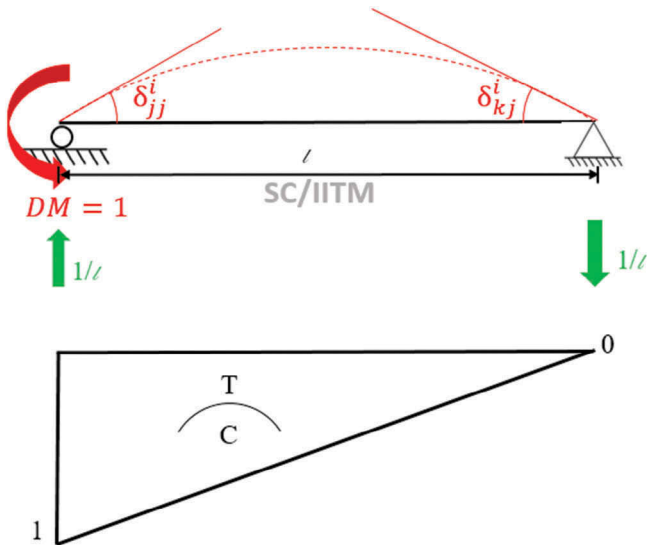


FIGURE 4.19 Simply supported beam with the unit moment at the j th end.

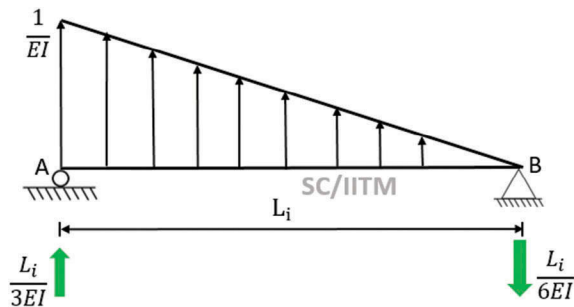


FIGURE 4.20 Conjugate beam.

$$V_B = \left[\left\{ \frac{1}{2} L_i \left(\frac{1}{EI} \right) \right\} \frac{1}{3} L_i \right] \frac{1}{L_i} = \frac{L_i}{6EI} \text{ (downward)} \quad (4.36a)$$

$$V_A = \left\{ \frac{1}{2} L_i \left(\frac{1}{EI} \right) \right\} - \frac{L_i}{6EI} = \frac{L_i}{3EI} \text{ (upward)} \quad (4.36b)$$

The same procedure is followed for the other case to derive the following flexibility matrix.

$$D_r = \begin{bmatrix} \frac{L}{3EI} & -\frac{L}{6EI} \\ -\frac{L}{6EI} & \frac{L}{3EI} \end{bmatrix} \quad (4.37)$$

$$k_r = [D_r]^{-1} = \frac{12(EI)^2}{L^2} \begin{bmatrix} \frac{L}{3EI} & \frac{L}{6EI} \\ \frac{L}{6EI} & \frac{L}{3EI} \end{bmatrix} = \begin{bmatrix} \frac{4EI}{L} & \frac{2EI}{L} \\ \frac{2EI}{L} & \frac{4EI}{L} \end{bmatrix} \quad (4.38)$$

Thus, from the above four rotational coefficients, the whole stiffness matrix can be derived as

$$K_i = \begin{bmatrix} \frac{4EI}{l} & \frac{2EI}{l} & \frac{6EI}{l^2} & -\frac{6EI}{l^2} \\ \frac{2EI}{l} & \frac{4EI}{l} & \frac{6EI}{l^2} & -\frac{6EI}{l^2} \\ \frac{6EI}{l^2} & \frac{6EI}{l^2} & \frac{12EI}{l^3} & -\frac{12EI}{l^3} \\ -\frac{6EI}{l^2} & -\frac{6EI}{l^2} & -\frac{12EI}{l^3} & \frac{12EI}{l^3} \end{bmatrix} \quad (4.39)$$

4.5 STABILITY FUNCTIONS

Consider a beam element, both ends fixed, as shown in Fig. 4.21. It is important to note that the beam element is subjected to axial compressive load, P_a , as shown in the figure.

4.5.1 ROTATION FUNCTIONS UNDER AXIAL COMPRESSIVE LOAD

To obtain the stiffness coefficients, let us now apply unit rotation at the j th end of the member. Fig. 4.22 shows the rotations and shear developed at both the ends of the member due to the unit rotation applied at the j th end of the member.

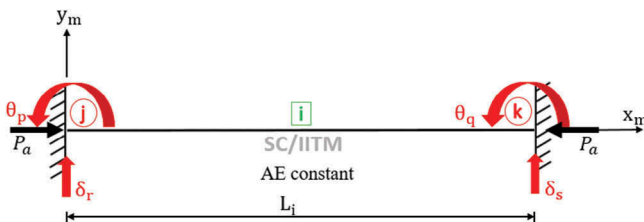


FIGURE 4.21 Fixed beam under axial compressive load.

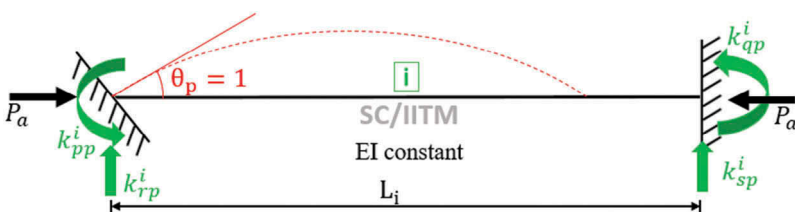


FIGURE 4.22 Unit rotation at the j th end of fixed beam.

From the above figure and based on the expressions derived in Section 4.7, the following expressions can be written as

$$\frac{(k_{pp} + k_{qp})}{L_i} = k_{rp} = -k_{sp} \quad (4.40)$$

A free-body diagram, under the influence of the applied unit rotation and the axial compressive load, is shown in Fig. 4.23.

With reference to figure, and applying the differential equation as given in Eq. (4.2), we get:

$$EI \frac{d^2y}{dx^2} = M \quad (4.41)$$

$$= -P_a(y) - k_{pp} + k_{rp}(x) \quad (4.42)$$

Substituting Eq. (4.40) into Eq. (4.42), we get:

$$EI \frac{d^2y}{dx^2} = -P_a(y) - k_{pp} + \frac{(k_{pp} + k_{qp})}{L_i}(x) \quad (4.43)$$

In the above equation, let us express the axial load (P_a as a function of Euler load (P_E), as follows:

$$P_a = \varphi_i P_E \quad (4.44)$$

Substituting Eq. (4.12) in the above equation, we get:

$$P_a = \frac{\pi^2 \varphi_i EI}{L_i^2} \text{ for } n = 1 \quad (4.45)$$

It is important to note that buckling is happening in the plane where unit rotation is applied. Therefore, Eq. (4.43) is modified as

$$EI \frac{d^2y}{dx^2} = -\frac{\pi^2 \varphi_i EI}{L_i^2} (y) - k_{pp} + \frac{(k_{pp} + k_{qp})}{L_i} (x) \quad (4.46)$$

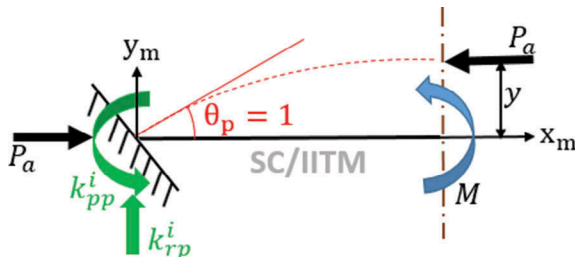


FIGURE 4.23 Free-body diagram under axial load and unit rotation at the j th end.

Dividing by (EI) and rearranging the terms, we get:

$$\frac{d^2y}{dx^2} + \frac{\pi^2\varphi_i}{L_i^2}(y) = \frac{1}{EI} \left[(k_{pp} + k_{qp}) \frac{x}{L_i} - (k_{pp}) \right] \quad (4.47)$$

The general solution of Eq. (4.47) is given as

$$y = A \sin \left[\frac{\alpha_i x}{L_i} \right] + B \cos \left[\frac{\alpha_i x}{L_i} \right] + \frac{L_i^2}{\alpha_i^2 EI} \left[(k_{pp} + k_{qp}) \frac{x}{L_i} - (k_{pp}) \right] \quad (4.48)$$

$$\alpha_i = \pi \sqrt{\varphi_i} \quad (4.49)$$

Applying the boundary conditions: $y = 0$ at $x = 0$, we get:

$$B = \frac{L_i^2}{\alpha_i^2 EI} k_{pp} \quad (4.50)$$

Substituting another boundary condition $y = 0$ at $x = L$ in Eq. (4.48), we get:

$$0 = A \sin(\alpha_i) + B \cos(\alpha_i) + \frac{L_i^2}{\alpha_i^2 EI} k_{qp} \quad (4.51a)$$

$$-\left[\frac{L_i^2}{\alpha_i^2 EI} \right] (k_{qp}) = A \sin(\alpha_i) + B \cos(\alpha_i) \quad (4.51b)$$

$$-\left[\frac{L_i^2}{\alpha_i^2 EI} \right] (k_{qp}) - \left[\frac{L_i^2}{\alpha_i^2 EI} \right] (k_{pp}) \cos(\alpha_i) = A \sin(\alpha_i) \quad (4.51c)$$

$$-\left[\frac{L_i^2}{\alpha_i^2 EI} \right] \left[\frac{(k_{qp}) + (k_{pp}) \cos(\alpha_i)}{\sin(\alpha_i)} \right] = A \quad (4.51d)$$

$$-\left[\frac{L_i^2}{\alpha_i^2 EI} \right] [k_{qp} \operatorname{cosec}(\alpha_i) + k_{pp} \cot(\alpha_i)] = A \quad (4.51e)$$

Substituting Eq. (4.51e) and Eq. (4.50) into Eq. (4.48), we get:

$$\begin{aligned} \frac{\alpha_i^2 EI}{L_i^2} y &= -[k_{pp} \cot(\alpha_i) + k_{qp} \operatorname{cosec}(\alpha_i)] \sin \left[\frac{\alpha_i x}{L_i} \right] + k_{pp} \cos \left[\frac{\alpha_i x}{L_i} \right] \\ &\quad + (k_{pp} + k_{qp}) \frac{x}{L_i} - k_{pp} \end{aligned} \quad (4.52)$$

Differentiating once, we get:

$$\frac{\alpha_i^2 EI}{L_i^2} \frac{dy}{dx} = -\frac{\alpha_i}{L_i} [k_{pp} \cot(\alpha_i) + k_{qp} \cosec(\alpha_i)] \cos\left[\frac{\alpha_i x}{L_i}\right] - \frac{\alpha_i}{L_i} k_{pp} \sin\left[\frac{\alpha_i x}{L_i}\right] + (k_{pp} + k_{qp}) \frac{1}{L_i} \quad (4.53)$$

$$\frac{\alpha_i^2 EI}{L_i} \frac{dy}{dx} = k_{pp} \left[1 - \alpha_i \sin\left[\frac{\alpha_i x}{L_i}\right] - \alpha_i \cot(\alpha_i) \cos\left[\frac{\alpha_i x}{L_i}\right] \right] + k_{qp} \left[1 - \alpha_i \cosec(\alpha_i) \cos\left[\frac{\alpha_i x}{L_i}\right] \right] \quad (4.54)$$

Note: at $x = 0$, slope (dy/dx) is equal to ϕ_p , which is equal to unity in the present case Applying the boundary condition (at $x = L$, $dy/dx = 0$), we get:

$$0 = k_{pp} [1 - \alpha_i \sin(\alpha_i) - \alpha_i \cot(\alpha_i) \cos(\alpha_i)] + k_{qp} [1 - \alpha_i \cosec(\alpha_i) \cos(\alpha_i)] \quad (4.55)$$

$$0 = k_{pp} - k_{pp} \alpha_i \left[\sin(\alpha_i) + \frac{\cos(\alpha_i)^2}{\sin(\alpha_i)} \right] + k_{qp} - k_{qp} \alpha_i \cot(\alpha_i) \quad (4.56)$$

The above equation is simplified to obtain the stiffness coefficient as

$$k_{qp} = \left[\frac{\alpha_i - \sin(\alpha_i)}{\sin(\alpha_i) - \alpha_i \cos(\alpha_i)} \right] k_{pp} \quad (4.57a)$$

Similarly, at $x = 0$, the slope is unity, which implies the following relationship:

$$k_{pp} = \left[\frac{\alpha_i (\sin(\alpha_i) - \alpha_i \cos(\alpha_i))}{2(1 - \cos(\alpha_i)) - \alpha_i \sin(\alpha_i)} \right] \frac{EI}{L_i} \quad (4.57b)$$

By expressing the stiffness coefficients as a function of rotation functions (r_i and c_i), we get the following set of equations:

$$r_i = \frac{\alpha_i (\sin(\alpha_i) - \alpha_i \cos(\alpha_i))}{2(1 - \cos(\alpha_i)) - \alpha_i \sin(\alpha_i)} \quad (4.58a)$$

$$c_i = \frac{\alpha_i - \sin(\alpha_i)}{\sin(\alpha_i) - \alpha_i \cos(\alpha_i)} \quad (4.58b)$$

The above equations are termed as *rotation functions* for compressive axial load case.

4.5.2 ROTATION FUNCTIONS UNDER ZERO AXIAL LOAD (SPECIAL CASE)

For a special case of *zero axial loads*, for which (α_i) becomes zero, one need to apply L'Hospital rule to obtain the limit of the quotient. L'Hospital rule is briefly explained for the benefit of the readers:

Suppose $f(x)$ and $g(x)$ are differentiable functions and $g'(x) \neq 0$ on an open interval I , which contains (a) {except at a }, then the following conditions apply:

Suppose, $\lim_{x \rightarrow a} f(x) = 0$; $\lim_{x \rightarrow a} g(x) = 0$ (or) $\lim_{x \rightarrow a} f(x) = \pm\infty$; $\lim_{x \rightarrow a} g(x) = \pm\infty$ then, it may reduce to a form $(0/0)$ or (∞/∞) . In such cases, the following equations hold good:

$$\lim_{x \rightarrow 0} \frac{f(x)}{g(x)} = \lim_{x \rightarrow 0} \frac{f'(x)}{g'(x)} \text{ if the limit of RHS exists. For example,}$$

$$\lim_{x \rightarrow 0} \frac{e^x - 1}{x^2 + x} = \lim_{x \rightarrow 0} \frac{\frac{d}{dx}(e^x - 1)}{\frac{d}{dx}(x^2 + x)} = \lim_{x \rightarrow 0} \frac{e^x}{(2x + 1)} = 1$$

L'Hospital rule uses derivatives to evaluate the limits involving indeterminate forms. It states that for indeterminate functions (or forms), where the unity tends to a form $(0/0)$ or (∞/∞) , the limit of that form is equal to the limit of the derivatives. L'Hospital rule may be applied as many times until the function does not reduce the form $(0/0)$ or (∞/∞) .

Now, let us consider Eqs. (4.58a–4.58b). As (α_i) approaches zero, both $\left[\frac{f(\alpha_i)}{g(\alpha_i)} \right]$ approaches zero. Then, one can apply the L'Hospital rule as explained earlier, which will yield the following results:

$$r_i @ \varphi_i=0 = 4 \quad (4.59a)$$

$$c_i @ \varphi_i=0 = 0.5 \quad (4.59b)$$

Hence, at zero axial loads, the stiffness coefficients reduce to the conventional carryover factors of the beam.

Substituting Eq. (4.58a–4.58b) into Eq. (4.57a, 4.57b), we get:

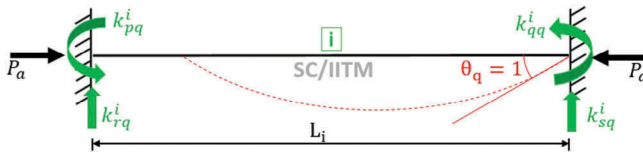
$$k_{pp} = r_i \frac{EI}{L_i} \quad (4.60a)$$

$$k_{qp} = c_i k_{pp} \quad (4.60b)$$

$$k_{rp} = \frac{k_{pp} + k_{qp}}{L_i} = r_i \frac{EI}{L_i^2} (1 + c_i) \quad (4.60c)$$

$$k_{sp} = -k_{rp} \quad (4.60d)$$

By applying unit rotation at the k th end (refer to Fig. 4.24), another set of stiffness coefficients can be derived as follows.

**FIGURE 4.24** Unit rotation at the k th end under axial load.

$$k_{pq} = c_i r_i \frac{EI}{L_i} \quad (4.61a)$$

$$k_{qq} = r_i \frac{EI}{L_i} \quad (4.61b)$$

4.5.3 ROTATION FUNCTIONS UNDER AXIAL TENSILE LOAD

If the beam member is subjected to axial tensile load, then (φ_i) becomes negative. In that case, the following condition holds good:

$$\beta_i = \pi\sqrt{-\varphi_i} = i \pi\sqrt{\varphi_i} = ia_i \quad (4.62)$$

Further,

$$\sin(\beta_i) = \frac{e^{i\beta_i} - e^{-i\beta_i}}{2i} \quad (4.63a)$$

$$\cos(\beta_i) = \frac{e^{i\beta_i} + e^{-i\beta_i}}{2} \quad (4.63b)$$

Substituting Eq. (4.62) into Eq. (4.63), we get:

$$\sin(\beta_i) = \frac{e^{i^2 \alpha_i} - e^{-i^2 \alpha_i}}{2i} = \frac{e^{-\alpha_i} - e^{\alpha_i}}{2i} \quad (4.64a)$$

$$\cos(\beta_i) = \frac{e^{i^2 \alpha_i} + e^{-i^2 \alpha_i}}{2} = \frac{e^{-\alpha_i} + e^{\alpha_i}}{2} \quad (4.64b)$$

Rotation constants at the j th end can be obtained by substituting Eq. (4.64a–4.64b) into Eq. (4.58), along with Eq. (4.62), as given below:

$$r_i = \frac{i a_i \left\{ \left[\frac{e^{-\alpha_i} - e^{\alpha_i}}{2i} \right] - i a_i \left[\frac{e^{-\alpha_i} + e^{\alpha_i}}{2} \right] \right\}}{2 \left[1 - \frac{e^{-\alpha_i} + e^{\alpha_i}}{2} \right] - i a_i \left[\frac{e^{-\alpha_i} - e^{\alpha_i}}{2i} \right]} \quad (4.65a)$$

$$c_i = \frac{i a_i - \left[\frac{e^{-\alpha_i} - e^{\alpha_i}}{2i} \right]}{\frac{e^{-\alpha_i} - e^{\alpha_i}}{2i} - i a_i \left[\frac{e^{-\alpha_i} + e^{\alpha_i}}{2} \right]} \quad (4.65b)$$

The above equations can be further simplified as follows:

$$r_i = \frac{\alpha_i \left\{ \left[\frac{e^{-\alpha_i} - e^{\alpha_i}}{2} \right] + \alpha_i \left[\frac{e^{-\alpha_i} + e^{\alpha_i}}{2} \right] \right\}}{2 \left[1 - \frac{e^{-\alpha_i} + e^{\alpha_i}}{2} \right] - \alpha_i \left[\frac{e^{-\alpha_i} - e^{\alpha_i}}{2} \right]} \quad (4.66a)$$

$$c_i = \frac{\alpha_i + \left[\frac{e^{-\alpha_i} - e^{\alpha_i}}{2} \right]}{- \left[\frac{e^{-\alpha_i} - e^{\alpha_i}}{2} \right] - \alpha_i \left[\frac{e^{-\alpha_i} + e^{\alpha_i}}{2} \right]} \quad (4.66b)$$

Using the following hyperbolic functions as given below:

$$\sinh \alpha_i = \frac{e^{\alpha_i} - e^{-\alpha_i}}{2} \quad (4.67a)$$

$$\cosh \alpha_i = \frac{e^{\alpha_i} + e^{-\alpha_i}}{2} \quad (4.67b)$$

By considering the absolute values of φ_i , Eq. (4.66) will reduce to the following form:

$$r_i = \frac{\alpha_i (\alpha_i \cosh \alpha_i - \sinh \alpha_i)}{2 (1 - \cosh \alpha_i) + \alpha_i \sinh \alpha_i} \quad (4.68a)$$

$$c_i = \frac{\alpha_i - \sinh \alpha_i}{\sinh \alpha_i - \alpha_i \cosh \alpha_i} \quad (4.68b)$$

Rotation constants of the member, under compressive and tensile axial loads, as derived above are plotted for a wide range of values of φ . Table 4.1 also gives these values at closer intervals, which are useful in calculating the critical buckling load. Examples, dealing with the estimate of critical buckling load, are presented in Section 4.11.

4.5.4 TRANSLATION FUNCTION UNDER AXIAL COMPRESSIVE LOAD

Fig. 4.25 shows unit translation at the j th end of the beam under axial compressive load.

By taking moments of all forces about the k th end of the member, we get:

$$P_a (1) - k_{pr} + k_{rr}(L_i) - k_{qr} = 0 \quad (4.69)$$

$$k_{rr} = \frac{P_a (1) - (k_{pr} + k_{qr})}{L_i} \quad (4.70)$$

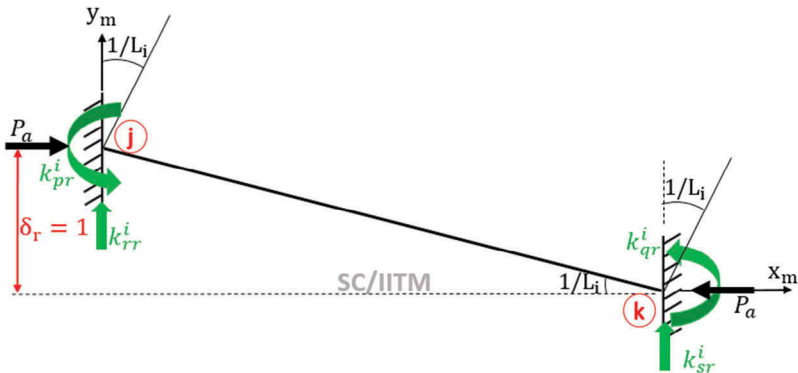


FIGURE 4.25 Unit translation at the j th end of the fixed beam under axial load.

$$k_{sr} = -k_{rr} \quad (4.71)$$

With reference to the Fig. 4.25, the following expressions can be written. Due to the end rotations, we get the end moments as

$$k_{pr} = r_i \left(\frac{EI}{L_i} \right) \left(\frac{1}{L_i} \right) + r_i c_i \left(\frac{EI}{L_i} \right) \left(\frac{1}{L_i} \right) \quad (4.72a)$$

$$k_{qr} = r_i c_i \left(\frac{EI}{L_i} \right) \left(\frac{1}{L_i} \right) + r_i \left(\frac{EI}{L_i} \right) \left(\frac{1}{L_i} \right) \quad (4.72b)$$

$$k_{qr} = k_{pr} = r_i (1 + c_i) \left(\frac{EI}{L_i^2} \right) \quad (4.72c)$$

Substituting Eq. (4.72) into Eq. (4.70), we get the expressions for end shear as

$$k_{rr} = -k_{sr} = 2 r_i (1 + c_i) \left(\frac{EI}{L_i^3} \right) - \frac{P_a}{L_i} \quad (4.73)$$

For zero axial load, the equation for the end shear reduces to the following form:

$$k_{rr} = -k_{sr} = 2 r_i (1 + c_i) \left(\frac{EI}{L_i^3} \right) \quad (4.74)$$

Hence, to make a general form, both in the presence and absence of axial load, the following function holds good to express end shear:

$$k_{rr} = -k_{sr} = t_i \left[2 r_i (1 + c_i) \left(\frac{EI}{L_i^3} \right) \right] \quad (4.75)$$

where t_i is known as the translation function. To obtain the translation function, let us now equate the axial load function as discussed below.

We know the following relationship (Eq. 4.45):

$$P_a = \frac{\pi^2 \varphi_i EI}{L_i^2} \text{ for } n = 1$$

Now equating (4.75) and (4.73), we get:

$$t_i \left[2 r_i (1 + c_i) \left(\frac{EI}{L_i^3} \right) \right] = 2 r_i (1 + c_i) \left(\frac{EI}{L_i^3} \right) - \frac{P_a}{L_i} \quad (4.76)$$

$$t_i = 1 - \left\{ \left[\frac{P_a}{2 r_i (1 + c_i)} \right] \left[\frac{L_i^2}{EI} \right] \right\} \quad (4.77)$$

Substituting for P_a , we get:

$$t_i = 1 - \frac{\pi^2 \varphi_i}{2 r_i (1 + c_i)} \quad (4.78)$$

Similarly, by inducing unit rotation at the k th end of the beam, other coefficients (k_{ps} , k_{qs} , k_{rs} , k_{ss}) will be generated as

$$k_{ps} = k_{rs} = -r_i (1 + c_i) \left(\frac{EI}{L_i^2} \right) \quad (4.79a)$$

$$k_{rs} = -k_{ss} = -2 t_i r_i (1 + c_i) \left(\frac{EI}{L_i^3} \right) \quad (4.79b)$$

By neglecting the axial deformation, member stiffness matrix of a fixed beam under axial load (either compressive or tensile) is given by the following form:

$$[K_i] = EI \begin{bmatrix} \frac{r_i}{L_i} & \frac{c_i r_i}{L_i} & \frac{r_i(1+c_i)}{L_i^2} & -\frac{r_i(1+c_i)}{L_i^2} \\ \frac{c_i r_i}{L_i} & \frac{r_i}{L_i} & \frac{r_i(1+c_i)}{L_i^2} & -\frac{r_i(1+c_i)}{L_i^2} \\ \frac{r_i(1+c_i)}{L_i^2} & \frac{r_i(1+c_i)}{L_i^2} & \frac{2t_i r_i(1+c_i)}{L_i^3} & -\frac{2t_i r_i(1+c_i)}{L_i^3} \\ -\frac{r_i(1+c_i)}{L_i^2} & -\frac{r_i(1+c_i)}{L_i^2} & -\frac{2t_i r_i(1+c_i)}{L_i^3} & \frac{2t_i r_i(1+c_i)}{L_i^3} \end{bmatrix} \quad (4.80)$$

4.6 LATERAL LOAD FUNCTIONS UNDER UNIFORMLY DISTRIBUTED LOAD

In this section, we shall derive the lateral load's functions for the fixed beam loaded under uniformly distributed load, in the presence of the axial load. Consider a fixed beam, loaded as shown in Fig. 4.26. Here, M_p does not refer to the plastic moment of resistance but indicates moment at the j th end under the rotation of θ_p . Alternatively, M_p also refers to the fixed end moment ($F_e M_p$).

Consider the free-body diagram, as shown in Fig. 4.27.

Under the fixed beam subjected to uniformly distributed load, end rotation and shear are developed as shown in the above figures. Following equation holds good:

$$EI \frac{d^2y}{dx^2} = M \quad (\text{for } x < aL_i) \quad (4.81)$$

$$= - \left[M_p - P_a(-y) - P_r(x) + (-w) \frac{x^2}{2} \right] \quad (4.82)$$

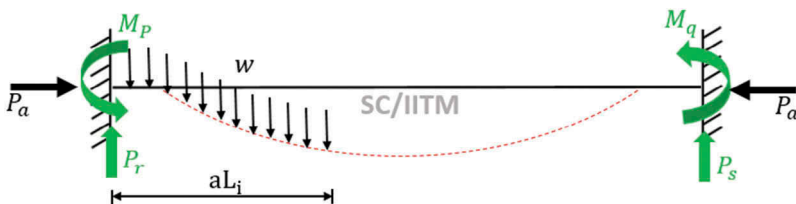


FIGURE 4.26 Fixed beam under uniformly distributed load and axial compressive load.

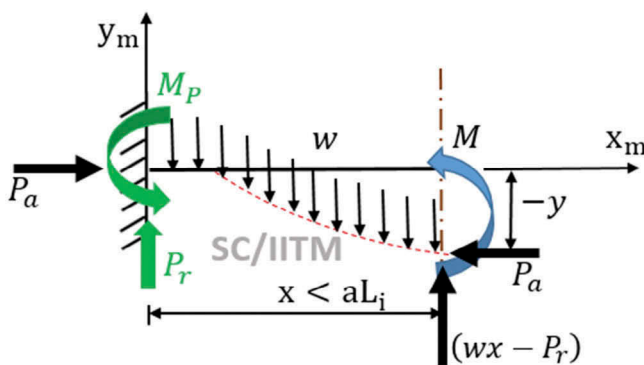


FIGURE 4.27 Free-body diagram ($x < aL_i$).

The general solution to Eq. (4.82) is given as

$$y = A \sin\left(\frac{\alpha_i x}{L_i}\right) + B \cos\left(\frac{\alpha_i x}{L_i}\right) - \frac{L_i^2}{\alpha_i^2 EI} \left[M_p + w \left(\frac{L_i^2}{\alpha_i^2} \right) - \frac{wx}{2} \left(\frac{2P_r}{w} + x \right) \right] \quad (4.83)$$

Differentiating once, we get:

$$\frac{dy}{dx} = \frac{\alpha_i}{L_i} A \cos\left(\frac{\alpha_i x}{L_i}\right) - \frac{\alpha_i}{L_i} B \sin\left(\frac{\alpha_i x}{L_i}\right) + \frac{L_i^2}{\alpha_i^2 EI} (P_r + wx) \quad (4.84)$$

Applying the boundary conditions:

$$@ x = 0, \begin{cases} y = 0 \\ \frac{dy}{dx} = 0 \end{cases} \quad (4.85)$$

$$B = \frac{L_i^2}{\alpha_i^2 EI} \left[M_p + w \left(\frac{L_i^2}{\alpha_i^2} \right) \right] \quad (4.86a)$$

$$A = - \left[\frac{L_i^3}{\alpha_i^3 EI} P_r \right] \quad (4.86b)$$

Substituting Eq. (4.86) into Eq. (4.83), we get:

$$\begin{aligned} \left(\frac{\alpha_i^2 EI}{L_i^2} \right) y &= - \left[\frac{L_i}{\alpha_i} P_r \right] \sin\left(\frac{\alpha_i x}{L_i}\right) + \left[M_p + w \left(\frac{L_i^2}{\alpha_i^2} \right) \right] \cos\left(\frac{\alpha_i x}{L_i}\right) \\ &\quad - M_p - w \left(\frac{L_i^2}{\alpha_i^2} \right) + \frac{wx}{2} \left(\frac{2P_r}{w} + x \right) \text{ for } 0 \leq x \leq aL_i \end{aligned} \quad (4.87a)$$

Substituting Eq. (4.86) into Eq. (4.84), we get:

$$\begin{aligned} \left(\frac{\alpha_i^2 EI}{L_i^2} \right) \frac{dy}{dx} &= - \left(\frac{\alpha_i}{L_i} \right) P_r \cos\left(\frac{\alpha_i x}{L_i}\right) - \frac{\alpha_i}{L_i} \left[M_p + w \left(\frac{L_i^2}{\alpha_i^2} \right) \right] \sin\left(\frac{\alpha_i x}{L_i}\right) \\ &\quad + (P_r + wx) \text{ for } 0 \leq x \leq aL_i \end{aligned} \quad (4.87b)$$

For the position of the uniformly distributed load ($x > aL_i$), Eq. (4.82–4.83) reduces to the following form (refer Fig. 4.28):

$$EI \frac{d^2y}{dx^2} = M = - \left[M_p - P_a(-y) - P_r(x) + (-waL_i) \left(x - \frac{aL_i}{2} \right) \right] \quad (4.88)$$

The general solution to Eq. (4.88) is given as

$$y = A \sin\left(\frac{\alpha_i x}{L_i}\right) + B \cos\left(\frac{\alpha_i x}{L_i}\right) - \frac{L_i^2}{\alpha_i^2 EI} \left[M_p + \frac{wa^2 L_i^2}{2} - (P_r + waL_i)x \right] \quad (4.89)$$

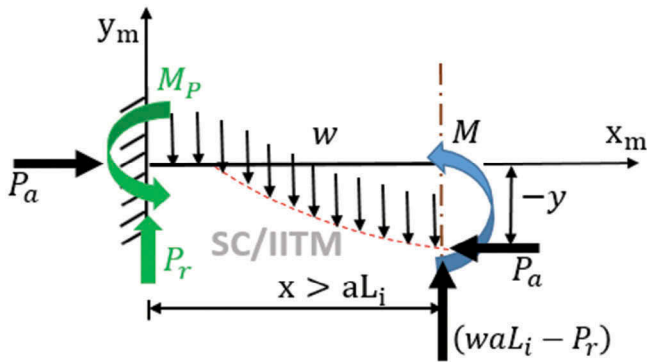


FIGURE 4.28 Free-body diagram ($x > aL_i$).

Differentiating once, we get the following form:

$$\frac{dy}{dx} = \frac{\alpha_i}{L_i} A \cos\left(\frac{\alpha_i x}{L_i}\right) - \frac{\alpha_i}{L_i} B \sin\left(\frac{\alpha_i x}{L_i}\right) + \frac{L_i^2}{\alpha_i^2 EI} (P_r + w a L_i) \quad (4.90)$$

Applying the boundary conditions:

$$@ x = L_i, \begin{cases} y = 0 \\ \frac{dy}{dx} = 0 \end{cases} \quad (4.91)$$

$$A = \frac{L_i^2}{\alpha_i^2 EI} \left[\left(M_p + \frac{w a^2 L_i^2}{2} \right) \sin(\alpha_i) - L_i (P_r + w a L_i) \left(\sin(\alpha_i) + \frac{\cos(\alpha_i)}{\alpha_i} \right) \right] \quad (4.92a)$$

$$B = \frac{L_i^2}{\alpha_i^2 EI} \left[\left(M_p + \frac{w a^2 L_i^2}{2} \right) \cos(\alpha_i) - L_i (P_r + w a L_i) \left(\cos(\alpha_i) - \frac{\sin(\alpha_i)}{\alpha_i} \right) \right] \quad (4.92b)$$

Substituting the above constants in Eq. (4.89, 4.90), we get:

$$\begin{aligned} \frac{\alpha_i^2 EI}{L_i^2} y = & \left[\left(M_p + \frac{w a^2 L_i^2}{2} \right) \sin(\alpha_i) - L_i (P_r + w a L_i) \left(\sin(\alpha_i) + \frac{\cos(\alpha_i)}{\alpha_i} \right) \right] \sin\left(\frac{\alpha_i x}{L_i}\right) \\ & + \left[\left(M_p + \frac{w a^2 L_i^2}{2} \right) \cos(\alpha_i) - L_i (P_r + w a L_i) \left(\cos(\alpha_i) - \frac{\sin(\alpha_i)}{\alpha_i} \right) \right] \cos\left(\frac{\alpha_i x}{L_i}\right) \\ & - \left[M_p + \frac{w a^2 L_i^2}{2} - (P_r + w a L_i)x \right] \text{ for } aL_i \leq x \leq L_i \end{aligned} \quad (4.93a)$$

$$\begin{aligned} \frac{\alpha_i^2 EI dy}{L_i^2 dx} = & \frac{\alpha_i}{L_i} \left[\left(M_p + \frac{w\alpha^2 L_i^2}{2} \right) \sin(\alpha_i) - L_i(P_r + waL_i) \left(\sin(\alpha_i) + \frac{\cos(\alpha_i)}{\alpha_i} \right) \right] \cos\left(\frac{\alpha_i x}{L_i}\right) \\ & - \frac{\alpha_i}{L_i} \left[\left(M_p + \frac{w\alpha^2 L_i^2}{2} \right) \cos(\alpha_i) - L_i(P_r + waL_i) \left(\cos(\alpha_i) - \frac{\sin(\alpha_i)}{\alpha_i} \right) \right] \sin\left(\frac{\alpha_i x}{L_i}\right) \\ & + (P_r + waL_i) \text{ for } aL_i \leq x \leq L_i \end{aligned} \quad (4.93b)$$

Now, for equating the displacement function (y) of both the segment lengths, one needs to equate Eq. (4.87a) and Eq. (4.93a). For equating the slope function (dy/dx) of both the segment lengths, one needs to equate Eq. (4.87b) and Eq. (4.93b). Equating as above and simplifying, we get the following:

$$P_r = waL_i \left(\frac{a}{2} - 1 \right) + \frac{M_p + M_q}{L_i} \quad (4.94a)$$

$$\begin{aligned} M_p = & -wL_i^2 \left\{ \left[\frac{\frac{a^2}{2}(1 - \cos(\alpha_i)) + \left(\frac{\sin(a\alpha_i)}{\alpha_i} - a \right) \left(\frac{\sin(\alpha_i)}{\alpha_i} - \cos(\alpha_i) \right)}{2(1 - \cos(\alpha_i)) - \alpha_i \sin(\alpha_i)} \right] \right. \\ & \left. + \left[\frac{\frac{1-\cos(a\alpha_i)}{\alpha_i} \left[\frac{1-\cos(\alpha_i)}{\alpha_i} - \sin(\alpha_i) \right]}{2(1 - \cos(\alpha_i)) - \alpha_i \sin(\alpha_i)} \right] \right\} \end{aligned} \quad (4.94b)$$

$$\begin{aligned} M_q = & wL_i^2 \left\{ \left[\frac{a\left(1 - \frac{a}{2}\right)(1 - \cos(\alpha_i)) + \left(\frac{\sin(a\alpha_i)}{\alpha_i} - a \right) \left(\frac{\sin(\alpha_i)}{\alpha_i} - \cos(\alpha_i) \right)}{2(1 - \cos(\alpha_i)) - \alpha_i \sin(\alpha_i)} \right] \right. \\ & \left. + \left[\frac{\frac{1-\cos(\alpha_i)}{\alpha_i} \left[\frac{1-\cos(a\alpha_i)}{\alpha_i} - \sin(a\alpha_i) \right]}{2(1 - \cos(\alpha_i)) - \alpha_i \sin(\alpha_i)} \right] \right\} \end{aligned} \quad (4.94c)$$

For the case of *zero axial loads*, one should apply L'Hospital rule to Eqs. (4.94), to obtain the following results:

$$M_p = -wa^2 L_i^2 \left(\frac{1}{2} - \frac{2}{3}a + \frac{1}{4}a^2 \right) \quad (4.95a)$$

$$M_q = wa^2 L_i^2 \left(\frac{1}{3} - \frac{1}{4}a \right) \quad (4.95b)$$

For the uniformly distributed load applied to the complete span of the beam, end moments shall take the following form:

$$M_p = -M_q = \frac{wL_i^2}{\alpha_i^2} \left[1 - \frac{\alpha_i \sin(\alpha_i)}{2(1 - \cos(\alpha_i))} \right] \quad (4.96)$$

Alternatively, they can also be expressed as

$$M_p = -M_q = m_i \frac{wL_i^2}{\alpha_i^2} \quad (4.97a)$$

$$m_i = \frac{12}{\alpha_i^2} \left[1 - \frac{\alpha_i \sin(\alpha_i)}{2(1 - \cos(\alpha_i))} \right] \quad (4.97b)$$

where m_i is termed as load function, which is to be multiplied to the end moments of a fixed beam under uniformly distributed load acting over the entire length of the member to account for the effect of the axial load. In the absence of axial compressive load ($\varphi_i = 0$), L'Hospital rule is applied to Eq. (4.96). This reduces to the following form, which is a standard expression for a fixed beam under uniformly distributed load acting upon its entire length.

$$(M_p)_{\text{@ } \varphi_i=0} = -(M_q)_{\text{@ } \varphi_i=0} = -\frac{wL_i^2}{12} \quad (4.98)$$

4.7 FIXED BEAM UNDER TENSILE AXIAL LOAD

Under tensile axial loads, the load function and end moments will take a different form. For a special case where (φ_i) is negative, Eq. (4.94b, 4.94c) will reduce to the following form. For details, refer to Section 4.8.3.

$$M_q = wL_i^2 \left\{ \left[\frac{\frac{a^2}{2}(1 - \cosh(\alpha_i)) + \left(\frac{\sinh(a\alpha_i)}{\alpha_i} - a \right) \left(\frac{\sinh(\alpha_i)}{\alpha_i} - \cosh(\alpha_i) \right)}{2(1 - \cosh(\alpha_i)) - \alpha_i \sinh(\alpha_i)} \right] - \left[\frac{\frac{1-\cosh(a\alpha_i)}{\alpha_i} \left[\frac{1-\cosh(\alpha_i)}{\alpha_i} - \sinh(a\alpha_i) \right]}{2(1 - \cosh(\alpha_i)) - \alpha_i \sinh(\alpha_i)} \right] \right\} \quad (4.99a)$$

$$M_q = wL_i^2 \left\{ \left[\frac{a(1 - \frac{a}{2})(1 - \cosh(\alpha_i)) + \left(\frac{\sinh(a\alpha_i)}{\alpha_i} - a \right) \left(\frac{\sinh(\alpha_i)}{\alpha_i} - \cosh(\alpha_i) \right)}{2(1 - \cosh(\alpha_i)) - \alpha_i \sinh(\alpha_i)} \right] - \left[\frac{\frac{1-\cosh(\alpha_i)}{\alpha_i} \left[\frac{1-\cosh(a\alpha_i)}{\alpha_i} - \sinh(a\alpha_i) \right]}{2(1 - \cosh(\alpha_i)) - \alpha_i \sinh(\alpha_i)} \right] \right\} \quad (4.99b)$$

For the uniformly distributed load applied to the complete span of the beam and in the presence of tensile axial load, end moments shall take the following form:

$$M_p = -M_q = \frac{wL_i^2}{\alpha_i^2} \left[1 + \frac{\alpha_i \sinh(\alpha_i)}{2(1 - \cosh(\alpha_i))} \right] \quad (4.100)$$

Alternatively, they can also be expressed as

$$M_p = -M_q = m_i \frac{wL_i^2}{\alpha_i^2} \quad (4.101a)$$

$$m_i = -\frac{12}{\alpha_i^2} \left[1 - \frac{\alpha_i \sinh(\alpha_i)}{2(1 - \cosh(\alpha_i))} \right] \quad (4.101b)$$

4.8 LATERAL LOAD FUNCTIONS FOR CONCENTRATED LOAD

In this section, we shall derive the lateral load's functions for the fixed beam loaded under concentrated load, in the presence of the axial load. Consider a fixed beam, loaded as shown in Fig. 4.29.

Consider the free-body diagram, where ($x < aL_i$), as shown in Fig. 4.30.

Under the fixed beam subjected to concentrated load, end rotations and shear are developed as shown in the above figures. Following equation holds good:

$$EI \frac{d^2y}{dx^2} = M \quad (\text{for } x < aL_i) \quad (4.102)$$

$$= -[M_p - P_a(-y) - P_r(x)] \quad (4.103)$$

The general solution to Eq. (4.103) is given as

$$y = A \sin\left(\frac{\alpha_i x}{L_i}\right) + B \cos\left(\frac{\alpha_i x}{L_i}\right) - \frac{L_i^2}{\alpha_i^2 EI} [M_p - P_r(x)] \quad (4.104)$$

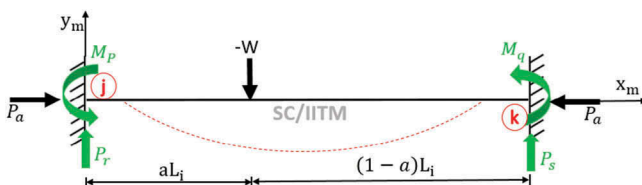


FIGURE 4.29 Fixed beam under concentrated load and axial compressive load.

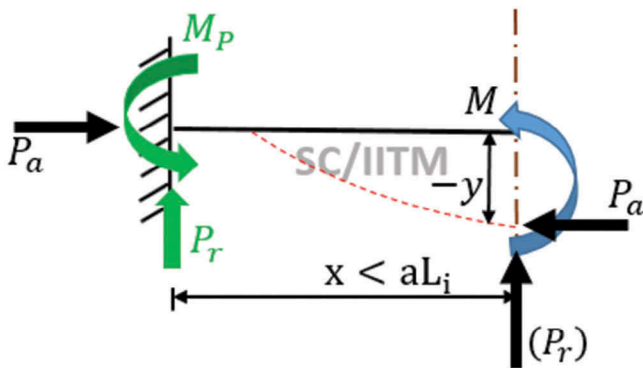


FIGURE 4.30 Free-body diagram ($x < aL_i$).

Differentiating once, we get:

$$\frac{dy}{dx} = \frac{\alpha_i}{L_i} A \cos\left(\frac{\alpha_i x}{L_i}\right) - \frac{\alpha_i}{L_i} B \sin\left(\frac{\alpha_i x}{L_i}\right) + \frac{L_i^2}{\alpha_i^2 EI} (P_r) \quad (4.105)$$

Applying the boundary conditions:

$$@ x = 0, \begin{cases} y = 0 \\ \frac{dy}{dx} = 0 \end{cases} \quad (4.106)$$

$$B = \frac{L_i^2}{\alpha_i^2 EI} [M_p] \quad (4.107a)$$

$$A = - \left[\frac{L_i^3}{\alpha_i^3 EI} P_r \right] \quad (4.107b)$$

Substituting Eq. (4.107) into Eq. (4.104), we get:

$$\left(\frac{\alpha_i^2 EI}{L_i^2} \right) y = - \left[\frac{L_i}{\alpha_i} P_r \right] \sin\left(\frac{\alpha_i x}{L_i}\right) + M_p \cos\left(\frac{\alpha_i x}{L_i}\right) - [M_p - P_r(x)] \text{ for } 0 \leq x \leq aL_i \quad (4.108a)$$

Substituting Eq. (4.107) into Eq. (4.105), we get:

$$\left(\frac{\alpha_i^2 EI}{L_i^2} \right) \frac{dy}{dx} = - \left(\frac{\alpha_i}{L_i} \right) P_r \cos\left(\frac{\alpha_i x}{L_i}\right) - \frac{\alpha_i}{L_i} [M_p] \sin\left(\frac{\alpha_i x}{L_i}\right) + P_r \text{ for } 0 \leq x \leq aL_i \quad (4.108b)$$

For the position of the concentrated load ($x > aL_i$), Eq. (4.102) reduces to the following form (refer Fig. 4.31):

$$EI \frac{d^2y}{dx^2} = M = -[M_p - P_a(-y) - P_r(x) + (-W)(x - aL_i)] \quad (4.109)$$

The general solution to Eq. (4.109) is given as

$$y = A \sin\left(\frac{\alpha_i x}{L_i}\right) + B \cos\left(\frac{\alpha_i x}{L_i}\right) - \frac{L_i^2}{\alpha_i^2 EI} [M_p + WaL_i - (P_r + W)x] \quad (4.110a)$$

Differentiating once, we get the following form:

$$\frac{dy}{dx} = \frac{\alpha_i}{L_i} A \cos\left(\frac{\alpha_i x}{L_i}\right) - \frac{\alpha_i}{L_i} B \sin\left(\frac{\alpha_i x}{L_i}\right) + \frac{L_i^2}{\alpha_i^2 EI} (P_r + W) \quad (4.110b)$$

Equating the expressions for deflection and slope for two segments (aL_i) and $(1 - a)L_i$, we can evaluate the constants. Now, equating Eq. (4.108a) and Eq. (4.110a) for the deflection, and Eq. (4.108b) and Eq. (4.110b) for the slope, respectively, we get the following:

$$A = -\frac{L_i^3}{\alpha_i^3 EI} [P_r + W \cos(a\alpha_i)] \quad (4.111a)$$

$$B = \frac{L_i^2}{\alpha_i^2 EI} \left[M_p + \frac{L_i W}{\alpha_i} \sin(a\alpha_i) \right] \quad (4.111b)$$

Substituting the above constants in Eqs. (4.110a and 4.110b), we get:

$$\begin{aligned} \frac{\alpha_i^2 EI}{L_i^2} y = & -\frac{L_i}{\alpha_i} [P_r + W \cos(a\alpha_i)] \sin\left(\frac{\alpha_i x}{L_i}\right) + \left[M_p + \frac{L_i W}{\alpha_i} \sin(a\alpha_i) \right] \cos\left(\frac{\alpha_i x}{L_i}\right) \\ & - [M_p + WaL_i - (P_r + W)x] \text{ for } aL_i \leq x \leq L_i \end{aligned} \quad (4.112a)$$

$$\begin{aligned} \frac{\alpha_i^2 EI}{L_i^2} \frac{dy}{dx} = & -[P_r + W \cos(a\alpha_i)] \cos\left(\frac{\alpha_i x}{L_i}\right) - \frac{\alpha_i}{L_i} \left[M_p + \frac{L_i W}{\alpha_i} \sin(a\alpha_i) \right] \sin\left(\frac{\alpha_i x}{L_i}\right) \\ & + [P_r + W] \text{ for } aL_i \leq x \leq L_i \end{aligned} \quad (4.112b)$$

Applying the following boundary conditions:

$$@ x = L, \begin{cases} y = 0 \\ \frac{dy}{dx} = 0 \end{cases} \quad (4.113)$$

Eliminating P_r from Eq. (4.112a) and Eq. (4.112b) after applying the above boundary conditions, end moment assumes the following form:

$$M_p = -W L_i \left\{ \left\{ \frac{\left[a(1 - \cos(\alpha_i)) \right] - \left[(1 - \cos(aa_i)) \sin\left(\frac{\alpha_i x}{L_i}\right) \right] - \cos(\alpha_i)}{2 (1 - \cos(\alpha_i)) - \alpha_i \sin(\alpha_i)} \right\} + \left\{ \frac{\left[\frac{1-\cos(\alpha_i)}{\alpha_i} - \sin(\alpha_i) \right] \sin(aa_i)}{2 (1 - \cos(\alpha_i)) - \alpha_i \sin(\alpha_i)} \right\} \right\} \quad (4.114)$$

For the case of zero axial loads, one can estimate the end moment by applying L'Hospital rule.

$$M_p = WaL_i(a^2 - 1) \quad (4.115)$$

Under tensile axial loads, which is a special case where (φ_i) is negative, Eq. (4.115) will reduce to the following form:

$$M_p = -WL_i \left\{ \left[\frac{a (1 - \cos h(\alpha_i)) - (1 - \coth(aa_i)) \left(\frac{\sinh(\alpha_i)}{\alpha_i} - \cosh(\alpha_i) \right)}{2 (1 - \cosh(\alpha_i)) + \alpha_i \sinh(\alpha_i)} \right] + \left[\frac{\left(\frac{1-\cosh(\alpha_i)}{\alpha_i} + \sinh(\alpha_i) \right) \sinh(aa_i)}{2 (1 - \cosh(\alpha_i)) + \alpha_i \sinh(\alpha_i)} \right] \right\} \quad (4.116)$$

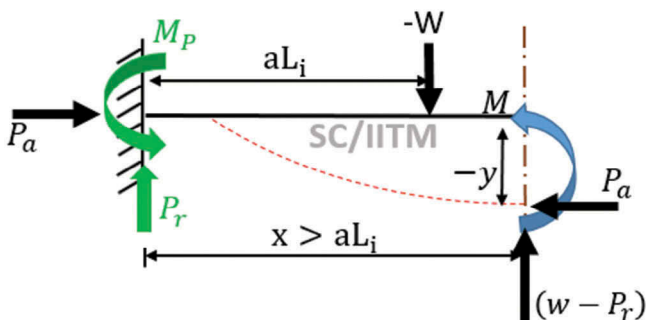
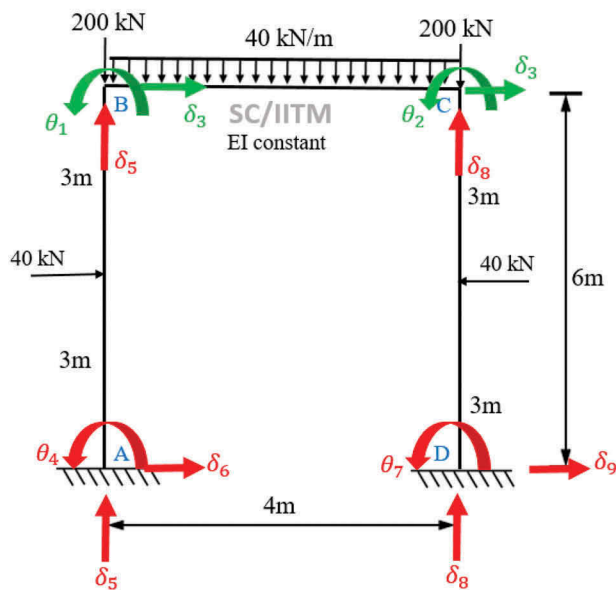
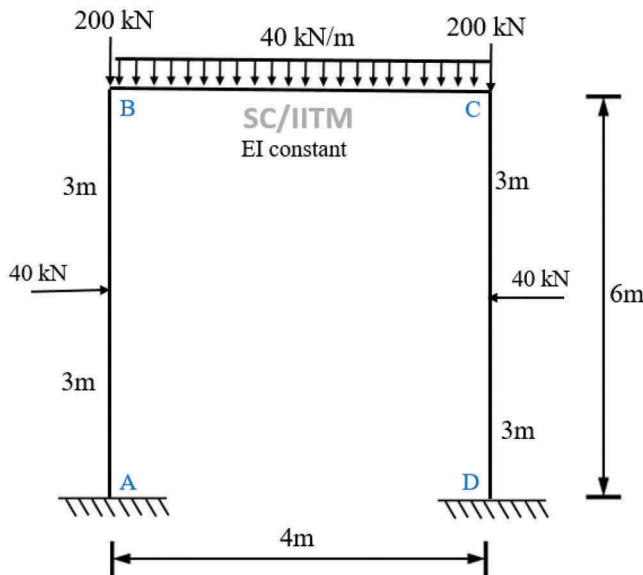


FIGURE 4.31 Free-body diagram ($x > aL_i$).

4.9 EXERCISE PROBLEMS ON STABILITY ANALYSIS



MATLAB® program (without axial load)

```

%% This MATLAB® code is for analysis of structures without considering
axial load
% Re-type the following code in MATLAB® new script and run the file to get the
output.
%% Input
clc;
clear;
n = 3; % number of members
I = [1 1 1]*8.333e-6; %Moment of inertia in m4
E = [1 1 1]*2.1e11; % Young's modulus
L = [6 4 6]; % length in m
uu = 3; % Number of unrestrained degrees of freedom
ur = 6; % Number of restrained degrees of freedom
uul = [1 2 3]; % global labels of unrestrained dof
url = [4 5 6 7 8 9]; % global labels of restrained dof
l1 = [1 4 3 6]; % Global labels for member 1
l2 = [1 2 5 8]; % Global labels for member 2
l3 = [2 7 3 9]; % Global labels for member 3
l= [l1; l2; l3];
dof = uu+ur;
Ktotal = zeros (dof);
fem1= [-30 30 -20 -20]; % Local Fixed end moments of member 1
fem2= [53.333 -53.333 280 280]; % Local Fixed end moments of member 2
fem3= [30 -30 20 20]; % Local Fixed end moments of member 3

%% rotation coefficients for each member
rc1 = 4.*E.*I./L;
rc2 = 2.*E.*I./L;

%% stiffness matrix 4 by 4 (axial deformation neglected)
for i = 1:n
    Knew = zeros (dof);
    k1 = [rc1(i); rc2(i); (rc1(i)+rc2(i))/L(i); (-(rc1(i)+rc2(i))/L(i))];
    k2 = [rc2(i); rc1(i); (rc1(i)+rc2(i))/L(i); (-(rc1(i)+rc2(i))/L(i))];
    k3 = [(rc1(i)+rc2(i))/L(i); (rc1(i)+rc2(i))/L(i); (2*(rc1(i)+rc2(i))/
(L(i)^2)); (-2*(rc1(i)+rc2(i))/(L(i)^2))];
    k4 = -k3;
    K = [k1 k2 k3 k4];
    fprintf ('Member Number =');
    disp (i);
    fprintf ('Local Stiffness matrix of member, [K] = \n');
    disp (K);
    for p = 1:4
        for q = 1:4
            Knew((l(i,p)),(l(i,q))) =K(p,q);
        end
    end
    Ktotal = Ktotal + Knew;
    if i == 1
        Kg1=K;
    elseif i == 2
        Kg2 = K;
    end
end

```

```

    else
        Kg3=K;
    end
end
fprintf ('Stiffness Matrix of complete structure, [Ktotal] = \n');
disp (Ktotal);
Kunr = zeros(uu);
for x=1:uu
    for y=1:uu
        Kunr(x,y) = Ktotal(x,y);
    end
end
fprintf ('Unrestrained Stiffness sub-matrix, [Kuu] = \n');
disp (Kunr);
KuuInv= inv(Kunr);
fprintf ('Inverse of Unrestrained Stiffness sub-matrix, [KuuInverse] = \n');
disp (KuuInv);

%% Creation of joint load vector
jl= [-23.333; 23.333; 0; -30; -280; 20; 30; -280; -20];
    % values given in kN or kNm
jlu = jl(1:uu,1); % load vector in unrestrained dof
delu = KuuInv*jlu;
fprintf ('Joint Load vector, [Jl] = \n');
disp (jl');
fprintf ('Unrestrained displacements, [DelU] = \n');
disp (delu');
delr = zeros (ur,1);
del = [delu; delr];
deli= zeros (4,1);
for i = 1:n
    for p = 1:4
        deli(p,1) = del((l(i,p)),1) ;
    end
    if i == 1
        delbar1 = deli;
        mbar1= (Kg1 * delbar1)+fem1';
        fprintf ('Member Number = ');
        disp (i);
        fprintf ('Global displacement matrix [DeltaBar] = \n');
        disp (delbar1');
        fprintf ('Global End moment matrix [MBar] = \n');
        disp (mbar1');
    elseif i == 2
        delbar2 = deli;
        mbar2= (Kg2 * delbar2)+fem2';
        fprintf ('Member Number = ');
        disp (i);
        fprintf ('Global displacement matrix [DeltaBar] = \n');
        disp (delbar2');
        fprintf ('Global End moment matrix [MBar] = \n');
        disp (mbar2');
    else
        delbar3 = deli;
    end
end

```

```

mbar3= (Kg3 * delbar3)+fem3';
fprintf ('Member Number =');
disp (i);
fprintf ('Global displacement matrix [DeltaBar] = \n');
disp (delbar3');
fprintf ('Global End moment matrix [MBar] = \n');
disp (mbar3');
end
end
%% check
mbar = [mbar1'; mbar2'; mbar3'];
jf = zeros(dof,1);
for a=1:n
    for b=1:4 % size of k matrix
        d = l(a,b);
        jfnew = zeros(dof,1);
        jfnew(d,1)=mbar(a,b);
        jf=jf+jfnew;
    end
end
fprintf ('Joint forces = \n');
disp (jf');

```

Output:

```

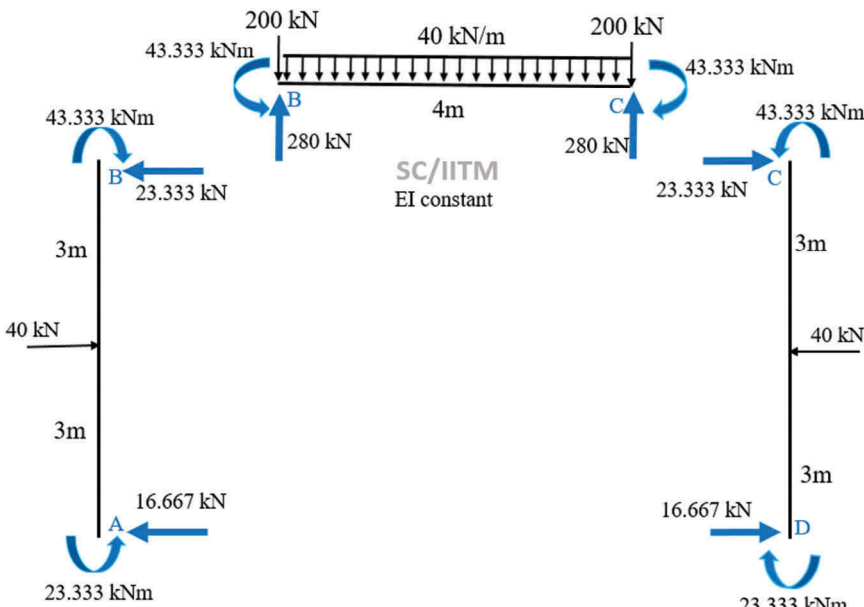
Member Number =      1
Local Stiffness matrix of member, [K] =
 1.0e+06 *
 1.1666   0.5833   0.2917   -0.2917
 0.5833   1.1666   0.2917   -0.2917
 0.2917   0.2917   0.0972   -0.0972
 -0.2917  -0.2917  -0.0972   0.0972
Member Number =      2
Local Stiffness matrix of member, [K] =
 1.0e+06 *
 1.7499   0.8750   0.6562   -0.6562
 0.8750   1.7499   0.6562   -0.6562
 0.6562   0.6562   0.3281   -0.3281
 -0.6562  -0.6562  -0.3281   0.3281
Member Number =      3
Local Stiffness matrix of member, [K] =
 1.0e+06 *
 1.1666   0.5833   0.2917   -0.2917
 0.5833   1.1666   0.2917   -0.2917
 0.2917   0.2917   0.0972   -0.0972
 -0.2917  -0.2917  -0.0972   0.0972
Stiffness Matrix of complete structure, [Ktotal] =
 1.0e+06 *
 2.9166   0.8750   0.2917   0.5833   0.6562  -0.2917       0  -0.6562       0
 0.8750   2.9166   0.2917       0   0.6562       0   0.5833  -0.6562  -0.2917
 0.2917   0.2917   0.1944   0.2917       0  -0.0972   0.2917       0  -0.0972
 0.5833       0   0.2917   1.1666       0  -0.2917       0       0       0
 0.6562   0.6562       0       0   0.3281       0       0  -0.3281       0
 -0.2917       0  -0.0972  -0.2917       0   0.0972       0       0       0
 0       0.5833   0.2917       0       0       0   1.1666       0  -0.2917

```

```

-0.6562 -0.6562      0      0 -0.3281      0      0  0.3281      0
      0 -0.2917 -0.0972      0      0      0 -0.2917      0  0.0972
Unrestrained Stiffness sub-matrix, [Kuu] =
 1.0e+06 *
 2.9166  0.8750  0.2917
 0.8750  2.9166  0.2917
 0.2917  0.2917  0.1944
Inverse of Unrestrained Stiffness sub-matrix, [KuuInverse] =
 1.0e-05 *
 0.0416  -0.0073  -0.0514
 -0.0073  0.0416  -0.0514
 -0.0514  -0.0514  0.6686
Joint Load vector, [J1] =
 -23.3330 23.3330 0 -30.0000 -280.0000 20.0000 30.0000 -280.0000 -20.0000
Unrestrained displacements, [DelU] =
 1.0e-04 *
 -0.1143  0.1143  -0.0000
Member Number = 1
Global displacement matrix [DeltaBar] =
 1.0e-04 *
 -0.1143  0  -0.0000  0
Global End moment matrix [MBar] =
 -43.3331  23.3334  -23.3333  -16.6667
Member Number = 2
Global displacement matrix [DeltaBar] =
 1.0e-04 *
 -0.1143  0.1143  0  0
Global End moment matrix [MBar] =
 43.3331  -43.3331  280.0000  280.0000

```



```

Member Number =      3
Global displacement matrix [DeltaBar] =
  1.Oe-04 *
  0.1143   0   -0.0000   0
Global End moment matrix [MBar] =
  43.3331   -23.3334   23.3333   16.6667
Joint forces =
  0   -0.0000      0  23.3334  280.0000 -16.6667 -23.3334  280.0000 16.6667
>>

```

MATLAB® Program (with axial load)

```

%% This MATLAB® code is for stability analysis of structures, which includes
%% the effect of axial load on the end moments and shear
% Re-type the following code in MATLAB® new script and run the file to get the
% output.
%% Input
clc;
clear;
n = 3; % number of members
I = [1 1 1]*8.333e-6; %Moment of inertia in m4
E = [1 1 1]*2.1e11; % Young's modulus in N/m^2
L = [6 4 6]; % length in m
uu = 3; % Number of unrestrained degrees of freedom
ur = 6; % Number of restrained degrees of freedom
uul = [1 2 3]; % global labels of unrestrained dof
url = [4 5 6 7 8 9]; % global labels of restrained dof
l1 = [1 4 3 6]; % Global labels for member 1
l2 = [1 2 5 8]; % Global labels for member 2
l3 = [2 7 3 9]; % Global labels for member 3
l= [l1; l2; l3];
dof = uu+ur;
Ktotal = zeros (dof);
fem1= [-30 30 -20 -20]; % Local Fixed end moments of member 1
fem2= [53.333 -53.333 280 280]; % Local Fixed end moments of member 2
fem3= [30 -30 20 20]; % Local Fixed end moments of member 3
pa = [280 23.333 280]*1000; %Axial load in N
load = [1 1 1]; % 0-zero load, 1-compression, 2-tension

%% Load and angle calculation
pe = pi*pi.*E.*I./(L.*L); % Euler's load in N
phi = pa./pe;
alrad = pi.*sqrt(phi);
al = radtodeg (alrad);
r = zeros(1,n);
c = zeros(1,n);
t = zeros(1,n);
for i = 1:n
    if load(i)==1
        % rotation coefficients only for compression loads
        r(i) = (alrad(i).*((sind(al(i)))-(alrad(i).*cosd(al(i)))))./((2.*%
        (1-cosd(al(i))))-(alrad(i).*(sind(al(i))))); % rotation function
        c(i) = (alrad(i)-sind(al(i)))./(sind(al(i))-(alrad(i).*cosd(al(i)))); %
        rotation function
        t(i) = 1-((pi*pi*phi(i))./(2.*r(i).* (1+c(i)))); %
    end
end

```

```
% Translation function
elseif load(i)==2
    % rotation coefficients only for tension loads
    r(i)= (alrad(i)*((alrad(i)*cosh(alrad(i)))-sinh(alrad(i))))/((2*
(1-cosh(alrad(i))))+(alrad(i)*sinh(alrad(i))));
    c(i) = (alrad(i)-sinh(alrad(i)))/(sinh(alrad(i))-(alrad(i)*
cosh(alrad(i))));
    t(i) = 1-((pi*pi*(-phi(i)))./(2.*r(i).* (1+c(i))));
else
    r(i) = 4;
    c(i) = 0.5;
    t(i) = 1;
end
end

%% rotation coefficients for each member
rc1 = r.*E.*I./L;
rc2 = c.*E.*I.*r./L;

%% stiffness matrix 4 by 4 (axial deformation neglected)
for i = 1:n
    Knew = zeros (dof);
    k1 = [rc1(i); rc2(i); (rc1(i)+rc2(i))/L(i); (-(rc1(i)+rc2(i))/
L(i))];
    k2 = [rc2(i); rc1(i); (rc1(i)+rc2(i))/L(i); (-(rc1(i)+rc2(i))/
L(i))];
    k3 = [(rc1(i)+rc2(i))/L(i); (rc1(i)+rc2(i))/L(i); (2*t(i)*(rc1(i)
+rc2(i))/(L(i)^2)); (-2*t(i)*(rc1(i)+rc2(i))/(L(i)^2))];
    k4 = -k3;
    K = [k1 k2 k3 k4];
    fprintf ('Member Number =');
    disp (i);
    fprintf ('Local Stiffness matrix of member, [K] = \n');
    disp (K);
    for p = 1:4
        for q = 1:4
            Knew((l(i,p)),(l(i,q))) =K(p,q);
        end
    end
    Ktotal = Ktotal + Knew;
    if i == 1
        Kg1=K;
    elseif i == 2
        Kg2 = K;
    else
        Kg3=K;
    end
end
fprintf ('Stiffness Matrix of complete structure, [Ktotal] = \n');
disp (Ktotal);
Kunr = zeros(uu);
for x=1:uu
    for y=1:uu
        Kunr(x,y)= Ktotal(x,y);
    end
end
```

```

    end
end
fprintf ('Unrestrained Stiffness sub-matix, [Kuu] = \n');
disp (Kunr);
KuuInv= inv(Kunr);
fprintf ('Inverse of Unrestrained Stiffness sub-matix, [KuuInverse] =
\n');
disp (KuuInv);

%% Creation of joint load vector
jl= [-23.333; 23.333; 0; -30; -280; 20; 30; -280; -20]; % values given in kN or
kNm
jlu = jl(1:uu,1); % load vector in unrestrained dof
delu = KuuInv*jlu;
fprintf ('Joint Load vector, [Jl] = \n');
disp (jl');
fprintf ('Unrestrained displacements, [DelU] = \n');
disp (delu');
delr = zeros (ur,1);
del = [delu; delr];
deli= zeros (4,1);
for i = 1:n
    for p = 1:4
        deli(p,1) = del((l(i,p)),1) ;
    end
    if i == 1
        delbar1 = deli;
        mbar1= (Kg1 * delbar1)+fem1';
        fprintf ('Member Number =');
        disp (i);
        fprintf ('Global displacement matrix [DeltaBar] = \n');
        disp (delbar1');
        fprintf ('Global End moment matrix [MBar] = \n');
        disp (mbar1');
    elseif i == 2
        delbar2 = deli;
        mbar2= (Kg2 * delbar2)+fem2';
        fprintf ('Member Number =');
        disp (i);
        fprintf ('Global displacement matrix [DeltaBar] = \n');
        disp (delbar2');
        fprintf ('Global End moment matrix [MBar] = \n');
        disp (mbar2');
    else
        delbar3 = deli;
        mbar3= (Kg3 * delbar3)+fem3';
        fprintf ('Member Number =');
        disp (i);
        fprintf ('Global displacement matrix [DeltaBar] = \n');
        disp (delbar3');
        fprintf ('Global End moment matrix [MBar] = \n');
        disp (mbar3');
    end
end

```

```

%% check
mbar = [mbar1'; mbar2'; mbar3'];
jf = zeros(dof,1);
for a=1:n
    for b=1:4 % size of k matrix
        d = l(a,b);
        jfnew = zeros(dof,1);
        jfnew(d,1)=mbar(a,b);
        jf=jf+jfnew;
    end
end
fprintf ('Joint forces = \n');
disp (jf');

```

Output:

```

Member Number =      1
Local Stiffness matrix of member, [K] =
 1.0e+05 *
  9.2333   6.5121   2.6242  -2.6242
  6.5121   9.2333   2.6242  -2.6242
  2.6242   2.6242   0.4081  -0.4081
 -2.6242  -2.6242  -0.4081   0.4081

Member Number =      2
Local Stiffness matrix of member, [K] =
 1.0e+06 *
  1.7375   0.8781     0.6539  -0.6539
  0.8781   1.7375     0.6539  -0.6539
  0.6539   0.6539     0.3211  -0.3211
 -0.6539  -0.6539    -0.3211   0.3211

Member Number =      3
Local Stiffness matrix of member, [K] =
 1.0e+05 *
  9.2333   6.5121   2.6242  -2.6242
  6.5121   9.2333   2.6242  -2.6242
  2.6242   2.6242   0.4081  -0.4081
 -2.6242  -2.6242  -0.4081   0.4081

Stiffness Matrix of complete structure, [Ktotal] =
 1.0e+06 *
 2.6608   0.8781   0.2624   0.6512   0.6539  -0.2624       0  -0.6539       0
 0.8781   2.6608   0.2624       0   0.6539       0   0.6512  -0.6539  -0.2624
 0.2624   0.2624   0.0816   0.2624       0  -0.0408   0.2624       0  -0.0408
 0.6512       0   0.2624   0.9233       0  -0.2624       0       0       0
 0.6539   0.6539       0       0   0.3211       0       0  -0.3211       0
-0.2624       0  -0.0408  -0.2624       0   0.0408       0       0       0
       0   0.6512   0.2624       0       0   0.9233       0  -0.2624
-0.6539  -0.6539       0       0  -0.3211       0       0   0.3211       0
       0  -0.2624  -0.0408       0       0   0.2624       0   0.0408

Unrestrained Stiffness sub-matix, [Kuu] =
 1.0e+06 *
 2.6608   0.8781   0.2624
 0.8781   2.6608   0.2624
 0.2624   0.2624   0.0816

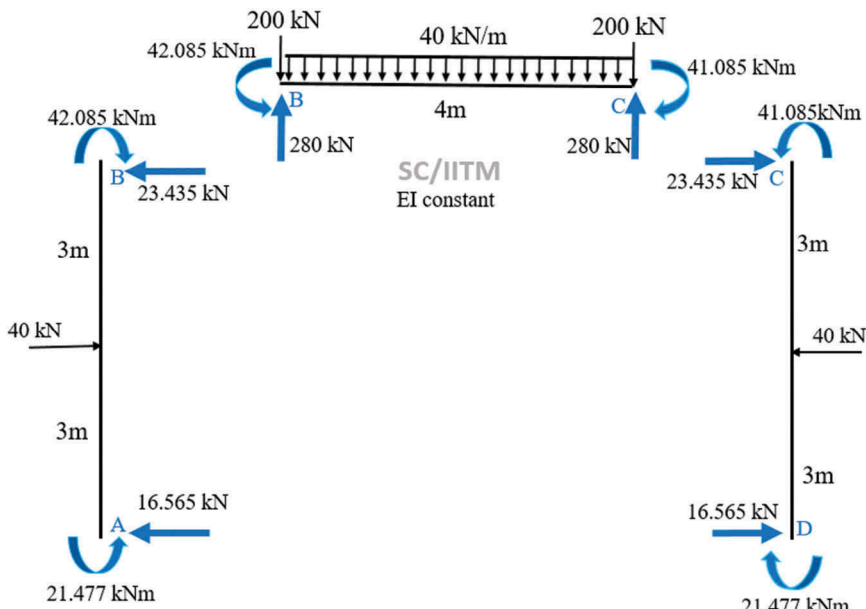
Inverse of Unrestrained Stiffness sub-matix, [KuuInverse] =
 1.0e-04 *

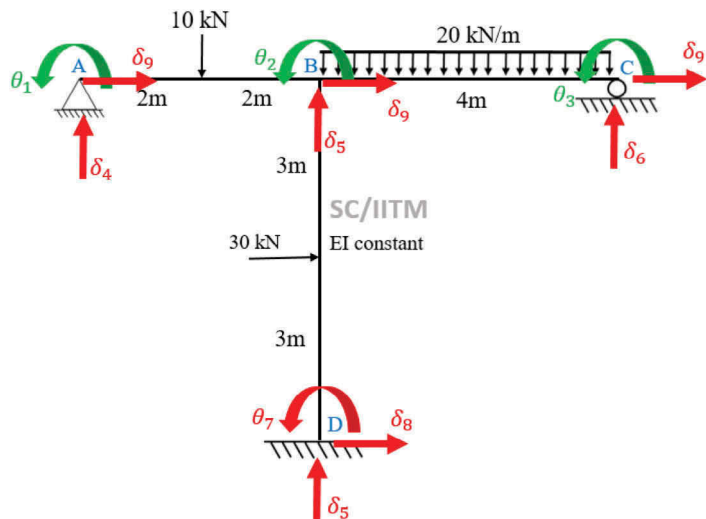
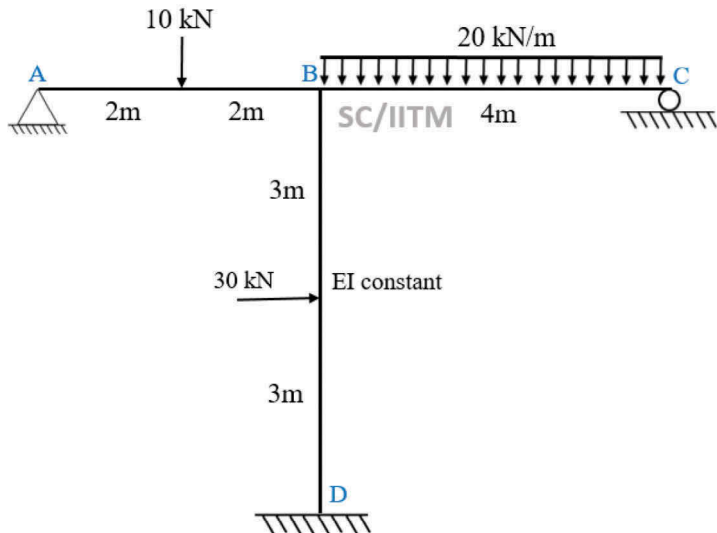
```

```

0.0055 -0.0001 -0.0174
-0.0001 0.0055 -0.0174
-0.0174 -0.0174 0.2342
Joint Load vector, [Jl] =
-23.3330 23.3330 0 -30.0000 -280.0000 20.0000 30.0000 -280.0000 -20.0000
Unrestrained displacements, [DelU] =
1.0e-04 *
-0.1309 0.1309 0
Member Number = 1
Global displacement matrix [DeltaBar] =
1.0e-04 *
-0.1309 0 0 0
Global End moment matrix [MBar] =
-42.0852 21.4765 -23.4348 -16.5652
Member Number = 2
Global displacement matrix [DeltaBar] =
1.0e-04 *
-0.1309 0.1309 0 0
Global End moment matrix [MBar] =
42.0852 -42.0852 280.0000 280.0000
Member Number = 3
Global displacement matrix [DeltaBar] =
1.0e-04 *
0.1309 0 0 0
Global End moment matrix [MBar] =
42.0852 -21.4765 23.4348 16.5652
Joint forces =
0.0000 -0.0000 0 21.4765 280.0000 -16.5652 -
21.4765 280.0000 16.5652
>>

```



Example 2

MATLAB® program input (without axial load)

```
n = 3; % number of members
I = [1 1 1]*8.333e-6; % Moment of inertias in m^4
E = [1 1 1]*2.1e11; % Young's modulus in N/m^2
L = [3 4 6]; % length in m
uu = 3; % Number of unrestrained degrees of freedom
ur = 6; % Number of restrained degrees of freedom
uul = [1 2 3]; % global labels of unrestrained dof
```

```

url = [4 5 6 7 8 9]; % global labels of restrained dof
l1 = [1 2 4 5]; % Global labels for member 1
l2 = [2 3 5 6]; % Global labels for member 2
l3 = [2 7 9 8]; % Global labels for member 3
fem1= [3.75 -3.75 5 5]; % Local Fixed end moments of member 1
fem2= [26.667 -26.667 40 40]; % Local Fixed end moments of member 2
fem3= [-22.5 22.5 -15 -15]; % Local Fixed end moments of member 3
j1= [-3.75; -0.417; 26.667; -5; -45; -40; -22.5; 15; 15]; % values given in kN
or kNm

```

Output:

```

Member Number = 1
Local Stiffness matrix of member, [K] =
1.0e+06 *
2.3332 1.1666 1.1666 -1.1666
1.1666 2.3332 1.1666 -1.1666
1.1666 1.1666 0.7777 -0.7777
-1.1666 -1.1666 -0.7777 0.7777

Member Number = 2
Local Stiffness matrix of member, [K] =
1.0e+06 *
1.7499 0.8750 0.6562 -0.6562
0.8750 1.7499 0.6562 -0.6562
0.6562 0.6562 0.3281 -0.3281
-0.6562 -0.6562 -0.3281 0.3281

Member Number = 3
Local Stiffness matrix of member, [K] =
1.0e+06 *
1.1666 0.5833 0.2917 -0.2917
0.5833 1.1666 0.2917 -0.2917
0.2917 0.2917 0.0972 -0.0972
-0.2917 -0.2917 -0.0972 0.0972

Stiffness Matrix of complete structure, [Ktotal] =
1.0e+06 *
2.3332 1.1666 0 1.1666 -1.1666 0 0 0 0
1.1666 5.2498 0.8750 1.1666 -0.5104 -0.6562 0.5833 -0.2917 0.2917
0 0.8750 1.7499 0 0.6562 -0.6562 0 0 0
1.1666 1.1666 0 0.7777 -0.7777 0 0 0 0
-1.1666 -0.5104 0.6562 -0.7777 1.1059 -0.3281 0 0 0
0 -0.6562 -0.6562 0 -0.3281 0.3281 0 0 0
0 0.5833 0 0 0 0 1.1666 -0.2917 0.2917
0 -0.2917 0 0 0 0 -0.2917 0.0972 -0.0972
0 0.2917 0 0 0 0 0.2917 -0.0972 0.0972

Unrestrained Stiffness sub-matix, [Kuu] =
2333240 1166620 0
1166620 5249790 874965
0 874965 1749930

Inverse of Unrestrained Stiffness sub-matix, [KuuInverse] =
1.0e-06 *
0.4877 -0.1182 0.0591
-0.1182 0.2365 -0.1182
0.0591 -0.1182 0.6306

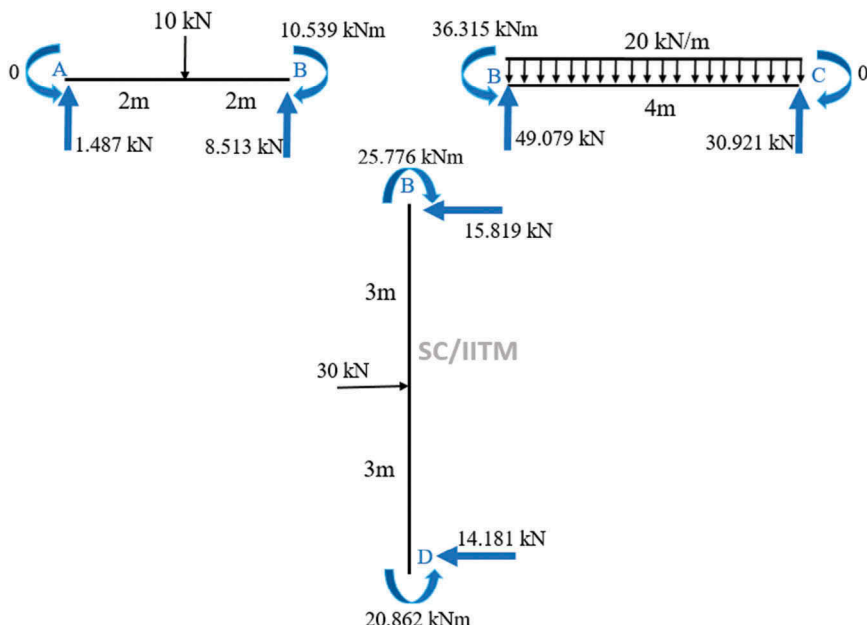
Joint Load vector, [J1] =
-3.7500 -0.4170 26.6670 -5.0000 -45.0000 -40.0000 -22.5000 15.0000 15.0000

```

```

Unrestrained displacements, [DelU] =
 1.0e-04 *
 -0.0020   -0.0281    0.1664
Member Number =  1
Global displacement matrix [DeltaBar] =
 1.0e-05 *
 -0.0203   -0.2808      0        0
Global End moment matrix [MBar] =
 0   -10.5390    1.4870    8.5130
Member Number =  2
Global displacement matrix [DeltaBar] =
 1.0e-04 *
 -0.0281    0.1664      0        0
Global End moment matrix [MBar] =
 36.3150      0   49.0787   30.9213
Member Number =  3
Global displacement matrix [DeltaBar] =
 1.0e-05 *
 -0.2808      0        0        0
Global End moment matrix [MBar] =
 -25.7760   20.8620   -15.8190  -14.1810
Joint forces =
 0  -0.0000      0  1.4870  57.5917  30.9213  20.8620  -14.1810  -15.8190
>>

```



MATLAB® Program additional input (with axial load)

```
pa = [15 15 45]*1000; %Axial load in N
load = [2 1 1]; % 1-compression, 2-tension
```

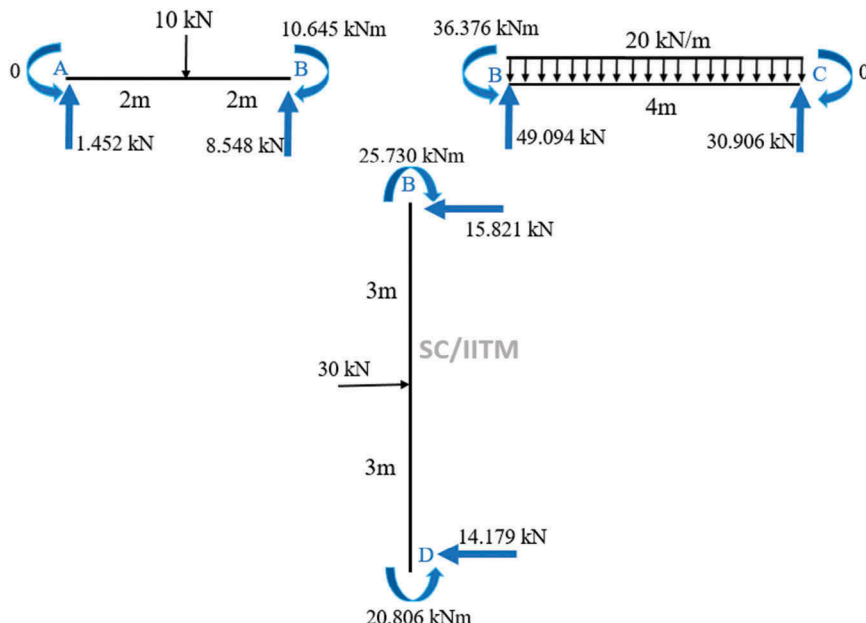
Output:

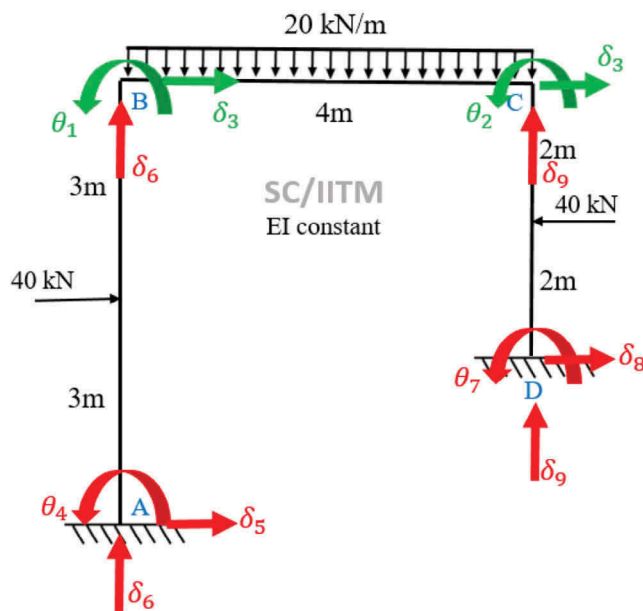
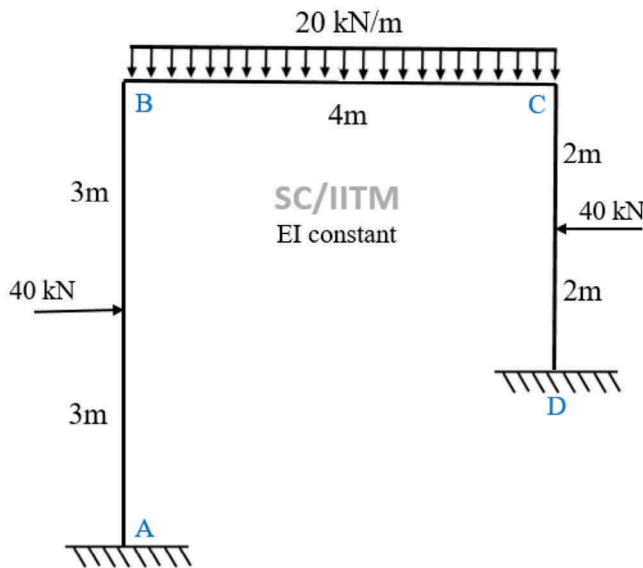
```
Member Number = 1
Local Stiffness matrix of member, [K] =
1.0e+06 *
2.3392  1.1651  1.1681 -1.1681
1.1651  2.3392  1.1681 -1.1681
1.1681  1.1681  0.7837 -0.7837
-1.1681 -1.1681 -0.7837  0.7837
Member Number = 2
Local Stiffness matrix of member, [K] =
1.0e+06 *
1.7419  0.8770  0.6547 -0.6547
0.8770  1.7419  0.6547 -0.6547
0.6547  0.6547  0.3236 -0.3236
-0.6547 -0.6547 -0.3236  0.3236
Member Number = 3
Local Stiffness matrix of member, [K] =
1.0e+06 *
1.1302  0.5926  0.2871 -0.2871
0.5926  1.1302  0.2871 -0.2871
0.2871  0.2871  0.0882 -0.0882
-0.2871 -0.2871 -0.0882  0.0882
Stiffness Matrix of complete structure, [Ktotal] =
1.0e+06 *
2.3392  1.1651      0  1.1681 -1.1681      0      0      0      0
1.1651  5.2113  0.8770  1.1681 -0.5134 -0.6547  0.5926 -0.2871  0.2871
      0  0.8770  1.7419      0  0.6547 -0.6547      0      0      0
1.1681  1.1681      0  0.7837 -0.7837      0      0      0      0
-1.1681 -0.5134  0.6547 -0.7837  1.1074 -0.3236      0      0      0
      0 -0.6547 -0.6547      0 -0.3236  0.3236      0      0      0
      0  0.5926      0      0      0      0  1.1302 -0.2871  0.2871
      0 -0.2871      0      0      0      0 -0.2871  0.0882 -0.0882
      0  0.2871      0      0      0      0  0.2871 -0.0882  0.0882
Unrestrained Stiffness sub-matix, [Kuu] =
1.0e+06 *
2.3392  1.1651      0
1.1651  5.2113  0.8770
      0  0.8770  1.7419
Inverse of Unrestrained Stiffness sub-matix, [KuuInverse] =
1.0e-06 *
0.4867 -0.1189  0.0599
-0.1189  0.2387 -0.1202
  0.0599 -0.1202  0.6346
Joint Load vector, [Jl] =
-3.7500 -0.4170 26.6670 -5.0000 -45.0000 -40.0000 -22.5000 15.0000 15.0000
Unrestrained displacements, [DelU] =
1.0e-04 *
-0.0018 -0.0286    0.1675
```

```

Member Number = 1
Global displacement matrix [DeltaBar] =
1.0e-05 *
-0.0179 -0.2858 0 0
Global End moment matrix [MBar] =
0.0000 -10.6453 1.4516 8.5484
Member Number = 2
Global displacement matrix [DeltaBar] =
1.0e-04 *
-0.0286 0.1675 0 0
Global End moment matrix [MBar] =
36.3757 0 49.0939 30.9061
Member Number = 3
Global displacement matrix [DeltaBar] =
1.0e-05 *
-0.2858 0 0 0
Global End moment matrix [MBar] =
-25.7304 20.8062 -15.8207 -14.1793
Joint forces =
0.0000 0.0000 0 1.4516 57.6423 30.9061 20.8062 -14.1793 -15.8207
>>

```



Example 3

MATLAB® program input (without axial load)

```

n = 3; % number of members
I = [1 1 1]*8.333e-6; %Moment of inertis in m4
E = [1 1 1]*2.1e11; % Young's modulus in N/m^2
L = [6 4 4]; % length in m
uu = 3; % Number of unrestrained degrees of freedom
ur = 6; % Number of restrained degrees of freedom
uul = [1 2 3]; % global labels of unrestrained dof
url = [4 5 6 7 8 9]; % global labels of restrained dof
l1 = [1 4 3 5]; % Global labels for member 1
l2 = [1 2 6 9]; % Global labels for member 2
l3 = [2 7 3 8]; % Global labels for member 3
l= [l1; l2; l3];
dof = uu+ur;
Ktotal = zeros (dof);
fem1= [-30 30 -20 -20]; % Local Fixed end moments of member 1
fem2= [26.667 -26.667 40 40]; % Local Fixed end moments of member 2
fem3= [20 -20 20 20]; % Local Fixed end moments of member 3
jl= [3.333; 6.667; 0; -30; 20; -40; 20; -20; -40]; % values given in kN or
kNm

```

Output:

```

Member Number =      1
Local Stiffness matrix of member, [K] =
1.0e+06 *
 1.1666   0.5833   0.2917   -0.2917
 0.5833   1.1666   0.2917   -0.2917
 0.2917   0.2917   0.0972   -0.0972
 -0.2917  -0.2917  -0.0972   0.0972
Member Number =      2
Local Stiffness matrix of member, [K] =
1.0e+06 *
 1.7499   0.8750   0.6562   -0.6562
 0.8750   1.7499   0.6562   -0.6562
 0.6562   0.6562   0.3281   -0.3281
 -0.6562  -0.6562  -0.3281   0.3281
Member Number =      3
Local Stiffness matrix of member, [K] =
1.0e+06 *
 1.7499   0.8750   0.6562   -0.6562
 0.8750   1.7499   0.6562   -0.6562
 0.6562   0.6562   0.3281   -0.3281
 -0.6562  -0.6562  -0.3281   0.3281
Stiffness Matrix of complete structure, [Ktotal] =
1.0e+06 *
 2.9166   0.8750   0.2917   0.5833  -0.2917   0.6562       0       0   -0.6562
 0.8750   3.4999   0.6562       0       0   0.6562   0.8750  -0.6562  -0.6562
 0.2917   0.6562   0.4253   0.2917  -0.0972       0   0.6562  -0.3281       0
 0.5833       0   0.2917   1.1666  -0.2917       0       0       0       0
 -0.2917       0  -0.0972  -0.2917   0.0972       0       0       0       0
 0.6562   0.6562       0       0       0   0.3281       0       0  -0.3281
       0   0.8750   0.6562       0       0       0   1.7499  -0.6562       0
       0  -0.6562  -0.3281       0       0       0  -0.6562   0.3281       0
 -0.6562  -0.6562       0       0       0  -0.3281       0       0   0.3281

```

Unrestrained Stiffness sub-matrix, [Kuu] =

$$\begin{matrix} 1.0e+06 * & \\ 2.9166 & 0.8750 & 0.2917 \\ 0.8750 & 3.4999 & 0.6562 \\ 0.2917 & 0.6562 & 0.4253 \end{matrix}$$

Inverse of Unrestrained Stiffness sub-matrix, [KuuInverse] =

$$\begin{matrix} 1.0e-05 * & \\ 0.0378 & -0.0065 & -0.0160 \\ -0.0065 & 0.0413 & -0.0593 \\ -0.0160 & -0.0593 & 0.3375 \end{matrix}$$

Joint Load vector, [J1] =

$$\begin{matrix} 3.3330 & 6.6670 & 0 & -30.0000 & 20.0000 & -40.0000 & 20.0000 & -20.0000 & -40.0000 \end{matrix}$$

Unrestrained displacements, [DelU] =

$$\begin{matrix} 1.0e-05 * & \\ 0.0830 & 0.2539 & -0.4486 \end{matrix}$$

Member Number = 1
Global displacement matrix [DeltaBar] =

$$\begin{matrix} 1.0e-05 * & \\ 0.0830 & 0 & -0.4486 & 0 \end{matrix}$$

Global End moment matrix [MBar] =

$$\begin{matrix} -30.3402 & 29.1758 & -20.1941 & -19.8059 \end{matrix}$$

Member Number = 2
Global displacement matrix [DeltaBar] =

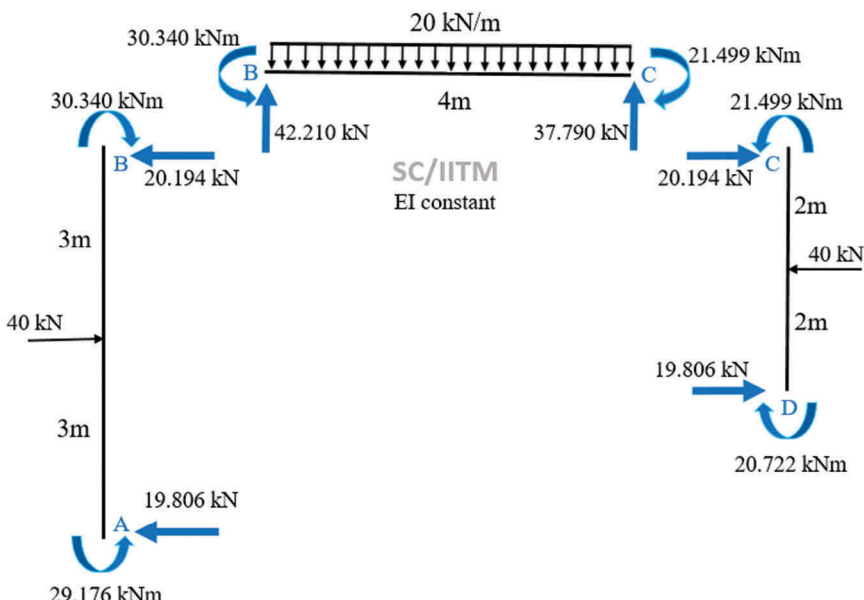
$$\begin{matrix} 1.0e-05 * & \\ 0.0830 & 0.2539 & 0 & 0 \end{matrix}$$

Global End moment matrix [MBar] =

$$\begin{matrix} 30.3402 & -21.4987 & 42.2104 & 37.7896 \end{matrix}$$

Member Number = 3
Global displacement matrix [DeltaBar] =

$$\begin{matrix} 1.0e-05 * & \\ 0.2539 & 0 & -0.4486 & 0 \end{matrix}$$



```

Global End moment matrix [MBar] =
 21.4987 -20.7224 20.1941 19.8059
Joint forces =
 0.0000 0 0.0000 29.1758 -19.8059 42.2104 -20.7224 19.8059 37.7896
>>

```

MATLAB® Program additional input (with axial load)

```

pa = [40 20 40]*1000; %Axial load in N
load = [1 1 1]; % 1-compression, 2-tension

```

Output:

```

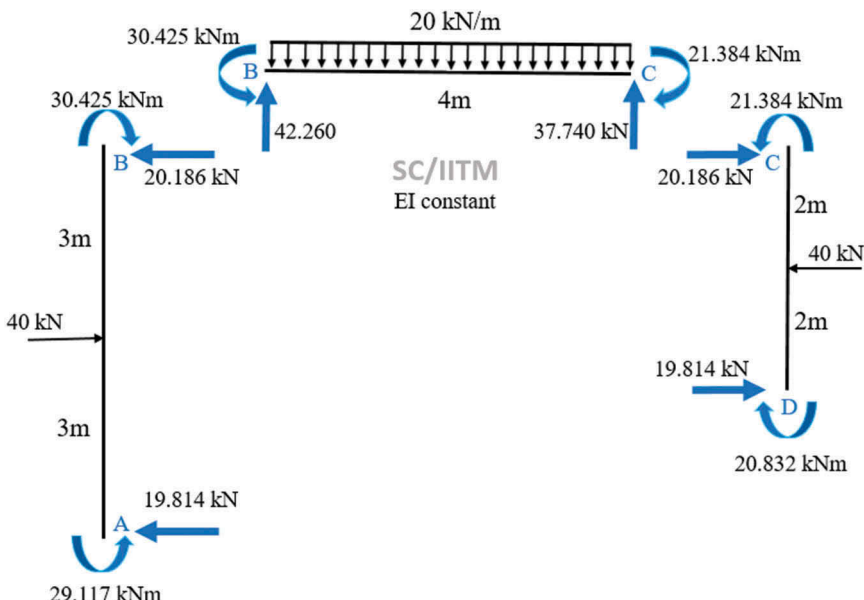
Member Number = 1
Local Stiffness matrix of member, [K] =
 1.0e+06 *
 1.1343 0.5915 0.2876 -0.2876
 0.5915 1.1343 0.2876 -0.2876
 0.2876 0.2876 0.0892 -0.0892
 -0.2876 -0.2876 -0.0892 0.0892
Member Number = 2
Local Stiffness matrix of member, [K] =
 1.0e+06 *
 1.7392 0.8776 0.6542 -0.6542
 0.8776 1.7392 0.6542 -0.6542
 0.6542 0.6542 0.3221 -0.3221
 -0.6542 -0.6542 -0.3221 0.3221
Member Number = 3
Local Stiffness matrix of member, [K] =
 1.0e+06 *
 1.7285 0.8804 0.6522 -0.6522
 0.8804 1.7285 0.6522 -0.6522
 0.6522 0.6522 0.3161 -0.3161
 -0.6522 -0.6522 -0.3161 0.3161
Stiffness Matrix of complete structure, [Ktotal] =
 1.0e+06 *
 2.8735 0.8776 0.2876 0.5915 -0.2876 0.6542 0 0 -0.6542
 0.8776 3.4677 0.6522 0 0 0.6542 0.8804 -0.6522 -0.6542
 0.2876 0.6522 0.4053 0.2876 -0.0892 0 0.6522 -0.3161 0
 0.5915 0 0.2876 1.1343 -0.2876 0 0 0 0
 -0.2876 0 -0.0892 -0.2876 0.0892 0 0 0 0
 0.6542 0.6542 0 0 0.3221 0 0 0 -0.3221
 0 0.8804 0.6522 0 0 0 1.7285 -0.6522 0
 0 -0.6522 -0.3161 0 0 0 -0.6522 0.3161 0
 -0.6542 -0.6542 0 0 0 -0.3221 0 0 0.3221
Unrestrained Stiffness sub-matrix, [Kuu] =
 1.0e+06 *
 2.8735 0.8776 0.2876
 0.8776 3.4677 0.6522
 0.2876 0.6522 0.4053
Inverse of Unrestrained Stiffness sub-matrix, [KuuInverse] =
 1.0e-05 *
 0.0385 -0.0066 -0.0167
 -0.0066 0.0425 -0.0637
 -0.0167 -0.0637 0.3610

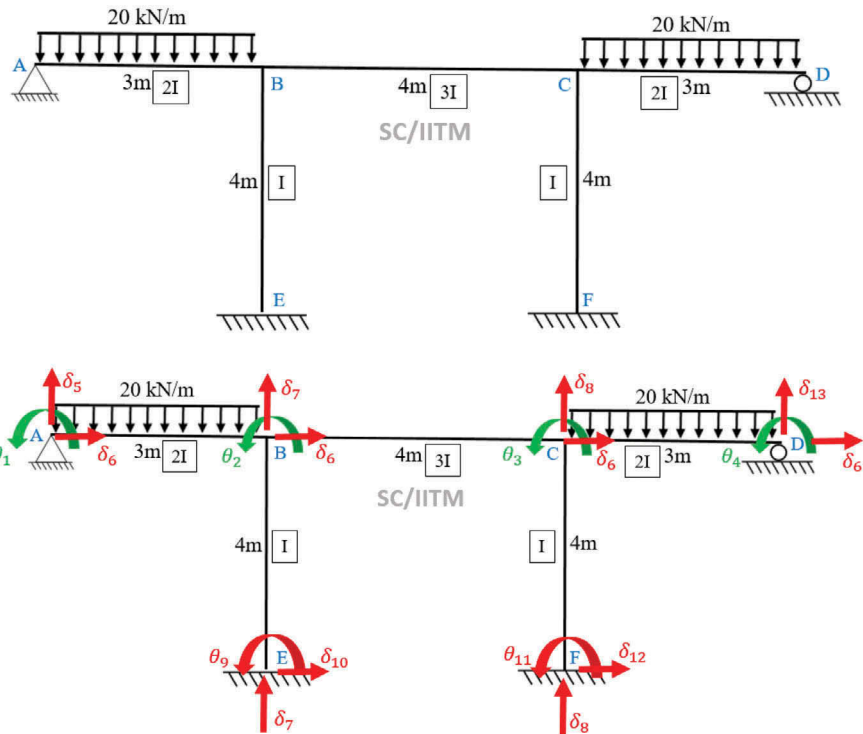
```

```

Joint Load vector, [Jl] =
 3.3330 6.6670 0 -30.0000 20.0000 -40.0000 20.0000 -20.0000 -40.0000
Unrestrained displacements, [DelU] =
 1.0e-05 *
 0.0843 0.2612 -0.4802
Member Number = 1
Global displacement matrix [DeltaBar] =
 1.0e-05 *
 0.0843 0 -0.4802 0
Global End moment matrix [MBar] =
 -30.4254 29.1173 -20.1860 -19.8140
Member Number = 2
Global displacement matrix [DeltaBar] =
 1.0e-05 *
 0.0843 0.2612 0 0
Global End moment matrix [MBar] =
 30.4254 -21.3838 42.2604 37.7396
Member Number = 3
Global displacement matrix [DeltaBar] =
 1.0e-05 *
 0.2612 0 -0.4802 0
Global End moment matrix [MBar] =
 21.3838 -20.8319 20.1860 19.8140
Joint forces =
 0 -0.0000 0 29.1173 -19.8140 42.2604 -20.8319 19.8140 37.7396
>>

```



Example 4

MATLAB® program input (without axial load)

```

n = 5; % number of members
I = [2 3 2 1 1]*8.333e-6; % Moment of inertia in m4
E = [1 1 1 1 1]*2.1e11; % Young's modulus
L = [3 4 3 4 4]; % length in m
uu = 4; % Number of unrestrained degrees of freedom
ur = 9; % Number of restrained degrees of freedom
uul = [1 2 3 4]; % global labels of unrestrained dof
url = [5 6 7 8 9 10 11 12 13]; % global labels of restrained dof
l1 = [1 2 5 7]; % Global labels for member 1
l2 = [2 3 7 8]; % Global labels for member 2
l3 = [3 4 8 13]; % Global labels for member 3
l4 = [2 9 6 10]; % Global labels for member 4
l5 = [3 11 6 12]; % Global labels for member 5
l= [l1; l2; l3; l4; l5];
dof = uu+ur;
Ktotal = zeros (dof,dof);
fem1= [15 -15 30 30]; % Local Fixed end moments of member 1
fem2= [0 0 0 0]; % Local Fixed end moments of member 2
fem3= [15 -15 30 30]; % Local Fixed end moments of member 3
fem4= [0 0 0 0]; % Local Fixed end moments of member 4

```

```
fem5= [0 0 0 0]; % Local Fixed end moments of member 5
jlu = [-15; 15; -15; 15]; % load vector in unrestrained dof
```

Output:

```
Member Number = 1
Local Stiffness matrix of member, [K] =
1.0e+06 *
4.6665  2.3332  2.3332  -2.3332
2.3332  4.6665  2.3332  -2.3332
2.3332  2.3332  1.5555  -1.5555
-2.3332 -2.3332 -1.5555  1.5555

Member Number = 2
Local Stiffness matrix of member, [K] =
1.0e+06 *
5.2498  2.6249  1.9687  -1.9687
2.6249  5.2498  1.9687  -1.9687
1.9687  1.9687  0.9843  -0.9843
-1.9687 -1.9687 -0.9843  0.9843

Member Number = 3
Local Stiffness matrix of member, [K] =
1.0e+06 *
4.6665  2.3332  2.3332  -2.3332
2.3332  4.6665  2.3332  -2.3332
2.3332  2.3332  1.5555  -1.5555
-2.3332 -2.3332 -1.5555  1.5555

Member Number = 4
Local Stiffness matrix of member, [K] =
1.0e+06 *
1.7499  0.8750  0.6562  -0.6562
0.8750  1.7499  0.6562  -0.6562
0.6562  0.6562  0.3281  -0.3281
-0.6562 -0.6562 -0.3281  0.3281

Member Number = 5
Local Stiffness matrix of member, [K] =
1.0e+06 *
1.7499  0.8750  0.6562  -0.6562
0.8750  1.7499  0.6562  -0.6562
0.6562  0.6562  0.3281  -0.3281
-0.6562 -0.6562 -0.3281  0.3281

Stiffness Matrix of complete structure, [Ktotal] =
1.0e+07 *
Columns 1 through 9
0.4666  0.2333    0      0   0.2333    0   -0.2333    0      0
0.2333  1.1666  0.2625    0   0.2333  0.0656 -0.0365 -0.1969  0.0875
      0  0.2625  1.1666  0.2333    0   0.0656  0.1969  0.0365    0
      0      0  0.2333  0.4666    0      0      0      0.2333    0
0.2333  0.2333    0      0   0.1555    0   -0.1555    0      0
      0  0.0656  0.0656    0      0   0.0656    0      0      0.0656
-0.2333 -0.0365  0.1969    0   -0.1555    0   0.2540 -0.0984    0
      0 -0.1969  0.0365  0.2333    0      0   -0.0984  0.2540    0
      0  0.0875    0      0   0.0656    0      0      0.1750
      0 -0.0656    0      0   0 -0.0328    0      0 -0.0656
      0      0  0.0875    0      0   0.0656    0      0      0
      0      0 -0.0656    0      0   0 -0.0328    0      0      0
      0      0 -0.2333 -0.2333    0      0      0 -0.1555    0
```

```

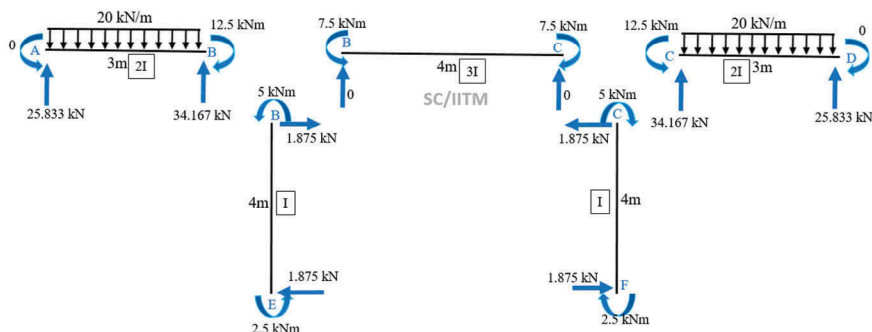
Columns 10 through 13
      0      0      0      0
-0.0656      0      0      0
      0  0.0875 -0.0656 -0.2333
      0      0      0 -0.2333
      0      0      0      0
-0.0328  0.0656 -0.0328      0
      0      0      0      0
      0      0      0 -0.1555
-0.0656      0      0      0
 0.0328      0      0      0
      0  0.1750 -0.0656      0
      0 -0.0656  0.0328      0
      0      0      0  0.1555
Unrestrained Stiffness sub-matrix, [Kuu] =
 4666480    2333240      0      0
 2333240   11666200    2624895      0
      0    2624895   11666200   2333240
      0          0   2333240   4666480
Inverse of Unrestrained Stiffness sub-matrix, [KuuInverse] =
 1.0e-06 *
 0.2397   -0.0508    0.0127   -0.0063
-0.0508    0.1016   -0.0254    0.0127
 0.0127   -0.0254    0.1016   -0.0508
-0.0063    0.0127   -0.0508    0.2397
Unrestrained Joint Load vector, [J1] =
 -15     15    -15     15
Unrestrained displacements, [DelU] =
 1.0e-05 *
 -0.4643    0.2857   -0.2857    0.4643
Member Number = 1
Global displacement matrix [DeltaBar] =
 1.0e-05 *
 -0.4643    0.2857      0      0
Global End moment matrix [MBar] =
 0.0000   -12.5000   25.8333   34.1667
Member Number = 2
Global displacement matrix [DeltaBar] =
 1.0e-05 *
 0.2857   -0.2857      0      0
Global End moment matrix [MBar] =
 7.5000   -7.5000   -0.0000    0.0000
Member Number = 3
Global displacement matrix [DeltaBar] =
 1.0e-05 *
 -0.2857    0.4643      0      0
Global End moment matrix [MBar] =
 12.5000      0   34.1667   25.8333
Member Number = 4
Global displacement matrix [DeltaBar] =
 1.0e-05 *
 0.2857      0      0      0
Global End moment matrix [MBar] =
 5.0000   2.5000   1.8750  -1.8750

```

```

Member Number =      5
Global displacement matrix [DeltaBar] =
  1.0e-05 *
 -0.2857          0          0          0
Global End moment matrix [MBar] =
 -5.0000   -2.5000   -1.8750    1.8750
Joint forces =
 Columns 1 through 9
 0.0000 -0.0000 -0.0000      0 25.8333 -0.0000 34.1667 34.1667 2.5000
 Columns 10 through 13
 -1.8750 -2.5000 1.8750 25.8333
>>

```



MATLAB® program input (with axial load)

```

pa = [1.875 1.875 1.875 34.1667 34.1667]*1000; %Axial load in N
load = [2 1 2 1 1]; % 0-zero load, 1-compression, 2-tension

```

Output:

```

Member Number =      1
Local Stiffness matrix of member, [K] =
  1.0e+06 *
  4.6672   2.3331   2.3334  -2.3334
  2.3331   4.6672   2.3334  -2.3334
  2.3334   2.3334   1.5562  -1.5562
 -2.3334  -2.3334  -1.5562   1.5562
Member Number =      2
Local Stiffness matrix of member, [K] =
  1.0e+06 *
  5.2488   2.6251   1.9685  -1.9685
  2.6251   5.2488   1.9685  -1.9685
  1.9685   1.9685   0.9838  -0.9838
 -1.9685  -1.9685  -0.9838   0.9838
Member Number =      3
Local Stiffness matrix of member, [K] =
  1.0e+06 *
  4.6672   2.3331   2.3334  -2.3334
  2.3331   4.6672   2.3334  -2.3334
  2.3334   2.3334   1.5562  -1.5562
 -2.3334  -2.3334  -1.5562   1.5562

```

```

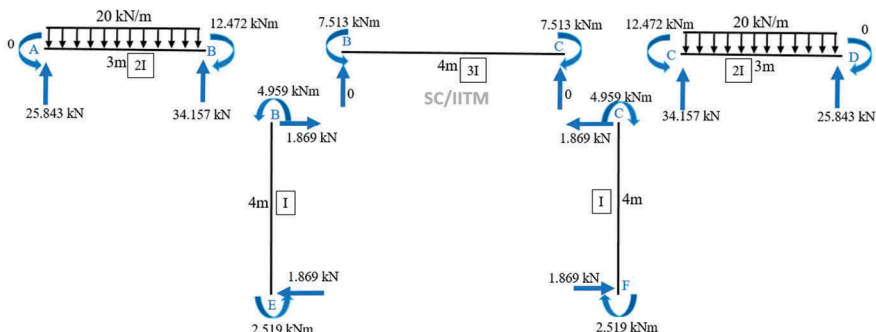
Member Number =      4
Local Stiffness matrix of member, [K] =
  1.0e+06 *
  1.7316   0.8796   0.6528  -0.6528
  0.8796   1.7316   0.6528  -0.6528
  0.6528   0.6528   0.3179  -0.3179
 -0.6528  -0.6528  -0.3179   0.3179
Member Number =      5
Local Stiffness matrix of member, [K] =
  1.0e+06 *
  1.7316   0.8796   0.6528  -0.6528
  0.8796   1.7316   0.6528  -0.6528
  0.6528   0.6528   0.3179  -0.3179
 -0.6528  -0.6528  -0.3179   0.3179
Stiffness Matrix of complete structure, [Ktotal] =
  1.0e+07 *
Columns 1 through 9
  0.4667   0.2333      0       0   0.2333      0   -0.2333      0       0
  0.2333   1.1648   0.2625      0   0.2333   0.0653  -0.0365  -0.1968  0.0880
      0   0.2625   1.1648   0.2333      0   0.0653   0.1968   0.0365      0
      0       0   0.2333   0.4667      0       0       0   0.2333      0
  0.2333   0.2333      0       0   0.1556      0   -0.1556      0       0
      0   0.0653   0.0653      0       0   0.0636      0       0   0.0653
-0.2333  -0.0365   0.1968      0  -0.1556      0   0.2540  -0.0984      0
      0  -0.1968   0.0365   0.2333      0       0  -0.0984   0.2540      0
      0   0.0880      0       0       0   0.0653      0       0   0.1732
      0  -0.0653      0       0       0  -0.0318      0       0  -0.0653
      0       0   0.0880      0       0   0.0653      0       0       0
      0       0  -0.0653      0       0  -0.0318      0       0       0
      0       0  -0.2333  -0.2333      0       0       0  -0.1556      0
Columns 10 through 13
      0       0       0       0
-0.0653      0       0       0
      0   0.0880  -0.0653  -0.2333
      0       0       0  -0.2333
      0       0       0       0
-0.0318   0.0653  -0.0318      0
      0       0       0       0
      0       0       0  -0.1556
-0.0653      0       0       0
  0.0318      0       0       0
      0   0.1732  -0.0653      0
      0  -0.0653   0.0318      0
      0       0       0   0.1556
Unrestrained Stiffness sub-matrix, [Kuu] =
  1.0e+07 *
  0.4667   0.2333      0       0
  0.2333   1.1648   0.2625      0
      0   0.2625   1.1648   0.2333
      0       0   0.2333   0.4667
Inverse of Unrestrained Stiffness sub-matrix, [KuuInverse] =
  1.0e-06 *
  0.2397  -0.0509   0.0127  -0.0064
-0.0509   0.1018  -0.0255   0.0127
  0.0127  -0.0255   0.1018  -0.0509

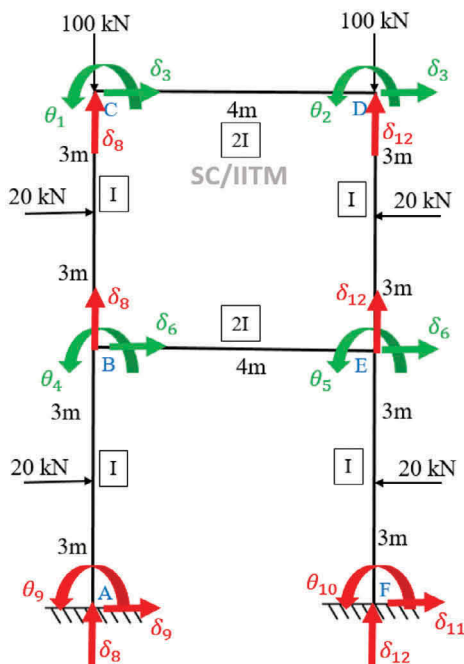
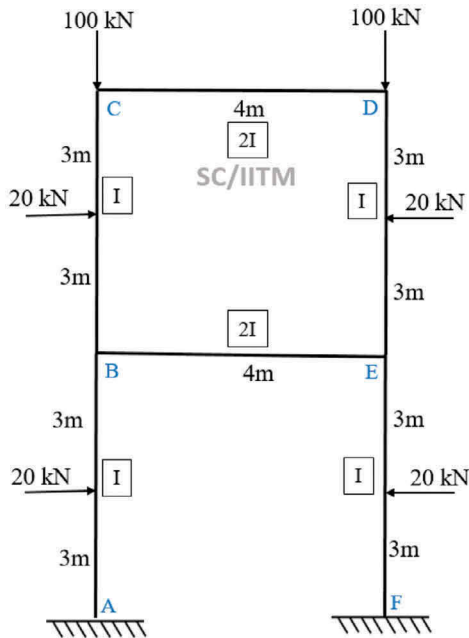
```

```

-0.0064  0.0127 -0.0509  0.2397
Unrestrained Joint Load vector, [J1] =
-15      15      -15      15
Unrestrained displacements, [DelU] =
1.0e-05 *
-0.4645    0.2864   -0.2864    0.4645
Member Number =      1
Global displacement matrix [DeltaBar] =
1.0e-05 *
-0.4645    0.2864        0        0
Global End moment matrix [MBar] =
0     -12.4723   25.8426   34.1574
Member Number =      2
Global displacement matrix [DeltaBar] =
1.0e-05 *
0.2864   -0.2864        0        0
Global End moment matrix [MBar] =
7.5134   -7.5134        0        0
Member Number =      3
Global displacement matrix [DeltaBar] =
1.0e-05 *
-0.2864    0.4645        0        0
Global End moment matrix [MBar] =
12.4723    0.0000   34.1574   25.8426
Member Number =      4
Global displacement matrix [DeltaBar] =
1.0e-05 *
0.2864        0        0        0
Global End moment matrix [MBar] =
4.9589   2.5188   1.8694  -1.8694
Member Number =      5
Global displacement matrix [DeltaBar] =
1.0e-05 *
-0.2864        0        0        0
Global End moment matrix [MBar] =
-4.9589   -2.5188  -1.8694   1.8694
Joint forces =
Columns 1 through 9
0 -0.0000  0.0000  0.0000  25.8426   0  34.1574  34.1574  2.5188
Columns 10 through 13
-1.8694  -2.5188  1.8694  25.8426
>>

```



Example 5

MATLAB® program input (without axial load)

```

n = 6; % number of members
I = [1 1 2 1 1 2]*8.333e-6; %Moment of inertis in m4
E = [1 1 1 1 1 1]*2.1e11; % Young's modulus
L = [3 4 3 4 4 5]; % length in m
uu = 6; % Number of unrestrained degrees of freedom
ur = 6; % Number of restrained degrees of freedom
uul = [1 2 3 4 5 6]; % global labels of unrestrained dof
url = [7 8 9 10 11 12]; % global labels of restained dof
l1 = [4 7 6 9]; % Global labels for member 1
l2 = [1 4 3 6]; % Global labels for member 2
l3 = [1 2 8 12]; % Global labels for member 3
l4 = [2 5 3 6]; % Global labels for member 4
l5 = [5 10 6 11]; % Global labels for member 5
l6 = [4 5 8 12]; % Global labels for member 5
l= [l1; l2; l3; l4; l5; l6];
dof = uu+ur;
Ktotal = zeros (dof);
fem1= [-15 15 -10 -10]; % Local Fixed end moments of member 1
fem2= [-15 15 -10 -10]; % Local Fixed end moments of member 2
fem3= [0 0 100 100]; % Local Fixed end moments of member 3
fem4= [15 -15 10 10]; % Local Fixed end moments of member 4
fem5= [15 -15 10 10]; % Local Fixed end moments of member 5
fem6= [0 0 0 0]; % Local Fixed end moments of member 5
jlu = [15; -15; 0; 0; 0; 0]; % load vector in unrestrained dof

```

Output:

```

Member Number =      1
Local Stiffness matrix of member, [K] =
 1.0e+06 *
 2.3332   1.1666   1.1666  -1.1666
 1.1666   2.3332   1.1666  -1.1666
 1.1666   1.1666   0.7777  -0.7777
 -1.1666  -1.1666  -0.7777   0.7777

Member Number =      2
Local Stiffness matrix of member, [K] =
 1.0e+06 *
 1.7499   0.8750   0.6562  -0.6562
 0.8750   1.7499   0.6562  -0.6562
 0.6562   0.6562   0.3281  -0.3281
 -0.6562  -0.6562  -0.3281   0.3281

Member Number =      3
Local Stiffness matrix of member, [K] =
 1.0e+06 *
 4.6665   2.3332   2.3332  -2.3332
 2.3332   4.6665   2.3332  -2.3332
 2.3332   2.3332   1.5555  -1.5555
 -2.3332  -2.3332  -1.5555   1.5555

Member Number =      4
Local Stiffness matrix of member, [K] =
 1.0e+06 *
 1.7499   0.8750   0.6562  -0.6562
 0.8750   1.7499   0.6562  -0.6562
 0.6562   0.6562   0.3281  -0.3281
 -0.6562  -0.6562  -0.3281   0.3281

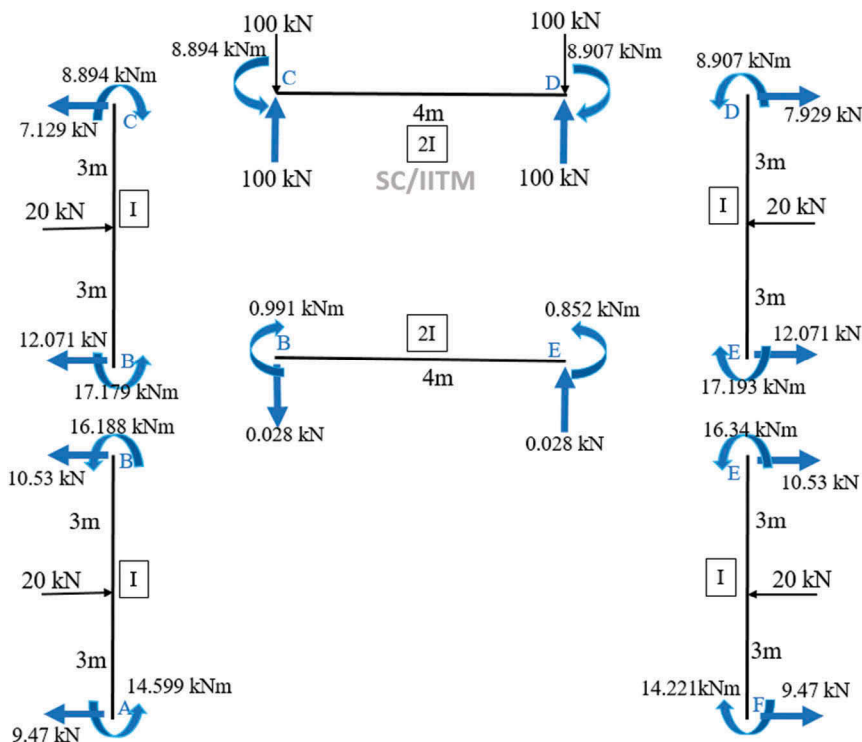
```

```

Member Number =      5
Local Stiffness matrix of member, [K] =
1.0e+06 *
 1.7499  0.8750  0.6562 -0.6562
 0.8750  1.7499  0.6562 -0.6562
 0.6562  0.6562  0.3281 -0.3281
-0.6562 -0.6562 -0.3281  0.3281
Member Number =      6
Local Stiffness matrix of member, [K] =
1.0e+06 *
 2.7999  1.3999  0.8400 -0.8400
 1.3999  2.7999  0.8400 -0.8400
 0.8400  0.8400  0.3360 -0.3360
-0.8400 -0.8400 -0.3360  0.3360
Stiffness Matrix of complete structure, [Ktotal] =
1.0e+06 *
Columns 1 through 9
 6.4164  2.3332  0.6562  0.8750      0 -0.6562      0  2.3332      0
 2.3332  6.4164  0.6562      0  0.8750 -0.6562      0  2.3332      0
 0.6562  0.6562  0.6562  0.6562 -0.6562      0      0      0
 0.8750      0  0.6562  6.8831  1.3999  0.5104  1.1666  0.8400 -1.1666
      0  0.8750  0.6562  1.3999  6.2997      0      0  0.8400      0
-0.6562 -0.6562 -0.6562  0.5104      0  1.7621  1.1666      0 -0.7777
      0      0  0  1.1666      0  1.1666  2.3332      0 -1.1666
 2.3332  2.3332      0  0.8400  0.8400      0      0  1.8915      0
      0      0  0 -1.1666      0 -0.7777 -1.1666      0  0.7777
      0      0  0      0  0.8750  0.6562      0      0      0
      0      0  0      0 -0.6562 -0.3281      0      0      0
-2.3332 -2.3332      0 -0.8400 -0.8400      0      0 -1.8915      0
Columns 10 through 12
      0      0 -2.3332
      0      0 -2.3332
      0      0      0
      0      0 -0.8400
 0.8750 -0.6562 -0.8400
 0.6562 -0.3281      0
      0      0      0
      0      0 -1.8915
      0      0      0
 1.7499 -0.6562      0
-0.6562  0.3281      0
      0      0  1.8915
Unrestrained Stiffness sub-matix, [Kuu] =
1.0e+06 *
 6.4164  2.3332  0.6562  0.8750      0 -0.6562
 2.3332  6.4164  0.6562      0  0.8750 -0.6562
 0.6562  0.6562  0.6562  0.6562  0.6562 -0.6562
 0.8750      0  0.6562  6.8831  1.3999  0.5104
      0  0.8750  0.6562  1.3999  6.2997      0
-0.6562 -0.6562 -0.6562  0.5104      0  1.7621
Inverse of Unrestrained Stiffness sub-matix, [KuuInverse] =
1.0e-05 *
 0.0195 -0.0060 -0.0144 -0.0017  0.0027  0.0002
-0.0060  0.0195 -0.0168  0.0028 -0.0016 -0.0002

```

```
-0.0144 -0.0168  0.4105 -0.0424 -0.0310  0.1535
-0.0017  0.0028 -0.0424  0.0205 -0.0005 -0.0213
 0.0027 -0.0016 -0.0310 -0.0005  0.0194 -0.0110
 0.0002 -0.0021  0.1535 -0.0213 -0.0110  0.1194
Unrestrained Joint Load vector, [J1] =
 15   -15    0    0    0    0
Unrestrained displacements, [DelU] =
 1.0e-05 *
 0.3814   -0.3816     0.0366   -0.0675   0.0642   0.0331
Member Number =      1
Global displacement matrix [DeltaBar] =
 1.0e-06 *
 -0.6748           0     0.3310           0
Global End moment matrix [MBar] =
 -16.1882   14.5990   -10.5298   -9.4702
Member Number =      2
Global displacement matrix [DeltaBar] =
 1.0e-05 *
 0.3814   -0.0675     0.0366     0.0331
Global End moment matrix [MBar] =
 -8.8938   17.1790   -7.9287  -12.0713
Member Number =      3
Global displacement matrix [DeltaBar] =
 1.0e-05 *
 0.3814   -0.3816           0           0
Global End moment matrix [MBar] =
 8.8938   -8.9073   99.9955  100.0045
Member Number =      4
Global displacement matrix [DeltaBar] =
 1.0e-05 *
 -0.3816   0.0642     0.0366     0.0331
Global End moment matrix [MBar] =
 8.9073   -17.1926   7.9287   12.0713
Member Number =      5
Global displacement matrix [DeltaBar] =
 1.0e-06 *
 0.6418           0     0.3310           0
Global End moment matrix [MBar] =
 16.3403   -14.2213   10.5298   9.4702
Member Number =      6
Global displacement matrix [DeltaBar] =
 1.0e-06 *
 -0.6748   0.6418           0           0
Global End moment matrix [MBar] =
 -0.9908   0.8523   -0.0277   0.0277
Joint forces =
  Columns 1 through 9
 0.0000 -0.0000  0.0000 -0.0000 -0.0000 -0.0000  14.5990  99.9678 -9.4702
  Columns 10 through 12
 -14.2213  9.4702  100.0322
>>
```


MATLAB® program input (with axial load)

```
pa = [100 100 7.9287 100 100 22.6011]*1000; %Axial load in N
load = [1 1 1 1 1 1]; % 0-zero load, 1-compression, 2-tension
```

Output:

```
Member Number = 1
Local Stiffness matrix of member, [K] =
```

$$1.0e+06 * \begin{matrix} 2.2930 & 1.1768 & 1.1566 & -1.1566 \\ 1.1768 & 2.2930 & 1.1566 & -1.1566 \\ 1.1566 & 1.1566 & 0.7377 & -0.7377 \\ -1.1566 & -1.1566 & -0.7377 & 0.7377 \end{matrix}$$

```
Member Number = 2
```

```
Local Stiffness matrix of member, [K] =
```

$$1.0e+06 * \begin{matrix} 1.6959 & 0.8887 & 0.6462 & -0.6462 \\ 0.8887 & 1.6959 & 0.6462 & -0.6462 \\ 0.6462 & 0.6462 & 0.2981 & -0.2981 \\ -0.6462 & -0.6462 & -0.2981 & 0.2981 \end{matrix}$$

```
Member Number = 3
```

```
Local Stiffness matrix of member, [K] =
```

$$1.0e+06 * \begin{matrix} 4.6633 & 2.3340 & 2.3324 & -2.3324 \\ 2.3340 & 4.6633 & 2.3324 & -2.3324 \end{matrix}$$

```

2.3324  2.3324  1.5523 -1.5523
-2.3324 -2.3324 -1.5523  1.5523
Member Number = 4
Local Stiffness matrix of member, [K] =
1.0e+06 *
1.6959  0.8887  0.6462 -0.6462
0.8887  1.6959  0.6462 -0.6462
0.6462  0.6462  0.2981 -0.2981
-0.6462 -0.6462 -0.2981  0.2981
Member Number = 5
Local Stiffness matrix of member, [K] =
1.0e+06 *
1.6959  0.8887  0.6462 -0.6462
0.8887  1.6959  0.6462 -0.6462
0.6462  0.6462  0.2981 -0.2981
-0.6462 -0.6462 -0.2981  0.2981
Member Number = 6
Local Stiffness matrix of member, [K] =
1.0e+06 *
2.7848  1.4037  0.8377 -0.8377
1.4037  2.7848  0.8377 -0.8377
0.8377  0.8377  0.3306 -0.3306
-0.8377 -0.8377 -0.3306  0.3306
Stiffness Matrix of complete structure, [Ktotal] =
1.0e+06 *
Columns 1 through 9
6.3593  2.3340  0.6462  0.8887      0 -0.6462      0  2.3324      0
2.3340  6.3593  0.6462      0  0.8887 -0.6462      0  2.3324      0
0.6462  0.6462  0.5962  0.6462  0.6462 -0.5962      0      0      0
0.8887      0  0.6462  6.7737  1.4037  0.5104  1.1768  0.8377 -1.1566
      0  0.8887  0.6462  1.4037  6.1767      0      0  0.8377      0
-0.6462 -0.6462 -0.5962  0.5104      0  1.6320  1.1566      0 -0.7377
      0      0      0  1.1768      0  1.1566  2.2930      0 -1.1566
2.3324  2.3324      0  0.8377  0.8377      0      0  1.8829      0
      0      0      0 -1.1566      0 -0.7377 -1.1566      0  0.7377
      0      0      0      0  0.8887  0.6462      0      0      0
      0      0      0      0 -0.6462 -0.2981      0      0      0
-2.3324 -2.3324      0 -0.8377 -0.8377      0      0 -1.8829      0
Columns 10 through 12
      0      0 -2.3324
      0      0 -2.3324
      0      0      0
      0      0 -0.8377
0.8887 -0.6462 -0.8377
0.6462 -0.2981      0
      0      0      0
      0      0 -1.8829
      0      0      0
1.6959 -0.6462      0
-0.6462  0.2981      0
      0      0  1.8829
Unrestrained Stiffness sub-matrix, [Kuu] =
1.0e+06 *
6.3593  2.3340  0.6462  0.8887      0 -0.6462

```

```

2.3340   6.3593   0.6462       0   0.8887   -0.6462
0.6462   0.6462   0.5962   0.6462   0.6462   -0.5962
0.8887       0   0.6462   6.7737   1.4037   0.5104
       0   0.8887   0.6462   1.4037   6.1767       0
-0.6462   -0.6462   -0.5962   0.5104       0   1.6320
Inverse of Unrestrained Stiffness sub-matrix, [KuuInverse] =
1.0e-05 *
0.0198   -0.0060   -0.0164   -0.0017   0.0030   0.0000
-0.0060   0.0199   -0.0192   0.0031   -0.0016   -0.0025
-0.0164   -0.0192   0.4696   -0.0483   -0.0354   0.1726
-0.0017   0.0031   -0.0483   0.0214   -0.0003   -0.0238
0.0030   -0.0016   -0.0354   -0.0003   0.0202   -0.0123
0.0000   -0.0025   0.1726   -0.0238   -0.0123   0.1307
Unrestrained Joint Load vector, [J1] =
15   -15   0   0   0
Unrestrained displacements, [DelU] =
1.0e-05 *
0.3879   -0.3882   0.0429   -0.0719   0.0677   0.0380
Member Number =      1
Global displacement matrix [DeltaBar] =
1.0e-06 *
-0.7188       0   0.3802       0
Global End moment matrix [MBar] =
-16.2084   14.5939   -10.5508   -9.4492
Member Number =      2
Global displacement matrix [DeltaBar] =
1.0e-05 *
0.3879   -0.0719   0.0429   0.0380
Global End moment matrix [MBar] =
-9.0287   17.2596   -7.9435   -12.0565
Member Number =      3
Global displacement matrix [DeltaBar] =
1.0e-05 *
0.3879   -0.3882       0       0
Global End moment matrix [MBar] =
9.0287   -9.0492   99.9932   100.0068
Member Number =      4
Global displacement matrix [DeltaBar] =
1.0e-05 *
-0.3882   0.0677   0.0429   0.0380
Global End moment matrix [MBar] =
9.0492   -17.2704   7.9435   12.0565
Member Number =      5
Global displacement matrix [DeltaBar] =
1.0e-06 *
0.6771       0   0.3802       0
Global End moment matrix [MBar] =
16.3939   -14.1526   10.5508   9.4492
Member Number =      6
Global displacement matrix [DeltaBar] =
1.0e-06 *
-0.7188   0.6771       0       0
Global End moment matrix [MBar] =
-1.0512   0.8765   -0.0350   0.0350

```

Joint forces =

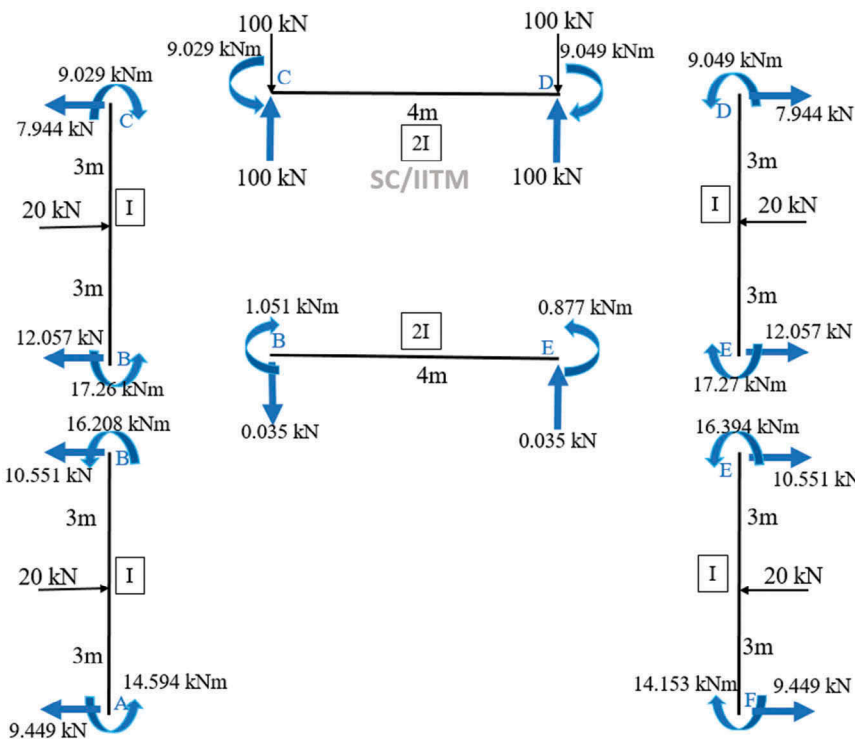
Columns 1 through 9

0.0000 0 -0.0000 0.0000 -0.0000 0.0000 14.5939 99.9582 -9.4492

Columns 10 through 12

-14.1526 9.4492 100.0418

>>



4.10 CRITICAL BUCKLING LOAD

One of the basic assumptions to obtain the buckling load of a structural system with rigid joints is that the deformation of the structure is sufficiently small in comparison to that of its initial condition. Therefore, to estimate the critical buckling load, one can apply the linear theory. It is also important to note that buckling loads of structural systems are estimated under the fact that the structural system is transferring only axial forces. Members that encounter transverse loads develop additional moments, which alter the relative stiffness of the members, significantly. Under such cases, where there is a continuous interaction of the moment and the applied axial load (P-M interaction), critical buckling load is estimated only through the iterative scheme. However, in the case of ideal members that are subjected to axial forces only, buckling loads can be estimated in a much simpler manner. By neglecting axial deformations the members undergo,

joint loads related to the un-restrained joint displacements are set to ZERO at all unrestrained joints.

$$\{J_{Lu}\} = \{0\} \quad (4.117)$$

However, from the fundamental equations of equilibrium, the following relationship holds good:

$$\{J_{Lu}\} = [K_{uu}]\{\Delta_u\} \quad (4.118)$$

where $[K_{uu}]$ is the submatrix of the stiffness matrix of the complete structural system, indicating only the unrestrained degrees of freedom, and Δ_u is the displacement vector of the unrestrained joints. By comparing the above two equations, it is obvious to note that Eq. (4.117) can be true only if Δ_u is a null vector. But, this is a trivial solution, which corresponds to no displacements of the unrestrained joints. Hence, to obtain the nontrivial solution to Eq. (4.117), the following condition should be satisfied:

$$|K_{uu}| = 0 \quad (4.119)$$

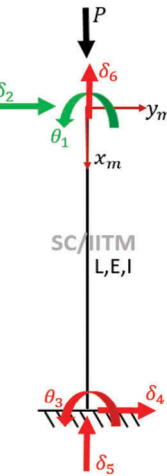
The above is termed as the characteristic determinant, whose expansion will yield the buckling condition of the structural system. It is important that, when the magnitude of the applied axial load is lesser than that of the critical buckling load, then the displacements of the unrestrained joints would be zero. Hence, $|K_{uu}|$ will be positive, which corresponds to a stable condition. On the other hand, if the applied axial load exceeds the critical buckling load, then it will refer to an unstable condition; in such case, $|K_{uu}|$ will be negative.

In a structural system, comprising of more number of members, it is possible that more than one member may be subjected to axial load. In such cases, it becomes necessary to establish a relationship (φ_i) between the respective axial load and buckling load, as explained in Eq. (4.44). This becomes more complicated when more than one member shares the applied axial load, at any joint. The axial load shared by each member at that joint need to be computed by a preliminary analysis. Then, the critical buckling load can be estimated using the following relationship:

$$P_{cr}^i = (\varphi_i)_{critical} \frac{\pi^2 EI}{L_i^2} \quad (4.120)$$

Example 1: Estimate the critical buckling load of the column member using stability functions

With reference to the above figure, kinematic degrees of freedom, both unrestrained and restrained are marked. A detailed procedure of analyzing a member using the stiffness method is discussed in Srinivasan Chandrasekaran (2018a, 2018b). The member stiffness matrix is given as below (this is the same as given by Eq. (4.80)). Numbers shown in circles are the labels of the degrees of freedom.



$$[K_i] = EI \begin{bmatrix} \textcircled{1} & \textcircled{3} & \textcircled{2} & \textcircled{4} \\ \frac{r}{L} & \frac{cr}{L} & \frac{r(1+c)}{L^2} & -\frac{r(1+c)}{L^2} \\ \frac{cr}{L} & \frac{r}{L} & \frac{r(1+c)}{L^2} & -\frac{r(1+c)}{L^2} \\ \frac{r(1+c)}{L^2} & \frac{r(1+c)}{L^2} & \frac{2tr(1+c)}{L^3} & -\frac{2tr(1+c)}{L^3} \\ -\frac{r(1+c)}{L^2} & -\frac{r(1+c)}{L^2} & -\frac{2tr(1+c)}{L^3} & \frac{2tr(1+c)}{L^3} \end{bmatrix} \begin{array}{c} \textcircled{1} \\ \textcircled{3} \\ \textcircled{2} \\ \textcircled{4} \end{array} \quad (4.121)$$

The above matrix can be partitioned to extract the unrestrained stiffness matrix, which will be of size 2×2 , as there are two unrestrained degrees of freedom for this problem. Unrestrained stiffness matrix, as extracted from Eq. (4.121) is given as

$$K_{uu} = EI \begin{bmatrix} \textcircled{1} & \textcircled{2} \\ \frac{r}{L} & \frac{r(1+c)}{L^2} \\ \frac{r(1+c)}{L^2} & \frac{2tr(1+c)}{L^3} \end{bmatrix} \begin{array}{c} \textcircled{1} \\ \textcircled{2} \end{array} \quad (4.122)$$

As there is no joint load applied in the unrestrained degrees of freedom, as per Eq. (4.119), let us set the determinant of Eq. (4.122) to zero. Expanding, we get as follows:

$$\left(\frac{r}{L}\right) \left[\frac{2tr(1+c)}{L^3} \right] - \left[\frac{r(1+c)}{L^2} \right]^2 = 0 \quad (4.123)$$

Simplifying the above expression, we get the following expression:

$$2t - c = 1 \quad (4.124)$$

Eq. (4.124) is called as the characteristic equation, defining the critical buckling condition in terms of the stability functions. Using Table 4.1, one can determine the value of φ_i , satisfying Eq. (4.124). MATLAB® given below helps to scan the appropriate values of the stability functions and determines φ_i as 0.25. The corresponding values of stability functions are: $r = 3.6598$, $t = 0.7854$ and $c = 0.5708$

Using Eq. (4.120), we get:

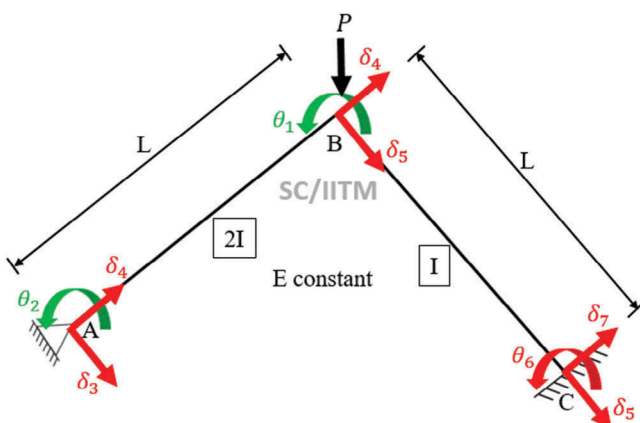
$$P_{cr} = \varphi \frac{\pi^2 EI}{L^2} = (0.25) \frac{\pi^2 EI}{L^2} \quad (4.125)$$

```
% getting phi value condition: 2t = 1+c
lhs = 2*t;
rhs = 1+c;
n = length(out);
for i=1:n
    if lhs(i) == rhs(i)
        phi_value = out(i,1);
    end
end
fprintf('Phi = %6.2f \n',phi_value);
```

Output:

Phi = 0.25

Example 2: Estimate the critical buckling load of the structure using stability functions



With reference to the above figure, kinematic degrees of freedom, both unrestrained and restrained are marked. The member stiffness matrix for both the members is given below.

Numbers shown in circles are the labels of the degrees of freedom of the respective member.

$$[K_1] = E(2I) \begin{bmatrix} 1 & 2 & 5 & 3 \\ \frac{r_1}{L_1} & \frac{c_1 r_1}{L_1} & \frac{r_1 (1+c_1)}{L_1^2} & -\frac{r_1 (1+c_1)}{L_1^2} \\ \frac{c_1 r_1}{L_1} & \frac{r_1}{L_1} & \frac{r_1 (1+c_1)}{L_1^2} & -\frac{r_1 (1+c_1)}{L_1^2} \\ \frac{r_1 (1+c_1)}{L_1^2} & \frac{r_1 (1+c_1)}{L_1^2} & \frac{2 t_1 r_1 (1+c_1)}{L_1^3} & -\frac{2 t_1 r_1 (1+c_1)}{L_1^3} \\ -\frac{r_1 (1+c_1)}{L_1^2} & -\frac{r_1 (1+c_1)}{L_1^2} & -\frac{2 t_1 r_1 (1+c_1)}{L_1^3} & \frac{2 t_1 r_1 (1+c_1)}{L_1^3} \end{bmatrix} \begin{matrix} 1 \\ 2 \\ 5 \\ 3 \end{matrix} \quad (4.126)$$

$$[K_2] = EI \begin{bmatrix} 1 & 6 & 4 & 7 \\ \frac{r_2}{L_2} & \frac{c_2 r_2}{L_2} & \frac{r_2 (1+c_2)}{L_2^2} & -\frac{r_2 (1+c_2)}{L_2^2} \\ \frac{c_2 r_2}{L_2} & \frac{r_2}{L_2} & \frac{r_2 (1+c_2)}{L_2^2} & -\frac{r_2 (1+c_2)}{L_2^2} \\ \frac{r_2 (1+c_2)}{L_2^2} & \frac{r_2 (1+c_2)}{L_2^2} & \frac{2 t_2 r_2 (1+c_2)}{L_2^3} & -\frac{2 t_2 r_2 (1+c_2)}{L_2^3} \\ -\frac{r_2 (1+c_2)}{L_2^2} & -\frac{r_2 (1+c_2)}{L_2^2} & -\frac{2 t_2 r_2 (1+c_2)}{L_2^3} & \frac{2 t_2 r_2 (1+c_2)}{L_2^3} \end{bmatrix} \begin{matrix} 1 \\ 6 \\ 4 \\ 7 \end{matrix} \quad (4.127)$$

The above matrices are assembled to obtain the unrestrained stiffness matrix, which will be of size 2×2 , as there are two unrestrained degrees of freedom for this problem. In the above equations of the stiffness matrices, substitute $L_1 = L_2 = L$. Unrestrained stiffness matrix, as assembled by combining Eq. (4.126) and Eq. (4.127) is given as

$$K_{uu} = EI \begin{bmatrix} 1 & 2 \\ \frac{2r_1 + r_2}{L} & \frac{2c_1 r_1}{L} \\ \frac{2c_1 r_1}{L} & \frac{2r_1}{L} \end{bmatrix} \begin{matrix} 1 \\ 2 \end{matrix} \quad (4.128)$$

As there is no joint load applied in the unrestrained degrees of freedom, let us set the determinant of Eq. (4.128) to zero. Expanding, we get as follows:

$$\left(\frac{2r_1 + r_2}{L}\right) \left(\frac{2r_1}{L}\right) - \left[\frac{2c_1 r_1}{L}\right]^2 = 0 \quad (4.129)$$

Simplifying, we get the following expression:

$$2r_1(1 - c_1^2) + r_2 = 0 \quad (4.130)$$

Eq. (4.130) is the characteristic equation, defining the critical buckling condition in terms of the stability functions. Also, we also know the following relationship with reference to the problem loading:

$$(P_{cr})_1 = (P_{cr})_2 = P_{cr}(0.707) \quad (4.131)$$

$$\varphi_1 = \frac{P (0.707)}{\left[\frac{\pi^2 E(2I)}{L^2} \right]} \quad (4.132)$$

$$\varphi_2 = \frac{P (0.707)}{\left[\frac{\pi^2 EI}{L^2} \right]} \quad (4.133)$$

From the above equations, the following relationship can be deduced:

$$2\varphi_1 = \varphi_2 \quad (4.134)$$

Using Table 4.1, one can determine the value of φ_i , satisfying both Eq. (4.130) and Eq. (4.134). MATLAB® code given below helps to scan the appropriate values of the stability functions and determines φ_1 as 1.01 and φ_2 as 2.02. The corresponding values of stability functions are: $r_1 = 2.4493$, $t_1 = -0.0124$, $c_1 = 1.0101$ and $r_2 = 0.1120$, $t_2 = -1.7148$, $c_2 = 31.6264$.

Using Eq. (4.132), we get:

$$P_{cr} = \varphi_1 \frac{\pi^2 E(2I)}{(0.707)L^2} \quad (4.135)$$

```
% getting phi value condition: 2*phi = r1*(1-c1^2) + r2 = 0
lhs = 2*phi;
rhs = phi;
n = length(out);
phi1 = zeros(n,1);
phi2 = zeros(n,1);
u=1;
for i=1:n
    for j=1:n
        if lhs(i) == rhs(j)
            r1 = r(i);
            c1 = c(i);
            r2 = r(j);
            if -0.00001 <= (2*r1*(1-(c1^2)))+r2 <=0.00001
                phi1(u) = phi(i);
                phi2(u) = phi(j);
                u=u+1;
            end
        end
    end
end
```

```

end
end
end
fprintf('Phi 1 = %6.2f \n',phi1(1));
fprintf('Phi 2 = %6.2f \n',phi2(1));

```

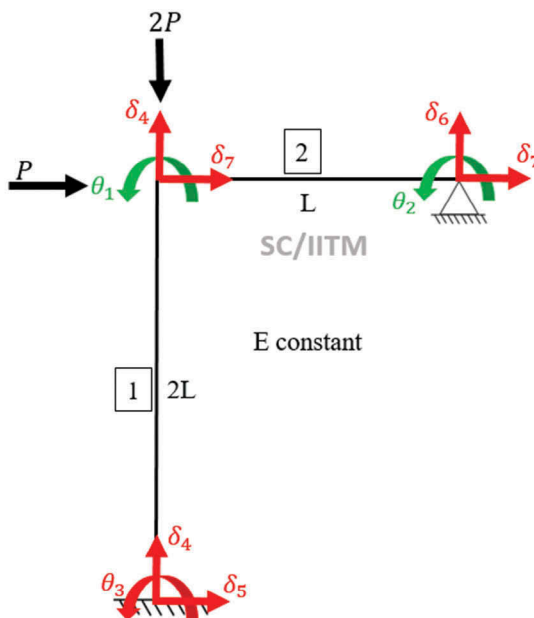
Output:

```

Phi 1 =      1.01
Phi 2 =      2.02

```

Example 3: Estimate the critical buckling load of the structure using stability functions



With reference to the above figure, kinematic degrees of freedom, both unrestrained and restrained are marked. The member stiffness matrix for both the members is given below. Numbers shown in circles are the labels of the degrees of freedom of the respective member.

$$[K_1] = EI \begin{bmatrix} \frac{r_1}{L_1} & \frac{c_1 r_1}{L_1} & \frac{r_1 (1+c_1)}{L_1^2} & -\frac{r_1 (1+c_1)}{L_1^2} \\ \frac{c_1 r_1}{L_1} & \frac{r_1}{L_1} & \frac{r_1 (1+c_1)}{L_1^2} & -\frac{r_1 (1+c_1)}{L_1^2} \\ \frac{r_1 (1+c_1)}{L_1^2} & \frac{r_1 (1+c_1)}{L_1^2} & \frac{2 t_1 r_1 (1+c_1)}{L_1^3} & -\frac{2 t_1 r_1 (1+c_1)}{L_1^3} \\ -\frac{r_1 (1+c_1)}{L_1^2} & -\frac{r_1 (1+c_1)}{L_1^2} & -\frac{2 t_1 r_1 (1+c_1)}{L_1^3} & \frac{2 t_1 r_1 (1+c_1)}{L_1^3} \end{bmatrix} \begin{matrix} (1) \\ (3) \\ (7) \\ (5) \end{matrix} \quad (4.136)$$

$$[K_2] = EI \begin{bmatrix} 1 & 2 & 4 & 6 \\ \frac{r_2}{L_2} & \frac{c_2 r_2}{L_2} & \frac{r_2 (1+c_2)}{L_2^2} & -\frac{r_2 (1+c_2)}{L_2^2} \\ \frac{c_2 r_2}{L_2} & \frac{r_2}{L_2} & \frac{r_2 (1+c_2)}{L_2^2} & -\frac{r_2 (1+c_2)}{L_2^2} \\ \frac{r_2 (1+c_2)}{L_2^2} & -\frac{r_2 (1+c_2)}{L_2^2} & \frac{2 t_2 r_2 (1+c_2)}{L_2^3} & -\frac{2 t_2 r_2 (1+c_2)}{L_2^3} \\ -\frac{r_2 (1+c_2)}{L_2^2} & -\frac{r_2 (1+c_2)}{L_2^2} & -\frac{2 t_2 r_2 (1+c_2)}{L_2^3} & \frac{2 t_2 r_2 (1+c_2)}{L_2^3} \end{bmatrix} \begin{array}{c} 1 \\ 2 \\ 4 \\ 6 \end{array} \quad (4.137)$$

The above matrices are assembled to obtain the unrestrained stiffness matrix, which will be of size 2×2 , as there are two unrestrained degrees of freedom for this problem. In the above equations of the stiffness matrices, substitute $L_1 = 2L$ and $L_2 = L$. Unrestrained stiffness matrix, as assembled by combining Eq. (4.136) and Eq. (4.137), is given as

$$K_{uu} = EI \begin{bmatrix} 1 & 2 \\ \frac{r_1+2r_2}{2L} & \frac{c_2 r_2}{L} \\ \frac{c_2 r_2}{L} & \frac{r_2}{L} \end{bmatrix} \begin{array}{c} 1 \\ 2 \end{array} \quad (4.138)$$

As there is no joint load applied in the unrestrained degrees of freedom, let us set the determinant of Eq. (4.138) to zero. Expanding, we get as follows:

$$\left(\frac{r_1 + 2r_2}{2L} \right) \left(\frac{r_2}{L} \right) - \left[\frac{c_2 r_2}{L} \right]^2 = 0 \quad (4.139)$$

Simplifying, we get the following expression:

$$r_1 = 2r_2(c_2^2 - 1) \quad (4.140)$$

Eq. (4.140) is the characteristic equation, defining the critical buckling condition in terms of the stability functions. Also, we also know the following relationship with reference to the problem loading:

$$(P_{cr})_1 = 2P \quad (4.141)$$

$$(P_{cr})_2 = P \quad (4.142)$$

$$\varphi_1 = \frac{2P}{\left[\frac{\pi^2 EI}{4L^2} \right]} = \frac{8P}{\left[\frac{\pi^2 EI}{L^2} \right]} \quad (4.143)$$

$$\varphi_2 = \frac{P}{\left[\frac{\pi^2 EI}{L^2} \right]} \quad (4.144)$$

From the above equations, the following relationship can be deduced:

$$\varphi_1 = 8\varphi_2 \quad (4.145)$$

Using Table 4.1, one can determine the value of φ_i , satisfying both Eq. (4.140) and Eq. (4.145). MATLAB® code given below helps to scan the appropriate values of the stability functions and determines φ_1 as 2.96 and φ_2 as 0.37. $r_1 = -4.6727$, $t_1 = -5.7540$, $c_1 = -1.4628$ and $r_2 = 3.4878$, $t_2 = 0.6754$, $c_2 = 0.6127$

Using Eq. (4.143), we get:

$$P_{cr} = \varphi_1 \frac{\pi^2 EI}{8L^2} \quad (4.146)$$

```
% getting phi value condition: φ₁ = 8φ₂ and r₁ = 2r₂ (c₂²-1)
```

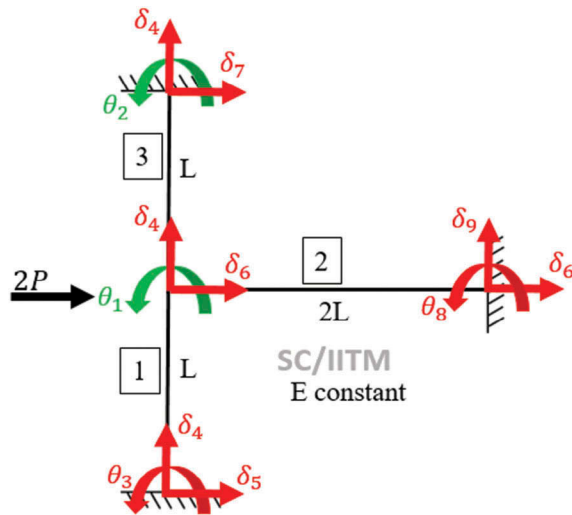
```
lhs = phi;
rhs = 8*phi;
n = length (out);
phil = zeros(n,1);
phi2 = zeros(n,1);
u=1;
for i=1:n
    for j=1:n
        if lhs(i) == rhs(j)
            r1 = r(i);
            c1 = c(i);
            r2 = r(j);
            c2 = c(j);
            if -0.00001 <= (r1-(2*r2*((c2^2)-1))) <=0.00001
                phil(u) = phi(i);
                phi2(u) = phi(j);
                u=u+1;
            end
        end
    end
end
fprintf('Phi 1 = %6.2f \n',phil(1));
fprintf('Phi 2 = %6.2f \n',phi2(1));
```

Output:

```
Phi 1 =      2.96
Phi 2 =      0.37
```

Example 4: Estimate the critical buckling load of the structure using stability functions

With reference to the above figure, kinematic degrees of freedom, both unrestrained and restrained are marked. The member stiffness matrix for both the members is given below. Numbers shown in circles are the labels of the degrees of freedom of the respective member.



$$[K_1] = EI \begin{bmatrix} 1 & 3 & 6 & 5 \\ \frac{r_1}{L_1} & \frac{c_1 r_1}{L_1} & \frac{r_1 (1+c_1)}{L_1^2} & -\frac{r_1 (1+c_1)}{L_1^2} \\ \frac{c_1 r_1}{L_1} & \frac{r_1}{L_1} & \frac{r_1 (1+c_1)}{L_1^2} & -\frac{r_1 (1+c_1)}{L_1^2} \\ \frac{r_1 (1+c_1)}{L_1^2} & \frac{r_1 (1+c_1)}{L_1^2} & \frac{2 t_1 r_1 (1+c_1)}{L_1^3} & -\frac{2 t_1 r_1 (1+c_1)}{L_1^3} \\ -\frac{r_1 (1+c_1)}{L_1^2} & -\frac{r_1 (1+c_1)}{L_1^2} & -\frac{2 t_1 r_1 (1+c_1)}{L_1^3} & \frac{2 t_1 r_1 (1+c_1)}{L_1^3} \end{bmatrix} \begin{matrix} 1 \\ 3 \\ 6 \\ 5 \end{matrix} \quad (4.147)$$

$$[K_2] = EI \begin{bmatrix} 2 & 1 & 7 & 6 \\ \frac{r_2}{L_2} & \frac{c_2 r_2}{L_2} & \frac{r_2 (1+c_2)}{L_2^2} & -\frac{r_2 (1+c_2)}{L_2^2} \\ \frac{c_2 r_2}{L_2} & \frac{r_2}{L_2} & \frac{r_2 (1+c_2)}{L_2^2} & -\frac{r_2 (1+c_2)}{L_2^2} \\ \frac{r_2 (1+c_2)}{L_2^2} & \frac{r_2 (1+c_2)}{L_2^2} & \frac{2 t_2 r_2 (1+c_2)}{L_2^3} & -\frac{2 t_2 r_2 (1+c_2)}{L_2^3} \\ -\frac{r_2 (1+c_2)}{L_2^2} & -\frac{r_2 (1+c_2)}{L_2^2} & -\frac{2 t_2 r_2 (1+c_2)}{L_2^3} & \frac{2 t_2 r_2 (1+c_2)}{L_2^3} \end{bmatrix} \begin{matrix} 2 \\ 1 \\ 7 \\ 6 \end{matrix} \quad (4.148)$$

$$[K_3] = EI \begin{bmatrix} \textcircled{1} & \textcircled{8} & \textcircled{4} & \textcircled{9} \\ \frac{r_3}{L_3} & \frac{c_3 r_3}{L_3} & \frac{r_3 (1+c_3)}{L_3^2} & -\frac{r_3 (1+c_3)}{L_3^2} \\ \frac{c_3 r_3}{L_3} & \frac{r_3}{L_3} & \frac{r_3 (1+c_3)}{L_3^2} & -\frac{r_3 (1+c_3)}{L_3^2} \\ \frac{L_3}{r_3} & \frac{L_3}{r_3} & \frac{L_3}{r_3} & \frac{L_3}{r_3} \\ \frac{r_3 (1+c_3)}{L_3^2} & \frac{r_3 (1+c_3)}{L_3^2} & \frac{2 t_3 r_3 (1+c_3)}{L_3^3} & -\frac{2 t_3 r_3 (1+c_3)}{L_3^3} \\ -\frac{r_3 (1+c_3)}{L_3^2} & -\frac{r_3 (1+c_3)}{L_3^2} & -\frac{2 t_3 r_3 (1+c_3)}{L_3^3} & \frac{2 t_3 r_3 (1+c_3)}{L_3^3} \end{bmatrix} \begin{matrix} \textcircled{1} \\ \textcircled{8} \\ \textcircled{4} \\ \textcircled{9} \end{matrix} \quad (4.149)$$

The above matrices are assembled to obtain the unrestrained stiffness matrix, which will be of size 2×2 , as there are two unrestrained degrees of freedom for this problem. In the above equations of the stiffness matrices, substitute $L_1 = L_2 = L$; $L_3 = 2L$. After appropriate substitution, unrestrained stiffness matrix as assembled by combining Eq. (4.147), Eq. (4.148) and Eq. (4.149) is given as

$$K_{uu} = EI \begin{bmatrix} \textcircled{1} & \textcircled{2} \\ \frac{2r_1+r_3}{2L} & \frac{c_2 r_2}{L} \\ \frac{2L}{c_2 r_2} & \frac{r_2}{L} \end{bmatrix} \begin{matrix} \textcircled{1} \\ \textcircled{2} \end{matrix} \quad (4.150)$$

As there is no joint load applied in the unrestrained degrees of freedom, let us set the determinant of Eq. (4.150) to zero. Expanding, we get as follows:

$$\left(\frac{2r_1+r_3}{2L}\right) \left(\frac{r_2}{L}\right) - \left[\frac{c_2 r_2}{L}\right]^2 = 0 \quad (4.151)$$

Simplifying, we get the following expression:

$$2r_1 + r_3 = 2r_2 c_2 \quad (4.152)$$

Eq. (4.152) is the characteristic equation, defining the critical buckling condition in terms of the stability functions. Also, we also know the following relationship with reference to the problem loading:

$$\varphi_1 = \varphi_2 = 0 \quad (4.153)$$

$$(P_{cr})_3 = 2P \quad (4.154)$$

$$\varphi_3 = \frac{2P}{\left[\frac{\pi^2 EI}{4L^2}\right]} = \frac{8P}{\left[\frac{\pi^2 EI}{L^2}\right]} \quad (4.155)$$

Using Table 4.1, one can determine the value of φ_i , satisfying Eq. (4.152), Eq. (4.153) and Eq. (4.155). MATLAB® code given below helps to scan

the appropriate values of the stability functions and determines φ_3 as 3.10; $r_3 = -6.0519$; $t_3 = -7.0072$; $c_3 = -1.3157$

Using Eq. (4.155), we get:

$$P_{cr} = \varphi_3 \frac{\pi^2 EI}{8L^2} \quad (4.156)$$

```
% getting phi value condition: phi1 = phi2 =0
r1 = 4;
r2 = 4;
c2 = 0.5;
r3 = (2*r2*c2*c2)-(2*r1);
n = length (out);
phi3 = zeros(n,1);
u=1;
for i = 1:n
    if r3 == round(r(i))
        if r(i)-r3 <=0.00001
            phi3(u) = phi(i);
            u=u+1;
        end
    end
end
fprintf('Phi 3 = %6.2f \n',phi3(1));
```

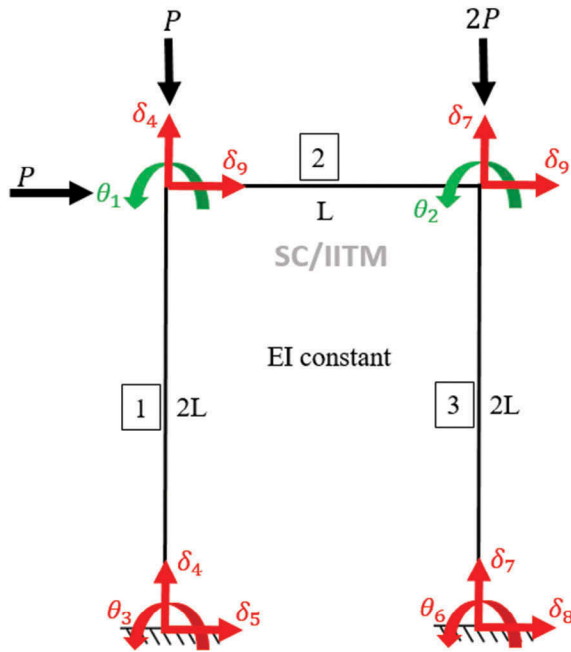
Output:

Phi 3 = 3.10

Example 5: Estimate the critical buckling load of the structure using stability functions

With reference to the above figure, kinematic degrees of freedom, both unrestrained and restrained are marked. The member stiffness matrix for both the members is given below. Numbers shown in circles are the labels of the degrees of freedom of the respective member.

$$[K_1] = EI \begin{bmatrix} \frac{r_1}{L_1} & \frac{c_1 r_1}{L_1} & \frac{r_1 (1+c_1)}{L_1^2} & -\frac{r_1 (1+c_1)}{L_1^2} \\ \frac{c_1 r_1}{L_1} & \frac{r_1}{L_1} & \frac{r_1 (1+c_1)}{L_1^2} & -\frac{r_1 (1+c_1)}{L_1^2} \\ \frac{r_1 (1+c_1)}{L_1^2} & \frac{r_1 (1+c_1)}{L_1^2} & \frac{2 t_1 r_1 (1+c_1)}{L_1^3} & -\frac{2 t_1 r_1 (1+c_1)}{L_1^3} \\ -\frac{r_1 (1+c_1)}{L_1^2} & -\frac{r_1 (1+c_1)}{L_1^2} & -\frac{2 t_1 r_1 (1+c_1)}{L_1^3} & \frac{2 t_1 r_1 (1+c_1)}{L_1^3} \end{bmatrix} \begin{matrix} 1 \\ 3 \\ 9 \\ 5 \end{matrix} \quad (4.157)$$



$$[K_2] = EI \begin{bmatrix} \frac{r_2}{L_2} & \frac{c_2 r_2}{L_2} & \frac{r_2 (1+c_2)}{L_2^2} & -\frac{r_2 (1+c_2)}{L_2^2} \\ \frac{c_2 r_2}{L_2} & \frac{r_2}{L_2} & \frac{r_2 (1+c_2)}{L_2^2} & -\frac{r_2 (1+c_2)}{L_2^2} \\ \frac{r_2 (1+c_2)}{L_2^2} & \frac{r_2 (1+c_2)}{L_2^2} & \frac{2 t_2 r_2 (1+c_2)}{L_2^3} & -\frac{2 t_2 r_2 (1+c_2)}{L_2^3} \\ -\frac{r_2 (1+c_2)}{L_2^2} & -\frac{r_2 (1+c_2)}{L_2^2} & -\frac{2 t_2 r_2 (1+c_2)}{L_2^3} & \frac{2 t_2 r_2 (1+c_2)}{L_2^3} \end{bmatrix} \quad (4.158)$$

(1) (2) (4) (7)

(1) (2) (4) (7)

$$[K_3] = EI \begin{bmatrix} \frac{r_3}{L_3} & \frac{c_3 r_3}{L_3} & \frac{r_3 (1+c_3)}{L_3^2} & -\frac{r_3 (1+c_3)}{L_3^2} \\ \frac{c_3 r_3}{L_3} & \frac{r_3}{L_3} & \frac{r_3 (1+c_3)}{L_3^2} & -\frac{r_3 (1+c_3)}{L_3^2} \\ \frac{r_3 (1+c_3)}{L_3^2} & \frac{r_3 (1+c_3)}{L_3^2} & \frac{2 t_3 r_3 (1+c_3)}{L_3^3} & -\frac{2 t_3 r_3 (1+c_3)}{L_3^3} \\ -\frac{r_3 (1+c_3)}{L_3^2} & -\frac{r_3 (1+c_3)}{L_3^2} & -\frac{2 t_3 r_3 (1+c_3)}{L_3^3} & \frac{2 t_3 r_3 (1+c_3)}{L_3^3} \end{bmatrix} \quad (4.159)$$

(2) (6) (9) (8)

(2) (6) (9) (8)

The above matrices are assembled to obtain the unrestrained stiffness matrix, which will be of size 2×2 , as there are two unrestrained degrees of freedom for this problem. In the above equations of the stiffness matrices, substitute $L_1 = L_3 = 2L$; $L_2 = L$. After appropriate substitution, unrestrained stiffness matrix, as assembled by combining Eq. (4.157), Eq. (4.158) and Eq. (4.159) is given as

$$K_{uu} = EI \begin{bmatrix} \frac{r_1+2r_2}{2L} & \frac{c_2 r_2}{L} \\ \frac{c_2 r_2}{L} & \frac{2r_2+r_3}{2L} \end{bmatrix} \begin{array}{c} (1) \\ (2) \end{array} \quad (4.160)$$

As there is no joint load applied in the unrestrained degrees of freedom, let us set the determinant of Eq. (4.160) to zero. Expanding, we get as follows:

$$\left(\frac{r_1 + 2r_2}{2L}\right) \left(\frac{2r_2 + r_3}{2L}\right) - \left[\frac{c_2 r_2}{L}\right]^2 = 0 \quad (4.161)$$

simplifying, we get the following expression:

$$r_1(2r_2 + r_3) + r_2(4r_2 + 2r_3) = 4r_2^2 c_2^2 \quad (4.162)$$

Eq. (4.162) is the characteristic equation, defining the critical buckling condition in terms of the stability functions. Also, we also know the following relationship with reference to the problem loading:

$$\varphi_1 = \frac{P}{\left[\frac{\pi^2 EI}{4L^2}\right]} = \frac{4P}{\left[\frac{\pi^2 EI}{L^2}\right]} \quad (4.163)$$

$$\varphi_2 = \frac{P}{\left[\frac{\pi^2 EI}{L^2}\right]} \quad (4.164)$$

$$\varphi_3 = \frac{2P}{\left[\frac{\pi^2 EI}{4L^2}\right]} = \frac{8P}{\left[\frac{\pi^2 EI}{L^2}\right]} \quad (4.165)$$

$$\varphi_1 = 4\varphi_2 \quad (4.166)$$

$$\varphi_3 = 8\varphi_2 \quad (4.167)$$

Using Table 4.1, one can determine the value of φ_i , satisfying Eq. (4.162), Eq. (4.166) and Eq. (4.167). MATLAB® code given below helps to scan the appropriate values of the stability functions and determines $\varphi_2 = 0.38$. The corresponding stability coefficients are $r_2 = 3.4732$; $t_2 = 0.6660$; $c_2 = 0.6165$.

Using Eq. (4.164), we get:

$$P_{cr} = \varphi_2 \frac{\pi^2 EI}{L^2} \quad (4.168)$$

```
% getting phi value condition: phil = 4phi2
n = length (out);
lhs = phi;
rhs = 4*phi;
phil = zeros(n,1);
phi2 = zeros(n,1);
phi3 = zeros(n,1);
u=1;
for i=1:n
    for j=1:n
        if lhs(i) == rhs(j)
            r1 = r(i);
            c1 = c(i);
            phi22 = phi(j);
            r2 = r(j);
            c2 = c(j);
            for k = 1:n
                if (8*phi22) == phi(k)
                    r3 = r(k);
                    if -0.00001 <= ((r1*((2*r2)+r3))+(r2*((2*r3)+(4*r2)))-(4*r2*r2*c2*c2)) <= 0.00001
                        phil(u) = phi(i);
                        phi2(u) = phi(j);
                        phi3(u) = phi(k);
                        u=u+1;
                    end
                end
            end
        end
    end
end
fprintf('Phi 1 = %6.2f \n',phil(1));
fprintf('Phi 2 = %6.2f \n',phi2(1));
fprintf('Phi 3 = %6.2f \n',phi3(1));
```

Output:

```
Phi 1 =      0.76
Phi 2 =      0.19
Phi 3 =     1.52
```

MATLAB® code for preparing the stability chart

```
% This MATLAB® code is for plotting the stability indices
% Re-type the following code in MATLAB® new script and run the file to get the
% output.
clc;
clear;
phi=0.01:0.01:4;
alrad=pi.*sqrt(phi);
al = radtodeg (alrad);
```

```
% Compression
r = (alrad.*((sind(al))-(alrad.*cosd(al))))./((2.* (1-cosd(al)))-(alrad.
    *(sind(al)))); % rotation function
c = (alrad-sind(al))./(sind(al)- (alrad.*cosd(al))); % rotation function
t = 1-((pi*pi*phi)./(2.*r.*(1+c))); % Translation function
outcomp = [phi' r' c' t'];
% for zero
outzero = [0 4.0 0.5 1.0];
% Tension
phit =10:-0.1:0.1;
alrad = pi.*sqrt(phit);
al = radtodeg (alrad);
rt = (alrad.*((alrad.*cosh(alrad))-sinh(alrad)))./((2.* (1-cosh(alrad)))
    +(alrad.*sinh(alrad)));
ct = (alrad-sinh(alrad))./(sinh(alrad)-(alrad.*cosh(alrad)));
tt = 1-((pi*pi*(-phit))./(2.*rt.* (1+ct)));
outten = [-phit' rt' ct' tt'];
% Stability chart
out = [outten; outzero; outcomp];
filename='StabilityChart.xlsx';
sheet=1;
xlswrite(filename,out,sheet);
phi = out(:,1);
r = out(:,2);
c = out(:,3);
t = out(:,4);
figure;
plot (phi,r,'b','linewidth',2)
xlabel('Phi');
ylabel('r');
grid on;
figure;
plot (phi,c,'b','linewidth',2)
xlabel('Phi');
ylabel('c');
grid on;
figure;
plot (phi,t, 'b','linewidth',2)
xlabel('Phi');
ylabel('t');
grid on;
```

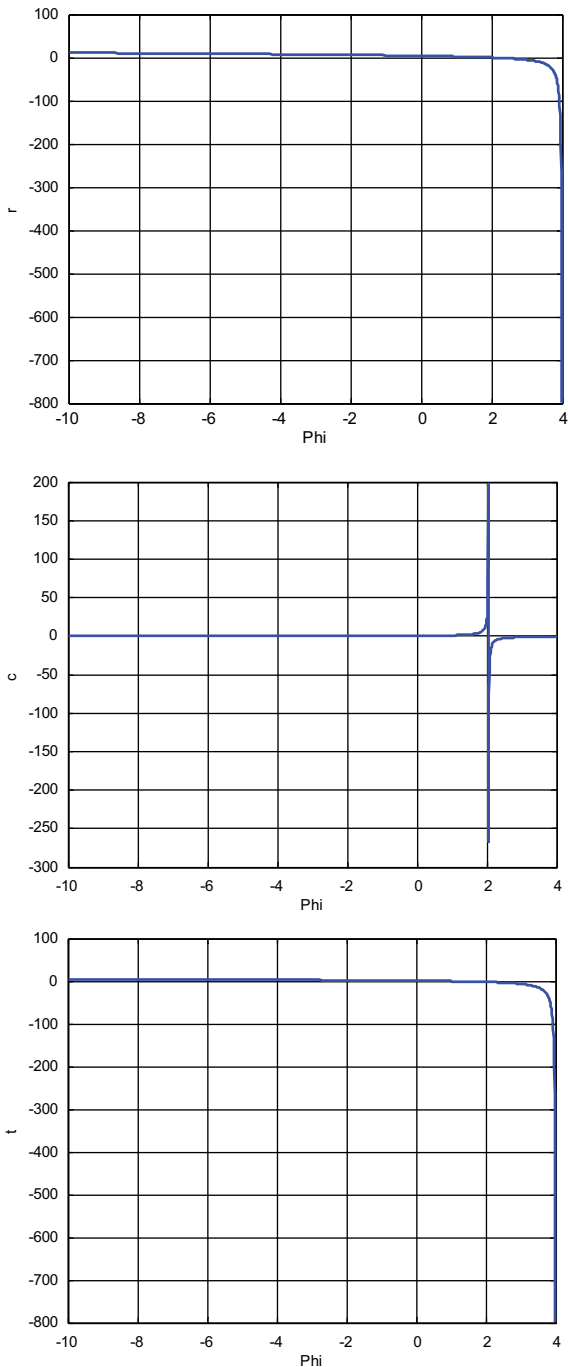
Output:

TABLE 4.1 Stability functions
(negative sign indicates tensile
axial load)

Phi	r	c	t
-10	11.1864	0.1118	4.9678
-9.9	11.1382	0.1124	4.9429
-9.8	11.0897	0.1131	4.9179
-9.7	11.0410	0.1137	4.8928
-9.6	10.9921	0.1144	4.8675
-9.5	10.9430	0.1150	4.8421
-9.4	10.8936	0.1157	4.8166
-9.3	10.8440	0.1164	4.7909
-9.2	10.7941	0.1171	4.7652
-9.1	10.7440	0.1178	4.7392
-9	10.6937	0.1185	4.7131
-8.9	10.6431	0.1193	4.6869
-8.8	10.5922	0.1200	4.6606
-8.7	10.5411	0.1208	4.6341
-8.6	10.4897	0.1215	4.6074
-8.5	10.4380	0.1223	4.5806
-8.4	10.3860	0.1231	4.5536
-8.3	10.3338	0.1239	4.5265
-8.2	10.2813	0.1248	4.4992
-8.1	10.2285	0.1256	4.4717
-8	10.1754	0.1265	4.4441
-7.9	10.1220	0.1274	4.4163
-7.8	10.0683	0.1283	4.3884
-7.7	10.0143	0.1292	4.3602
-7.6	9.9600	0.1301	4.3319
-7.5	9.9054	0.1311	4.3034
-7.4	9.8504	0.1321	4.2747
-7.3	9.7951	0.1331	4.2458
-7.2	9.7395	0.1341	4.2167
-7.1	9.6835	0.1351	4.1875
-7	9.6272	0.1362	4.1580
-6.9	9.5706	0.1373	4.1283
-6.8	9.5136	0.1384	4.0984
-6.7	9.4562	0.1395	4.0683
-6.6	9.3984	0.1407	4.0380
-6.5	9.3403	0.1419	4.0074
-6.4	9.2817	0.1431	3.9766
-6.3	9.2228	0.1444	3.9456

(Continued)

TABLE 4.1 (Cont.)

Phi	r	c	t
-6.2	9.1635	0.1457	3.9144
-6.1	9.1037	0.1470	3.8829
-6	9.0436	0.1483	3.8512
-5.9	8.9830	0.1497	3.8192
-5.8	8.9220	0.1511	3.7869
-5.7	8.8605	0.1526	3.7544
-5.6	8.7986	0.1541	3.7216
-5.5	8.7362	0.1556	3.6885
-5.4	8.6733	0.1572	3.6551
-5.3	8.6100	0.1588	3.6215
-5.2	8.5461	0.1604	3.5875
-5.1	8.4818	0.1621	3.5532
-5	8.4169	0.1639	3.5187
-4.9	8.3515	0.1657	3.4838
-4.8	8.2855	0.1676	3.4485
-4.7	8.2190	0.1695	3.4129
-4.6	8.1520	0.1715	3.3770
-4.5	8.0843	0.1735	3.3407
-4.4	8.0161	0.1757	3.3040
-4.3	7.9472	0.1778	3.2669
-4.2	7.8777	0.1801	3.2295
-4.1	7.8075	0.1824	3.1916
-4	7.7367	0.1848	3.1533
-3.9	7.6652	0.1873	3.1146
-3.8	7.5930	0.1899	3.0755
-3.7	7.5201	0.1926	3.0359
-3.6	7.4465	0.1954	2.9958
-3.5	7.3721	0.1983	2.9552
-3.4	7.2969	0.2013	2.9141
-3.3	7.2209	0.2044	2.8725
-3.2	7.1441	0.2076	2.8304
-3.1	7.0664	0.2110	2.7877
-3	6.9878	0.2145	2.7444
-2.9	6.9084	0.2182	2.7005
-2.8	6.8280	0.2220	2.6560
-2.7	6.7466	0.2260	2.6108
-2.6	6.6642	0.2302	2.5650
-2.5	6.5808	0.2346	2.5185
-2.4	6.4963	0.2392	2.4712
-2.3	6.4107	0.2440	2.4232

(Continued)

TABLE 4.1 (Cont.)

Phi	r	c	t
-2.2	6.3239	0.2491	2.3744
-2.1	6.2360	0.2544	2.3248
-2	6.1468	0.2600	2.2743
-1.9	6.0564	0.2659	2.2230
-1.8	5.9645	0.2721	2.1706
-1.7	5.8714	0.2787	2.1174
-1.6	5.7767	0.2857	2.0631
-1.5	5.6806	0.2931	2.0077
-1.4	5.5828	0.3010	1.9512
-1.3	5.4835	0.3094	1.8935
-1.2	5.3824	0.3183	1.8346
-1.1	5.2795	0.3279	1.7743
-1	5.1748	0.3381	1.7127
-0.9	5.0681	0.3490	1.6496
-0.8	4.9593	0.3608	1.5850
-0.7	4.8483	0.3735	1.5187
-0.6	4.7351	0.3872	1.4508
-0.5	4.6194	0.4021	1.3809
-0.4	4.5013	0.4183	1.3092
-0.3	4.3804	0.4360	1.2354
-0.2	4.2567	0.4553	1.1593
-0.1	4.1299	0.4765	1.0809
0	4.0000	0.5000	1.0000
0.01	3.9868	0.5025	0.9918
0.02	3.9736	0.5050	0.9835
0.03	3.9604	0.5075	0.9752
0.04	3.9471	0.5101	0.9669
0.05	3.9338	0.5127	0.9585
0.06	3.9204	0.5153	0.9502
0.07	3.9070	0.5179	0.9418
0.08	3.8936	0.5206	0.9333
0.09	3.8802	0.5233	0.9249
0.1	3.8667	0.5260	0.9164
0.11	3.8531	0.5288	0.9078
0.12	3.8396	0.5316	0.8993
0.13	3.8260	0.5344	0.8907
0.14	3.8123	0.5372	0.8821
0.15	3.7987	0.5401	0.8735
0.16	3.7849	0.5430	0.8648
0.17	3.7712	0.5460	0.8561

(Continued)

TABLE 4.1 (Cont.)

Phi	r	c	t
0.18	3.7574	0.5490	0.8474
0.19	3.7436	0.5520	0.8386
0.2	3.7297	0.5550	0.8298
0.21	3.7158	0.5581	0.8210
0.22	3.7019	0.5612	0.8122
0.23	3.6879	0.5644	0.8033
0.24	3.6739	0.5676	0.7943
0.25	3.6598	0.5708	0.7854
0.26	3.6457	0.5741	0.7764
0.27	3.6315	0.5774	0.7674
0.28	3.6174	0.5807	0.7584
0.29	3.6031	0.5841	0.7493
0.3	3.5889	0.5875	0.7402
0.31	3.5746	0.5910	0.7310
0.32	3.5602	0.5945	0.7218
0.33	3.5458	0.5981	0.7126
0.34	3.5314	0.6017	0.7034
0.35	3.5169	0.6053	0.6941
0.36	3.5024	0.6090	0.6848
0.37	3.4878	0.6127	0.6754
0.38	3.4732	0.6165	0.6660
0.39	3.4586	0.6203	0.6566
0.4	3.4439	0.6242	0.6471
0.41	3.4292	0.6281	0.6376
0.42	3.4144	0.6321	0.6281
0.43	3.3995	0.6361	0.6185
0.44	3.3847	0.6402	0.6089
0.45	3.3698	0.6443	0.5992
0.46	3.3548	0.6485	0.5895
0.47	3.3398	0.6528	0.5798
0.48	3.3247	0.6571	0.5701
0.49	3.3096	0.6614	0.5603
0.5	3.2945	0.6659	0.5504
0.51	3.2793	0.6703	0.5405
0.52	3.2640	0.6749	0.5306
0.53	3.2487	0.6795	0.5206
0.54	3.2334	0.6841	0.5106
0.55	3.2180	0.6889	0.5006
0.56	3.2025	0.6937	0.4905
0.57	3.1870	0.6985	0.4804

(Continued)

TABLE 4.1 (Cont.)

Phi	r	c	t
0.58	3.1715	0.7035	0.4702
0.59	3.1559	0.7085	0.4600
0.6	3.1403	0.7136	0.4498
0.61	3.1246	0.7187	0.4395
0.62	3.1088	0.7239	0.4291
0.63	3.0930	0.7292	0.4187
0.64	3.0771	0.7346	0.4083
0.65	3.0612	0.7401	0.3978
0.66	3.0453	0.7456	0.3873
0.67	3.0293	0.7513	0.3768
0.68	3.0132	0.7570	0.3661
0.69	2.9971	0.7628	0.3555
0.7	2.9809	0.7687	0.3448
0.71	2.9646	0.7746	0.3340
0.72	2.9484	0.7807	0.3233
0.73	2.9320	0.7869	0.3124
0.74	2.9156	0.7932	0.3015
0.75	2.8991	0.7995	0.2906
0.76	2.8826	0.8060	0.2796
0.77	2.8660	0.8126	0.2686
0.78	2.8494	0.8193	0.2575
0.79	2.8327	0.8261	0.2463
0.8	2.8159	0.8330	0.2351
0.81	2.7991	0.8400	0.2239
0.82	2.7822	0.8472	0.2126
0.83	2.7653	0.8544	0.2013
0.84	2.7483	0.8618	0.1899
0.85	2.7312	0.8693	0.1784
0.86	2.7141	0.8770	0.1669
0.87	2.6969	0.8848	0.1554
0.88	2.6797	0.8927	0.1438
0.89	2.6623	0.9008	0.1321
0.9	2.6450	0.9090	0.1204
0.91	2.6275	0.9173	0.1086
0.92	2.6100	0.9258	0.0968
0.93	2.5924	0.9345	0.0849
0.94	2.5748	0.9433	0.0729
0.95	2.5570	0.9523	0.0609
0.96	2.5392	0.9615	0.0489
0.97	2.5214	0.9709	0.0367

(Continued)

TABLE 4.1 (Cont.)

Phi	r	c	t
0.98	2.5035	0.9804	0.0246
0.99	2.4855	0.9901	0.0123
1	2.4674	1.0000	0.0000
1.01	2.4493	1.0101	-0.0124
1.02	2.4311	1.0204	-0.0248
1.03	2.4128	1.0309	-0.0373
1.04	2.3944	1.0416	-0.0498
1.05	2.3760	1.0526	-0.0625
1.06	2.3575	1.0638	-0.0752
1.07	2.3389	1.0752	-0.0879
1.08	2.3202	1.0868	-0.1007
1.09	2.3015	1.0987	-0.1136
1.1	2.2827	1.1109	-0.1266
1.11	2.2638	1.1233	-0.1396
1.12	2.2448	1.1360	-0.1527
1.13	2.2258	1.1490	-0.1658
1.14	2.2066	1.1623	-0.1790
1.15	2.1874	1.1759	-0.1923
1.16	2.1681	1.1898	-0.2057
1.17	2.1487	1.2040	-0.2192
1.18	2.1293	1.2185	-0.2327
1.19	2.1097	1.2335	-0.2463
1.2	2.0901	1.2487	-0.2599
1.21	2.0704	1.2644	-0.2737
1.22	2.0506	1.2804	-0.2875
1.23	2.0307	1.2968	-0.3014
1.24	2.0107	1.3137	-0.3153
1.25	1.9906	1.3309	-0.3294
1.26	1.9705	1.3487	-0.3435
1.27	1.9502	1.3669	-0.3577
1.28	1.9299	1.3855	-0.3720
1.29	1.9094	1.4047	-0.3864
1.3	1.8889	1.4244	-0.4009
1.31	1.8683	1.4447	-0.4154
1.32	1.8476	1.4655	-0.4300
1.33	1.8267	1.4869	-0.4447
1.34	1.8058	1.5089	-0.4595
1.35	1.7848	1.5316	-0.4744
1.36	1.7637	1.5549	-0.4894
1.37	1.7425	1.5790	-0.5044

(Continued)

TABLE 4.1 (Cont.)

Phi	r	c	t
1.38	1.7212	1.6038	-0.5196
1.39	1.6997	1.6293	-0.5348
1.4	1.6782	1.6557	-0.5502
1.41	1.6566	1.6828	-0.5656
1.42	1.6348	1.7109	-0.5811
1.43	1.6130	1.7399	-0.5967
1.44	1.5910	1.7699	-0.6125
1.45	1.5690	1.8009	-0.6283
1.46	1.5468	1.8329	-0.6442
1.47	1.5245	1.8661	-0.6602
1.48	1.5021	1.9005	-0.6763
1.49	1.4796	1.9361	-0.6925
1.5	1.4570	1.9731	-0.7089
1.51	1.4342	2.0114	-0.7253
1.52	1.4114	2.0512	-0.7418
1.53	1.3884	2.0926	-0.7585
1.54	1.3653	2.1356	-0.7752
1.55	1.3420	2.1804	-0.7921
1.56	1.3187	2.2271	-0.8090
1.57	1.2952	2.2757	-0.8261
1.58	1.2716	2.3264	-0.8433
1.59	1.2479	2.3794	-0.8606
1.6	1.2240	2.4348	-0.8781
1.61	1.2000	2.4927	-0.8956
1.62	1.1759	2.5534	-0.9133
1.63	1.1516	2.6170	-0.9311
1.64	1.1272	2.6838	-0.9490
1.65	1.1027	2.7540	-0.9670
1.66	1.0780	2.8278	-0.9852
1.67	1.0532	2.9056	-1.0035
1.68	1.0282	2.9877	-1.0219
1.69	1.0031	3.0744	-1.0405
1.7	0.9779	3.1662	-1.0592
1.71	0.9525	3.2635	-1.0780
1.72	0.9270	3.3667	-1.0969
1.73	0.9013	3.4766	-1.1160
1.74	0.8754	3.5936	-1.1353
1.75	0.8494	3.7187	-1.1546
1.76	0.8233	3.8524	-1.1741
1.77	0.7969	3.9960	-1.1938

(Continued)

TABLE 4.1 (Cont.)

Phi	r	c	t
1.78	0.7705	4.1504	-1.2136
1.79	0.7438	4.3169	-1.2336
1.97	0.2339	14.8562	-1.6208
1.98	0.2038	17.1355	-1.6440
1.99	0.1734	20.2327	-1.6674
2	0.1428	24.6841	-1.6910
2.01	0.1120	31.6264	-1.7148
2.02	0.0809	43.9616	-1.7388
2.03	0.0497	71.9627	-1.7631
2.04	0.0182	197.3863	-1.7875
2.05	-0.0135	-267.2161	-1.8122
2.06	-0.0455	-79.8138	-1.8371
2.07	-0.0777	-46.9612	-1.8622
2.08	-0.1101	-33.2921	-1.8875
2.09	-0.1428	-25.8013	-1.9130
2.1	-0.1757	-21.0722	-1.9388
2.11	-0.2089	-17.8154	-1.9648
2.12	-0.2423	-15.4361	-1.9911
2.13	-0.2760	-13.6217	-2.0176
2.14	-0.3099	-12.1925	-2.0444
2.15	-0.3441	-11.0376	-2.0714
2.16	-0.3786	-10.0850	-2.0986
2.17	-0.4134	-9.2858	-2.1261
2.18	-0.4485	-8.6059	-2.1539
2.19	-0.4838	-8.0203	-2.1820
2.2	-0.5194	-7.5107	-2.2103
2.21	-0.5553	-7.0632	-2.2389
2.22	-0.5916	-6.6673	-2.2678
2.23	-0.6281	-6.3143	-2.2970
2.24	-0.6649	-5.9978	-2.3264
2.25	-0.7020	-5.7124	-2.3562
2.26	-0.7395	-5.4537	-2.3863
2.27	-0.7773	-5.2181	-2.4166
2.28	-0.8154	-5.0027	-2.4473
2.29	-0.8538	-4.8050	-2.4783
2.3	-0.8926	-4.6230	-2.5096
2.31	-0.9318	-4.4547	-2.5413
2.32	-0.9713	-4.2988	-2.5733
2.33	-1.0111	-4.1540	-2.6056
2.34	-1.0513	-4.0190	-2.6383

(Continued)

TABLE 4.1 (Cont.)

Phi	r	c	t
2.35	-1.0919	-3.8930	-2.6713
2.36	-1.1328	-3.7750	-2.7047
2.37	-1.1742	-3.6644	-2.7384
2.38	-1.2159	-3.5604	-2.7725
2.39	-1.2580	-3.4626	-2.8070
2.4	-1.3006	-3.3703	-2.8419
2.41	-1.3435	-3.2831	-2.8772
2.42	-1.3869	-3.2006	-2.9129
2.43	-1.4307	-3.1225	-2.9490
2.44	-1.4749	-3.0484	-2.9855
2.45	-1.5196	-2.9780	-3.0224
2.46	-1.5647	-2.9111	-3.0598
2.47	-1.6103	-2.8473	-3.0976
2.48	-1.6563	-2.7865	-3.1359
2.49	-1.7028	-2.7286	-3.1746
2.5	-1.7499	-2.6732	-3.2138
2.51	-1.7974	-2.6202	-3.2534
2.52	-1.8454	-2.5695	-3.2936
2.53	-1.8939	-2.5210	-3.3342
2.54	-1.9430	-2.4744	-3.3754
2.55	-1.9926	-2.4298	-3.4170
2.56	-2.0427	-2.3869	-3.4592
2.57	-2.0934	-2.3457	-3.5020
2.58	-2.1447	-2.3061	-3.5452
2.59	-2.1965	-2.2680	-3.5891
2.6	-2.2490	-2.2312	-3.6335
2.61	-2.3020	-2.1959	-3.6785
2.62	-2.3557	-2.1618	-3.7241
2.63	-2.4100	-2.1289	-3.7704
2.64	-2.4650	-2.0971	-3.8172
2.65	-2.5206	-2.0665	-3.8647
2.66	-2.5769	-2.0369	-3.9128
2.67	-2.6339	-2.0082	-3.9616
2.68	-2.6915	-1.9805	-4.0111
2.69	-2.7499	-1.9538	-4.0613
2.7	-2.8091	-1.9278	-4.1122
2.71	-2.8690	-1.9027	-4.1639
2.72	-2.9296	-1.8784	-4.2162
2.73	-2.9911	-1.8548	-4.2694
2.74	-3.0533	-1.8319	-4.3233

(Continued)

TABLE 4.1 (Cont.)

Phi	r	c	t
2.75	-3.1164	-1.8097	-4.3781
2.76	-3.1803	-1.7882	-4.4336
2.77	-3.2451	-1.7673	-4.4900
2.78	-3.3108	-1.7470	-4.5473
2.79	-3.3774	-1.7273	-4.6055
2.8	-3.4449	-1.7081	-4.6645
2.81	-3.5133	-1.6895	-4.7245
2.82	-3.5828	-1.6714	-4.7854
2.83	-3.6532	-1.6538	-4.8474
2.84	-3.7246	-1.6366	-4.9103
2.85	-3.7972	-1.6200	-4.9742
2.86	-3.8707	-1.6038	-5.0392
2.87	-3.9454	-1.5880	-5.1053
2.88	-4.0213	-1.5726	-5.1725
2.89	-4.0983	-1.5576	-5.2409
2.9	-4.1765	-1.5430	-5.3104
2.91	-4.2559	-1.5288	-5.3811
2.92	-4.3366	-1.5149	-5.4531
2.93	-4.4186	-1.5014	-5.5263
2.94	-4.5019	-1.4882	-5.6008
2.95	-4.5866	-1.4754	-5.6767
2.96	-4.6727	-1.4628	-5.7540
2.97	-4.7602	-1.4506	-5.8327
2.98	-4.8492	-1.4387	-5.9129
2.99	-4.9398	-1.4270	-5.9946
3	-5.0320	-1.4157	-6.0778
3.01	-5.1258	-1.4046	-6.1627
3.02	-5.2212	-1.3937	-6.2491
3.03	-5.3184	-1.3832	-6.3373
3.04	-5.4174	-1.3728	-6.4273
3.05	-5.5182	-1.3628	-6.5191
3.06	-5.6209	-1.3529	-6.6127
3.07	-5.7256	-1.3433	-6.7083
3.08	-5.8323	-1.3339	-6.8058
3.09	-5.9410	-1.3247	-6.9055
3.1	-6.0519	-1.3157	-7.0072
3.11	-6.1651	-1.3069	-7.1111
3.12	-6.2805	-1.2983	-7.2174
3.13	-6.3984	-1.2899	-7.3259
3.14	-6.5186	-1.2817	-7.4369

(Continued)

TABLE 4.1 (Cont.)

Phi	r	c	t
3.15	-6.6415	-1.2737	-7.5505
3.16	-6.7669	-1.2659	-7.6666
3.17	-6.8951	-1.2582	-7.7854
3.18	-7.0262	-1.2508	-7.9071
3.19	-7.1601	-1.2434	-8.0316
3.2	-7.2971	-1.2363	-8.1592
3.21	-7.4373	-1.2293	-8.2899
3.22	-7.5807	-1.2224	-8.4238
3.23	-7.7276	-1.2157	-8.5611
3.24	-7.8779	-1.2092	-8.7019
3.25	-8.0320	-1.2028	-8.8464
3.26	-8.1899	-1.1965	-8.9947
3.27	-8.3518	-1.1904	-9.1469
3.28	-8.5178	-1.1844	-9.3032
3.29	-8.6881	-1.1786	-9.4639
3.3	-8.8629	-1.1729	-9.6290
3.31	-9.0425	-1.1673	-9.7988
3.32	-9.2269	-1.1618	-9.9734
3.33	-9.4165	-1.1565	-10.1532
3.34	-9.6114	-1.1512	-10.3382
3.35	-9.8119	-1.1461	-10.5289
3.36	-10.0183	-1.1412	-10.7253
3.37	-10.2308	-1.1363	-10.9279
3.38	-10.4497	-1.1315	-11.1369
3.39	-10.6755	-1.1269	-11.3526
3.5	-13.7190	-1.0824	-14.2840
3.51	-14.0601	-1.0789	-14.6148
3.52	-14.4149	-1.0755	-14.9591
3.53	-14.7842	-1.0722	-15.3180
3.54	-15.1689	-1.0690	-15.6922
3.55	-15.5702	-1.0659	-16.0829
3.56	-15.9890	-1.0628	-16.4912
3.57	-16.4267	-1.0599	-16.9183
3.58	-16.8845	-1.0570	-17.3655
3.59	-17.3640	-1.0542	-17.8343
3.6	-17.8668	-1.0514	-18.3264
3.61	-18.3946	-1.0488	-18.8435
3.62	-18.9494	-1.0462	-19.3875
3.63	-19.5335	-1.0438	-19.9608
3.64	-20.1492	-1.0413	-20.5657

(Continued)

TABLE 4.1 (Cont.)

Phi	r	c	t
3.65	-20.7993	-1.0390	-21.2049
3.66	-21.4868	-1.0367	-21.8814
3.67	-22.2150	-1.0345	-22.5987
3.68	-22.9879	-1.0324	-23.3606
3.69	-23.8096	-1.0304	-24.1713
3.7	-24.6852	-1.0284	-25.0358
3.71	-25.6201	-1.0265	-25.9597
3.72	-26.6208	-1.0247	-26.9492
3.73	-27.6945	-1.0229	-28.0117
3.74	-28.8496	-1.0212	-29.1556
3.75	-30.0960	-1.0196	-30.3907
3.76	-31.4449	-1.0180	-31.7284
3.77	-32.9098	-1.0165	-33.1820
3.78	-34.5066	-1.0151	-34.7673
3.79	-36.2539	-1.0138	-36.5033
3.8	-38.1745	-1.0125	-38.4124
3.81	-40.2956	-1.0112	-40.5220
3.82	-42.6506	-1.0101	-42.8655
3.83	-45.2809	-1.0090	-45.4842
3.84	-48.2381	-1.0079	-48.4298
3.85	-51.5874	-1.0070	-51.7674
3.86	-55.4130	-1.0061	-55.5813
3.87	-59.8247	-1.0052	-59.9813
3.88	-64.9691	-1.0045	-65.1139
3.89	-71.0459	-1.0037	-71.1789
3.9	-78.3349	-1.0031	-78.4560
3.91	-87.2400	-1.0025	-87.3492
3.92	-98.3675	-1.0020	-98.4647
3.93	-112.6696	-1.0015	-112.7548
3.94	-131.7337	-1.0011	-131.8069
3.95	-158.4168	-1.0008	-158.4779
3.96	-198.4334	-1.0005	-198.4823
3.97	-265.1166	-1.0003	-265.1534
3.98	-398.4666	-1.0001	-398.4912
3.99	-798.4833	-1.0000	-798.4956
4	65,535.0000	-1.0000	INF



Taylor & Francis

Taylor & Francis Group

<http://taylorandfrancis.com>

@Seismicisolation

5 Mathieu Stability of Compliant Structures

5.1 INTRODUCTION

Structural systems that are designed as form dominant are also compelled to remain as positive buoyant while encountering the lateral loads. Offshore floating platforms, ships and large vessels, semi-submersibles and offshore production platforms that are moored to the seabed fall in this category. While they are flexible in the horizontal plane, they remain very stiff in the vertical plane, imposing motion constraints to the topside. Mathieu equation describes the stability of compliant structures to their parametric oscillations whose solution is dependent on Mathieu parameters and represented as Mathieu stability chart (Chandrasekaran & Kiran, 2017). Mathieu stability conditions should be satisfied to ensure the safe operations of these structures. Position restrained by high pretension tethers, floating and compliant offshore platforms exhibit larger stiffness in the vertical plane. These platforms are generally moored to the seabed using mooring lines or tethers, which ensure position restraint of the platform under the lateral loads caused by ocean waves. They experience coupled response between the displacements in a horizontal and vertical plane under the environmental loads, resulting in the dynamic tether tension variations in the mooring lines (Chandrasekaran, 2015b). Under the displaced position, the horizontal component of tether force enables recentering of the deck while the vertical component imposes heave restraint. Thus, a major contribution to their stability under operational loads is achieved by tethers. Classic examples of such structural systems are tension leg platforms, triceratops, buoyant-leg storage, regasification platforms and semi-submersibles. Their dynamic tension variations impose a challenge to its stability, which can be described using the Mathieu equation. Detailed studies on spar platforms showed Mathieu-type instability in systems where the natural pitch period is about twice as that of the heave (Haslum & Faltinsen, 1999; Koo et al., 2004). Dynamic behavior under such unstable conditions showed chaotic behavior, which is critical to ensure safe functionality of the platform (Rho et al., 2005).

5.2 MOORING SYSTEMS

Mooring systems play a significant role in position restraining and recentering of offshore compliant and floating structures. Mooring lines that extend from the structure to the seabed may be of the following types (i) steel chain type,

(ii) steel wire ropes and (iii) synthetic ropes. A specific type of the mooring is chosen according to the strength and elasticity requirements, apart from the structural and functional requirements of the platforms that are moored.

The catenary mooring system is the most common type of the mooring system deployed in the offshore industry. Catenary mooring systems have mooring length much greater than that of the water depth; hence, they are freely suspended from the structure, resulting in a catenary shape formed when freely suspended due to its self-weight. Catenary moorings resist the loads by their self-weight alone. When the structure responds to an external force, it tends to lift the mooring lines. In such cases, self-weight of the lines pulls down by applying an equivalent restoring force and thus holding down the structure. Guyed towers and semi-submersibles are examples of offshore structures using catenary mooring systems.

Taut mooring systems are used for positively buoyant offshore platforms like tension leg platforms (TLPs). In this type, the moorings are tightly stretched to accommodate a very high initial pretension. Pretension is imposed on the moorings by altering the draft of the platform, which is usually done by ballasting and deballasting. Unlike the earlier type, taut moorings require high axial stiffness and elasticity. Upon the response of the structure to lateral loads, moorings get stretched. It invokes an equivalent magnitude of the restoring force, which arises from the axial stiffness of moorings. Taut-mooring system provides high stiffness in the vertical plane and better load distribution between the mooring lines. Unlike catenary moorings, a taut mooring imposes high vertical forces in the anchor, and thus anchors should be designed for sustaining this pullout. Taut mooring may be vertical or inclined.

Turret-mooring system, as shown in Fig. 5.1, consists of a vertical assembly with a rotating holder to hold the mooring lines. It is a single-point-mooring



FIGURE 5.1 Turret-mooring system.

system commonly deployed in vessels and FPSOs. The lower end of the moorings is fixed to the seabed while the other end to the turret, which is integrated into the vessel. Turret-mooring system can be either internal or external.

5.3 MATHIEU EQUATION

Mathieu equation describes the stability of compliant structures for their parametric oscillations. The solution to this equation depends upon the Mathieu parameters, which are represented in the Mathieu stability chart (Chandrasekaran & Kiran, 2018). Mathieu equation to assess the stability of floating structures that are anchored to seabed is given by the following expression:

$$\frac{d^2y}{dz^2} + (\delta - 2q\cos(2z))y = 0 \quad (5.1)$$

where δ and q are known as Mathieu parameters. Mathieu equation is a special form of Hills equation with a single harmonic mode. A general solution cannot be obtained for this equation as it depends on the values of the parameters. Therefore, the solution to the Mathieu equation is described by the Floquet's theorem as follows:

$$\gamma_\gamma(z) = e^{i\sqrt{\lambda}z} p(z) \quad (5.2)$$

where γ is a function of Mathieu parameters δ and q , $p(z)$ is a periodic function with same period of cosine function as shown in Eq. (5.1). Solution of the equation is periodic with periods varying from (π or 2π), if γ is real and integer. The solution is said to be unstable, if γ is an imaginary number for which the periodic function will vary in the range $(-\infty, +\infty)$. Mathieu equation shall be satisfied by one of the periodic solutions given below:

$$y = \sum_{n=0}^{\infty} A_{2n} \cos 2nz \quad (5.3a)$$

$$y = \sum_{n=0}^{\infty} A_{2n+1} \cos (2n+1)z \quad (5.3b)$$

$$y = \sum_{n=0}^{\infty} B_{2n+1} \cos (2n+1)z \quad (5.3c)$$

$$y = \sum_{n=0}^{\infty} B_{2n+2} \cos (2n+2)z \quad (5.3d)$$

The recurrence relation is obtained by substituting Eq. (5.3) in Eq. (5.2) and equating cosine and sine function to zero for $n = 0, 1, 2, 3, \dots$. For the given

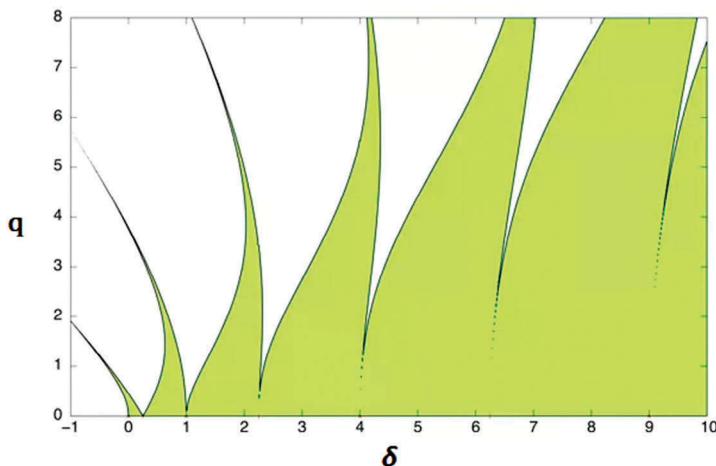


FIGURE 5.2 Mathieu stability chart.

values of n , Mathieu parameters (q, δ) are obtained by trial and error method. These are plotted to obtain the Mathieu stability chart. Figure 5.2 shows a typical Mathieu stability chart, where the colored region shows stable area while the uncolored ones represent the unstable region.

5.4 MATHIEU STABILITY FOR COMPLIANT STRUCTURES

The new-generation offshore compliant structures namely triceratops and buoyant leg storage and regasification platform (BLSRP) are inspired from the existing offshore structures (Chandrasekaran & Lognath, 2016; Chandrasekaran et al., 2015b). Both the new platforms are form-dominant design, where the structural form is conceived to counteract the applied lateral loads (Chandrasekaran & Nannaware, 2014). The structure remains floating in the sea but position restrained by tethers with high initial pretension (Chandrasekaran & Nassery, 2015b). As both the platforms are compliant (means, flexible in the horizontal plane), they alleviate the lateral loads that arise from waves, wind and current by undergoing large displacements but not by their strength of the members (Chandrasekaran & Mayank, 2017; Chandrasekaran et al., 2015b). Patel and Park (1991) investigated the dynamic analysis of tethers under low pretension for the parametric oscillation of tethers using Mathieu equation. They considered tether as a simply supported column element subjected to constant axial tension and neglected the nonlinear damping term. Lateral motion of tethers is expressed as a partial differential equation, which is further reduced to a nonlinear Mathieu equation using Galerkin's method. Even though stability charts for small parameters exists (Goldstein, 1929; Ince, 1925), Mathieu stability chart is extended to large parameters using the perturbation method.

Simos and Pesce (1997) generated a dynamic model for the Mathieu equation for TLP tethers using a linear cable equation. Lateral vibration of tethers is assumed to arise from the submerged mass of the tethers, resulting in dynamic tension variation in tethers. Chandrasekaran et al. (2006b) illustrated the stability of tension leg platforms at different water depths and examined the effect of geometric shape on Mathieu stability. Tao and Jun (2006) showed that the presence of damping eliminates Mathieu-type stability in high-order unstable zones. Mathieu instability is found to be critical in lower stability zones due to limited effects of damping. Stability chart with damping for regular waves was generated, and generation of stability chart for damped irregular wave condition remains highly challenging.

Haslum and Faltinsen (1999) presented Mathieu instability in pitch response of spar platforms for different geometric forms of the spar platform; heave-pitch coupling effects are included in the Mathieu stability analysis. Extreme heave response was observed under unstable condition, resulting from a larger pitch response. It verifies the fact that pitch damping shall reduce the unstable motion of the compliant structures. Rho et al. (2005) verified through experimental investigations that Mathieu-type instability occurs when the natural pitch period is twice as that of the heave. Koo et al. (2004) also investigated the heave and pitch coupling effects using a modified Mathieu equation. They showed that under unstable condition, a lock-in phenomenon is noted in pitch response. They also confirmed that increased pitch damping reduces instability.

Further, they suggested that shifting of the natural frequency of the pitch motion has a significant effect on stability; it can be achieved by considering the riser buoyancy. Rho et al. (2005) showed that a larger heave response makes the metacentric height negative, which in turn results in unstable configuration and cause dynamic instability. The addition of helical stakes and damping plates restricts the heave resonance motion and thus helps stabilize the unstable nonlinear motion.

Tethers play a significant role in the stability of taut-moored compliant structures, and hence understanding tether stability is important. Further section deals with the stability analysis of triceratops and BLSRP in detail.

5.5 MATHIEU STABILITY OF TRICERATOPS

Mathieu equation and parameters are used to examine the stability of various systems such as stability of oscillations, electrical circuits with varying resistance, the vibration of structures under stretched strings and column subjected to periodic axial pull (Mclachlan, 1947). Mathieu stability chart represents the solution for Mathieu's equation (Goldstein, 1929). A general solution does not exist as they are dependent on Mathieu's problem-specific parameters (Ince, 1925). The environmental load on taut-moored structures induces dynamic tension variation in tethers. It may cause instability in tethers, which can be identified using the Mathieu equation (Koo et al., 2004). Mathieu equation is a second order, linear, homogeneous differential equation whose canonical form is given in Eq. (5.1), where (δ, q) are termed as Mathieu parameters. Mathieu equation is

a special form of Hills equation with single harmonic mode. Solution to this equation can be obtained using Hill's method or Floquet's theory. However, for obtaining solution involving large parameters, the perturbation method is used to obtain the solution; the latter is required in case of offshore compliant structures. It is important to note that the Mathieu parameters (δ , q) are required to be derived for each case under study.

5.5.1 FORMULATION OF MATHIEU EQUATION

Dynamic equation of tether is formulated using an idealized linear model (Simos & Pesce, 1997). Dynamic equation of tether vibration is formulated using an idealized linear model (Chandrasekaran & Kiran, 2017; Chandrasekaran & Seeram, 2012). It is similar to that of the straight, slender column with simply supported ends under varying axial tension caused by its submerged mass (Nagavinothini & Chandrasekaran, 2019). Ignoring the effects caused by the flexural rigidity, the dynamic equation for the lateral motion of tethers is given as

$$M \frac{\partial^2 y}{\partial t^2} - \frac{\partial}{\partial x} \left[T(x) \cdot \frac{\partial y}{\partial x} \right] + Bv \left| \frac{\partial y}{\partial t} \right| \cdot \frac{\partial y}{\partial t} = 0 \quad (5.4)$$

where M is the total mass of the tether, which is the sum of added mass and physical mass per unit length. $T(x)$ is the total tension in the tether, which is the sum of static tension and dynamic tension and is given as

$$T(x) = P + mg(L - x) - A \cos(\omega t) \quad (5.5)$$

where P is the initial pretension in tethers, m is the mass per unit length of the tether, L is the length of the tether, A is the tension amplitude, ω is the wave frequency and Bv is the viscous damping coefficient. For free lateral vibration of tether, Eq. (5.4) reduces to the following form:

$$M \frac{\partial^2 y}{\partial t^2} - \frac{\partial T(x)}{\partial x} = 0 \quad (5.6)$$

Let the lateral motion under n th mode is assumed as

$$y_n(X_n t) = f_n(t) \cdot X_n(x) \quad (5.7)$$

Substituting, Eq. (5.6) will result into the classical Sturm–Liouville problem:

$$\left[\frac{P}{M} + \frac{mg(L - x)}{M} \right] X_n + \omega_n^2 X_n = 0 \quad (5.8)$$

Eq. (5.8) can be rewritten using a new variable η . It shall reduce a modified Bessel equation as given below:

$$\eta^2 X_n + \eta X_n + 4\beta_n^2 \eta^2 X_n = 0 \quad (5.9)$$

$$\eta = \sqrt{1 + \frac{mg(L-x)}{P}} \quad (5.10)$$

$$\beta_n^2 = \frac{PM}{(mg)^2} \omega_n^2 \quad (5.11)$$

Solution for Eq. (5.8) is obtained in the form of Bessel functions (J_0 , Y_0) (Bowman, 1958):

$$X_n(n) = C_1 J_0(2\beta_n \eta) + C_2 Y_0(2\beta_n \eta) \quad (5.11)$$

Constants C_1 and C_2 can be deduced by applying the following boundary conditions:

$$X_n(\eta|\tau=0) = 0 \text{ and } X_n(\eta|\tau=1) = 0 \quad (5.12)$$

Eq. (5.11) reduces to the following form:

$$X_n(x) = J_0 \left(2\beta_n \sqrt{1 + \frac{mg(L-x)}{P}} \right) - \frac{J_0(2\beta_n)}{Y_0(2\beta_n)} Y_0 \left(2\beta_n \sqrt{1 + \frac{mg(L-x)}{P}} \right) \quad (5.13)$$

where β_n is obtained as the solution of the equation and is given as

$$J_0 \left(2\beta_n \sqrt{1 + \frac{mgL}{P}} \right) Y_0(2\beta_n) - Y_0 \left(2\beta_n \sqrt{1 + \frac{mgL}{P}} \right) J_0(2\beta_n) = 0 \quad (5.14)$$

By substituting and applying Galerkin's variation method, Eq. (5.4) is reduced to the following form:

$$\frac{d^2 f}{d\tau^2} + (\delta - q \cos(2\tau)) f + c \left| \frac{df}{d\tau} \right| \frac{df}{d\tau} = 0 \quad (5.15)$$

where $2\tau = \omega t$ (τ is a dimensionless time variable), (δ , q) are Mathieu parameters given by Patel and Park (1991):

$$\delta_n = \frac{4}{M\omega^2} \left\{ mg \frac{(I_2 + I_4)}{I_1} \right\} - (P + mgL) \frac{I_3}{I_1} \quad (5.16a)$$

$$q_n = -\frac{2A}{M\omega^2} \frac{I_3}{I_1} \quad (5.16b)$$

$$C_n = \frac{B}{M} \frac{I_5}{I_1} \quad (5.16c)$$

$$I_1 = \int_0^L X_n^2(x) dx \quad (5.17a)$$

$$I_2 = \int_0^L \frac{dX_n}{dx} dx \quad (5.17b)$$

$$I_3 = \int_0^L \frac{d^2X_n}{dx^2} X_n dx \quad (5.17c)$$

$$I_4 = \int_0^L \frac{d^2X_n}{dx^2} X_n x dx \quad (5.17d)$$

$$I_5 = \int_0^L x^3(x) dx \quad (5.17e)$$

Fig. 5.3 shows the stability chart extended to large parameters (Patel & Park, 1991; Rho et al., 2005) where shaded regions show instability.

5.5.2 MATHEMATICAL MODEL

A mathematical model is developed using MATLAB® to obtain the Mathieu parameters to study the dynamic stability of tethers. The lateral motion of tethers is computed for the first mode of frequency. Lateral motions of higher modes are neglected as they are insignificant in the present case. Tether properties such as pretension, length and area are applied along with tension amplitude from a numerical model to obtain the coefficients I_1 , I_2 , I_3 , I_4 and I_5 . Mathieu parameters are obtained for each case, appropriately. The Mathieu parameters thus obtained are plotted in stability chart to get the stability condition of the structure. The mathematical model generated using MATLAB® is validated with the existing results from the literature (Chandrasekaran et al., 2006b). The mathematical model developed has a maximum error of about 3.25%, which is well within the acceptable limits.

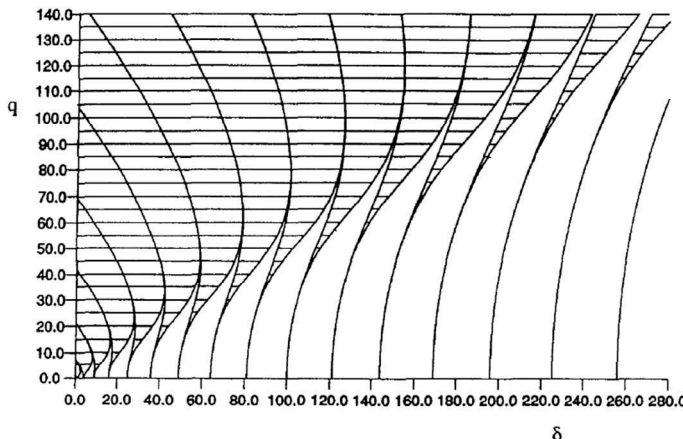


FIGURE 5.3 Mathieu extended stability chart (Patel & Park, 1991).

5.6 INFLUENCE OF PARAMETERS ON STABILITY

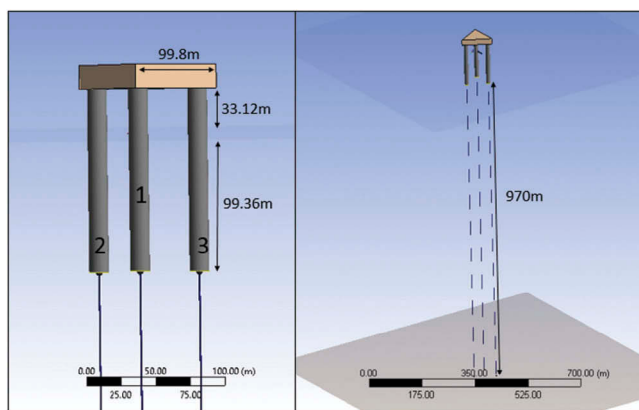
Numerical analysis of offshore triceratops for hydrodynamic response and dynamic tether tension variation are carried out. Triceratops consisting of three circular buoyant legs and the triangular deck are modeled using the software. As buoyant legs qualify for Morison region, they are modeled using line elements. Each buoyant leg is modeled with an outer diameter of 14.14 m and wall thickness of 0.15 m. The mass of buoyant legs, ballast load and weight of the deck is assigned to the mass center on the vertical plane. Each buoyant leg is modeled as an independent, rigid body as they are not interconnected. The deck consists of quadrilateral and triangular plate elements with appropriate mass properties. Buoyant legs are connected to the deck using ball joints. Tethers, those extending from the keel of the buoyant leg to seabed, are modeled as flexible elements. Buoyant legs are connected to the seabed with groups of tethers containing four tethers in each group. Total numbers of 12 tethers in three groups are used, one group per buoyant leg is used for mooring system. Geometric and structural details of the platform under study are given in Table 5.1. Fig. 5.4 shows the numerical model of the triceratops.

5.6.1 INFLUENCE OF WAVE HEIGHT

The numerical model is subjected to a regular wave of wave height 5.1 m and wave period 6.8 s for 500 s, and the tether tension variations are obtained. Figs. 5.5–5.7 show the dynamic tether tension variations in each buoyant leg, which will be further used to compute the stability. Triceratops is analyzed under different wave heights for a constant wave frequency, at a water depth 970 m. To investigate the influence of wave height on Mathieu parameters, the wave height is varied in the range of 8–15 m for a wave period of 15 s.

TABLE 5.1 Properties of triceratops

Description	Value	Units
Water depth	1069.36	m
Total mass	320,500	kN
Buoyant force	470,440	kN
Diameter of buoyant leg	14.14	m
Plan dimension	99.40	m
Freeboard	33.12	m
Draft	99.36	m
Length of buoyant leg	132.48	m
Total tether force	149,940	kN
Pretension in one tether	12,495	kN
Tether length	970	m
No. of tethers (three groups)	12	4 tethers in each group
Axial stiffness of tethers	57,623	kN/m
Unit weight of material	7850	kg/m ³
Unit weight of surrounding fluid	10.25	kN/m ³
r_{xx} of buoyant leg	76.65	m
r_{yy} of buoyant leg	76.65	m
r_{zz} of buoyant leg	6.99	m
r_{xx} of the deck	36.32	m
r_{yy} of the deck	54.35	m
r_{zz} of the deck	63.87	m

**FIGURE 5.4** Numerical model of offshore triceratops.

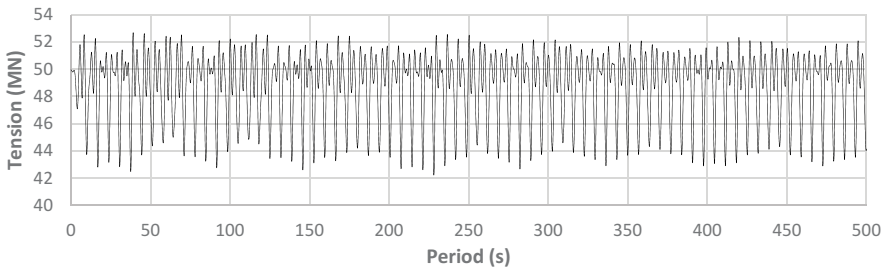


FIGURE 5.5 Tether tension variation in buoyant leg 1.

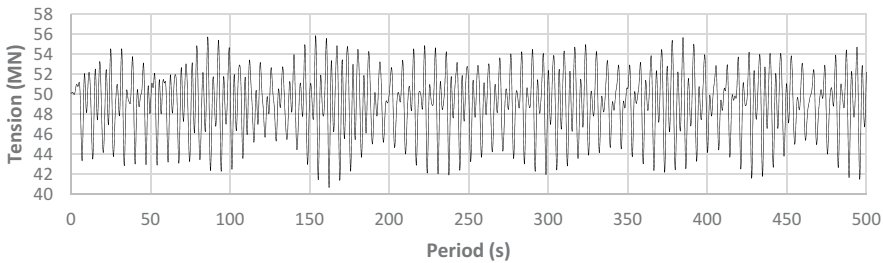


FIGURE 5.6 Tether tension variation in buoyant leg 2.

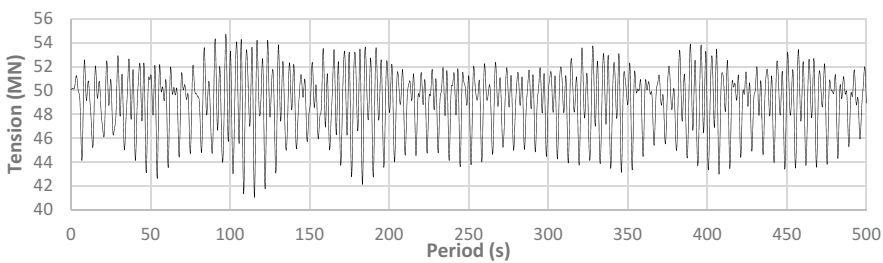


FIGURE 5.7 Tether tension variation in buoyant leg 3.

Maximum tension in each tether for each case is summarized in Table 5.2. It is observed from the table that tension variation increases with an increase in wave height. Corresponding to the maximum wave height of 15 m, a maximum tension variation of 11.14% of initial pretension is observed. With the tension variation obtained and tether properties, Mathieu stability analysis was done using the mathematical model, and the Mathieu parameters and its

TABLE 5.2 Tension variation in tethers for different wave height (wave period 15 s)

Wave height (m)	Buoyant leg 1 (MN)	Buoyant leg 2 (MN)	Buoyant leg 3 (MN)	Initial pretension (MN)
8	50.79	52.32	52.03	49.98
10	51.08	53.00	52.76	
12	51.46	53.82	53.74	
15	52.93	56.45	55.55	

TABLE 5.3 Influence of wave height on Mathieu parameters (wave period 15 s)

Wave height (m)	Mathieu parameters		Stability condition
	δ	q	
8	359.90	7.56	Stable
10	359.90	9.76	Stable
12	359.90	12.43	Stable
15	359.90	20.93	Stable

stability conditions are expressed in Table 5.3. From the table, it is noted that the Mathieu parameter (δ) remains unaffected but (q) increases with the increase in wave height. Since tension variation is not large enough to provoke Mathieu instability, the platform remains stable for all wave heights considered in the present study. However, the increase in parameter (q) independent of the parameter (δ) shows that the stability condition tends to shift towards the unstable region from a stable region. Depending upon the region of Mathieu parameters, an increase in wave height may lead to the unstable condition as a vertical shift in parameters is observed for the increase in wave height.

5.6.2 INFLUENCE OF WAVE PERIOD

To investigate the influence of wave frequency on Mathieu parameters, the triceratops is analyzed under different wave frequencies at a water depth of 970 m. Wave period is varied as 10, 12, 15 and 18 s for a constant wave height of 8 m. Maximum tension variation for each case is obtained from the numerical model and summarized in Table 5.4. The Mathieu parameters obtained from the mathematical model is listed in Table 5.5 along with its stability condition. The maximum tension in each tether is not influenced by the change in the wave period. Parameters show that the platform is stable under

TABLE 5.4 Tension variation in tethers for different wave frequencies

Wave period (s)	Buoyant leg 1 (MN)	Buoyant leg 2 (MN)	Buoyant leg 3 (MN)	Initial pretension (MN)
10	51.56	54.20	54.46	49.98
12	50.85	52.81	52.08	
15	50.79	52.32	52.03	
18	52.68	55.86	54.72	

TABLE 5.5 Mathieu parameters for different wave frequencies (wave height 8 m)

Wave period (s)	Mathieu parameters		Stability condition
	δ	q	
10	159.95	6.44	Stable
12	230.33	5.85	Stable
15	359.90	7.56	Stable
18	518.25	27.40	Stable

all wave periods considered in the study. However, the significant increase in the Mathieu parameter (δ) is noted for an increase in wave period while parameter (q) increases with a marginal variation. The increase in parameter (δ) shifts the parameters to a more stable region and hence increase in the wave period is advantageous to the stability condition. Thus, ensuring increased stability condition with an increase in the wave period.

5.6.3 INFLUENCE OF WATER DEPTH

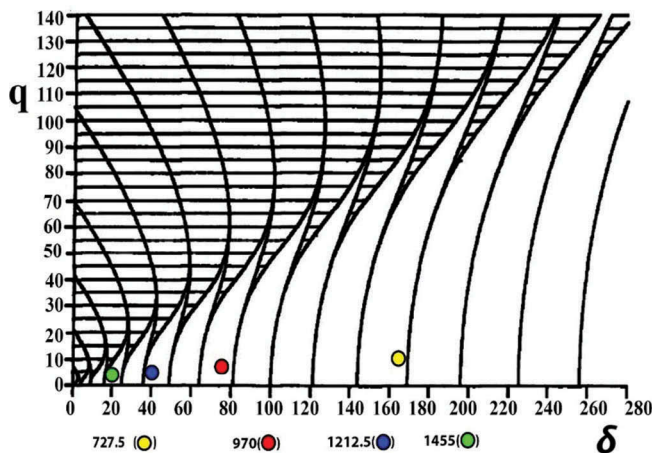
Triceratops under different water depth is analyzed under regular waves of (5 m, 6.8 s) for the dynamic tether tension variation. As stiffness remains unaltered, it is seen from the study that dynamic tether tension variation is not much significant. Maximum tension variation in each buoyant leg is given in Table 5.6. Stability analysis is carried out using a mathematical model, considering the changes in tether length and area of tethers for varying water depth and the parameters obtained are listed in Table 5.7. Corresponding points are traced on the extended stability chart, as shown in Fig. 5.8, and the stability conditions are obtained and listed in Table 5.7. As seen from the figure, a combination of larger values of (δ) and smaller values of (q) ensure stable condition. It is also evident that with

TABLE 5.6 Dynamic tension variation in tethers for different water depths

Water depth (m)	Stiffness (MN/m)	Buoyant leg 1 (MN)	Buoyant leg 2 (MN)	Buoyant leg 3 (MN)	Initial pretension (MN)
485.00	76.83	53.24	56.91	57.60	49.98
727.50		52.9	56.15	56.94	
970.00		52.68	55.86	54.72	
1212.50		52.98	56.61	57.68	
1455.00		53.17	58.73	57.75	

TABLE 5.7 Mathieu parameters for different water depth

Water depth (m)	Stiffness (MN/m)	Mathieu parameters		Stability condition
		δ	q	
485.00	76.83	544.81	40.32	Stable
727.50		167.35	10.95	Stable
970.00		73.969	3.91	Stable
1212.50		40.03	2.63	Stable
1455.00		24.69	1.74	Stable

**FIGURE 5.8** Mathieu stability for different water depths.

the increase in water depth, Mathieu parameters decrease and shift towards the first zone of stability region. It is important to note that in this region, even a minor variation in the Mathieu parameters significantly affect the stability condition. Hence, Mathieu stability analysis is more critical for deep water structures.

5.6.4 INFLUENCE OF TETHER STIFFNESS

Influence of axial stiffness of tethers on Mathieu stability is examined for a fixed water depth of 970 m; axial stiffness of tethers is varied. Tension variation in each leg of tethers is summarized in Table 5.8. It is seen from the table that tension variation in tethers decreases with the increase in stiffness and reduction in stiffness induces more tension in tethers as response increase. Mathieu parameters for each case are computed and summarized in Table 5.9; corresponding values are also mapped on the chart, as shown in Fig. 5.9. The shaded region shows an unstable condition. As expected, a reduction in stiffness to about 40% causes instability, which resulted in chaotic time history. Mathieu-type instability occurs for this case from the Mathieu parameters plotted in the figure. Since the parameters are not exhibiting linear variation, we cannot predict or extrapolate the Mathieu parameters. However, there is a direct correlation between the stiffness and stability, increase in stiffness

TABLE 5.8 Tension variation in tethers for different stiffness

Stiffness (MN/m)	% variation	Buoyant leg 1 (MN)	Buoyant leg 2 (MN)	Buoyant leg 3 (MN)	Initial pretension (MN)
92.20	+20	53.15	53.09	53.91	49.98
76.83	Normal	52.68	55.86	54.72	
61.46	-20	54.17	58.08	58.18	
36.88	-40	127.60	127.97	128.35	

TABLE 5.9 Mathieu parameters for different stiffness

Stiffness (MN/m)	% variation in stiffness	Mathieu parameters		Stability condition
		δ	q	
92.20	+20	62.93	2.18	Stable
76.83	normal	73.96	3.91	Stable
61.46	-20	90.53	6.80	Stable
36.88	-40	118.17	86.20	Unstable

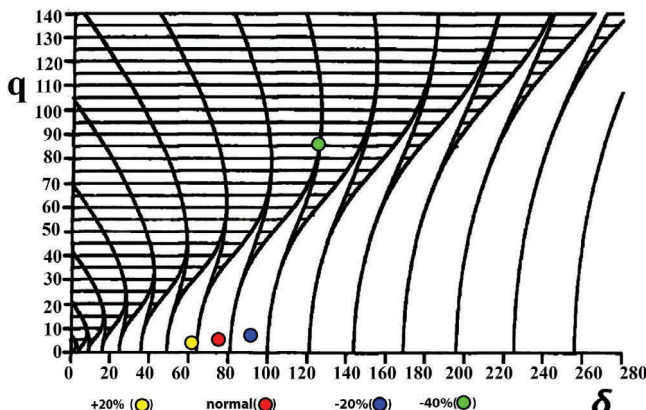


FIGURE 5.9 Mathieu stability chart for different tether stiffness.

increases the stability condition, and a decrease in stiffness leads to Mathieu instability.

5.6.5 INFLUENCE OF INCREASED PAYLOAD

The increased payload is admitted in the analysis to create a postulated failure under which tether stability is examined. It is important to note that increased payload results in the reduction of pretension in tethers. The magnitude of increase in the payload is expected to occur (and not unusual) in production and drilling platforms; such scenarios can even occur under normal operating conditions. Six different cases of postulated failure with increased payload are analyzed for tether tension variation under regular waves (5 m, 6.8 s), which corresponds to a normal operational sea state of deep water offshore platforms. The increase in payload and the corresponding reduction in initial tension is listed in Table 5.10. The amplitude of maximum tension in each

TABLE 5.10 Total mass and reduced pretension

Description	Case 1	Case 2	Case 3	Case 4	Case 5	Case 6
Increase in payload	–	5%	10%	15%	20%	25%
Total mass (kN)	320,500	336,525	352,550	368,575	384,600	400,625
Total tether force (MN)	149.940	133.915	117.890	101.865	85.840	69.815
Tether force in each leg (MN)	49.980	44.638	39.296	33.955	28.613	23.272
Pretension in each tether (MN)	12.495	11.159	9.824	8.488	7.153	5.817
% reduction in pretension	–	10.69	21.37	32.06	42.75	53.44

TABLE 5.11 Maximum tension variation under the increased payload

Description	Maximum tension in each leg (MN)			Initial tension in each leg (MN)
	1	2	3	
Case 1	52.553	55.597	54.621	49.980
Case 2 (5%)	50.654	63.001	62.499	44.638
Case 3 (10%)	58.246	62.917	58.818	39.296
Case 4 (15%)	66.335	78.912	72.455	33.955
Case 5 (20%)	101.928	83.372	90.697	28.613
Case 6 (25%)	105.323	94.725	92.779	23.271

TABLE 5.12 Mathieu parameters for increased payload

Description	Mathieu parameters		Stability condition
	δ	q	
Case 1	73.96	3.73	Stable
Case 2 (5%)	66.86	12.21	Stable
Case 3 (10%)	59.77	15.73	Stable
Case 4 (15%)	52.69	30.01	Unstable
Case 5 (20%)	45.62	49.12	Unstable
Case 6 (25%)	38.46	55.18	Unstable

leg is obtained using a numerical model and listed in Table 5.11. It is seen from the table that tension variation increases with the increase in payload. For an increase in payload more than 15%, tension variation is significantly high, and it becomes essential to examine tether stability under such variations.

Tether stability is examined under the dynamic tether tension variation using Mathieu's stability chart. Under the maximum tension variation (amplitude), dynamic analysis is carried out to obtain Mathieu parameters for each of the postulated failure cases; Mathieu parameters thus obtained are listed in Table 5.12, and the corresponding points are plotted in Mathieu's stability chart, as shown in Fig. 5.10; points that fall in the shaded region indicate that the platform is unstable. From the Mathieu stability analysis, it is seen that an increase in payload more than 15% causes Mathieu-type instability.

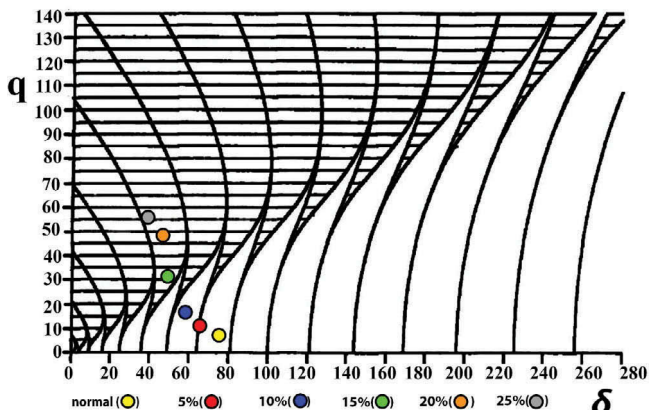


FIGURE 5.10 Mathieu stability chart for increased payload cases.

5.7 MATHIEU STABILITY OF BLSRP

The new geometric form of BLSRP is derived based on the functional requirements including salient advantages of different offshore structures (Chandrasekaran & Lognath, 2016, 2017a, 2017b). The deep-draft buoyant legs provide higher stiffness in the vertical plane as that of the spar while the positive buoyancy and taut-mooring system resemble the TLP. BLSRP is a form-dominant compliant structure, which resists environmental loads by its compliance. Compliance is allowing flexibility in the structure, and hence displacements of the buoyant legs are expected. Transfer of rotational degrees of freedom from buoyant leg to the deck causes discomfort, and hence hinged joints are used between legs and the deck to isolate the rotational degrees of freedom, an idea borrowed from offshore triceratops platforms where ball joints are used to isolate the deck. BLSRP is a hybrid geometry comprising the merits of different existing platforms in the offshore industry. Salient features of BLSRP are (i) positively buoyant structure, (ii) spread taut mooring system with high initial pretension, (iii) six buoyant legs placed symmetrically, (iv) isolation of rotational degrees of freedom in the deck using hinged joints, (v) deep draft buoyant legs and (vi) insensitivity to wave direction. Buoyant leg structures have few other advantages such as easy installation, transportation, fabrication and technical. This section shall describe the stability analyses of BLSRP in detail.

5.7.1 NUMERICAL MODELING

Numerical analysis of BLSRP is carried out in detail. BLSRP consists of a circular deck with the 100 m diameter and six buoyant legs placed symmetrically at 60° to each other. The draft of the legs are at three-fourths that of the

length of the buoyant legs, and thus making the buoyant legs as deep-draft systems. The circular deck is connected to legs using hinged joints, which isolates the rotational degrees of freedom. Buoyant legs are modeled as line elements since it qualifies for Morison region. Tethers that connect the legs to the seabed are modeled as flexible elements. Since BLSRP is positive-buoyant structure, it is position-restrained using high pretension tethers, comprising four tethers on each leg with a total of 24 tethers. Spread mooring system with 20° inclination is used to hold down the platform in position. Fig. 5.11 shows the numerical model, and Table 5.13 shows the structural details of the platform, which is under investigation. The static equilibrium between the mass, buoyancy force and the initial tether force is given as

$$F_b = W + 6T_0 \cos(20^\circ) \quad (5.18)$$

Without altering the static equilibrium, the geometric properties are derived considering the huge storage capacity of the regasification units, giving rise to a large mass.

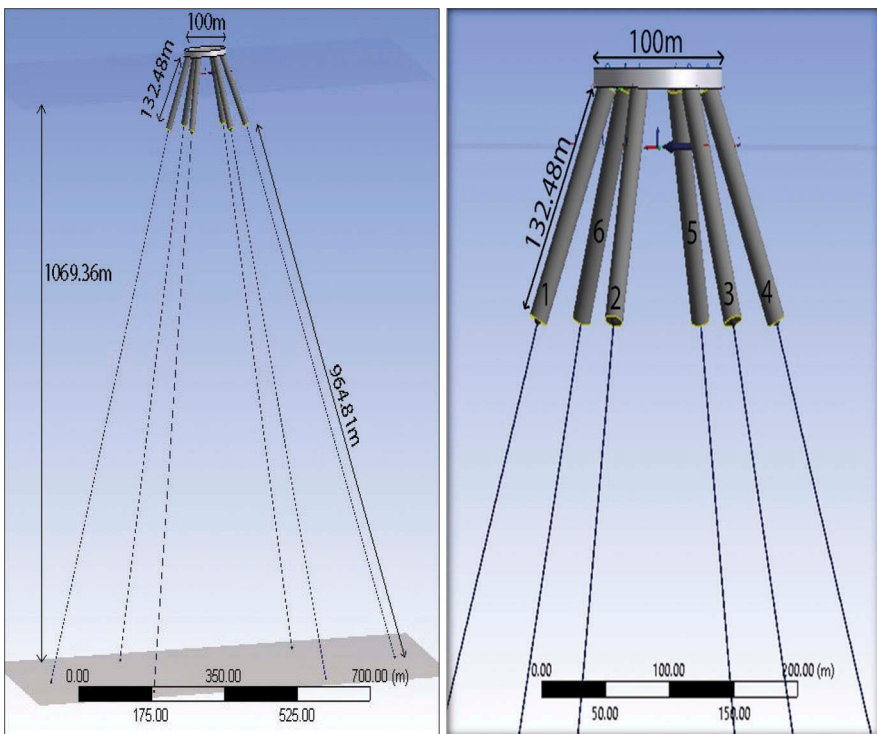


FIGURE 5.11 Numerical model of BLSRP.

TABLE 5.13 Structural properties of BLSRP (Chandrasekaran et al., 2015b)

Description	BLSRP	Units
Water depth	1069.36	M
Total mass	641,000	kN
Buoyant force	940,880	kN
Diameter of buoyant leg	14.14	m
Plan dimension	100	m
Freeboard	33.12	m
Draft	99.36	m
Length of buoyant leg	132.48	m
Total tether force	319,125.60	kN
Pretension in each leg	53,187.61	kN
Tether length	964.81	m
No. of tethers (six groups)	24	4 tethers/group
Axial stiffness of tethers	76,830.67	kN/m
Unit weight of material	7850	kg/m ³
Unit weight of surrounding fluid	10.25	kN/m ³
r_{xx} of buoyant leg	76.65	m
r_{yy} of buoyant leg	76.65	m
r_{zz} of buoyant leg	6.99	m
r_{xx} of deck	38.40	m
r_{yy} of deck	38.40	m
r_{zz} of deck	8.11	m

The numerical model of BLSRP is analyzed for hydrodynamic responses under a regular wave of height of 5.1 m and wave period of 6.8 s. The dynamic tether tension variation is obtained and plotted, as shown in Figs. 5.12–5.17, for each leg. The dynamic tether tension induces different heave responses in each leg, which is subsequently transferred to the deck as the platform is stiff in the vertical plane.

5.7.2 MATHIEU STABILITY UNDER TETHER PULLOUT

Two postulated failure conditions under tether pullout are discussed in this section. The effect of tether pullout on the stability of the structure is investigated using Mathieu stability analysis and compared with that of the normal condition (case 1). First postulated condition examined is single leg tether pullout (case 2), where the tethers in the wave-facing buoyant leg are removed (Fig. 5.18a). Second, the postulated condition is when the tethers of two buoyant legs are removed (Fig. 5.18b), i.e., buoyant leg one and four, which are opposite to each other (case 3).

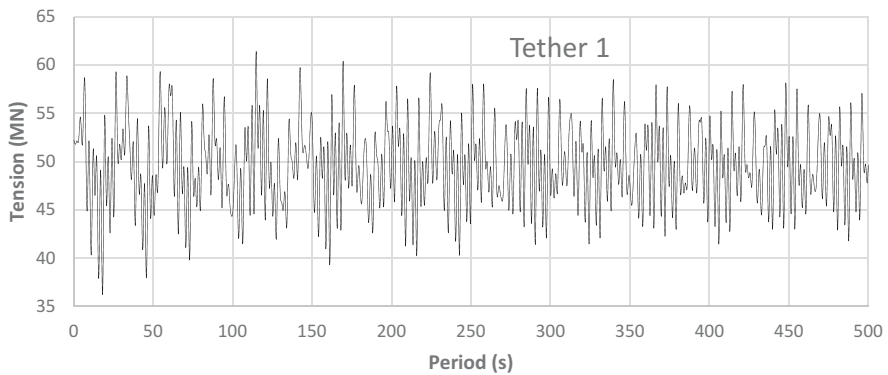


FIGURE 5.12 Tether tension variation in buoyant leg 1.

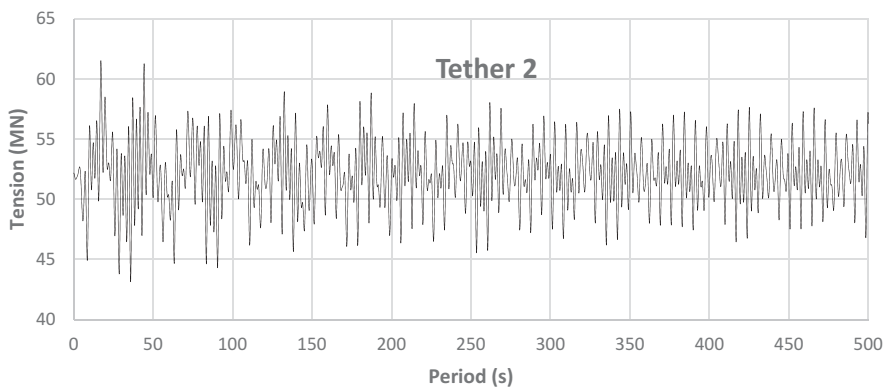


FIGURE 5.13 Tether tension variation in buoyant leg 2.

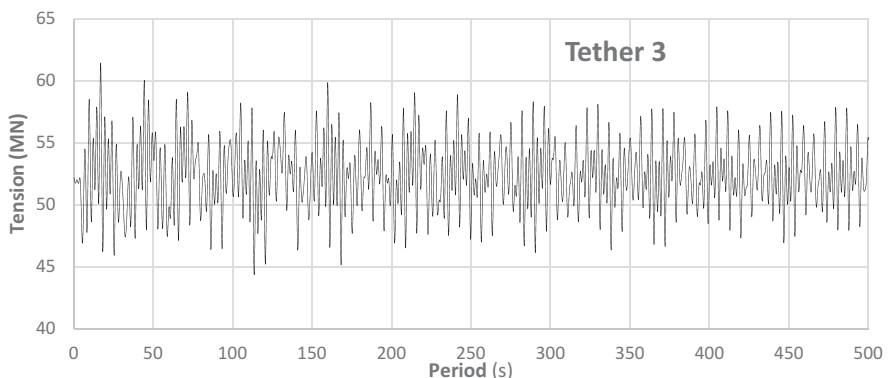


FIGURE 5.14 Tether tension variation in buoyant leg 3.

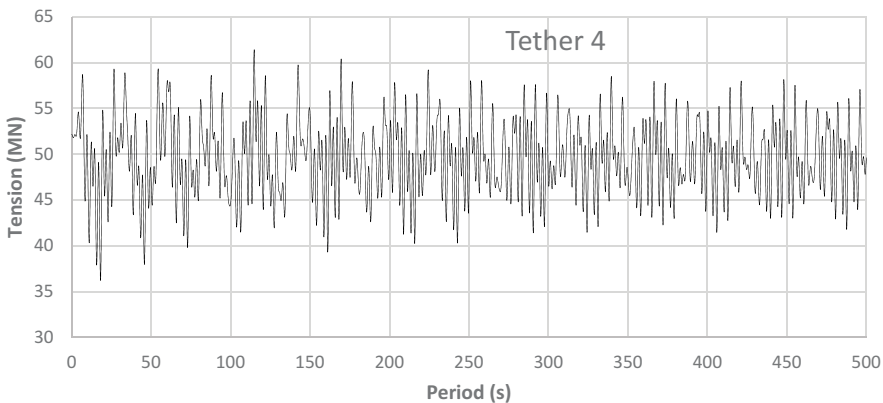


FIGURE 5.15 Tether tension variation in buoyant leg 4.

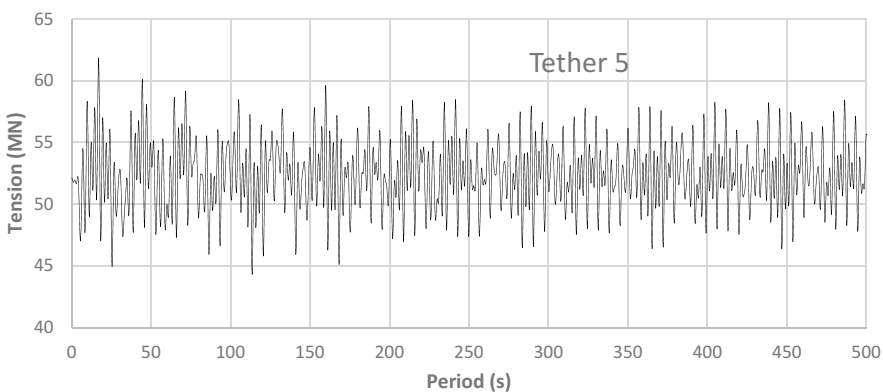


FIGURE 5.16 Tether tension variation in buoyant leg 5.

Dynamic response analysis is carried out under the postulated failure cases for a regular wave (5.1 m, 6.8 s) for 500 s. Upon the removal of tethers, redistribution of initial tether tension is noted in both the cases, inducing higher initial pretension in the tethers (Chandrasekaran & Kiran, 2018b; Chandrasekaran & Madhuri, 2015; Chandrasekaran et al., 2013c). For case 3, the removal of tethers in two legs increases the initial pretension by 50%. Table 5.14 shows the maximum tension amplitude in tethers, obtained from the dynamic analysis under the postulated failure cases.

Mathieu parameters are obtained for each case and listed in Table 5.15, along with its stability condition obtained from plotting the parameters in the

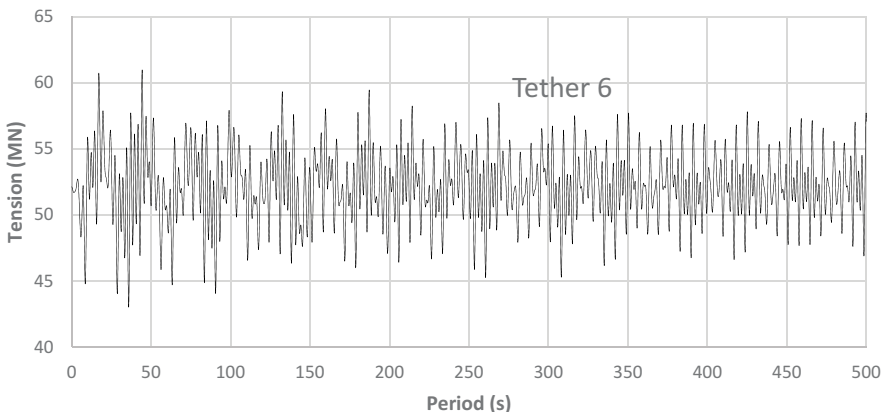


FIGURE 5.17 Tether tension variation in buoyant leg 6.

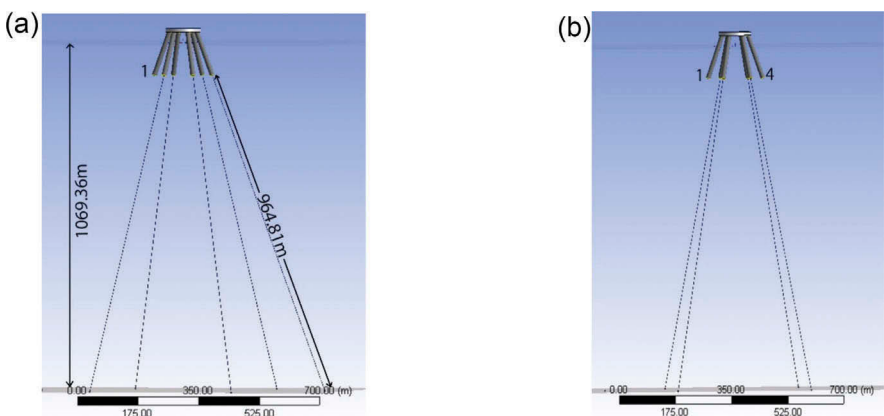


FIGURE 5.18 Postulated failure cases: (a) one leg affected and (b) two legs affected.

stability chart. Fig. 5.19 shows the plot. The parameter ' δ ' which depends on tether properties remains constant for all the cases, whereas parameter ' q ' increases for each case, which is very critical. The stability analysis shows that when the tethers of two buoyant legs are pulled out, Mathieu-type instability occurs indicating a chaotic nature in the tether tension.

As seen from the figure, for normal condition (case 1) where no tether pull-out is postulated, it confirms a stable condition. For the postulated case of failure case 2, stability parameters, even though move vertically toward the unstable region, the structure remains stable and Mathieu instability does not

TABLE 5.14 Maximum tension amplitude in tethers for postulated cases of failure

Description	Leg 1 (MN)	Leg 2 (MN)	Leg 3 (MN)	Leg 4 (MN)	Leg 5 (MN)	Leg 6 (MN)	Maximum tension (MN)
Normal (case 1)	62.49	61.53	61.43	61.40	61.85	60.97	62.49
Postulated failure (case 2)	–	94.93	81.0	89.92	94.57	97.41	97.41
Postulated failure (case 3)	–	148.28	142.98	–	141.30	144.28	148.28

TABLE 5.15 Mathieu parameters under postulated failure

Description	δ	q	Stability condition
Normal (case 1)	75.07	5.9	Stable
Case 2	75.07	28.06	Stable
Case 3	75.07	60.34	Unstable

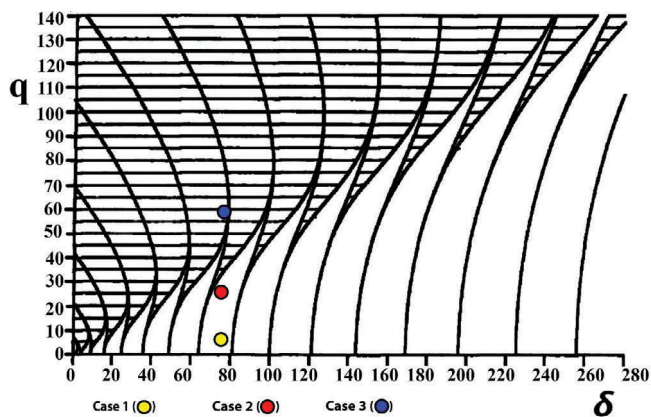


FIGURE 5.19 Mathieu stability chart for BLSRP under tether pullout cases.

occur. Further removal of tether 4 as in case 3 leads to instability. As seen from the table, one of the stability parameter (δ) remains unaltered for all the cases under consideration as this depends on tether stiffness and initial pretension. Significant increase in the other parameter q is observed under postulated cases of failure.

5.7.3 MATHIEU STABILITY ANALYSIS UNDER ECCENTRIC LOADING

Probability of eccentric loading is unavoidable in offshore platforms, which may occur under operational conditions. It is important to note that floating and compliant structures will be highly influenced under such conditions, and their stability will be challenged (Chandrasekaran & Lognath, 2015). Eccentricity may also result from the position of various equipment like cranes used for drilling. The presence of regasification units and storage tanks, which is one of the prime functions of the platform, imposes large mass to the platform. This section describes a detailed dynamic analysis carried out under probable eccentric loading and stability is assessed for each case. To investigate the effect of eccentric loading in BLSRP, three different cases of loading are considered. Figs. 5.20 to 5.22 show the position of eccentric loads on the deck. Each case of eccentric loading is analyzed for two load values, 5% and 10% of that of the total mass of the platform.

BLSRP is analyzed for tether tension variation under a regular wave (5 m, 6.8 s) in the condition of two eccentric loads: 32,050 kN (5%) and 64,100 kN (10%). Maximum tension variation is obtained for each leg of tethers for all the cases is listed in Table 5.16.

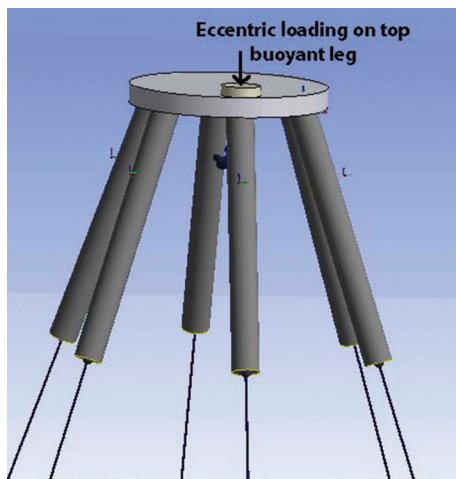


FIGURE 5.20 Eccentric loading on top of the buoyant leg (case 2).

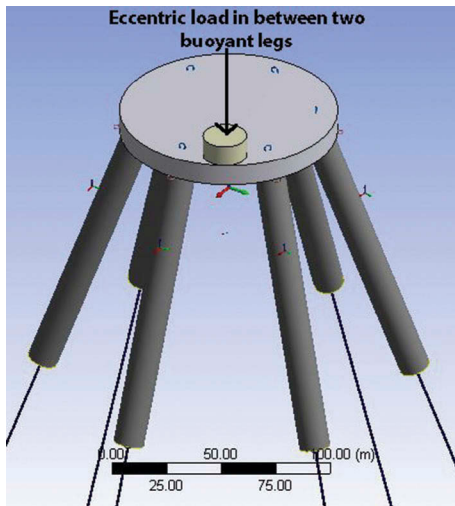


FIGURE 5.21 Eccentric load between two buoyant legs (case 3).

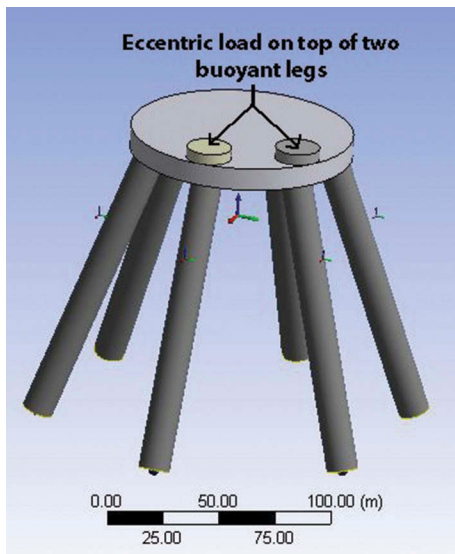
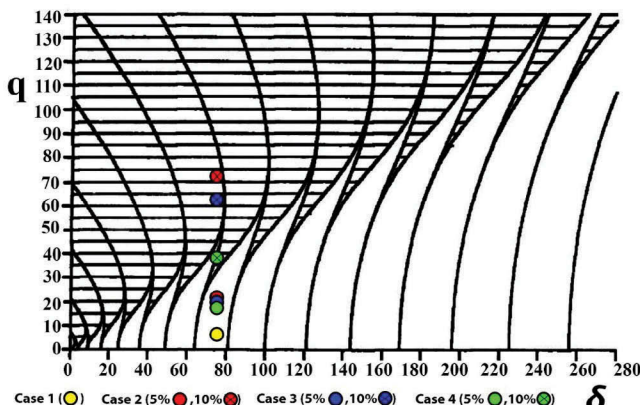


FIGURE 5.22 Eccentric load on top of two consecutive buoyant legs (case 4).

Detailed Mathieu stability analysis is carried out for all cases, and the Mathieu parameters are obtained and plotted in the extended Mathieu stability chart (Fig. 5.23). The parameter ' δ ' which depends on the stiffness and initial pretension of the tether remains constant for all the cases, whereas

TABLE 5.16 Tether tension variation for different eccentric loading cases

Description	Load	Cable 1 (MN)	Cable 2 (MN)	Cable 3 (MN)	Cable 4 (MN)	Cable 5 (MN)	Cable 6 (MN)	Max (MN)
Case 1	–	62.49	61.53	61.43	61.40	61.85	60.97	62.49
Case 2	5%	89.99	71.78	59.08	63.56	65.76	73.70	89.99
	10%	168.54	140.70	76.40	128.80	80.79	136.04	168.54
Case 3	5%	85.06	18.52	68.28	67.98	65.11	77.17	85.06
	10%	153.42	112.99	103.06	100.50	110.26	144.23	153.42
Case 4	5%	82.34	64.45	64.91	64.57	63.22	69.21	82.34
	10%	112.36	99.39	73.37	68.76	80.14	107.94	112.36

**FIGURE 5.23** Mathieu stability chart for eccentric loading.**TABLE 5.17** Mathieu parameters under eccentric loading

Description	Load	δ	q	Stability condition
Case 1	–	75.07	5.9	Stable
Case 2	5%	75.07	23.35	Stable
	10%	75.07	73.19	Unstable
Case 3	5%	75.07	20.22	Stable
	10%	75.07	63.6	Unstable
Case 4	5%	75.07	18.49	Stable
	10%	75.07	37.54	Stable (boundary)

parameter ‘ q ’ depends on the tension variation and hence differs for different cases. The stability condition obtained for each case along with Mathieu parameters is listed in Table 5.17.

For normal condition, case 1 and eccentric loading with 5% load for all cases show stable condition. For eccentric loading of 10%, case 2 and case 3 show an unstable condition, indicating a chaotic nature. It is vital to note that irrespective of the position of eccentric load considered, platform undergoes Mathieu-type instability for eccentric load >10% of the total mass of the structure.

5.8 NUMERICAL MODELING EXAMPLE OF TRICERATOPS

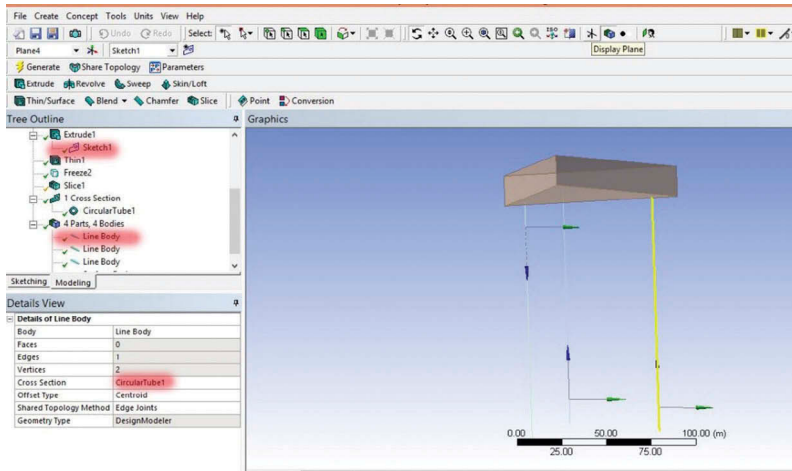
This section illustrates the step-by-step procedure to model the example problems in Ansys Aqwa software. Table 5.18 shows the structural properties of both triceratops and BLSRP platforms

TABLE 5.18 Structural properties of triceratops and BLSRP of example problems

Description	Triceratops	BLSRP	Units
Water depth	1069.36	1000	m
Total mass	320,500	641,000	kN
Buoyant force	470,440	940,880	kN
Diameter of buoyant leg	14.14	14.14	m
Plan dimension	99.80	100	m
Freeboard	33.12	33.12	m
Draft	99.36	99.36	m
Length of buoyant leg	132.48	132.48	m
Total tether force	149,940	319,125.60	kN
Pretension in each leg	49,980	53,187.61	kN
Tether length	970	964.81	m
No. of tethers	12	24	
Axial stiffness	76,830.67	76,830.67	kN/m

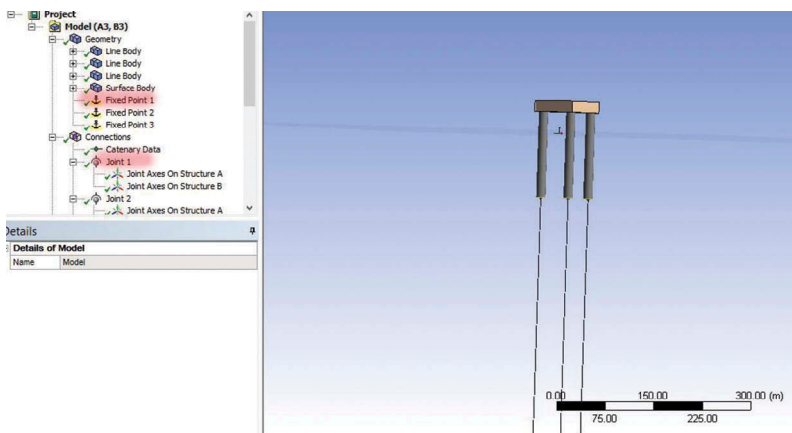
Step 1: Modeling of the deck and buoyant legs

The deck is modeled as a plate element, comprising of quadrilateral and triangular plate elements with appropriate mass properties. Buoyant legs are modeled as line elements as they qualify for the Morison region. An appropriate cross section is assigned to the buoyant legs.



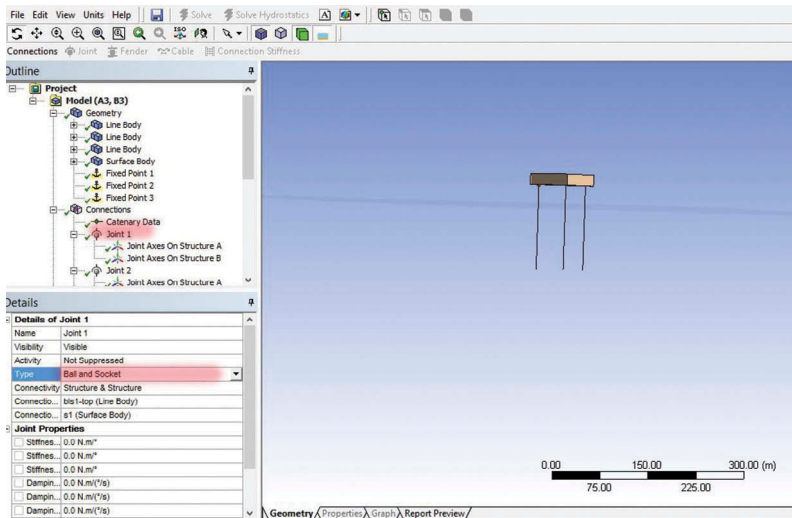
Step 2: Complete the numerical model

Buoyant legs and the deck are interconnected using ball joints. Buoyant legs are connected to the seabed using tethers to achieve the desired structural form of the model.



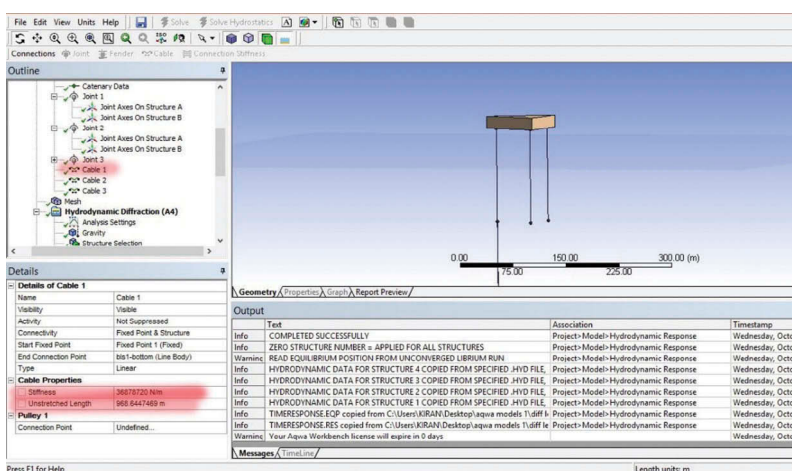
Step 3: Ball joints

Appropriate joints are created between the structural elements.



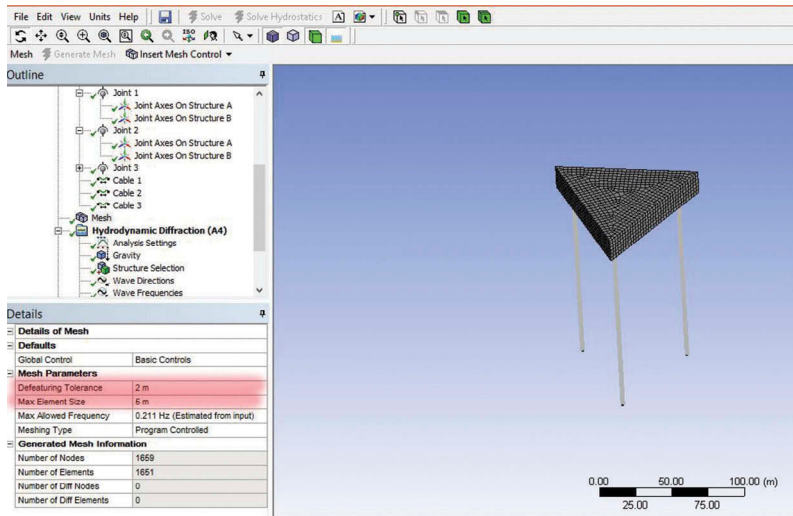
Step 4: Tethers and pretension

Cables properties and connections are defined. Pretension is applied to cables using appropriate stiffness. Length before applying tension is modeled as the unstretched length. By this manner, when the cable is stretched from seabed to bottom of the leg, required pretension is achieved in the cable, automatically. Once pretension is applied to the structure, it is balanced, and there exists an equilibrium between the draft, mass and tether force ($F_b - W - 3T_0 = 0$).



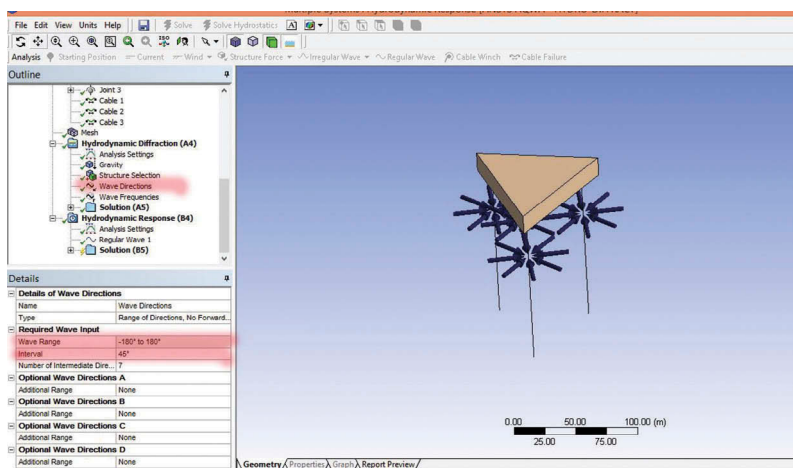
Step 5: Meshing

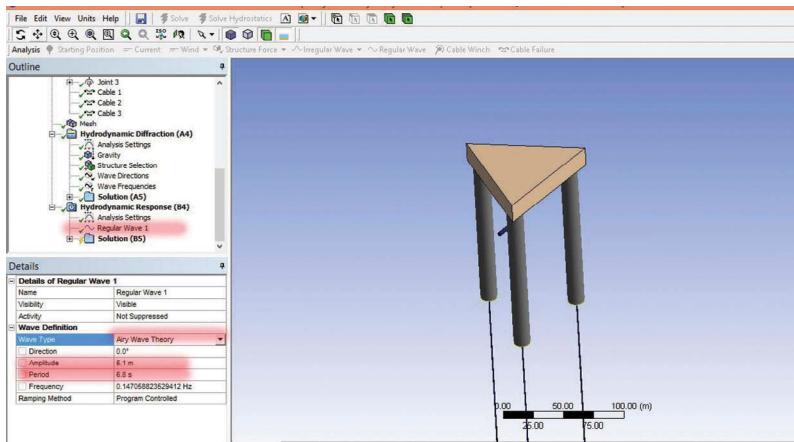
Once structural detailing and connections are completed, the mesh size of the model is fixed to suit the analysis requirements.



Step 6: Loading

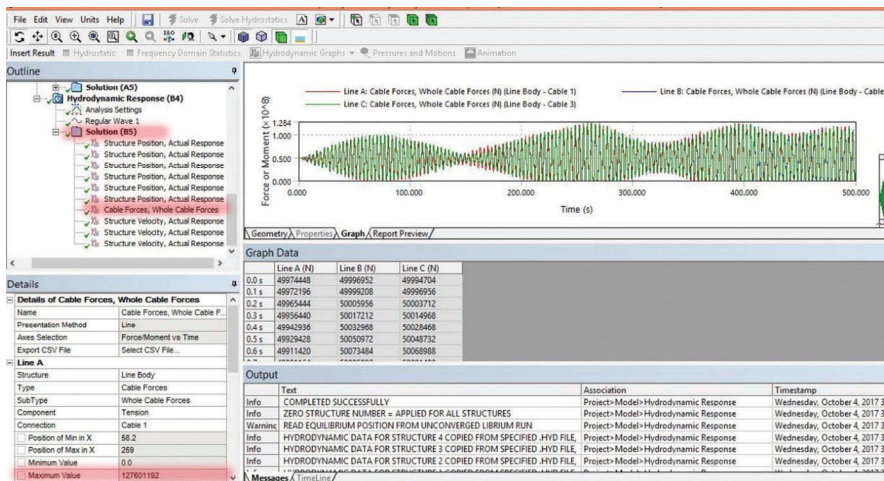
Self-weight of the members is added as a point mass to their respective mass center. The appropriate type of wave loading is selected (e.g., random or regular) from the menu with appropriate wave characteristics and direction.



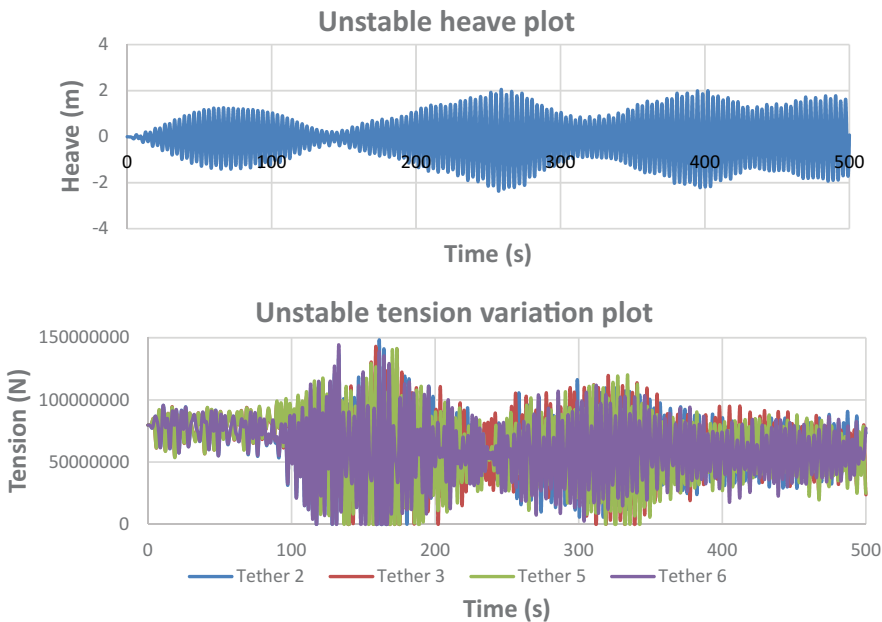


Step 7: Solver

Once analysis under regular wave load is completed, results for the response of the system in the time domain and frequency domain can be obtained. For Mathieu stability analysis, tether tension variation in the time domain is required.



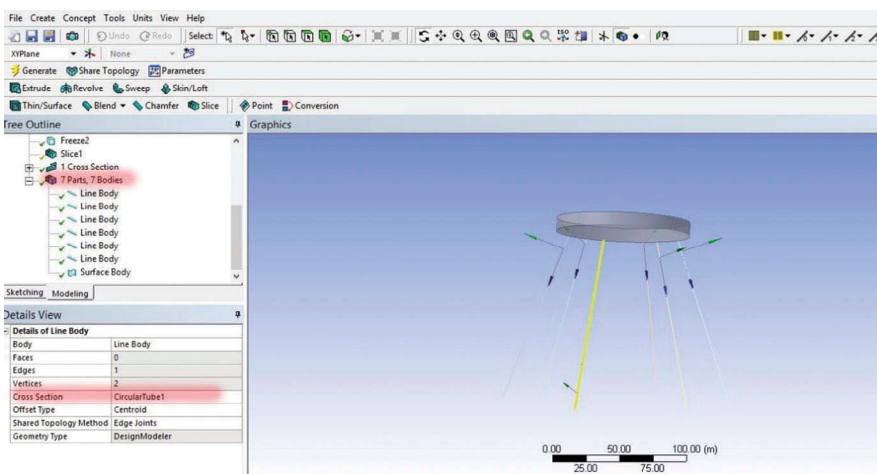
5.8.1 TYPICAL PLOTS OF MEMBERS SHOWING INSTABILITY



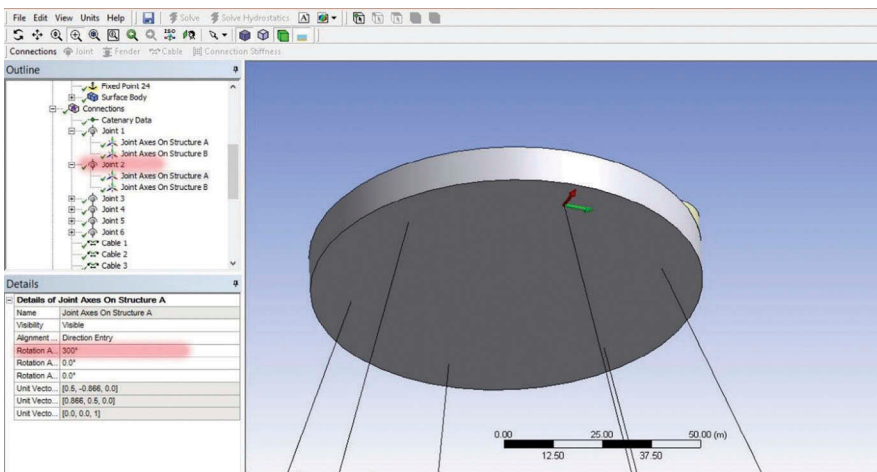
5.9 NUMERICAL MODEL OF BLSRP

Step 1: Basic geometry

Basic geometric changes such as a circular deck, six buoyant legs placed symmetrically.



Step 2: Hinged joint and its direction



All other steps are similar to that of the previous model. One can run the model to obtain the response plots.

References

- Agarwal, A. K., & Jain, A. K. 2003. Dynamic behavior of offshore spar platforms under regular sea waves. *Ocean Engineering*, 30(4): 487–516. 10.1016/S0029-8018(02)00034-3
- Amdahl, J., & Eberg, E. 1993. Ship collision with offshore structures. In Proc. of 2nd European Conf. on St. Dynamics (EURODYN'93), Trondheim, Norway, June (pp. 21–23).
- American Petroleum Institute. 2000. Recommended practice for planning, designing, and constructing fixed offshore platforms-working stress design. *API RP 2A*.
- Bowman, F. 1958. *Introduction to Bessel functions*, Dover Publications, New York.
- Burgen, B. A., Hamdan, F. H., Barker, D. D., & Puskar, F. J. 2003. Response of topside structures to fires and explosions: recent findings. In Proc. of ASME 22nd International Conference on Offshore Mechanics and Arctic Engineering. 155–162, 10.1115/OMAE2003-37183
- Cerik, B. C., Shin, H. K., & Cho, S. R. 2015. On the resistance of steel ring-stiffened cylinders subjected to low-velocity mass impact. *International Journal Impact Engineering*, 84: 108–123. 10.1016/j.ijimpeng.2015.04.011
- Chandak, N. R., & Chandrasekaran, S. 2009. Structural response of triangular tension leg platforms using dynamic Morison equation. In. Proc. of Second International Symposium on Computational Mechanics and Twelfth International Conference on Enhancing Computational methods in Engineering and Science (EPMESC), Hong Kong and Macao, 30 November–3 December. 10.1063/1.3452127
- Chandrasekaran, S. 2015a. *Advanced marine structures*, CRC Press, Boca Raton, FL.
- Chandrasekaran, S. 2015b. *Dynamic analysis and design of offshore structures*, 2nd ed., Springer, Singapore.
- Chandrasekaran, S. 2015c. *Dynamic analysis and design of offshore structures*, Springer, New Delhi.
- Chandrasekaran, S., & Chandak, N. R. 2004a. Offshore TLPs – A state of art. In. Proc. of National Conference on Materials and Structures (MAST), NIT, Warangal, India, pp. 204–209.
- Chandrasekaran, S., & Chandak, N. R. 2004b. Seismic behavior of road bridge abutments. Concrete India. *Journal of IC-ACI*, 19(1): 3–5.
- Chandrasekaran, S., Chandak, N. R., & Anupam, G. 2006a. Stability analysis of TLP tethers. *Technical Note of the Journal of Ocean Engineering*, 33(3–4): 471–482. 10.1016/j.oceaneng.2005.04.015
- Chandrasekaran, S., & Dubey, A. 2006. Modal pushover analysis for RC framed buildings. In Proc. of the National Conference on Earthquake Disaster: Technology and Management (EARTH-2006), Indian Geotechnical Society, Allahabad, 11–12 February, pp. II-10 - II-16.
- Chandrasekaran, S., Dubey, A. K., & Tripathi, U. K. 2006. Seismic behavior of SMRF under various structural irregularities. In Proc. of International Conference on Earthquake Engineering, School of Civil Engg, SASTRA, Deemed University, Tanjavur, Tamilnadu, February 25–26, pp. 139–148.
- Chandrasekaran, S., & Gaurav. 2008. Offshore triangular TLP earthquake motion analysis under distinctly high sea waves. *Ship and Offshore Structures*, 3(3): 173–184.

- Chandrasekaran, S., Gaurav, & Jain, A. K. 2009a. Ringing response of offshore compliant structures. In Proc. of International Conference in Ocean Engineering (ICOE 2009), IIT Madras, India, 1–5 February 2009, pp. 55–56.
- Chandrasekaran, S., Gaurav, & Srivastava, S. 2007d. Response behavior of TLPs under vertical ground excitation. Structural Engg. World Congress, Bangalore, India, December 2007, CD-ROM (Paper No. 167).
- Chandrasekaran, S., Gaurav, & Srivastava, S. 2008a. Steady and transient response of triangular TLPs under random wave load. In Seventh European Conference on Structural Dynamics (EuroDyn 2008), 7–9 July 2008, Southampton, UK, p. 50 (CD-ROM: Ref No. E64).
- Chandrasekaran, S., Gaurav, & Srivastava, S. 2008b. Structural response of Offshore TLPs under seismic excitations. *International Engineering and Technology Journal of Civil & Structures*, 1(1): 7–12.
- Chandrasekaran, S., & Gupta, V. 2007a. Nonlinear seismic analysis of buildings. In Proc. of International Conference on Vibration Problems, Bengal Engineering College, Kolkata, 28 January–3 February.
- Chandrasekaran, S., & Gupta, V. 2007b. Pushover analysis of RC framed structures structural engineering. In Proc. of World Congress, Bangalore, India, Dec.
- Chandrasekaran, S., Gupta, V., & Sharma, A. 2006b. Modal analysis of high rise buildings. In Proc. of 13th Symposium on Earthquake Engineering, IIT-Roorkee, 18–20 December 2006, Vol. 2, pp. 650–657.
- Chandrasekaran, S., & Jain, A. K. 2002a. Dynamic behavior of square and triangular offshore tension leg platforms under regular wave loads. *Ocean Engineering*, 29(3): 279–313.
- Chandrasekaran, S., & Jain, A. K. 2002b. Triangular configuration tension leg platform behaviour under random sea wave loads. *Ocean Engineering*, 29(15): 1895–1928. 10.1016/S0029-8018(01)00111-1
- Chandrasekaran, S., & Jain, A. K. 2016. *Ocean structures: Construction, Materials and Operations*, CRC Press, Boca Raton, FL.
- Chandrasekaran, S., Jain, A. K., & Chandak, N. R. 2004a. Offshore triangular TLP behavior under random sea waves using iterative frequency domain. In Proc. of 3rd National Conference in Harbour & Ocean Engineering (Inchoe-2004), NIOT, Goa, Vol. 1, pp. 315–325.
- Chandrasekaran, S., Jain, A. K., & Chandak, N. R. 2004b. Influence of hydrodynamic coefficients in the response behavior of triangular TLPs in regular waves. *Ocean Engineering*, 31(17–18): 2319–2342.
- Chandrasekaran, S., Jain, A. K., & Chandak, N. R. 2006c. Seismic analysis of offshore triangular Tension Leg Platforms. *International Journal of Structural Stability and Dynamics*, 6(1): 1–24.
- Chandrasekaran, S., Jain, A. K., & Chandak, N. R. 2007e. Response behavior of triangular Tension Leg Platforms under regular waves using stokes nonlinear wave theory. *Journal of Waterway, Port, Coastal, and Ocean Engineering*, 133(3): 230–237. 10.1061/(ASCE)0733-950X(2007)133:3(230)
- Chandrasekaran, S., Jain, A. K., & Gupta, A. 2007h. Influence of wave approach angle on TLP's response. *Ocean Engineering*, 8–9(34): 1322–1327.
- Chandrasekaran, S., Jain, A. K., Gupta, A., & Srivastava, A. 2007f. Response behavior of triangular tension leg platforms under impact loading. *Ocean Engineering*, 34 (1): 45–53.

- Chandrasekaran, S., Jain, A. K., Gupta, A., & Srivastava, A. 2007g. Response behaviour of triangular tension leg platforms under impact loading. *Ocean Engineering*, 34 (1): 45–53. 10.1016/j.oceaneng.2006.01.002
- Chandrasekaran, S., Jain, A. K., & Gupta, V. 2006a. Performance based design for RC framed buildings". In e-Proc. of 2nd International Congress on Computational Mechanics & Simulation (ICCMS-06), IIT, Guwahati, 8–10 December 2006.
- Chandrasekaran, S., Jain, A. K., & Kumar, M. 2006c. Blast vulnerability of coal waste dump during production blasting. In Proc. of International Conference on Earthquake Engineering, School of Civil Engineering, SASTRA, Deemed University, Tanjavur, Tamilnadu, February 25–26, pp. 516–526.
- Chandrasekaran, S., Jain, A. K., Serino, G., Spizzuoco, M., Srivastava, S., & Gupta, V. 2007c. Risk assessment of seismic vulnerabilities of RC framed buildings due to asymmetry. Eighth Pacific Conference on Earthquake Engineering, 5–7 December, 2007, Singapore, p. 110, CD ROM (Paper No. 026).
- Chandrasekaran, S., Jain, A. K., Sharma, A., & Srivastava, S. 2007b. Comparative study of square and triangular TLPs with varying hydrodynamic coefficients. Structural Engg. World Congress, Bangalore, India, December 2007, CD-ROM (Paper No. 152).
- Chandrasekaran, S., & Khader, S. A. 2016. Hydrodynamic performance of a moored barge in irregular wave. *International Journal of Environment, Chemical and Ecological Engineering*, 10(1): 47–54.
- Chandrasekaran, S., & Kiran, P. A. 2018a. Mathieu stability of offshore triceratops under postulated failure. *Ships and Offshore Structures*, 13(2): 143–148. 10.1080/17445302.2017.133578
- Chandrasekaran, S., & Kiran, P. A. 2018b. Mathieu stability of buoyant leg storage and regasification platform. *Journal of Ocean Systems Engineering*, 8(3): 345–360. 10.12989/ose.2018.8.3.345
- Chandrasekaran, S., Lahiri, S., Kumar, V., & Tripathi, U. K. 2003a. Study of seismic vulnerability and subsequent retrofitting of Ganga Mahal, Banaras. In Proc. of 2nd Specialty Conference in conceptual approach to structural design, Milan, Italy, 1–2 July 2003, Vol. 2, pp. 567–574.
- Chandrasekaran, S., Lahiri, S., & Kumar, V. 2003b. Study of seismic vulnerability and retrofitting techniques for heritage buildings in Banaras. In Proc. of International Conference on recent trends in concrete technology and structures (Incontest 2003), Coimbatore, India, pp. 699–707.
- Chandrasekaran, S., & Lognath, R. S. 2016. Dynamic analyses of Buoyant Leg Storage Regasification Platform (BLSRP) under regular waves: experimental investigations. *Ships and Offshore Structures*, 12(2): 171–181.
- Chandrasekaran, S., & Lognath, R. S. 2017a. Dynamic analyses of buoyant leg storage and re-gasification platforms: numerical studies. *Journal of Marine Systems and Ocean Technology*, 12(2): 39–48. 10.1007/s40868-017-0022-6
- Chandrasekaran, S., & Lognath, R. S. 2017b. Dynamic analyses of Buoyant leg storage and regasification platforms: numerical studies. *Journal of Marine Systems and Ocean Technology*, 12(2): 39–48.
- Chandrasekaran, S., Lognath, R. S., & Jain, A. 2015. Dynamic analysis of buoyant leg storage and regasification platform under regular waves. In Proc. of International Conference on Offshore Mechanics and Arctic Engineering, Volume 3: Structures, Safety and Reliability: V003T02A082. 10.1115/OMAE2015-41154.

- Chandrasekaran, S., & Madhuri, S. 2015. Dynamic response of offshore triceratops: numerical and experimental investigations. *Ocean Engineering*, 109: 401–409. 10.1016/j.oceaneng.2015.09.042
- Chandrasekaran, S., Madhuri, S., & Jain, A. K. 2013a. Aerodynamic response of offshore triceratops. *Ships and Offshore Structures*, 8(2): 123–140. 10.1080/17445302.2012.691271
- Chandrasekaran, S., & Mayank, S. 2017. Dynamic analyses of stiffened triceratops under regular waves: experimental investigations. *Ships and Offshore Structures*, 12 (5): 697–705. 10.1080/17445302.2016.1200957
- Chandrasekaran, S., Mayank, S., & Jain, A. K. 2015a. Dynamic response behaviour of stiffened triceratops under regular waves: experimental investigations. In ASME International Conference on Offshore Mechanics and Arctic Engineering, Volume 3: Structures, Safety and Reliability: V003T02A083. 10.1115/OMAE2015-41376
- Chandrasekaran, S., Muranjan, H., & Srivastava, S. 2006b. Seismic evaluation of RCC buildings with plan irregularities. In Proc. of 13th Symposium on Earthquake Engineering, IIT-Roorkee, 18–20 December 2006, Vol. 2, pp. 736–746.
- Chandrasekaran, S., & Nannaware, M. 2014. Response analyses of offshore triceratops to seismic activities. *Ships and Offshore Structures*, 9(6): 633–642. 10.1080/17445302.2013.843816
- Chandrasekaran, S., & Nassery, J. 2015a. Springing and ringing response of offshore triceratops. In ASME 2015 34th International Conference on Ocean, Offshore and Arctic Engineering (pp. V007T06A039-V007T06A039). American Society of Mechanical Engineers. 10.1115/OMAE2015-41551
- Chandrasekaran, S., & Nassery, J. 2015b. Springing and ringing response of offshore triceratops. In Proc. of 34th International Conference on Ocean, Offshore and Arctic Engineering (OMAE 2015), St. John's, NL, Canada, May 31–June 5, 2015. OMAE2015-41551
- Chandrasekaran, S., & Nassery, J. 2017a. Nonlinear response of stiffened triceratops under impact and non-impact waves. *International Journal of Ocean Systems Engineering*, 7(3): 179–193. 10.12989/ose.2017.7.3.179
- Chandrasekaran, S., & Nassery, J. 2017b. Ringing response of offshore triceratops. *Journal of Innovative Infrastructure Solutions*. 10.1007/s41062-017-0092-5
- Chandrasekaran, S., Nunziante, L., Serino, G., & Carannante, F. 2010a. Axial force-bending moment limit domain and flow rule for reinforced concrete elements using Euro Code. *International Journal of Damage Mechanics*, 19: 523–558.
- Chandrasekaran, S., Nunziante, L., Gupta, V., & Carannante, F. 2008a. Nonlinear seismic analyses of high rise reinforced concrete buildings. *ICFAI Journal of Structural Design, ICFAI Press*, 1(1): 7–24.
- Chandrasekaran, S., Nunziante, L., Serino, G., & Carannante, F. 2011a. Curvature ductility of RC sections based on Euro Code: analytical procedure. *Journal of Civil Engineering, Korean Society of Civil Engineers, Springer*, 15(1): 131–144.
- Chandrasekaran, S., & Roy, A. 2006. Seismic evaluation of multi-storey RC frames using modal pushover analysis. *International Journal of Nonlinear Dynamics*, 43(4): 329–342.
- Chandrasekaran, S., & Roy, A. 2004a. Comparison of modal combination rules in seismic analysis of multi-storey RC frames. In Proc. of 3rd International Conference on Vibration Engineering & Technology of Machinery and 4th Asia Pacific Conference on System Integrity & Maintenance (Vetomac-3), IIT-Kanpur, India, December 6–9, 2004, pp. 161–169.

- Chandrasekaran, S., & Roy, A. 2004b. Computational wave theories for deep water compliant Offshore structures. In. Proc. of International Conference on Environmental Fluid Mechanics (ICIFEM), IIT, Guwahati, March 2–3, pp. 138–145.
- Chandrasekaran, S., Roy, A., & Chandak, N. R. 2005a. Modal pushover analysis of multi-storey moment resisting framed buildings. In Proc. of International Conference on Structures and Road Transport (START 2005), IIT-Kharagpur, India, pp. 355–362.
- Chandrasekaran, S., & Seeram, M. 2012. Stability studies on offshore triceratops. *International Journal of Innovative Research and Development*, 1(10): 398–404.
- Chandrasekaran, S., Serino, G., & Gupta, V. 2008b. Performance evaluation assessment of buildings under seismic loading. In Tenth International Conference on Structures Under Shock and Impact (SUSI-2008), 14–16 May, 2008, Portugal, pp. 313–322.
- Chandrasekaran, S., Serino, G., & Gupta, V. 2007c. Performance evaluation & damage assessment of buildings subjected to seismic loading. In Sixth International Conference on Earthquake Resistant Engineering Structures (EERS-2007), 11–13 June, Bologna, Italy, CD-ROM (Paper No. 055).
- Chandrasekaran, S., & Sharma, A. 2010a. Dynamic response of floating offshore structures with perforated columns. In. Proc. of 9th International Conference on Hydro-science and Engineering (ICHE 2010), Madras, India, 2–5 August, 2010.
- Chandrasekaran, S., & Sharma, A. 2010b. Potential flow based numerical study for the response of floating offshore structures with perforated columns. *Ships and Offshore Structures*, 5(4): 327–336.
- Chandrasekaran, S., Sharma, A., & Srivastava, S. 2007a. Offshore triangular TLP behavior using dynamic Morison equation. *Structural Engineering*, 34(4): 291–296.
- Chandrasekaran, S., Srivastav, A., & Naha, P. 2005b. Analytical tools for shell structures. In Proc. of International Conference on Structures and Road Transport (START 2005), IIT-Kharagpur, India, pp. 167–175.
- Chandrasekaran, S., & Srivastava, A. 2006. Design aids for multi-barrel RC cylindrical shells. *Structural Engineering*, 33(4): 1–10.
- Chandrasekaran, S., & Srivastava, G. 2018. *Design aids of offshore structures under special environmental loads including fire resistance*, Vol. 11, Springer. 10.1007/978-981-10-7608-4
- Chandrasekaran, S., & Srivastava, S. 2007. Nonlinear dynamic analysis of asymmetric buildings under seismic forces. In Proc. of International Conference on Vibration Problems, Bengal Engineering College, Kolkata, 28 January–3 February.
- Chandrasekaran, S., & Thomas, M. 2016a. Suppression system for offshore cylinders under vortex induced vibration. *Vibroengineering Procedia*, 7: 1–6.
- Chandrasekaran, S., & Thomas, M. 2016b. Suppression system for offshore cylinders under vortex induced vibration. In Proc. of 21st Vibro-Engineering Conference, Berno, Czech Republic, 31 August–1 September, Vol., 7, pp. 1–6.
- Chandrasekaran, S., & Tripathi, U. K. 2005. Geometric irregularity effects on seismic vulnerability of buildings. *Advances in Vibration Engineering*, 4(2): 115–123.
- Chandrasekaran, S., & Tripathi, U. K. 2004. Seismic vulnerability of irregular buildings. In Proc. of 2nd International Conference on Protection of Structures against hazards, Singapore, 1–3 December, pp. 129–137.
- Chandrasekaran, S., Tripathi, U. K., & Srivastav, M. 2003. Study of plan irregularity effects and seismic vulnerability of moment resisting RC framed structures. In Proc. of 5th Asia Pacific Conference on Shock and Impact Loads, November 12–14, Changsha, China, pp. 125–136.

- Chandrasekaran, S. 2013a. Advanced marine structures, video course on NPTEL portal. Available at: <http://nptel.ac.in/courses/114106037>
- Chandrasekaran, S. 2013b. Dynamics of ocean structures, video course on NPTEL portal. Available at <http://nptel.ac.in/courses/114106036/>
- Chandrasekaran, S. 2013c. Ocean structures and materials, video course on NPTEL portal. Available at <http://nptel.ac.in/courses/114106035/>
- Chandrasekaran, S. 2014. *Advanced theory on offshore plant FEED engineering*, Changwon National University Press, Republic of Korea, p. 237.
- Chandrasekaran, S. 2015b. Dynamic analysis of offshore structures, video course on MOOC, NPTEL portal at https://onlinecourses.nptel.ac.in/noc15_oe01/preview
- Chandrasekaran, S. 2017a. *Dynamic analysis and design of ocean structures*, 2nd ed., Springer, Singapore.
- Chandrasekaran, S. 2017b. Offshore structures under special loads including fire resistance, Video course under MOOC, NPTEL portal. <http://nptel.ac.in/courses/114106043>
- Chandrasekaran, S. 2018a. *Advanced structural analysis with MATLAB*, CRC Press, Boca Raton, FL.
- Chandrasekaran, S. 2018b. Computer methods of analysis of offshore structures, Video course under MOOC, NPTEL portal <http://nptel.ac.in/courses/114106045>
- Chandrasekaran, S. 2018c. Structural health monitoring, video course under MOOC, NPTEL portal https://onlinecourses.nptel.ac.in/noc18_oe05/preview.
- Chandrasekaran, S. 2019a. Rerun course on offshore structures under special loads including fire resistance, video course under MOOC, NPTEL
- Chandrasekaran, S. 2019b. *Structural health monitoring with application to offshore structures*, World Scientific Publishing Co., Singapore.
- Chandrasekaran, S., Anchuri, P. K., & Dubey, A. 2005. Seismic vulnerability of asymmetric reinforced concrete framed buildings. In Proc. of International Convention of Structural Engineering Convention (SEC 2005), IISc Bangalore, p. 398.
- Chandrasekaran, S., & Bhattacharyya, S. K. 2012. Analysis and design of offshore structures with illustrated examples, p. 285. Human Resource Development Center for Offshore and Plant Engineering (HOPE Center), Changwon National University Press, Republic of Korea.
- Chandrasekaran, S., & Chithambaram, T. 2016. Health monitoring of offshore structures using wireless sensor network: experimental investigations. In Proc. SPIE 9804, Nondestructive Characterization and Monitoring of Advanced Materials, Aerospace, and Civil Infrastructure 2016, 980416 (April 8, 2016). Mar 20–24, Las Vegas, NV. 10.1117/12.2219208.
- Chandrasekaran, S., Chithambaram, T., & Khader, S. 2016. Structural health monitoring of offshore structures using wireless sensor networking under operational and environmental variability. In Proc. of 18th International Conference on Coastal and Ocean Engineering. January 12–13, Zurich, Switzerland, pp. 695–701.
- Chandrasekaran, S., Gaurav, & Jain, A. K. 2010a. Ringing response of offshore compliant structures. *International Journal of Ocean and Climate Systems*, 1(3–4): 133–144.
- Chandrasekaran, S., Gaurav, Serino, G., & Miranda, S. 2011b. Springing and ringing response of triangular TLPs. *International Shipbuilding Progress*, 58(2–3): 141–163.
- Chandrasekaran, S., Gupta, S. K., & Carnanannte, F. 2010b. Design aids for fixed support reinforced concrete cylindrical shells under uniformly distributed loads. *International Journal of Engineering, Science and Technology*, 1(1): 148–171.

- Chandrasekaran, S., Jain, A. K., & Chandak, N. R. 2007. Response behavior of triangular TLPs under regular waves using stokes non-linear wave theory. *ASCE Journal of Waterway, Port, Coastal and Ocean Engineering*, 133(3): 230–237.
- Chandrasekaran, S., & Kiran, P. A. 2017. Mathieu stability of offshore buoyant leg storage and regasification platform. In Proc. of 19th International Conference on Coastal and Ocean Engineering, World Academy of Science, Engineering and Technology (WASET), Paris, France, 21–22 September 2017, pp. 1605–1608.
- Chandrasekaran, S., & Koshti, Y. 2013. Dynamic analysis of a tension leg platform under extreme waves. *Journal of Naval Architecture Arch and Marine Engineering*, 10: 5968. 10.3329/jname.v10i1.14518
- Chandrasekaran, S., Kumar, D., & Ramanathan, R. 2013b. Dynamic response of tension leg platform with tuned mass dampers. *Journal of Naval Architecture and Marine Engineering*, 10(2): 149–156.
- Chandrasekaran, S., Kumar, D., & Ramanathan, R. 2014. Response control of TLP using tuned mass dampers, In Proc. of 33rd International Conference on Ocean, Offshore and Arctic Engineering, OMAE 2014, 8–13, June, San Francisco.
- Chandrasekaran, S., & Lognath, R. S. 2015. Dynamic analyses of buoyant leg storage regasification platform (BLSRP) under regular waves: experimental investigations. *Ships and Offshore Structures*, 12(2): 227–232.
- Chandrasekaran, S., & Madavi, N. 2014a. Retrofitting of offshore structural member using perforated cylinders. *SFA Newsletter*, 13: 10–11.
- Chandrasekaran, S., & Madhavi, N. 2014b. Variation of water particle kinematics with perforated cylinder under regular waves. In Proc. of ISOPE 2014, 15–20 June, Busan, South Korea (paper accepted- 2014-TPC-0254).
- Chandrasekaran, S., & Madhavi, N. 2014c. Hydrodynamic performance of retrofitted structural member under regular waves. *International Journal of Forensic Engineering, InderScience*, 2(2): 100–121.
- Chandrasekaran, S., & Madhavi, N. 2014d. Variations of water particle kinematics of offshore TLP's with perforated members: numerical investigations. In Proc. of Structural Engineering Convention 2014, IIT Delhi, India. 22–24 December, 2014.
- Chandrasekaran, S., & Madhavi, N. 2014e. Numerical study on geometrical configurations of perforated cylindrical structures under regular waves. *Journal of Performance of Constructional Facilities, ASCE*, 30(1): 04014185–1 to 12. 10.1061/(ASCE) CF.1943-5509.0000687
- Chandrasekaran, S., & Madhavi, N. 2015a. Estimation of force reduction on ocean structures with perforated members. In Proc. of 34th International Conference on Ocean, Offshore and Arctic Engineering (OMAE2015), St. John's, NL, Canada, May 31–June 5, 2015. OMAE2015-41153.
- Chandrasekaran, S., & Madhavi, N. 2015b. Flow field around a outer perforated circular cylinder under regular waves: numerical study. *International Journal of Marine System and Ocean Technology*, 10(2): 91–100.
- Chandrasekaran, S., & Madhavi, N. 2015c. Design aids for offshore structures with perforated members. *Ships and Offshore Structures*, 10(2): 183–203. 10.1080/17445302.2014.918309
- Chandrasekaran, S., & Madhavi, N. 2015d. Retrofitting of offshore cylindrical structures with different geometrical configuration of perforated outer cover. *International Journal of Shipbuilding Progress*, 62(1–2): 43–56. 10.3233/ISP-150115
- Chandrasekaran, S., & Madhavi, N. 2015e. Variation of flow field around twin cylinders with and without outer perforated cylinder: numerical studies. *China Ocean Engineering*, 30(5): 763–771.

- Chandrasekaran, S., Madhavi, N., & Natarajan, C. 2014a. Variations of hydrodynamic characteristics with the perforated cylinder. In Proc. of 33rd International Conference on Ocean, Offshore and Arctic Engineering, OMAE 2014, 8–13, June, San Francisco (paper accepted- 23455).
- Chandrasekaran, S., Madhavi, N., & Sampath, S. 2014b. Force reduction on ocean structures with perforated members. In Proc. of Structural Engineering Convention 2014, IIT Delhi, India. December 22–24, 2014.
- Chandrasekaran, S., & Madhuri, S. 2012. Free vibration response of offshore triceratops: experimental and analytical investigations. In 3rd Asian Conference on Mechanics of Functional Materials and Structures (ACFMS), 8–9 Dec, IIT Delhi, pp. 965–968.
- Chandrasekaran, S., Mayank, S., & Jain, A. 2015b. Dynamic response behavior of stiffened triceratops under regular waves: experimental investigations. In Proc. of 34th International Conference on Ocean, Offshore and Arctic Engineering (OMAE 2015), St. John's, NL, Canada, May 31–June 5, 2015. OMAE2015-41376.
- Chandrasekaran, S., & Nagavinothini, R. 2017a. Analysis and design of offshore triceratops in ultra-deep waters. In Proc. International Conference of Offshore Structures Analysis and Design, Nov 29–30, Melbourne, Australia.
- Chandrasekaran, S., & Nagavinothini, R. 2018a. Dynamic analyses and preliminary design of offshore triceratops in ultra-deep waters. *International Journal of Innovative Infrastructure Solutions*. 10.1007/s41062-017-0124-1
- Chandrasekaran, S., & Nagavinothini, R. 2018b. Dynamic analysis of offshore triceratops under forces due to ice crushing in ultra-deep waters. In Proc. 11th International Conference on marine Technology, MARTEC-2018, August 13–14, Kuala Lumpur, Malaysia.
- Chandrasekaran, S., & Nagavinothini, R. 2018c. Tether analyses of offshore triceratops under wind, wave and current. *Journal of Marine Systems and Ocean Technology*, 13: 34–42. 10.1007/s40868-018-0043-9
- Chandrasekaran, S., & Nagavinothini, R. 2019a. Ice-induced response of offshore triceratops. *Ocean Engineering*, 180: 71–96. 10.1016/j.oceaneng.2019.03.063
- Chandrasekaran, S., & Nagavinothini, R. 2019b. Tether analyses of offshore triceratops under ice loads due to continuous crushing. *International Journal of Innovative Infrastructure Solutions*. (in print). 10.1007/s41062-019-0212-5
- Chandrasekaran, S., & Nagavinothini, R. 2017b. Analysis and design of offshore triceratops under ultra-deep waters. *International Journal of Structural & Constructional Engineering, World Academy of Science, Engineering and Technology*, 11(11): 1505–1513.
- Chandrasekaran, S., Natarajan, M., & Saravanakumar, S. 2013c. Hydrodynamic response of offshore tension leg platforms with perforated members. *International Journal of Ocean and Climate Systems*, 4(3): 182–196.
- Chandrasekaran, S., Nunziate, L., Seriino, G., & Caranannate, F. 2009b. *Seismic design aids for nonlinear analysis of reinforced concrete structures*, CRC Press, Boca Raton, FL.
- Chandrasekaran, S., Pannerselvam, R., & Saravanakumar, S. 2012. Retrofitting of offshore tension leg platforms with perforated cylinders. In 3rd Asian Conf. on Mechanics of Functional Materials and Structures (ACFMS), 8–9 December, IIT Delhi.
- Chandrasekaran, S., Ranjani, R., & Kumar, D. 2017. Response control of tension leg platform with passive Damper: experimental investigations. *Ships and Offshore Structures*, 12(2): 171–181.

- Chandrasekaran, S., & Roy, A. 2005. Phase plane study of offshore structures subjected to nonlinear hydrodynamic loading. In Proc. of International Convention of Structural Engineering Convention (SEC 2005), IISc Bangalore, p. 397.
- Chandrasekaran, S., Seeram, M., Jain, A. K., & Gaurav. 2010b. Dynamic response of offshore triceratops under environmental loads. In Proc. International Conference of Marine Technology (MARTEC-2010), 11–12 December 2010, Dhaka, Bangladesh, pp. 61–66.
- Chandrasekaran, S., Serino, G., Jain, A. K., Miranda, S., Gupta, A., Gaurav, & Sharma, A. 2008c. Influence of varying inertia coefficient and wave directionality on TLP geometry. In Eighth ISOPE Asia/Pacific Offshore Mechanics Symposium (ISOPE-PACOMS -2008), 10–13 November 2008, Bangkok, Thailand.
- Chandrasekaran, S., & Srinath, V. 2013. Experimental investigations of dynamic response of tension leg platforms with perforated members. In Proc. of 32nd International Conf. on Ocean, Offshore and Arctic Engineering, OMAE 2013, Nantes, France, 9–14 June, 2013, OMAE 2013-10607.
- Chandrasekaran, S., & Srivastava, G. 2017. *Design aids for offshore structures under special environmental loads including fire resistance*, Springer, Singapore.
- Chandrasekaran, S., & Thailammai, C. T. 2018. Health monitoring of tension leg platform using wireless sensor networking: experimental investigations. *Journal of Marine Science and Technology*, 17: 87–100. 10.1007/s00773-018-0531-9
- Chen, Y., Zimmer, R. A., de Oliveira, J. G., & Jan, H. Y. 1985. Buckling and ultimate strength of stiffened cylinders: model experiments and strength formulations. In Offshore Technology Conference. Document ID: OTC-4853-MS.
- Cho, S. R., Choi, S. I., & Son, S. K. 2015. Dynamic material properties of marine steels under impact loadings. In Proc. of the 2015 World Congress on Advances in Structural Engineering and Mechanics, ASEM15. Incheon, South Korea.
- Davenport, A. G. 1961. The spectrum of horizontal gustiness near the ground in high winds. *Journal of Royal Meteorological Society*, 87(372): 194–211. 10.1002/qj.49708737208
- Do, Q. T., Muttaqie, T., Shin, H. K., & Cho, S. R. 2018. Dynamic lateral mass impact on steel stringer-stiffened cylinders. *International Journal of Impact Engineering*, 116: 105–126. 10.1016/j.ijimpeng.2018.02.007
- Donegan, E. M. 1991. The behaviour of offshore structures in fires. In Offshore Technology Conference. Offshore Technology Conference, Houston, Texas. 10.4043/6637-MS
- Ertas, A., & Lee, J. H. 1989. Stochastic response of tension leg platform to wave and current forces. *Journal of Energy Resources Technology*, 111(4): 221–230. 10.1115/1.3231428
- Feng, Y., Li, H., Li, C., Ruan, J., Zhang, Q., & Xu, W. (2017, June). Investigation on the structure strength and stability of ring stiffened cylindrical shell with long compartment and large stiffener. In ASME 2017 36th International Conference on Ocean, Offshore and Arctic Engineering (pp. V03BT02A034-V03BT02A034). American Society of Mechanical Engineers. 10.1115/OMAE2017-62153
- Fraldi, M., Nunziante, L., Chandrasekaran, S., Carannante, F., & Pernice, M. C. 2009. Mechanics of distributed fibre optic sensors for strain measurements on rods. *Structural Engineering*, 35(5): 323–333.
- Gambhir, M. L. 2004. *Stability analysis and design of structures*, Springer, New York.
- Glanville, R. S., Paulling, J. R., Halkyard, J. E., & Lehtinen, T. J. 1991. Analysis of the spar floating drilling production and storage structure. In Proc. Offshore Tech Conference. doi:10.4043/6701-MS

- Goldstein, S. 1929. Mathieu functions. *Transactions of Cambridge Philosophical Society*, 23: 303–336.
- Gruben, G., Langseth, M., Fagerholt, E., & Hopperstad, O. S. 2016. Low-velocity impact on high-strength steel sheets: an experimental and numerical study. *International Journal of Impact Engineering*, 88: 153–171. 10.1016/j.ijimpeng.2015.10.001
- Halkyard, J. E. (1996, January). Status of spar platforms for deepwater production systems. In *The Sixth International Offshore and Polar Engineering Conference*. International Society of Offshore and Polar Engineers. Document ID:ISOPE-I-96-039.
- Harding, J. E., Onoufriou, A., & Tsang, S. K. 1983. Collisions—what is the danger to offshore rigs. *Journal of Constructional Steel Research*, 3(2): 31–38. 10.1016/0143-974X(83)90020-2
- Haritos, N. 1985. Modelling the response of tension-leg platforms to the effects of wind using simulated traces. *Mathematics and Computers in Simulation*, 27(2–3): 231–240. 10.1016/0378-4754(85)90044-8
- Haslum, H.A., & Faltinsen, O.M. 1999. Alternative shape of spar platforms for use in hostile areas. In Proceedings of the 31st Offshore Technology Conference, Houston, pp. 217–228, (OTC 10953).
- Ince, E. L. 1925. Researches into the characteristic numbers of the Mathieu equation. *Proceedings of Royal Society of Edinburgh*, 46: 9–20.
- Jain, A. K., & Chandrasekaran, S. 1997. Aerodynamic effects of offshore TLPs. In Proc. of 2nd National Seminar on Wind Effects on Structures, SERC, Ghaziabad, pp. 147–156.
- Jain, A. K., & Chandrasekaran, S. 2004. Aerodynamic behavior of offshore triangular TLPs. Proc. of 14th International Society of Offshore and Polar Engineering Conference (ISOPE), Toulon, France, May 23–28, pp. 564–569.
- Jefferys, E. R., & Patel, M. H. 1982. Dynamic analysis models of tension leg platforms. *Journal of Energy Resources Technology*, 104: 217–223.
- Jin, W. L., Song, J., Gong, S. F., & Lu, Y. 2005. Evaluation of damage to offshore platform structures due to collision of large barge. *Engineering Structures*, 27(9): 1317–1326. 10.1016/j.engstruct.2005.02.010
- Jin, Y., & Jang, B. S. 2015. Probabilistic fire risk analysis and structural safety assessment of FPSO topside module. *Ocean Engineering*, 104: 725–737. 10.1016/j.oceaneng.2015.04.019
- Karroum, C. G., Reid, S. R., & Li, S. 2007. Indentation of ring-stiffened cylinders by wedge-shaped indenters—Part 1: an experimental and finite element investigation. *International Journal of Mechanical Sciences*, 49(1): 13–38. 10.1016/j.ijmecsci.2006.08.020
- Khedmati, M. R., & Nazari, M. 2012. A numerical investigation into strength and deformation characteristics of preloaded tubular members under lateral impact loads. *Marine Structures*, 25(1): 33–57. 10.1016/j.marstruc.2011.07.003
- Kim, K. J., Lee, J. H., Park, D. K., Jung, B. G., Han, X., & Paik, J. K. 2016. An experimental and numerical study on nonlinear impact responses of steel-plated structures in an Arctic environment. *International Journal of Impact Engineering*, 93: 99–115. 10.1016/j.ijimpeng.2016.02.013
- Koo, B. J., Kim, M. H., & Randall, R. E. 2004. Mathieu instability of a spar platform with mooring and risers. *Ocean Engineering*, 31(17–18): 2175–2208.
- Liu, B., & Soares, C. G. 2016. Experimental and numerical analysis of the crushing behaviour of stiffened web girders. *International Journal of Impact Engineering*, 88: 22–38. 10.1016/j.ijimpeng.2015.09.004

- Livesley, R. K., & Chandler, D. B. 1956. *Stability functions for structural framework*, Manchester University Press, Manchester, UK.
- Manco, M. R., Vaz, M. A., Cyrino, J. C., & Landesmann, A. 2013. Behavior of stiffened panels exposed to fire. In Proc. of IV MARSTRUCT, Espoo, Finland, 101–108.
- McLachlan, N. W. 1947. *Theory and application of Mathieu functions*, Clarendon Press, Oxford, UK.
- Morin, D., Kårstad, B. L., Skajaa, B., Hopperstad, O. S., & Langseth, M. 2017. Testing and modelling of stiffened aluminium panels subjected to quasi-static and low-velocity impact loading. *International Journal of Impact Engineering*, 110: 97–111. 10.1016/j.ijimpeng.2017.03.002
- Nagavinothini, R., & Chandrasekaran, S. 2019. Dynamic analyses of offshore triceratops in ultra-deep waters under wind, wave, and current. *Structures*, 20: 279–289. Elsevier. 10.1016/j.istruc.2019.04.009
- Oltedal, H. A. 2012. Ship-platform collisions in the North Sea. In The 11th International Probabilistic Safety Assessment and Management Conference and the Annual European Safety and Reliability Conference (ESREL), Helsinki, Finland. <http://hdl.handle.net/11250/151419>.
- Paik, J. K., & Czujko, J. 2013. Engineering and design disciplines associated with management of hydrocarbon explosion and fire risks in offshore oil and gas facilities. *Transactions SNAME*, 120: 167–197.
- Paik, J. K., Czujko, J., Kim, J. H., Park, S. I., Islam, S., & Lee, D. H. 2013. A new procedure for the nonlinear structural response analysis of offshore installations in fires. *Transactions SNAME*, 121: 224–250.
- Patel, M. H., & Park, H. I. 1991. Dynamics of tension leg platform tethers at low tension. Part I – Mathieu stability at large parameters. *Marine Structures*, 4(3): 257–273.
- Quiel, S. E., & Garlock, M. E. 2010. Calculating the buckling strength of steel plates exposed to fire. *Thin-Walled Structures*, 48(9): 684–695. 10.1016/j.tws.2010.04.001
- Reddy, D. V., & Swamidas, A. S. J. 2016. *Essentials of offshore structures: framed and gravity platforms*, CRC Press, Boca Raton, FL.
- Rho, J. B., Choi, H. S., Shin, H. S., & Park, I. K. 2005. A study on mathieu-type instability of conventional spar platform in regular waves. *International Society of Offshore and Polar Engineers*, 15(2): 104–108.
- Ronalds, B. F., & Dowling, P. J. 1988. Collision resistance of orthogonally stiffened shell structures. *Journal of Constructional Steel Research*, 9(3): 179–194. 10.1016/0143-974X(88)90088-0
- Roy, S., Ghosh, V., Dey, S., Vimmadi, S., & Banik, A. K. 2017. A coupled analysis of motion and structural responses for an offshore spar platform in irregular waves. *Ships and Offshore Structures*, 12(Suppl. 1): S296–S304. 10.1080/17445302.2016.1256183
- Serino, G., Chandrasekaran, S., Marsico, M. R., & Spizzuoco, M. 2008c. Description and analytical modelling of the JETPACS prototype steel frame". In 2nd Annual Meeting of Reluis Executive Project, Reluis- DPC 2005-2008, 17–18 January 2008, Florence, Italy.
- Serino, G., Marsico, M. R., Chandrasekaran, S., & Spizzuoco, M. 2008a. Seismic isolation and modelling of a worship structure. In Proc. of Fourth European Conference on Structural Control, Vol. 2, Institute of Problems in Mechanical Engineering, Russian Academy of Sciences, 8–12 September 2008, Saint Petersburg, Russia, pp. 711–718.
- Serino, G., Spizzuoco, M., Marsico, M. R., & Chandrasekaran, S. 2008b. The monitoring system of an isolated religious building in Italy: a recent acquisition of the

- Italian observatory of structures". In Proc. of Fourth European Conference on Structural Control, Institute of Problems in Mechanical Engineering, Russian Academy of Sciences, September 8–12 2008, Saint Petersburg, Russia, Vol. 2, pp. 737–744.
- Shaver, C. B., Capanoglu, C. C., & Serrahn, C. S. 2001. Buoyant leg structure preliminary design, constructed cost and model test results. In The Eleventh International Offshore and Polar Engineering Conference. International Society of Offshore and Polar Engineers. Document ID: ISOPE-1-01-065.
- Siddiqui, N. A., & Ahmad, S. 2001. Fatigue and fracture reliability of TLP tethers under random loading. *Marine Structures*, 14(3): 331–352. 10.1016/S0951-8339(01)00005-3
- Simos, A. N., & Pesce, C. P. 1997. Mathieu stability in the dynamics of TLP tether considering variable tension along the length. *Transactions on Built Environment*, 29: 175–186.
- Singh, N. K., Cadoni, E., Singha, M. K., & Gupta, N. K. 2011. Dynamic tensile behavior of multi-phase high yield strength steel. *Materials & Design*, 32(10): 5091–5098. 10.1016/j.matdes.2011.06.027
- Soares, C. G., Gordo, J. M., & Teixeira, A. P. 1998. Elasto-plastic behaviour of plates subjected to heat loads. *Journal of Constructional Steel Research*, 45(2): 179–198. 10.1016/S0143-974X(97)00062-X
- Soares, C. G., & Teixeira, A. P. 2000. Strength of plates subjected to localised heat loads. *Journal of Constructional Steel Research*, 53(3): 335–358. 10.1016/S0143-974X(99)00045-0
- Storheim, M., & Amdahl, J. 2014. Design of offshore structures against accidental ship collisions. *Marine Structures*, 37: 135–172. 10.1016/j.marstruc.2014.03.002
- Tao, W., & Jun, Z. 2006. Hydrodynamics in Deep water TLP tendon design. *Journal of Hydrodynamics, Ser. B*, 18(3, Supplement): 386–393.
- Timoshenko, S. P., & Gere, J. M. 1961. *Theory of elastic stability*, McGraw-Hill Book Co., New York.
- Ufuah, E. 2012. The behaviour of stiffened steel plated decks subjected to unconfined pool fires. In Proc. of the World Congress on Engineering and Computer Science, San Francisco, Vol. 2, pp. 24–26.
- Ufuah, E., & Tashok, T. H. 2013. Behaviour of stiffened steel plates subjected to accidental loadings. *Engineering Letters*, 21(2). www.engineeringletters.com/issues_v21/issue_2/EL_21_2_07.pdf.
- DNVGL-RP-C204. 2010b. Design against accidental loads. *Recommended Practice* p. 114.
- Villavicencio, R., & Soares, C. G. 2012. Numerical modelling of laterally impacted plates reinforced by free and end connected stiffeners. *Engineering Structures*, 44: 46–62. 10.1016/j.engstruct.2012.05.024
- Wang, B., Tang, Y., Li, W., & Zhai, J. 2016. Dynamic analysis of a tension leg platform under combined wind and wave loads within the typhoon area. In ASME 2016 35th International Conference on Ocean, Offshore and Arctic Engineering (pp. V007T06A059-V007T06A059). American Society of Mechanical Engineers. 10.1115/OMAE2016-54576

Index

Note: Page locators in italics refers to “figures” and page locators in bold refers to “tables”

A

- Ansys, 116–18, 124
- auto-ignition temperature (AIT), 109–11
- blast loads, 91–2
 - designs, buildings, 99–104
 - frame loading, 103
 - front wall load, 99–100
 - rear wall load, 102
 - roof load, 102
 - side wall load, 100–2
- blast-resistant design, 89–91
 - Deep-Water Horizon, 90
 - design example, 104–8
 - Piper Alpha, 89

B

- blast wavelength (L_w), 96, 97
- blast wave parameters
 - blast wavelength (L_w), 97
 - negative impulse (I_o), 96
 - negative phase duration (t_d), 96
 - peak dynamic pressure (q_o), 97
 - peak reflected pressure (P_r), 96
 - peak side-on negative overpressure (P_{so}), 96
 - peak side-on positive overpressure (P_{so}), 96
 - positive impulse (I_o), 96
 - positive phase duration (t_d), 95, 96
 - pressure waves (P-waves), 94
 - shock front velocity (U), 97
 - shock wave (S-waves), 94
- blast waves, 91, 104, 110
- BLS, *see* buoyant leg structures (BLS)
- BLSRP, *see* buoyant leg storage and regasification platform (BLSRP)
- buckling load
 - kinematic degrees of freedom, 202–14
 - stability functions, 202–14, **218–29**
- buoyant leg storage and regasification platform (BLSRP), 7–9, 8, 234, 235
 - features of, 248
 - Mathieu stability, 248–58
 - numerical modeling, 248–50, 249
- buoyant leg structures (BLS), 5, 6, 248

C

- Castigliano’s theorem, 35

- catenary mooring system, 232
- CFD, *see* computational fluid dynamics (CFD)
- Chamberlain equation, 112
- circular section, 57–8
- collapse load, 65, 66
 - estimation exercises, 68–74
- compliance, 248
- computational fluid dynamics (CFD), 91
- condensed phase explosion, 94
- curved beams, 32–41

D

- ductility, 1, 49, 50, 120
- ductility design, 121
- dust explosions, 94
- dynamic buckling, 138
- dynamic equation, 236

E

- elastic analysis *vs.* plastic analysis, 74
- elastic–plastic method, 119–20
- Euler critical load, 139–41
- Euler’s static criterion, 133–4
- explosions, classifications of, 92–4
- extrados, 36, 40

F

- FGM, *see* functionally graded material (FGM)
- fire
 - categorization of, 109–10
 - characteristics of, 110–11
 - classification of, 111–13
 - design for, 119–20
 - explosion, 108
 - protection system, 113–14
 - fireball, 93, 111, 113
 - fire load, 108–9
 - fire point, 109–11
 - flame arrestor, 113
 - flash fire, 93, 113
 - flashpoint, 111
 - flexural buckling (FB), 135
 - flexural–torsional buckling (FTB), 135–7
- floating storage regasification units (FSRU), 7
- Floquet theorem, 233
- functionally graded material (FGM), 129–32

- material characteristics, 132
stress-strain curve, 131
- H**
Hooke's law, 51
- I**
instability, 8, 134, 135, 138, 139, 231, 235, 245
intrados, 36, 40
- J**
jet fire, 112–13
- K**
kinematic theorem, 66–8, 76
kinetic energy, 121–2
- L**
lateral load functions
 concentrated load, 164–7
 under uniformly distributed load, 159–63
lateral motion, 234, 238
lateral-torsional buckling (LTB), 135, 137, 138, 138
L'Hospital rule, 154, 162, 163, 167
Liapunov's condition, 134
linear elastic method, 119
load carrying capacity, 49, 65, 133–5
load–deformation relationship, 124, 135
lower bound theorem, *see* static theorem
- M**
Mathieu equation, 231, 233–6
 Floquet theorem, 233
 formulation of, 236–8
 Galerkin method, 234
 mathematical model, 238–9
 perturbation method, 236
Mathieu extended stability chart, 239
Mathieu instability, 235
Mathieu parameters, 233, 235, 236, 238
Mathieu stability, 231, 234, 234, 235
 BLSRP, 248–58
 compliant structures, 234–5
 eccentric loading, 255–7, 255–8, 257
 numerical model, 248–9
 tether pullout, 250–5, 254
 tether stiffness, 245–6, 246
 triceratops, 235–9
moment curvature relationship, 63–5
- mooring lines
 steel chain, 231
 steel wire ropes, 232
 synthetic ropes, 232
- mooring systems
 catenary, 232
 taut, 232
 turret, 232–3, 232
- N**
new-generation offshore platforms, 5–9
Newmark's equation, 96
non-uniplanar bending, *see* unsymmetrical bending
NORSOK, 120
numerical model
 BLSRP, 263–4
 triceratops, 239, 240, 258–63
- O**
offshore deck plate, behaviour of, 116–18
offshore platforms, 113, 122
 complaint, 2–5
 energy absorption, 122–4
 new-generation, 5–9
 steel deck, 116–18
- P**
plastic analysis
 advantages, 74
 assumptions, 51–2
 disadvantages, 74
 structures of, 51
 theorems, 66, 68
plastics, design of
 collapse load estimation, 68–74
 kinematic theorem, 66–8
 mechanism, 65–6
 moment curvature relationship, 63–5
 shape factors, 54–8
 static theorem, 66
 uniqueness theorem, 68
plastic, structural behaviour, 49–54
pool fire, 111–12
pressure vessel explosion (PVE), 93–4
pressure waves (P-waves), 94, 95
PVE, *see* pressure vessel explosion (PVE)
- R**
recentering, 5, 134, 231
rectangular section, 54–5
reserve strength, 49

S

shape factor, 54, **58**
shape factor, MATLAB code, 58–61
shared-energy design, 121
ship-platform collision, 89, 120–2
shock waves (S-waves), 94, 95
stability, 1–2, **136**
 buckling and instability, 134–9
 conditions of, 133–4
 criteria of, 133
 failures of, 2
 functions, 150–8, **218–29**
 illustrations, 136
 structural system, 1
stability analysis, exercise problems, 168–201
stability parameters, influence of, 239–48
 increased payload, 246–8, **247**, 248
 tether stiffness, **245**, 245–6, 246
 water depth, 243–5, **244**, **244**
 wave height, 239–42
 wave period, 242–3
standard beam element, 141–50, **142**
 degree of freedom, 142
 rotational coefficients, 147–50
 stiffness coefficients, 143
static theorem, 66, 75
steel, 1, 50, 114
 at high temperature, 114–16
 stress-strain curve, 49
stiffened cylinders, design of, 9–15
 buckling modes, 9
 classification of, 9
stiffeners, 9
strength design, 121
stress–strain curve, 49
stress–strain relationship, 2, 119
stringers, 9
structural systems, 231
 buckling load, 201–29
 examples of, 231
 stability, 1–2, 133–4

T

taut-moored tethers, 4, 7, 8
taut mooring systems, 232
tensile axial load, 163–4
tension buoyant tower, 5
tension leg platform (TLP), 2, 4–7, 133, 134, 231, 232, 235, 248
tethers
 lateral motion, 234, 238
TLP, *see* tension leg platform (TLP)
torsional buckling (TB), 135, 136
toughness, 1
triangular section, 55–7, **56**
triceratops, 6–7, 7, 124, 234, 239, 242, 243
 buoyant legs, impact analysis, 124–9
 numerical model, 239, 240, 258–63
turret-mooring system, 232, 232, 232–3

U

uniqueness theorem, 68
unsymmetrical bending, 15–20
upper bound theorem, *see* kinematic theorem

V

vapor cloud explosion (VCE), 92–3
Von-Mises yield criteria, 117

W

Winkler Bach equation, 40

Y

Young's modulus, 119, 120, 124, 132

Z

zero axial loads, 154, 157, 162, 167
zone method, 119



Taylor & Francis Group
an informa business

Taylor & Francis eBooks

www.taylorfrancis.com

A single destination for eBooks from Taylor & Francis with increased functionality and an improved user experience to meet the needs of our customers.

90,000+ eBooks of award-winning academic content in Humanities, Social Science, Science, Technology, Engineering, and Medical written by a global network of editors and authors.

TAYLOR & FRANCIS EBOOKS OFFERS:

A streamlined experience for our library customers

A single point of discovery for all of our eBook content

Improved search and discovery of content at both book and chapter level

REQUEST A FREE TRIAL
support@taylorfrancis.com

 **Routledge**
Taylor & Francis Group

 **CRC Press**
Taylor & Francis Group

@Seismicisolation